Growth characteristics and physical properties of $PbTe/BaF_2$ prepared under nonequilibrium conditions

S. V. Plyatsko

Institute of Semiconductor Physics, Ukrainian National Academy of Sciences, 252650 Kiev, Ukraine
(Submitted May 26, 1997; accepted for publication July 14, 1997)
Fiz. Tekh. Poluprovodn. **32**, 257–260 (March 1998)

$PbTe/BaF_2$ films were grown under nonequilibrium conditions by laser-modulated epitaxy. The structural properties of the layers were investigated by x-ray crystallographic methods and scanning tunneling microscopy. It was established that the films obtained under nonequilibrium conditions on (III)BaF_2 substrates are granular ($d \leqslant 250$ Å) with (001) orientation. The electrophysical and photoelectric properties of the films depend on the technological conditions of growth and are determined by states at intergrain boundaries. © *1998 American Institute of Physics.* [S1063-7826(98)01603-2]

There are a large number of works on the preparation and investigation of layers of IV–VI semiconductor compounds. Most of these works studied the electrophysical and photoelectric properties of PbSnTe films grown by different thermal methods on BaF_2 and NaCl(KCl) substrates, whose thermal expansion coefficient and lattice constant are closest to those of the solid solutions PbSnTe. The properties of the grown layers are virtually identical to those of the bulk single crystals. New methods of growth have now been developed — laser-molecular and electron-beam epitaxy, which in application to IV–VI compounds have shown that it is possible to obtain layers whose properties differ substantially from those of films and bulk single crystals grown by conventional methods.[1–5]

In the present work we performed diverse investigations of $PbTe/BaF_2$ films (electrophysical, photoelectric, structural) grown by modulated deposition with laser vaporization of the source–target in a wide range of substrate temperatures and laser radiation power densities. In contrast to laser-molecular epitaxy,[6,7] where a semiconductor target is vaporized by radiation pulses with a high power density ($W > 10^6$ W/cm^2) and photon energy $\hbar\omega \geqslant E_g$, we employed an infrared (IR) laser ($\hbar\omega < E_g$) with modulated radiation and power density on target $W \leqslant 10^5$ W/cm^2. The laser-modulated epitaxy (LME) apparatus contains, besides an IR laser, an optical system for introducing and focusing the radiation, a mechanical modulation system, a vacuum chamber, a radiation scanning apparatus (rotation of the source is combined with translational motion), and a unit for heating and controlling the temperature of the substrates. The layers were deposited with a residual vapor pressure $p = (1-2) \times 10^{-6}$ torr and radiation power density on target $W = (10^4 - 10^5)$ W/cm^2. The pulse duration was $\tau = (3-6) \times 10^{-3}$ s and the pulse repetition frequency was 12–25 Hz. The substrate temperature T_s was varied from 20 to 400 °C. The deposition rate depended on the power density of the laser radiation, the pulse duration, and the distance between the substrates and the target–source.

Modulated or pulsed laser radiation is required to vaporize the target–source material so as to localize the delivered energy in the zone of the laser spot without substantial heat being removed by the crystal during the time the laser pulse acts. This is possible if the semiconductor source has a low thermal conductivity and a high vapor pressure. Furthermore, if the source is a binary or more complicated compound, then its dissociation energy is important. When the compound dissociates, a liquid phase, which has a lower vapor pressure, of the metallic component accumulates in the zone of action of the radiation and is carried out by the erosion plume into the condensation region, i.e., onto the substrate. One of the few semiconductor compounds satisfying these requuirements are narrow-gap IV–VI semiconductors and their solid solutions.

The main mechanism of radiation ($\hbar\omega < E_g$) absorption by the target–source is absorption by free carriers. Depending on the carrier density in the single-crystal target ($P^{\mathrm{PbTe}} = 10^{18} - 10^{19}$ cm^{-3}) the absorption coefficient α can reach values $\alpha = (10^2 - 10^3)$ cm^{-1}. For such values of the absorption coefficient $\alpha^{-1} \ll (Dt)^{1/2}$ ($D = K/c\rho$ is the thermal diffusivity, K is the thermal conductivity, c is the specific heat, ρ is the density of the material, and t is the time) the surface temperature of the sample will equal

$$T = T_0 + 2P_0^*(\pi Dt)^{1/2}/\pi K, \tag{1}$$

where T_0 is the temperature of the semiconductor crystal before the action of the laser radiation, $P_0^* = (1-R)P_0$, R is the reflection coeffcient, and P_0 is the power density of the laser radiation. Estimates (using the parameters K, c, ρ, and R for PbTe)[8] show that the temperature in the zone where the laser radiation interacts with the target–source during the deposition process can reach $T \simeq 2520$ K. The vapor pressure of the sputtered PbTe at this temperature is 10^6 times higher than the equilibrium value. This indicates that when laser radiation is used for vaporizing the target–source, the growth of PbTe films occurs under extermely nonequilibrium conditions. Considering the fact that the surface energy of the condensed material is much lower than that of the BaF_2 substrate, such conditions of growth should promote a decrease

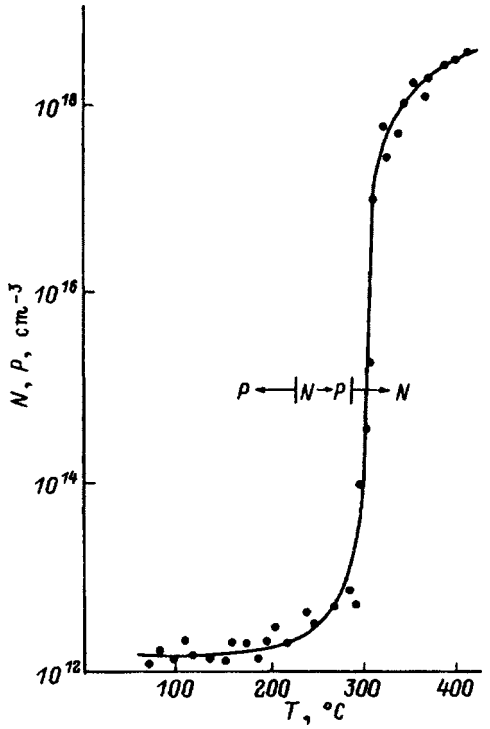

FIG. 1. Current carrier density ($T=77$ K) in PbTe/BaF_2 films versus substrate temperature with laser power density $W=8.5\times10^4$ W/cm^2 on the target–source.

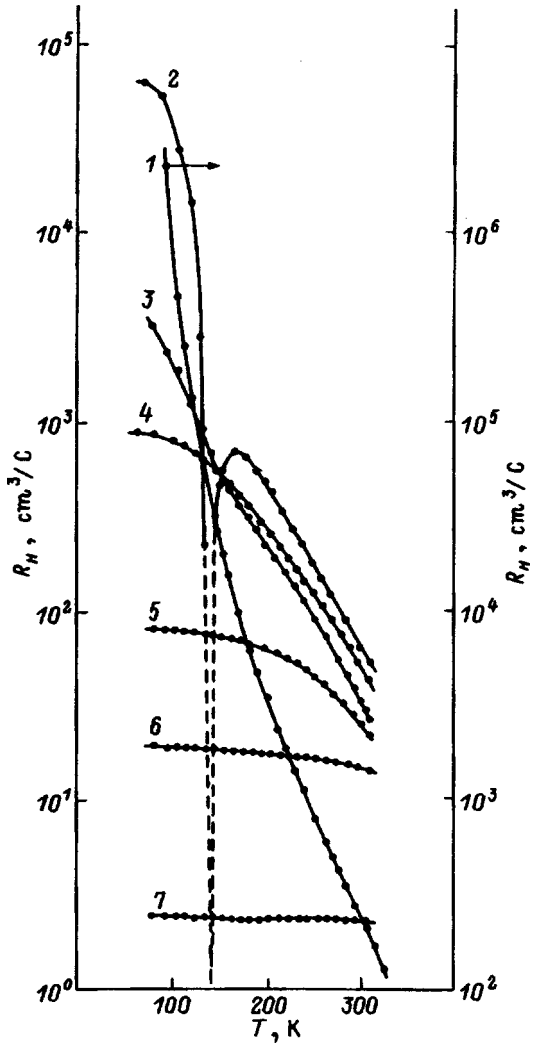

FIG. 2. Temperature dependences of the Hall coefficient $R_H(T)$ of PbTe/BaF_2 films grown with different substrate temperatures and power density on target $W=8.5\times10^4$ W/cm^2. T_s, °C: *1* — 160, *2* — 295, *3* — 310, *4* — 320, *5* — 330, *6* — 350, *7* — 380.

in the size of critical nuclei, while the film will consist of a close-packed continuous fine-grain structure. Another important factor is that on account of the high growth rates ($V=2-28$ Å/pulse) the ''effective'' vacuum, which is equivalent in terms of the conditions of purity, is five to six orders of magnitude higher than the residual pressure in the vacuum system.[9] This virtually competely eliminates the possibility of the vapor phase interacting with the residual oxygen atmosphere and thereby oxidizing the condensate during the growth process.

Stoichiometric Czochralski single-crystal PbTe with free hole density $P=(3-5)\times10^{18}$ cm^{-3} was used as the target–source to obtain the layers.

X-ray crystallographic investigations of the PbTe/BaF_2 films grown showed that under such conditions of growth the films possess predominantly (001) orientation with a degree of disorientation that is determined both by the growth temperature and by the power density of the laser radiation on the target.

Figure 1 shows the current-carrier density in PbTe/BaF_2 films grown with constant laser radiation power density $W=8.5\times10^4$ W/cm^2 versus the temperature of the BaF_2 substrate. Varying the laser power density in the range $10^4\leqslant W\leqslant10^5$ W/cm^2 did not produce any substantial changes in the electrophysical properties of the films in the interval $100\leqslant T_s\leqslant400$ °C.

As one can see from Fig. 1, at low growth temperatures $100\leqslant T_s\leqslant260$ °C the films are *p*-type, while in the temperature interval $260\leqslant T_s\leqslant380$ °C the films change to *n*-type.

This is an unusual $P,N(T_s)$ dependence for IV–VI compounds. In the first place, the current-carrier density in the most perfect films grown by conventional thermal methods is at least 2×10^{16} cm^{-3}. In the second place, hole-type conduction can be obtained only by using an additional source of the chalcogen, whose vacancies are donors in IV–VI compounds. In the third place, *n*-type conduction with current-carrier density $N_{77}=4\times10^{17}$ cm^{-3} is possible only with additional doping with donor impurities. Thus, the dependence $P,N(T_s)$ is not associated with a phase diagram, but rather it is caused by the peculiarities of PbTe film growth under extremely nonequilibrium conditions on (111) BaF_2 substrates.

Detailed investigations of the temperature dependences of the Hall coefficient for samples prepared at different substrate temperatures T_s are presented in Fig. 2. For substrate temperatures $330\leqslant T_s\leqslant380$ °C the dependences $R_H(T)$ are virtually identical to $R_H(T)$ for films with the same electron density but grown by different methods. At lower substrate temperatures the dependence $R_H(T)$ is of an activational character. Moreover, in a quite wide temperature range $260\leqslant T_s\leqslant300$ °C the films grown are characterized by anomalous low-temperature inversion $n\rightarrow p$ of the conduc-

tion type, and the inversion temperature is virtually independent of the growth temperature T_s ($T_{\text{inv}} \simeq 140$ K).

To explain the results obtained we investigated the surface morphology the PbTe/BaF_2 films by the method of scanning tunneling microscopy. Analysis of the images obtained showed[10] that the complicated electronic structure of the film surface is due to the polycrystalline nature of the film with crystallite size $d \leqslant 250$ Å. X-Ray structural investigations confirm the results obtained.

For crystallites of such sizes, away from the surface the conduction- and valence-band edges cannot reach positions relative to the Fermi level that they should occupy in the volume of a bulk sample with the same doping level. For this reason the bands acquire a small curvature. The distribution of the potential and charge-carrier density in the films will be almost uniform, while a weak potential relief will appear only at low temperatures, where $\Delta U \simeq kT$.

The high-resistance state ($T=77$ K) of the PbTe/BaF_2 films ($P,N=10^{11}-10^{12}$) cm^{-3}, while in single-crystal PbTe/KCl(KBr) films prepared in a single cycle the carrier density is ($10^{16}-10^{17}$ cm^{-3}) can be explained by the formation of states in the band gap at grain boundaries that can manifest acceptor or donor character depending on the preparation conditions. Depending on the doping level N and the crystallite size l, it is possible to have situations in which the density of surface states $N_s \geqslant lN$ or $N_s \leqslant lN$. In the first case a grain is completely devoid of charge carriers and the intergrain states are partially occupied, which corresponds to the appearance of a high-resistance hole-type state (Fig. 2). The second case can be realized by increasing the electron density in a crystallite with fixed N_s and l or by decreasing N_s, which will result in an inversion of the conduction type and a low-resistance state in the region of electronic conduction.

It was established experimentally that in the high-resistance p- and n-type states the temperature dependences $\sigma(1/T)$ and $P,N(1/T)$ are characterized by three activation sections E_1, E_2, and E_3, while $\mu(1/T)$ is of an activational character only at low temperatures. The temperature dependences $\sigma(1/T)$ and $P(1/T)$ for films obtained at low substrate temperatures $T_s \leqslant 210$ °C are exceptions. In this case only two activational sections E_1 and E_3 are observed. In both cases an activational increase of the mobility occurs below $T=110-120$ K. As the preparation temperature increases, this region shifts to 250 K. The slope decreases and for $T_s \geqslant 380$ °C $\mu(T)$ has a temperature dependence characteristic for lead telluride.

The conduction activation energies and the carrier densities in the high-resistance state in the region where the mobility grows exponentially with temperature are virtually identical for n- and p-type conduction ($T_s \geqslant 210$ K): $E_{1\sigma} \simeq -1.7\times10^{-2}$ eV, $E_{1p,n} \simeq -1.0\times10^{-2}$ eV, and $E_{1\mu} \simeq E_{1\sigma}-E_{1p,n}$, as expected for samples with a potential relief. In films grown at $T_s=150$ °C the activation energies are somewhat higher — $E_{1\sigma} \simeq -2.8\times10^{-2}$ eV, $E_{1p,n} \simeq -5.2\times10^{-2}$ eV, $E_{1\mu} \simeq -1.3\times10^{-2}$ eV, and in addition $E_{1\mu} \neq E_{1\sigma}-E_{1p}$.

At higher temperatures the functions $\sigma(1/T)$ and $P,N(1/T)$ for layers grown at $T_s \geqslant 210$ K exhibit two slopes $E_{2\sigma}=E_{2p,n}=(0.11-0.12)$ eV and $E_{3\sigma}=E_{3p,n}=E_g^{\text{PbTe}}$, while at lower growth temperatures only $E_{3\sigma}=E_{3p} \simeq 0.24$ eV $\geqslant E_g^{\text{PbTe}}=0.19$ eV is present.

In n-type samples E_2 and E_3 shift toward the conduction band as temperature increases. The activational section corresponding to E_1 vanishes.

The temperature at which shallow traps in the high-resistance samples ($T=110$ K) are completely emptied corresponds to the temperature at which long-time relaxations and ''frozen'' photoconductivity, which appear under equilibrium background radiation conditions at temperatures $T \leqslant 110$ K, vanish under the same conditions at $T=77$ K. For this reason the low-temperature activational sections of $N(T)$ and $\sigma(T)$ apparently can be attributed to the appearance of covariant modulation of the conduction and valence bands of the crystallites in PbTe/BaF_2 films.

The relaxation kinetics of photoconductivity is very sensitive to the background illumination. When the background level was increased, the relaxation time of the photoconductivity decreased substantially and reached $\tau \simeq 1\times10^{-6}$ s for background radiation corresponding to room temperature.

The current carrier density and the conduction type in layers with such a crystalline structure should be determined by the density and the degree of filling of intergrain states, i.e., the current carrier density in a grain.

As the investigations showed, the density of states at the intergrain boundaries depends strongly on the growth temperature and near $T_s=150$ °C at power densities at the target–source $W=1\times10^5$ W/cm^2 (the electron density in the PbTe/KCl(KBr) films under such growth conditions reaches $N \simeq 1\times10^{19}$ cm^{-3}, which gives a basis for assuming that it is the same in crystallites) the PbTe/BaF_2 layers are hole-type $P=(10^{11}-10^{13})$ cm^{-3}, i.e., the density of intergrain states cannot be lower than $N_{s2} \geqslant 10^{13}$ cm^{-2}. As the growth temperature increases, the density of states decreases substantially, as is indicated by the inversion of the conduction type in films even with electron density in grains $N \simeq 1\times10^{17}$ cm^{-3}, i.e., $10^{10} \leqslant N_{s2} \leqslant 10^{11}$ cm^{-2}. Such dependences $N_{s2}(T_s)$ and $E_2(T_s)$, as x-ray crystallographic investigations show, could be due to the large decrease in the disorientation of the grains with increasing growth temperature, while the grain size does not change.

The results obtained indicate that in our case the electrophysical and photoelectric properties of lead telluride for $T_s \leqslant 120$ K must be treated just as for polycrystalline samples and just as for a uniform film at higher temperatures.

The following can also be said about the nature of the crystallites. Since growth, which was discussed above, occurs under extremely nonequilibrium conditions, vapor condenses under conditions of strong supercooling and high pressure of the vapor flux. These conditions promote the appearance of metastable states, each of which is characterized by its own free energy,[11] i.e., the condensed layer can consist of an entire collection of crystalline phases of PbTe[4] which are unlikely to appear under equilibrium conditions. Indeed, x-ray crystallographic investigations of layers showed the presence of not only a phase corresponding to a NaCl-type structure but also a CsCl-type phase. In addition, the specific weight of the phases depends on the technological conditions of growth. This indicates that such objects should be treated

not simply as polycrystalline compounds with a predominant orientation but rather as complicated heterophase structures.

It should also be noted that similar results were obtained with substrates consisting of semiconductor single crystals as well as amorphous materials which are characterized by a higher free surface energy than PbTe.

When the target–source consisted of pressed tablets prepared from fine-grain PbTe powder, the films were always *p*-type with hole density $P=(2-3)\times 10^{18}$ cm^{-3}. This is explained by the large oxygen content in the target-source.

In summary, it was shown in this work that the LME method of growing PbTe/BaF_2 makes it possible to obtain PbTe layers whose properties are determined by the characteristic features of the crystalline structure, which consists of a granular structure with grain size $d\simeq 250$ Å, and whose (001) crystallographic orientation is insensitive to the orientation of the substrate, while the degree of disorientation and the energy position and density of intergrain states depend on the technological conditions of growth.

[1] M. H. Maksimov, L. V. Vassilev, Iu. G. Besedin, and T. Dyakov, Infrared Phys. **31**, 199 (1991).
[2] M. Baleva and E. Mateeva, J. Phys.: Condens. Matter **5**, 7959 (1993).
[3] M. Baleva and E. Mateeva, J. Phys.: Condens. Matter **5**, 7971 (1993).
[4] M. Baleva, L. Bozukov, and E. Tzukeva, Semicond. Sci. Technol. **8**, 1208 (1993).
[5] M. H. Maksimov and L. V. Vassilev, J. Mater. Sci. Lett. **9**, 1465 (1990).
[6] K. L. Saenger, Proc. Adv. Mater. **2**, 1 (1993).
[7] K. L. Saenger, Proc. Adv. Mater. **3**, 63 (1993).
[8] A. V. Novoselov [Ed.], *Handbook of Physicochemical Properties of Semiconductor Materials* [in Russian], Nauka, Moscow, 1979.
[9] B. K. Kotlyarchuk, L. G. Mansurov, G. V. Plyatsko, D. I. Popovich, and V. N. Savitskiĭ, Ukr. Fiz. Zh. **27**, 1066 (1982).
[10] Z. E. Kulumbetov, A. I. Liptuga, T. Piotrowski, and S. V. Plyatsko, in *3 Seminarium ''Powierzchia i Structury Cienkowarstwowe,''* Spala, Polska, 1995, p. 60.
[11] N. N. Sirota, Zh. Tekh. Fiz. **18**, 1138 (1948).

Translated by M. E. Alferieff

On the effect of a dopant on the formation of disordered regions in GaAs under irradiation with fast neutrons

V. P. Klad'ko and S. V. Plyatsko

Institute of Semiconductor Physics, Ukrainian National Academy of Sciences, 252028 Kiev, Ukraine
(Submitted May 5, 1997; accepted for publication July 14, 1997)
Fiz. Tekh. Poluprovodn. **32**, 261–263 (March 1998)

The effect of the irradiation dose and the density and type of dopant on the size of disordered regions in GaAs was studied by x-ray methods. The role of the impurity in the formation of disordered regions and their evolution with dose was analyzed. © *1998 American Institute of Physics.* [S1063-7826(98)01703-7]

The irradiation of semiconductors with heavy particles leads to, together with the generation of point defects (PDs) in the volume of the semiconductor, the formation of disordered regions (DRs).[1] Being a collection of points defects integrated in a local volume, a DR possesses properties which are specific to the semiconductor matrix and are, as a rule, mainly responsible for the degradation of the optical and electrophysical properties of the semiconductor.[2] In this connection it is important to determine the main parameters of DRs experimentally and to study the factors determining these parameters.

In the present work we investigated the effect of the type and level of doping on the effective size of DRs in the case of irradiation of gallium arsenide with fast neutrons. To this end samples of n- and p-type single-crystal GaAs, grown in the [100] direction by the Czochralski method, were selected. The n-GaAs crystals differed by the density N_{Sn} of the main donor impurity $\mathrm{Sn_{Ga}}$. The density n_0 of equilibrium electrons in these crystals was determined by the dopant density and at $T=300$ K equalled $2\times10^{16}-2\times10^{18}$ cm^{-3}. The p-type crystals were doped with zinc atoms ($\mathrm{Zn_{Ga}}$) and the hole density in the crystals was $p_0=2\times10^{18}$ cm^{-3} at $T=300$ K. The dislocation density was virtually the same in the experimental n-GaAs(Sn) and p-GaAs(Zn) crystals and equalled $(2-3)\times10^4$ cm^{-2}. The samples were irradiated with fast neutrons (average energy $E_n=2$ MeV) with doses $\Phi_n=10^{15}-10^{17}$ neutrons/cm^2 in a reactor channel with forced cooling (the temperature of the samples did not exceed 60 °C). The density N_S of point defects induced by neutron irradiation with dose Φ_n and the density N^* of disordered regions are proportional to Φ_n and equal $50\cdot\Phi_n$ and $0.21\cdot\Phi_n$, respectively.[3] As is well known, when semiconductors are irradiated with fast electrons with dose Φ_e, TDs are produced (their density equals $5\cdot\Phi_e$), while DRs do not form right up to very high doses.

The irradiated crystals were investigated by x-ray topography and diffractometry methods.[4,5] According to the x-ray topographic data, the dislocation density remained virtually unchanged during irradiation. The static Debye–Waller factor L, which characterizes the relative volume fraction of the distorted lattice in the crystal, was determined by the method of Ref. 5. On the basis of the fact that the dislocation density in the crystals remained unchanged during irradiation, all changes (ΔL) in the value of the static factor can be attributed to the formation of DRs. The correction ΔL is related with the density N^* of DRs and the average effective size R_{av} for the cluster model by the formula[6]

$$\Delta L = N^* \cdot R_{av}^5 . \tag{1}$$

Thus, using the dose dependence of N^*, the value of R_{av} and its evolution as a function of the irradiation dose can be easily calculated from the experimental values of ΔL. The dose dependences of R_{av} calculated from Eq. (1) for irradiated n- and p-type crystals are presented in Fig. 1. The change in the ratio of the components in the crystals during irradiation was monitored by measuring the total intensities for quasiforbidden reflections.[7] These results are presented in Fig. 2.

To analyze the dependences obtained we shall proceed from the model for DRs which has become firmly established in the last few years.[2] Four basic stages are distinguished in the process leading to the formation of DRs: cascade, postcascade, quasichemical, and accomodation. During the first two stages a 50–150 Å nucleus of a DR forms over very short times ($10^{-14}-10^{-13}$ and $10^{-11}-10^{-10}$ s, respectively). During the quasichemical stage PDs (mainly interstitial atoms As_i and Ga_i) displaced from the cascade actively diffuse toward sinks in the semiconductor matrix, where they either recombine or form complicated defects or defect–impurity complexes (DICs). The sinks can be both growth defects and PDs induced in the matrix. These so-called accomodation processes occur during the entire accumulation time of the irradiation dose.

Thus, the size of a DR will be determined by the size of the defect-impurity shell (DIS), consisting of cluster of different types of DICs, that forms around the nucleus of the DR. From the standpoint of x-ray measurements, a DIS is a distorted region of the crystal lattice of GaAs near the nucleus of the DR. The effective size of this distorted region is proportional to the deformation gradient produced by the distribution of DICs between the DR nucleus and the unperturbed matrix. As the DR density increases (overlap process), the deformation level of the entire crystal increases and the detected limit of the deformation gradient shifts closer to the DR nucleus (the effective size R_{av} decreases).

As one can see from the curves presented in Fig. 1, the effect of the doping level on the value of R_{av} is substantial at low irradiation doses ($\Phi_n=10^{15}$ neutrons/cm^2). As the dose increases, the dependence of R_{av} on the density of the dopant atoms decreases and completely vanishes when $\Phi_n>10^{16}$

 1063-7826/98/030235-03$15.00

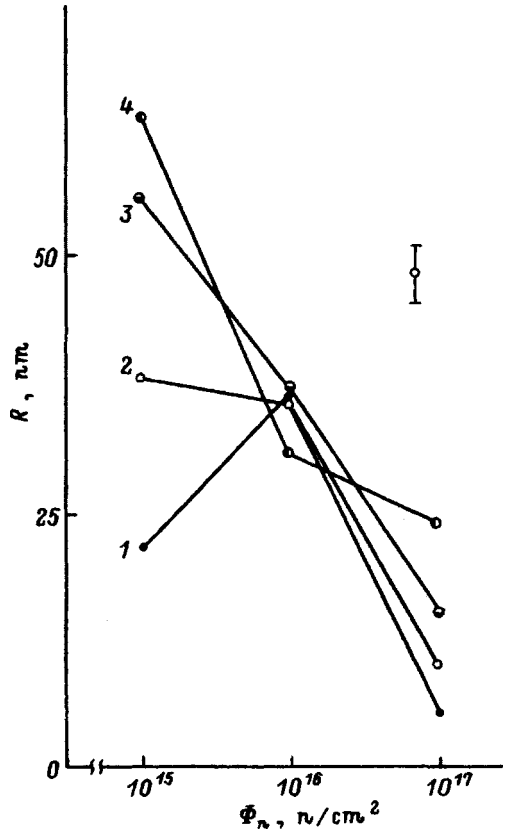

FIG. 1. Effective sizes R of disordered regions in GaAs versus the neutron irradiation dose and doping level. *1, 2, 3* — Crystals doped with Sn to density 2×10^{16}, 2×10^{17}, 2×10^{18} cm^{-3}, respectively; *4* — Zn with $N_{Zn}=2\times10^{18}$ cm^{-3}.

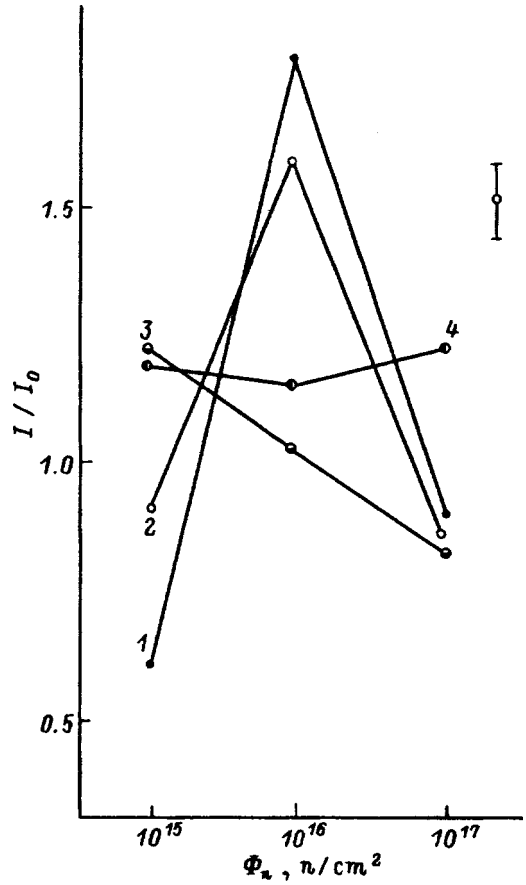

FIG. 2. Ratio I/I_0 of the total intensities of quasiforbidden x-ray reflections (200) measured in the irradiated (I) and initial (I_0) crystals versus the irradiation dose and doping level. The designations are the same as in Fig. 1.

neutrons/cm^2. The character of the variation of R_{av} with irradiation dose in samples with different doping levels shows that R_{av} is determined by several basic factors. In the case of low doses the generation of PDs in the GaAs matrix has virtually no effect on the properties of the matrix and, specifically, $N_S<N_{Sn}$ for all values of N_{Sn}. Moreover, since the DR density is low, the average distance between separate DRs is greater than R_{av}, i.e., the DRs are isolated (their DISs do not overlap). These considerations and the data presented above suggest that for low irradiation doses a) DRs form mainly at the quasichemical stage (accomodation processes have virtually no effect on the formation of DRs) and b) the increase in R_{av} with increasing doping level is due to the PDs displaced from the cascade interacting effectively with the Sn_{Ga} atoms accompanied by the formation of DICs. Analysis of Fig. 2 shows that the number of As_i and Sn in DRs increases. As the irradiation dose increases, on the one hand N^* increases and at a definite value of Φ_n the DRs can no longer be regarded as being isolated (i.e., their DISs start to overlap), as a result of which R_{av} should decrease. On the other hand, as Φ_n increases so does N_S, for a given value of N_{Sn} $N_S>N_{Sn}$, and R_{av} can increase as a result of decoration by PDs generated in the matrix. As one can see from the dose dependences of R_{av}, at the maximum value of N_{Sn}, for which R_{av} of an isolated DR is maximum, increasing Φ_n results in overlapping of the DRs and a decrease in the value of R_{av}. At the minimum level of doping and, correspondingly, the minimum value of R_{av} of an isolated DR, increasing the dose load increases R_{av} as a result of accomodation processes as long as the DRs are isolated. For $\Phi_n>10^{16}$ neutrons/cm^2 the overlapping of the DISs is the dominating factor and for all samples, irrespective of the value of N_{Sn}, the effective size of the DRs decreases.

It is important to note that the character of the change in R_{av} with irradiation dose Φ_n is virtually the same in GaAs samples with different types of conduction but the same dopant density ($N_{Sn}=N_{Zn}$) (Fig. 1). This also attests to the fact that the dopant atoms are effective sinks for PDs during the formation of DRs.

In summary, the radiation defects produced by irradiation with fast neutrons are not purely vacancy defects. Most likely, in our case complexes of vacancies and interstitial atoms as well as complexes of of primary defects with technological impurities (dopants) are formed in the regions of disordering. The largest changes in the system of point defects occur at a dose of 10^{16} cm^{-2} (Fig. 2), In addition, these changes are all the larger, the lower the doping level of the crystals. An increase in the size of the DRs is also observed up to irradiation doses of 10^{16} cm^{-2}. Further limitation on size is due to the overlapping of the deformation fields of different DISs.

[1] N. A. Ukhin, *Radiation Physics of Nonmetallic Crystals* [in Russian], Naukova Dumka, Kiev, 1971.
[2] A. I. Baranov and S. S. Smirnov, Fiz. Tekh. Poluprovodn. **7**, 2227 (1973) [Sov. Phys. Semicond. **7**, 1482 (1973)].
[3] V. L. Vinetskiĭ and G. A. Kholodar', *Radiation Physics of Semiconductors* [in Russian], Naukova Dumka, Kiev, 1979.
[4] M. Ya. Skorokhod, A. N. Gureev, and L. I. Datsenko, Ukr. Fiz. Zh. **18**, 1860 (1973).
[5] L. I. Datsenko, Ukr. Fiz. Zh. **24**, 1306 (1979).
[6] P. H. Dedericks, Phys. Rev. B **1**, 1306 (1970).
[7] I. Fujimoto, Jpn. J. Appl. Phys. **25**, 291 (1986).

Translated by M. E. Alferieff

On the mechanisms of long-term relaxation of the conductivity in compensated Si⟨B,S⟩ and Si⟨B,Rh⟩ as a result of irradiation

M. S. Yunusov, M. Karimov, and B. L. Oksengendler

Institute of Nuclear Physics, Academy of Sciences of Uzbekistan, 702132 Ulugbek, Uzbekistan
(Submitted July 21, 1995; accepted for publication July 14, 1997)
Fiz. Tekh. Poluprovodn. **32**, 264–267 (March 1998)

Experimental data on the long-term relaxation of the photocurrent in compensated samples of Si⟨B,S⟩ and Si⟨B,Rh⟩ are analyzed on the basis of three mechanisms (sticking levels, recombination processes via levels with large relaxation, and separation of carriers in the spatial inhomogeneity field). It is shown that in a number of cases irradiation (by ^{60}Co γ-rays at different temperatures) makes it possible to determine the dominant mechanisms. © *1998 American Institute of Physics.* [S1063-7826(98)00103-3]

Long-term relaxation of current carriers, which has been studied in a number of semiconductor systems,[1–10] is of special interest in silicon compensated by deep-level impurities since it is in just such materials that the three main mechanisms responsible for long-term relaxation are realized:

- carrier capture at a sticking level;[2,4–6]
- recombination through defects with large relaxation;[3]
- separation of carriers by barriers due to spatial inhomogeneities in the distribution of unscreened impurities.[1,2,7–10]

Separating these mechanisms is in many cases a nontrivial problem, and the irradiation method can be important in this case. Below we present the results of studies based on this method.

We examined the relaxation kinetics of the photoconductivity in the compensated materials Si⟨B,S⟩ and Si⟨B,Rh⟩ before and after irradiation by ^{60}Co γ-rays at 77 K at the same light intensity (150 lux). The applied voltage was 1 V.

As the starting material we used p-type silicon with initial resistivity $1-2\ \Omega\cdot$cm (sulfur-compensated) and $7\text{-}10\ \Omega\cdot$cm (rhodium-compensated). Doping was performed by thermal diffusion in the temperature interval 1250–1290 °C for ~20 h. We thus succeeded in attaining mean concentrations $\overline{N}_S \sim 10^{16}$ cm^{-3} and $\overline{N}_{Rh} \sim 5\times10^{15}$ cm^{-3}, and mean resistivities $\overline{\rho}\sim(8-10)\times10^4\ \Omega\cdot$cm in both types of samples at room temperature.

The sulfur center and rhodium center concentrations were determined by the conductivity compensation method, i.e., $N_{S,Rh}=p_0-p$, where p_0 and p are the hole concentrations before and after S and Rh diffusion. The sulfur center and rhodium center concentrations were varied by varying the diffusion temperature; reproducibility of the parameters of the samples was achieved by experimentally selecting the diffusion temperature with small steps (~5 °C) for each starting sample of p-type silicon.

Ohmic contacts were prepared by melting-in aluminum in vacuum at a temperature of ~700 °C for ~30 s. The dimensions of the samples were $6\times3\times0.6$ mm.

Irradiation was produced by a γ-source with a power of ~2800 R/s up to doses of $\sim1\times10^9$ R at a channel temperature of ~60 °C.

Results of our studies are plotted in Fig. 1. The decrease in the photoconductivity can be represented, in general, with adequate accuracy by the formula

$$I_p = A_1\exp(-t/\tau_1)^{\beta_1} + A_2\exp(-t/\tau_2)^{\beta_2},$$

where $A_1 \gg A_2$, $\tau_1 \ll \tau_2$, and $[\beta_1,\beta_2]<1$. Here A_j and τ_j $(j=1,2)$ depend on the concentration of electrically active sulfur atoms in p-type Si⟨B,S⟩ and electrically active rhodium atoms in p-type Si⟨B,Rh⟩ (t is the observation time and τ_j is the time constant of the process) (Fig. 1).

Irradiation with γ-rays substantially alters the kinetics of long-term relaxation, where the quantity τ_2 seems to be the most sensitive: $d\tau_2/d\Phi>0$; i.e., this phase of long-term relaxation is extended with increasing radiation dose (see Fig. 2).

It is significant that the observed trend remains valid at different measurement temperatures $T=77$ and 300 K, where the rate of change of τ_2 with dose varies more rapidly at low temperatures (Fig. 3).

These results allow us to analyze the mechanisms of long-term relaxation in a quite convincing fashion.

The mechanism of sticking levels. As was shown in Ref. 2, if we start from the scheme of relaxation stretching due to participation of sticking levels in the kinetics of the processes, then a criterion of realization of this mechanism is satisfaction of the inequality $\tau_2 \leqslant \tau_{max} \simeq (v\cdot\sigma_{min}\cdot\Delta p)^{-1}$, where $\sigma_{min}\geqslant(10^{-22}-10^{-23})$ cm^2 is the minimum cross section for the capture of carriers at the local level;[2,4] $\Delta p=[N_{S,N_{Rh}}]<10^{16}$ cm^{-3} since the free hole concentration reaches $\sim(5-10)\times10^{15}$ cm^{-3} upon illumination; and $v\sim10^7$ cm/s is the thermal velocity of the electrons. For these quantities we obtain $\tau_{max}\leqslant1$ s. Obviously (see Fig. 1), $\tau_2 \gg \tau_{max}$; i.e., the mechanism of sticking levels is inefficient in this case.

The mechanism of recombination through levels with large relaxation. To interpret the results of the existence of long-term relaxation before irradiation and its augmentation

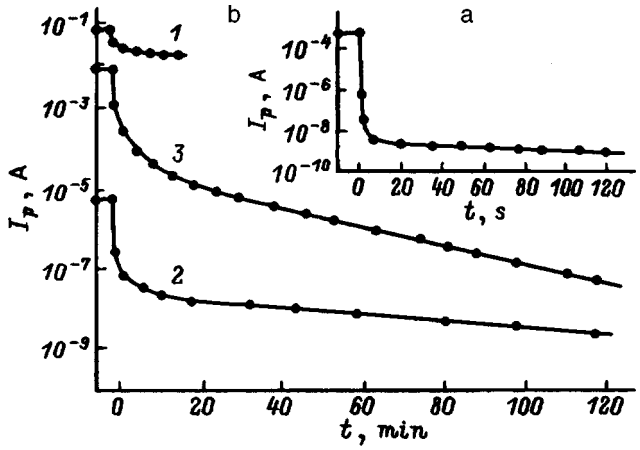

FIG. 1. Kinetics of photocurrent relaxation in samples of n-Si⟨B,Rh⟩ ($N_{\mathrm{Rh}}^{d}\sim 2.5\times 10^{15}$ cm^{-3}) (a) and n-Si⟨B,S⟩ (b) for different concentrations of sulfur atoms N_{S} (the measurements were performed at 77 K):*1*—$\sim 8.5\times 10^{15}$ cm^{-3}, *2*—$\sim 9.1\times 10^{15}$ cm^{-3}, *3*—$\sim 1.1\times 10^{16}$ cm^{-3}.

after irradiation, we propose the following scheme. Before irradiation the sample has a deep center (M_1) with large relaxation, the cross section for recombination through which depends on temperature according to the law $\sigma_1=\sigma_0^{(1)}\exp(-E_1/kT)$, where E_1 is the recombination barrier, and $\sigma_0^{(1)}$ is the pre-exponential factor.[11] As a result of irradiation, vacancies (V) and intrinsic interstitial atoms (I) are generated. These vacancies and atoms interact with the impurities (D) in the sample in such a way as to increase either the concentration of M_1 centers (which is not observed in the experiment) or to form a new radiation center (M_2) with large relaxation, for which the capture cross section is $\sigma_2=\sigma_0^{(2)}\exp(-E_2/kT)$, where $E_2>E_1$. This center possesses particular kind of kinetics of accumulation $N_2\sim f(t_{\mathrm{irr}})$, which corresponds to a particular scheme of quasichemical reactions and which is described by the system of equations

$$\begin{cases} dV/dt=\lambda-k_1VI-k_2VD-V/\tau_V \\ dI/dt=\lambda-k_1VI-I/\tau_I, \\ D\simeq \text{const}, \\ dN_2/dt=k_2VD-N_2/\tau_D, \end{cases}$$

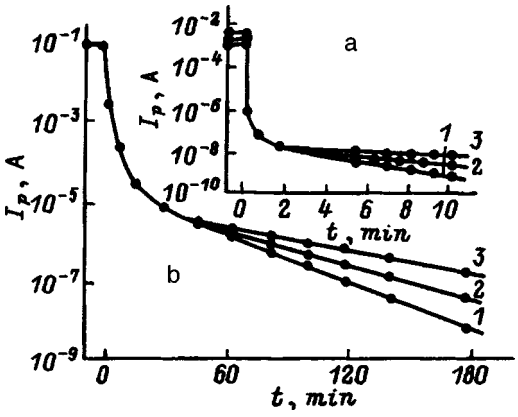

FIG. 2. Kinetics of photocurrent relaxation in n-Si⟨B,Rh⟩ (a) and n-Si⟨B,S⟩ (b) for different radiation doses of ^{60}Co γ-rays (the measurements were performed at 77 K): *1*—before irradiation; *2*—$\sim 5\times 10^{7}$ R; *3*—$\sim 5\times 10^{8}$ R.

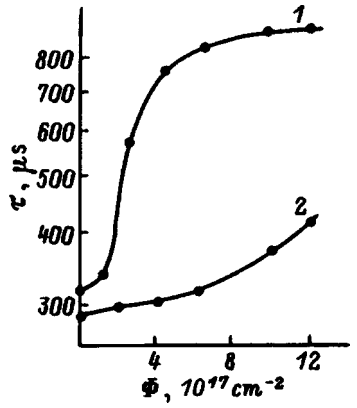

FIG. 3. Relaxation time τ versus the flux of the ^{60}Co γ-rays in Si⟨B,Rh⟩: *1*—77 K, *2*—300 K.

where V, I, and D are the concentrations of the corresponding defects and impurities, τ_V, τ_I, and τ_D are the corresponding relaxation times, λ is the rate of introduction of the primary defects, and k_1 and k_2 are the quasichemical reaction rate constants.

For the initial conditions $t=0$, $V=I=N_2=0$ we obtain

$$N_2=N_2^{(\infty)}(1-e^{-t/\tau_D}), \quad \text{where} \quad N_2^{(\infty)}=k_2\lambda\tau_V D\tau_D .$$

In the solution of this system, as is customary, we assumed that the fastest process is relaxation of intrinsic interstitial atoms and that $k_2\ll k_1$. In this case the expression for τ_2 has the form

$$\tau_2\simeq[N_1v\sigma_1(T)+N_2v\sigma(T)]^{-1}.$$

This gives

$$d\tau_2/d\Phi\sim d\tau_2/Idt=(d\tau_2/IdN_2)(dN_2/dt)\sim e^{E_2/dT},$$

which is in qualitative agreement with the results shown in Figs. 2 and 3. Note, however, that in this case the concentration of the M_1 centers should decrease, while the concentration of the M_2 centers should increase to some noticeable value N_2, which is not observed experimentally. The decrease in the concentration of the M_1 centers is small ($N_{\mathrm{S}}\sim 10^{16}$ cm^{-3} for Si⟨B,S⟩, while for Si⟨B,Rh⟩ $N_{\mathrm{Rh}}\sim 5\times 10^{15}$ cm^{-3}), whereas the concentration of radiation centers for the set of doses used reaches $N_2\sim 10^{15}$ cm^{-3} (Ref. 12). Consequently, we may conclude that the mechanism of recombination through levels with large relaxation is unrealizable in this case.

The mechanism for separation of carriers by spatial inhomogeneities. This mechanism is connected with separation of nonequilibrium electrons and holes by barriers caused by impurity concentration fluctuations. As is well known,[2] carriers separated by such barriers relax with characteristic relaxation time

$$\tau=\tau_0\exp(\Delta_0/kT),$$

where τ_0 is the pre-exponential factor, and Δ_0 is the barrier between the high-resistance (p) and low-resistance (p^+) regions in compensated samples of Si⟨B,S⟩ and Si⟨B,Rh⟩.

As the sample is irradiated, with efficient formation of various complexes of defects and impurities, the Fermi level

of the entire system shifts. This shift is much smaller in the low-resistance regions than in the high-resistance regions, so that the barriers separating these regions grow with the radiation dose. Let us consider the effect associated with the formation of divacancies (W) since the other complexes (A, E, and K centers) in the investigated samples have levels located far from the Fermi level in the high-resistance regions; i.e., their participation in the compensation of carriers is virtually nonexistent.

The kinetics of the quasichemical reactions in this case has the form

$$\begin{cases} dV/dt=\lambda-k_1VI-k_2V^2-V/\tau_V+k_3IW, \\ dI/dt=\lambda-k_1VI-I/\tau_I-k_3IW, \\ dW/dt=k_1IV\ -\ I/\tau_I\ -\ k_3IW, \end{cases}$$

with the initial conditions $t=0$, $V=I=W=0$, where k_1, k_2, and k_3 are the quasichemical reaction rate constants, and W is the divacancy concentration.

For the characteristic hierarchy of rates of the defect-formation processes ($dI/dt>dV/dt>dW/dt$) we then have $I\simeq\lambda\tau_I$, $V|_{t\to\infty}\simeq\lambda\tilde{\tau}_V$, and $W(t)=k_2\tilde{\tau}_V/k_3\tau_I[1-e^{-k_3\tau_I t}]$, where $1/\tilde{\tau}_V=k_1\lambda\tau_I+1/\tau_V$. The divacancies capture current carriers and compensate the conductivity, which effectively increases the barrier $\Delta>\Delta_0$. When the low-resistance and high-resistance regions come in contact with each other,[1)] we have respectively: a) for p-Si, $\Delta=\Delta_0+kT\ W(t)/n$; b) for n-Si, $\Delta=\Delta_0+kT\ W(t)/p$. This leads to a corresponding increase in the lifetime of the current carriers: a) $\tau(t)=\tau_0[1+W(t)/n]$; b) $\tau(t)=\tau_0[1+W(t)/p]$. Clearly, as the temperature is lowered (from 300 to 77 K), the quantities n and p decrease rapidly, which leads to an amplification of the dose dependence $\tau(t)\to\tau(\Phi)$, in agreement with experiment (Fig. 3).

Thus, in our analysis of the results of the experiments on the basis of the three indicated mechanisms we must give preference to the last one.

It is expected[13] that in strongly inhomogeneous samples, where the Δ values are different, a relaxation law that is not purely exponential applies. For many cases, a dependence of Kohlrausch type is realized $\sim\exp(-t/\tau)^\beta$, where $\beta<1$ (Ref. 14). We analyzed our experimental results from this point of view (Fig. 2). We see that in fact, $\beta=0.89$.

In summary, we can say that irradiation is a very efficient mean of determining the mechanism for long-term relaxation of the photocurrent.

[1)]If we assume that the fluctuations in the distribution of initial carriers are of the order of $\pm5\%$, and that the compensating impurities are of the order of $\pm20\%$, then for complete compensation, regions are realized with different ρ and conductivity type (n^+,p^+,n,p). A general analysis of their role in the conductivity is given, for example, in Ref. 12.

[1] S. M. Ryvkin, Fiz. Tekh. Poluprovodn. **8**, 373 (1974) [Sov. Phys. Semicond. **8**, 237 (1974)]; Fiz. Tekh. Poluprovodn. **11**, 2378 (1977) [Sov. Phys. Semicond. **11**, 1399 (1977)].
[2] M. K. Sheĭnkman and A. Ya. Shik, Fiz. Tekh. Poluprovodn. **10**, 209 (1976) [Sov. Phys. Semicond. **10**, 128 (1976)].
[3] *Deep Centers in Semiconductors*, edited by S. Pantelides (P 1 Press, New York, 1986), p. 950.
[4] A. A. Lebedev, N. A. Sultanov, and V. M. Tuchkevich, Fiz. Tekh. Poluprovodn. **5**, 31 (1971) [Sov. Phys. Semicond. **5**, 25 (1971)].
[5] A. A. Lebedev, A. T. Mamadalimov, and Sh. Makhkamov, Fiz. Tekh. Poluprovodn. **8**, 262 (1974) [Sov. Phys. Semicond. **8**, 169 (1974)].
[6] Sh. Makhkamov, N. A. Tursunov, and M. Ashurov, in *Photoelectric Phenomena in Semiconductors* [in Russian] (Abstracts of the All-Union Conference) (Fan, Tashkent, 1989), p. 326.
[7] M. K. Bakhadyrkhanov, in *Deep Levels in Semiconductors* [in Russian], edited by V. I. Fistul' (Tashkent, 1981), p. 52.
[8] M. K. Bakhadyrkhanov and S. Z. Zaĭnabidinov, Uzb. Fiz. Zh., No. 6, 5 (1991).
[9] B. Z. Sharipov, N. Norkulov, and Kh. Sh. Askarov, in *Photoelectric Phenomena in Semiconductors* [in Russian] (Abstracts of the All-Union Conference) (Fan, Tashkent, 1989), p. 33.
[10] Sh. I. Askarov and B. Z. Sharipov, in *Photoelectric Phenomena in Semiconductors* [in Russian] (Abstracts of the All-Union Conference) (Fan, Tashkent, 1989), p. 237.
[11] V. I. Fistul', *Introduction to Semiconductor Physics* [in Russian] (Vysshaya Shkola, Moscow, 1984).
[12] J. M. Meese and P. Gleron, in *Neutron Transmutation Doping in Semiconductors*, edited by J. M. Meese (Plenum Press, New York, 1979).
[13] V. V. Emtsev, T. V. Mashovets, and E. Kh. Nazaryan, Fiz. Tekh. Poluprovodn. **15**, 1018 (1981) [Sov. Phys. Semicond. **15**, 587 (1981)].
[14] L. Pietronero and E. Tosatti, eds., *Fractals in Physics* (North-Holland, Elsevier, 1989).

Translated by Paul F. Schippnick

Tin telluride based thermoelectrical alloys

V. P. Vedeneev, S. P. Krivoruchko, and E. P. Sabo

Sukhumi Physicotechnical Institute, Abkhasian Academy of Sciences, Sukhumi, Georgia
(Submitted March 26, 1997; accepted for publication July 14, 1997)
Fiz. Tekh. Poluprovodn. **32**, 268–271 (March 1998)

The effect on the Hall hole concentration and the thermoelectric coefficient of various elemental impurities in SnTe containing excess Te and in some solid solutions based on it is investigated in the temperature interval 300–900 K. The variation of the kinetic parameters is treated on the basis of the concept of resonance states bound to cation vacancies and to the impurities determining the hole concentration. The low values of the thermoelectric coefficient in SnTe is explained by selectivity of scattering of charge carriers with more probable transition of the holes to the resonance states and vice versa. In isomorphic solid solutions based on SnTe, because of a shift in the energy position of the resonance states relative to the band edges and the Fermi level, it is possible to alter the nature of the resonance scattering and raise the thermoelectric coefficient to values which are optimal from the standpoint of obtaining maximum thermoelectric efficiency. In solid solutions of chalcogenides of group-IV elements with SnTe content about 40 mol% of the dimensionless parameter of thermoelectric efficiency $ZT=1$ at temperatures above 700 K. [S1063-7826(98)00203-8]

Tellurides of group-IV elements and alloys based on them have find wide application in the construction of thermoelectric generators. Sodium-doped tintelluride, and solid solutions based on GeTe are the most efficient thermoelectric materials of p-type in the intermediate temperature range with figure of merit $ZT=1.1-1.4$. For SnTe this value does not exceed 0.35, but thanks to such attributes as its chemical compatibility with many metals, it continues to be one of the widely used materials.[1–3] In view of this circumstance, raising the thermoelectric efficiency of SnTe is still a task of current importance. Within the scope of efforts to solve this problem for SnTe containing excess Te, and some alloys based on it, we conducted a study of the effect of various elemental impurities on the Hall hole concentration and the thermoelectric coefficient.

The test samples were prepared by melting in vacuum-sealed quartz cells the components of the material to be prepared, with no less than 99.99% purity, with subsequent grinding of the ingots and hot vacuum pressing of the powders at a temperature above the recrystallization temperature. The multicomponent alloy samples were annealed at 825 K for 150–300 h with the aim of homogenization.

The hole concentration was determined from the Hall effect. The measurements were conducted by the double-modulation method with a frequency of 20 Hz. The thermoelectric coefficient, electrical conductivity, and thermal conductivity were measured in steady-state regime at temperatures of 300–900 K with error no greater than 5%. Figure 1 plots the thermoelectric coefficient as a function of the Hall hole concentration (solid lines) at room temperature (300 K) for SnTe samples with different impurity contents (see Table I). The hole concentration in the samples with the impurity content held fixed was varied by means of deviations from stoichiometry. The dashed lines in Fig. 1 plot these dependences for two concentrations of excess Te—0.5 and 1.5 at. %. Elements of groups I, II, and III of the periodic table exhibit donor properties in SnTe, which occupy the Sn atom sites and which apparently decrease the number of metallic vacancies. Elements of group IV (Pb, Ge, and Si) even at concentrations as high as 5 at. % have a weak effect on the electrical properties of SnTe. Elements of group V (Bi, Sb, As) by virtue of their position in the periodic table can replace Te and Sn, but in the given experiment they act as weak donors. Iodine atoms exhibit their inherent donor properties, replacing Te atoms.

Attention is drawn to the fact that if the Hall hole concentration grows with growth of the excess Te content and, consequently, the number of cation vacancies, then the accompanying change in the thermoelectric coefficient depends on the type of dopant impurity and can increase as well as decrease. For a fixed deviation from stoichiometry (the dashed curves in Fig. 1) the thermoelectric coefficient increases with decreasing Hall hole concentration when SnTe is doped with a single impurity, but this dependence reverses with combined doping. Figure 2 plots isotherms of the dependence of the thermoelectric coefficient on the Hall hole concentration for SnTe co-doped with 1 mol % indium monotelluride and 1 mol % silver monotelluride, and also with different amounts (up to 2.0 at. %) of excess Te, indicated alongside the dashed curves (in at. %). The isotherms, without hardly changing their slope, shift with growth of the temperature toward higher values of the thermoelectric coefficient with a significant increase in the Hall hole concentration in the high-temperature region. According to theoretical (and subsequently experimentally confirmed) estimates, the optimal value of the thermoelectric coefficient ensuring maximum thermoelectric efficiency is found in the range $200-240$ μV/K. Such values of the thermoelectric coefficient are not reached in doped samples of SnTe and the value of the thermoelectric efficiency parameter at its maximum does not exceed 0.6×10^{-3} K^{-1} (Refs. 1 and 2), which, however, is higher than in the undoped alloy.

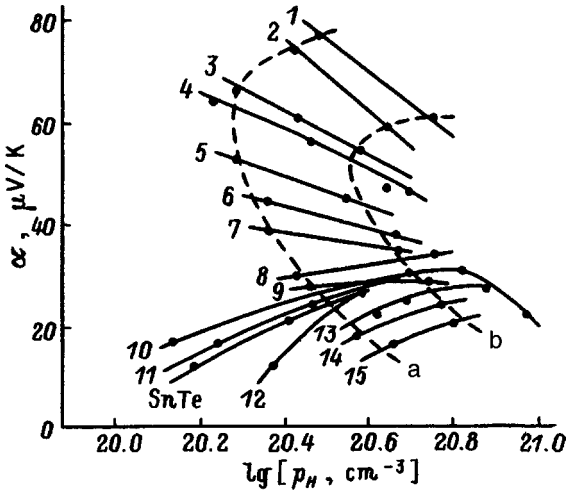

FIG. 1. Dependence of the thermoelectric coefficient α on the Hall hole concentration p_H, at 300 K for SnTe containing excess Te and dopant impurities. The type and quantity of the impurities are indicated in Table I. The dashed lines are drawn through the experimental points for samples containing excess Te in the percent amount (%): a—0.5, b—1.5.

The dependence of the thermoelectric coefficient on the Hall hole concentration at 300 K for solid solutions of some compositions of the ternary system of group-IV tellurides is plotted in Fig. 3. The compositions of the samples can be read off the concentration triangle (inset, Fig. 3), where they are denoted by the same letters as the corresponding curves in Fig. 3. Each of the compositions contains an additional 2% SbTe with varying contents (up to 4 at. %) of excess Te. The composition of the alloy H_1'' (see curve L in Fig. 3) corresponds to the point H'' of the concentration triangle and to the alloy in which 5 mol % GeTe is replaced by the same amount of SiTe. The introduction of Si into the alloy, like the substitution of Se or S for part of the Te, leads to a moderate increase in the Hall hole concentration and to a more vigorous falloff of the thermoelectric coefficient. Figure 3 shows curves for SnTe with 30% substitution of tellurium by sulfur and selenium. The dashed curves correspond to a content of 2 and 3 at. % excess Te, respectively, in the alloys. The Hall

TABLE I. Data on the type and quantity of impurities for the $\alpha(p_H)$ curves in Fig. 1.

Curve No.	Type of impurity	Amount of impurity, at. %
1	In+Cd+Ag	1+1+1
2	In+Cd	1+1
3	In+Ag	1+1
4	In	1
5	Gd	1
6	Tl	1
7	Cd	1
8	I	1
9	Ag	1
10	Pb	5
11	Ge	5
12	Si	5
13	Sb	1
14	Bi	1
15	As	1

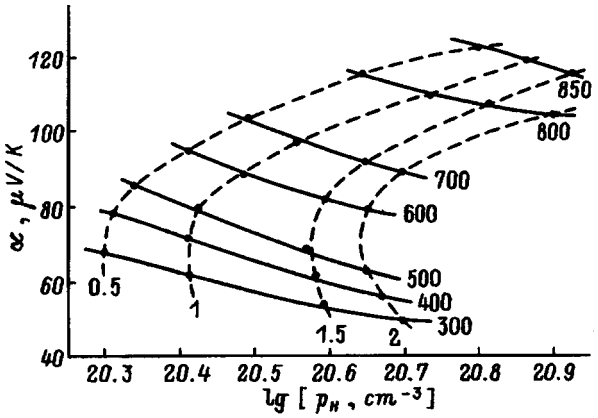

FIG. 2. Isotherms of the dependence of the thermoelectric coefficient on the hole concentration for SnTe containing 1 at. % In, 1 at. % Ag and different amounts of excess Te indicated in at. % alongside the dashed curves. The numbers next to the solid lines indicate temperature of the isotherms in K.

hole concentration is observed to grow when the GeTe content is increased (movement along the axis $C \rightarrow M$) and to fall when the PbTe content is increased (movement along the axis $H' \rightarrow H''$). However, the thermoelectric coefficient grows in both cases.

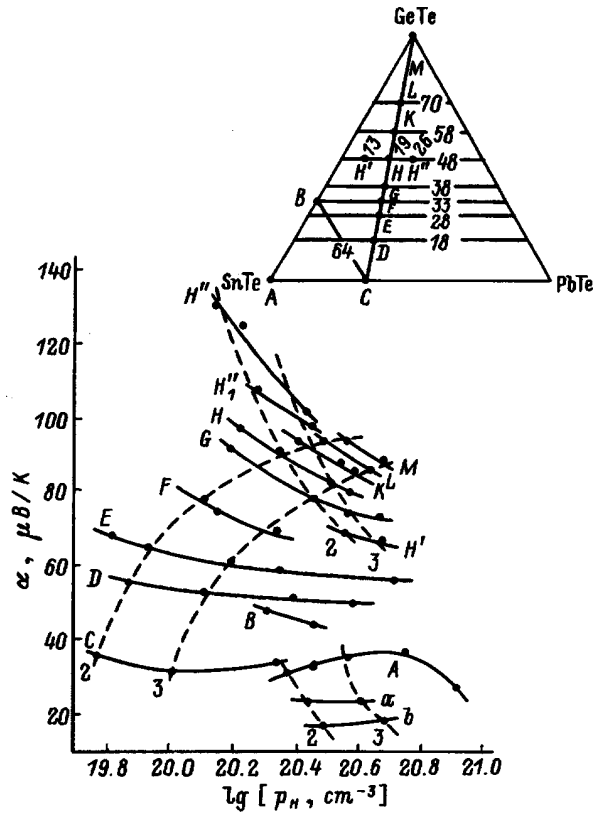

FIG. 3. Dependence of the thermoelectric coefficient α on the hole concentration p_H, at 300 K for the cases indicated in the concentration triangle of alloys doped with 2 mol% SbTe and containing different amounts of excess Te, indicated in at. % alongside the dashed curves. The capital letters alongside the solid curves correspond to the points (compositions) in the inset with the additional cases a—$SnTe_{0.7}Se_{0.3}$ and b—$SnTe_{0.7}S_{0.3}$. The inset locates the various solid-solution compositions examined in this study on the concentration triangle. The two-digit figures on the straight lines parallel to the lower and upper-right sides of the triangle indicate the composition of the corresponding component in at. %.

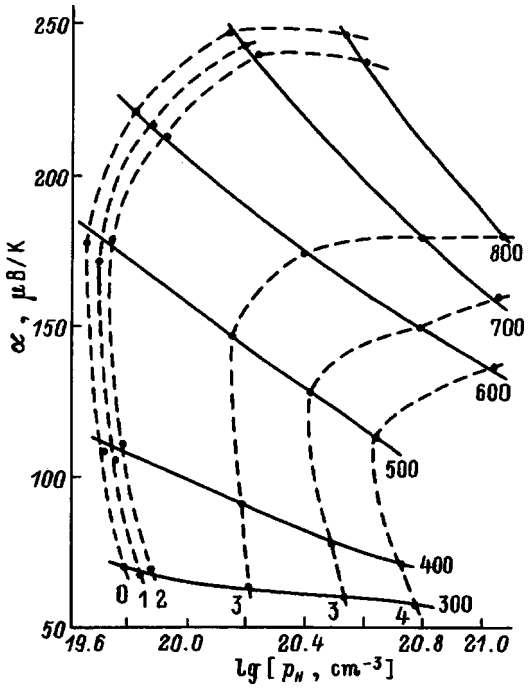

FIG. 4. Isotherms of the dependence of thermoelectric coefficient α on the hole concentration p_H, for alloys with the composition $Sn_{0.46}Pb_{0.26}Ge_{0.28}Te$ (the point E on the concentration triangle in Fig. 3) doped with Sb_2Te_3 (2 mol %) and containing various amounts of excess Te, indicated in at. % alongside the dashed curves. The numbers alongside the solid lines indicate the temperature of the isotherms in K.

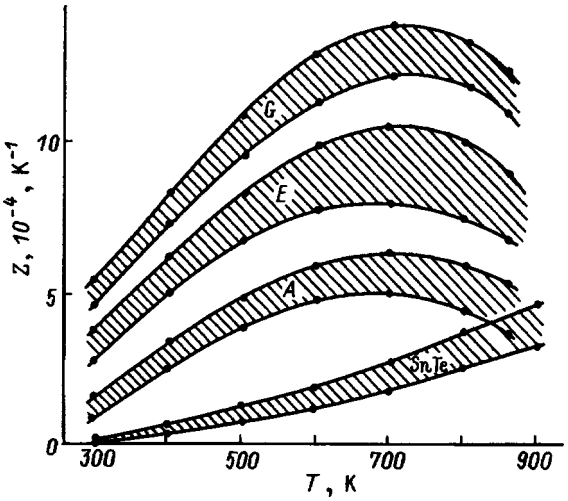

FIG. 5. Temperature dependence of the thermoelectric efficiency for: A—SnTe, doped with 1 at. % In and 1 at. % Ag or Cd; E—$Sn_{0.46}Pb_{0.26}Ge_{0.28}Te$, doped with 2 mol % Sb_2Te_3; C—$Sn_{0.40}Pb_{0.22}Ge_{0.38}Te$, doped with 2 mol % Sb_2Te_3. Excess Te content no greater than 2 at. %.

Figure 4 plots the dependence of the thermoelectric coefficient on the Hall hole concentration for alloys of the composition $Sn_{0.46}Pb_{0.26}Ge_{0.28}Te$ (the point E of the concentration triangle in Fig. 3) containing 2 mol% Sb_2Te_3, with different deviations from stoichiometry. The thermoelectric coefficient grows as the temperature is increased; however, for alloys with large Te content the optimal values of the thermoelectric coefficient are not reached. In samples containing 2 at. % Te, which corresponds to introducing 2 mol% Sb_2Te_3 into the stoichiometric solid solution, like for lower Te contents, the thermoelectric coefficient is higher, with its maximum at a temperature about 700 K.

In the same temperature region we see a maximum of the thermal efficiency parameter, whose temperature dependence is plotted in Fig. 5 in the form of a field of values for some of the investigated compositions with excess tellurium content in the range 0.5−2.0 at. %. The thermoelectric efficiency of the alloy $Sn_{0.46}Pb_{0.26}Ge_{0.28}Te$ (composition E), doped with Sb_2Te_3 (2 mol %), is significantly higher than for SnTe, whose doping leads to a marked increase in this parameter primarily in the low-temperature region (up to 700 K). Figure 5 plots values of the thermoelectric efficiency parameter for SnTe (composition A), co-doped with 1 at. % In and 1 at. % Cd or Ag. As the GeTe content of the solid solution is increased (the segment $C \rightarrow M$, see Fig. 3, inset) the thermoelectric efficiency grows and for the alloy $Sn_{0.40}Pb_{0.22}Ge_{0.38}Te$ (composition G), doped with 2 mol % Sb_2Te_3, it reaches values in the range $(1.2-1.4)\times10^{-3}$ K^{-1} and the thermoelectric figure of merit ZT is equal to 1.0.

It follows from these results that modification of the properties of SnTe-based alloys, like its nearest analog GeTe,[4,5] is hindered by the complex dependences of its thermoelectric and other physical parameters on the temperature, composition, and mode of doping. An explanation of many of these dependences may be sought in the band structure. However, none of the considered models which make use of subbands or the distorted shape of the Fermi surface such as ''trefoil,'' which allow one to represent some variation of the dispersion laws of the current carriers, gives a comprehensive description of the experimental results for the available calculational accuracy, which puts in doubt the possibility of the practical use of these models even at a qualitative level.

A more conducive description of changes in the kinetic parameters of SnTe based alloys may come from a picture based on resonance states. Smeared bands of resonance states bound to vacancies have been detected in PbTe and GeTe by measuring the thermal conductivity of the free charge carriers.[6,7] Resonance states formed by impurities have also been examined in sufficient detail in PbTe.[8] Since the behavior of the kinetic coefficients in materials based on PbTe, GeTe, and SnTe is characterized by a number of general regularities, there is every reason to believe that impurity and structural defects also form resonance levels in SnTe and alloys based on it. Their contribution to scattering is of a selective nature, which finds its reflection in the complicated dependence of the thermoelectric coefficient on the composition.

[1] A. R. Regel', ed., *Thermoelectric Generators* [in Russian] (Atomizdat, Moscow, 1976), p. 62.
[2] N. Kh. Abrikosov and L. E. Shelimova, *IV–VI Based Semiconductor Materials* [in Russian] (Nauka, Moscow, 1975), p. 65.
[3] L. L. Silin and Yu. B. Shubin, Fiz. Khim. Obrab. Mater. **5**, 127 (1967).
[4] M. A. Korzhuev, *Germanium Telluride and Its Physical Properties* [in Russian] (Nauka, Moscow, 1986).

[5] O. A. Kazanskaya, B. A. Efimova, and L. E. Moskaleva, in *Abstracts of the Sixth All-Union Conference on the Physicochemical Principles of Doping of Semiconductor Materials* [in Russian] (Nauka, Moscow, 1988), p. 195.
[6] I. A. Chernik, P. P. Konstantinov, A. G. Vyshinskiĭ, and A. V. Berezin, Fiz. Tverd. Tela **28**, 1939 (1986) [Sov. Phys. Solid State **28**, 1084 (1986)].
[7] I. A. Chernik, A. V. Berezin, S. I. Lykov, E. P. Sabo, and Yu. D. Titarenko, JETP Lett. **48**, 596 (1988).
[8] V. I. Kaĭdanov and Yu. I. Ravich, Usp. Fiz. Nauk **145**, 51 (1985) [Sov. Phys. Usp. **28**, 31 (1985)].

Translated by Paul F. Schippnick

Lock-in-phase analysis of *n*-GaAs photoreflectance spectra

A. V. Ganzha and R. V. Kus'menko

Voronezh State University, 394000 Voronezh, Russia
Fachbereich Physik der Martin-Luther Universität Halle-Wittenberg, D-06108 Halle (Saale), Germany

W. Kircher, J. Schreiber, and S. Hildebrandt

Fachbereich Physik der Martin-Luther Universität Halle-Wittenberg, D-06108 Halle (Saale), Germany
(Submitted January 8, 1997; accepted for publication September 9, 1997)
Fiz. Tekh. Poluprovodn. **32**, 272–277 (March 1998)

The phase dependence of the photoreflectance signal in the region of the E_0 transitions in GaAs samples has been investigated using the two-channel lock-in technique. The spectral components and their synchronous phases have been established as the result of a detailed analysis of the photoreflectance spectra. The time constants of the photoreflectance signal have been calculated for the observed single-component and multicomponent photoreflectance spectra. The time dependence $\Delta R/R_j \sim \pm \exp(-t/\tau_j)$ of the photoreflectance signal is due to the delayed reaction to the photomodulation of the electric field in the region of the semiconductor surface or interface. © *1998 American Institute of Physics.* [S1063-7826(98)00303-2]

The photoreflectance is a sensitive, nondestructive, contact-free, optical method for examining the surface and interface properties of semiconductors and semiconductor structures. The acquisition of the information contained in photoreflectance spectra proceeds, in general, by means of an analysis of the different spectral components making up the spectrum. As a rule, it is assumed that the reflection response to optical modulation takes place instantaneously. This is contradicted, however, by many experimental results[1–4] indicating a phase delay of the photoreflectance signal relative to the optical modulation.

The photoreflectance was modulated by means of periodic illumination of the surface of the investigated object by an additional optical source, as a rule, a laser, whose light passes through a mechanical shutter with frequency f.

The photoreflectance signal possesses a time dependence $R(t)$, which in the simplest case—for rectangular modulation, is described by an exponential function with a single characteristic time constant τ

$$R(t)=\begin{cases} R_0+\Delta R-\dfrac{\Delta R}{1+e^{-T/2\tau}}e^{-t/\tau}, \\ R_0+\dfrac{\Delta R}{1+e^{-T/2\tau}}e^{-t+T/2/\tau}, \end{cases} \tag{1}$$

where t is time, and $T=1/f$ is the modulation period. The first term describes the behavior of the reflection signal R in the presence of laser excitation, and the second describes it in the absence of laser light.

The use of a two-channel lock-in amplifier, i.e., an amplifier whose output is a complex signal consisting of a signal in phase with the modulation and a second imaginary component shifted relative to it by 90°, leads to the result that the photoreflectance spectrum, with the time dependence of the reflection signal $R(t)$ taken into account, is described as follows:

$$\overline{\frac{\Delta R}{R}}(E,F_s(\tau,\omega))=\frac{\Delta R}{R}(E,F_s)\frac{2}{\pi(1+\omega^2\tau^2)}(1-i\omega\tau), \tag{2}$$

where E is the photon energy, F_s is the electric field intensity, and $\omega=2\pi f$ is the modulation frequency. The time dependence $R(t)$ yields the phase delay δ of the photoreflectance signal relative to the phase of the modulating light.

The lock-in amplifier defines the amplitude of the first Fourier component of the input signal at the reference frequency and for the preset phase θ. Using a two-channel lock-in amplifier, one can determine either the component of the signal in phase with the reference frequency (X) and the component shifted by 90° (Y), or the amplitude $r(E)$ and phase $\delta(E)$ of the modulated variable signal relative to the modulating signal (Fig. 1):

$$\frac{\Delta R}{R}(E)=r(E)e^{i\delta(E)}=x(E)+iy(E). \tag{3}$$

The phase of the signal δ is defined in Fig. 1 as the angle between the phase of the scattered modulating light and the photoreflectance signal. The negative value of the angle δ means that between the modulation and the response there is a time delay. The figure also shows the preset phase θ, whose practical significance is explained in the experimental section.

Figure 2 shows a parametric representation of the output signal of the two-channel lock-in amplifier—components $Y(E)$ and $X(E)$—for a two-component spectrum. Working with a software package developed for modeling and nonlinear fitting of experimental spectra, we calculated two typical spectral shapes of the photoreflectance. Let us consider the spectrum (see the upper right part of Fig. 2, component *1*), typical for the photoreflectance in the low-field case or for exciton transitions.[5] The phase of this spectrum is delayed relative to the laser modulation by the angle δ_1. The vector representation of the photoreflectance signal is shown in the

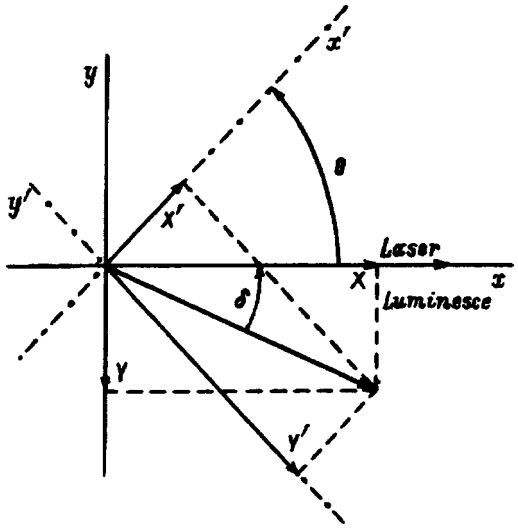

FIG. 1. Phase position of the photoreflectance signal (indicated by the thick arrow) relative to the modulating light. The phase of the signal, measured with a lock-in amplifier, in the absence (coordinate system x,y) and presence (coordinate system x',y') of a preset phase θ. The true value of the phase delay angle δ is found for $\theta=0°$.

upper left part of Fig. 2 for one of the points of this spectrum. The set of all points of the spectrum $X(E=h\nu)$, $Y(E=h\nu)$ should thus form a straight line subtending the angle δ_1 with the X axis (the latter by definition coincides with the phase of the modulating laser light). A completely analogous result is expected for all photoreflectance spectra consisting of only one spectral component whose time dependence is defined by only one time constant.

Thus, for the given representation, called the phase diagram, we have for $\tan\delta$

$$\tan\delta=\frac{y(E)}{x(E)}=\frac{\mathrm{Im}(1-i\omega\tau)}{\mathrm{Re}(1-i\omega\tau)}=-\omega\tau. \tag{4}$$

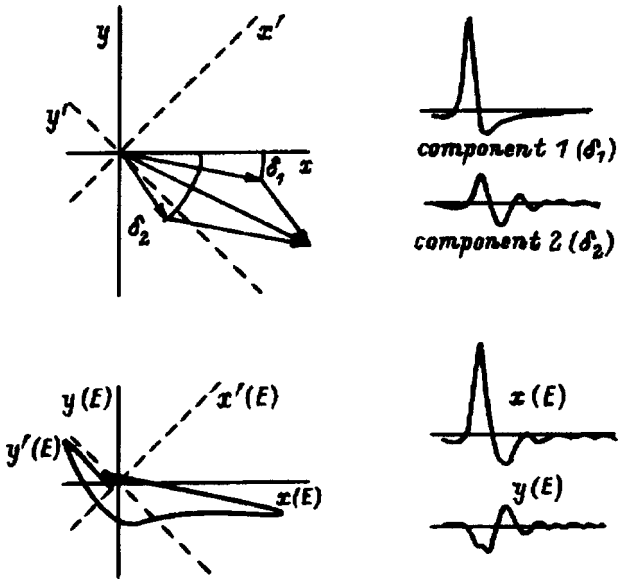

FIG. 2. Phase diagrams of the photoreflectance spectra. The influence of the photoreflectance signal on the form of the phase diagram was demonstrated by simulating the two-component spectrum for the X and Y channels of the lock-in amplifier.

It is clear that for only one spectral component and constant modulation frequency the quantity $\omega\tau$ remains constant [here the photon energy E, and hence $\Delta R/R(E)$, remains the only variable quantity], which makes it possible from the phase position of the photoreflectance spectrum and frequency ω to determine the characteristic time constant of the modulation process τ.

In the case $\omega\tau=0$, the real part of the photoreflectance signal (X) has the maximum value and is synchronous with the modulation ($\delta=0$), which is possible both for $\tau=0$ and for vanishing modulation frequency ($\omega\to0$). In the other limiting case, $\omega\tau=\infty$, the magnitude of the photoreflectance signal becomes vanishingly small, while the phase delay (the angle δ) approaches $-\pi/2$. The phase line thus lies completely in the fourth quadrant. Since the values of the photoreflectance amplitude can take both positive and negative values, the values of the phase $\delta(E)$ can also lie in the second quadrant; in this case, however, the relation $0\geqslant\delta\geqslant-\pi/2$ still holds.

To demonstrate the behavior of multicomponent spectra, we modulated the second spectral component (in the upper right corner of Fig. 2, component *2*), a characteristic feature of which is the so-called Franz–Keldysh oscillations (FKO).[6] The phase delay angle of this component relative to the laser modulation is δ_2.

Each spectral point of the two-component spectrum, the latter consisting of a superposition of components *1* and *2*, is defined by the vector sum of the two spectral contributions (see the upper left part of Fig. 2). The magnitude of the vector sum and its phase position depend on the spectral shape, relative amplitude, and time delay of the individual components. Thus, for each point of the superposition spectrum vectors with different signal phases $\delta(E)$. For the phase diagram of the resulting spectrum we have the parametric representation of the $X(E)$ and $Y(E)$ components, shown in the lower left part of Fig. 2, which have the photon energy as the parameter; the spectral shape of these components for the X and Y outputs, where these components are formed by superposition of the spectra shown in the upper right part of Fig. 2, is shown in the lower right quarter of the figure.

While the phase diagrams of the single-component spectra are straight lines lying in the second and fourth quadrants, when at least two components are superimposed, any signal phase $\delta(E)$ is possible.

In the case where the spectrum consists of n components, Eq. (2), which describes the shape of the spectrum, takes the form

$$\frac{\overline{R}}{R}(E,F_s,\tau,\omega)=\sum_{j=1}^{n}\frac{\Delta R_j}{R}(E,F_s)\times\frac{2}{\pi(1+\omega^2\tau_j^2)}(1-i\omega\tau_j). \tag{5}$$

Each of the components of the photoreflectance has its own phase delay δ_j and its own time constant τ_j

$$\tan\delta_j=\frac{y_j(E)}{x_j(E)}=-\omega\tau_j, \tag{6}$$

which, however, can be established only after performing the complete procedure of fitting the shape of the spectrum, for both the X and Y channels of the lock-in amplifier. The accuracy of the fit is determined in the given case by comparing the phase diagrams of the experimental and model spectra.

We should briefly consider the physical reasons for the appearance of the time dependence $\Delta R(t)$ and the phase delay of the various spectral components of the photoreflectance following from it. Since the most frequent reason for the appearance of a photoreflectance signal is optical modulation of the electric fields in the space charge region on a semiconductor surface or interface of two semiconductors, the recharging dynamics of the electron states in the modulation regions plays a large role for the observed temporal effects. Of special importance here for the appearance of the phase shift between the optical modulation and the reflectance signal are the capture, remission, and recombination rates of the photogenerated charge carriers in these states.[2,7,8]

Since modulation of the electric fields on a surface or interface is accompanied by a change in the bending of the bands and of the depth of the space charge region, capacitance effects in the surface region, described by the time constant $\tau = RC$, may also be responsible for the appearance of the phase shift of the photoreflectance signal.

The boundaries of the region in which the time constants τ can be measured are determined by the specifications of the apparatus and for our instrument are

$$30\ \text{ms} \geqslant \tau > 0.6\ \mu\text{s}.$$

Since all the constants we recorded lie above the lower limit 0.6 μs, we should exclude the influence of the faster processes of charge-carrier diffusion and drift on the time constant τ.

Let us turn now to a consideration of the experimental results obtained for GaAs samples in the region of the transition E_0. All of the experiments were carried out in air at room temperature.

Figure 3 presents results of photoreflectance experiments on a sample of GaAs [$n(\text{Si}) = 1\times 10^{16}\text{cm}^{-3}$]. Before start of the measurements, the phase θ of the lock-in amplifier was preset to the value $\theta = 45°$, which produced comparable signal amplitudes for the $X(E)$ and $Y(E)$ components [in the absence of the preset phase the signal $Y(E)$ becomes comparable with the noise level].

The form of the phase diagram (Fig. 3b) and the coincidence of the fitting parameters used to fit the $X(E)$ and $Y(E)$ components (Fig. 3a) confirm the single-component nature of the photoreflectance spectrum.

Figure 4 presents a two-component photoreflectance spectrum in the region of the transition E_0, obtained for a sample of GaAs [$n(\text{Si}) = 1\times 10^{18}\text{cm}^{-3}$]. At first glance, without carrying out a phase analysis, it is impossible to establish its multicomponent character. However, by introducing the preset phase $\theta = 89°$ in the $X(E)$ component it is possible to suppress one of the two spectral contributions (the mean-field component) such that it became possible to separate out the second component (the impurity structure) in its pure spectral form (Fig. 4a, upper spectrum). The given

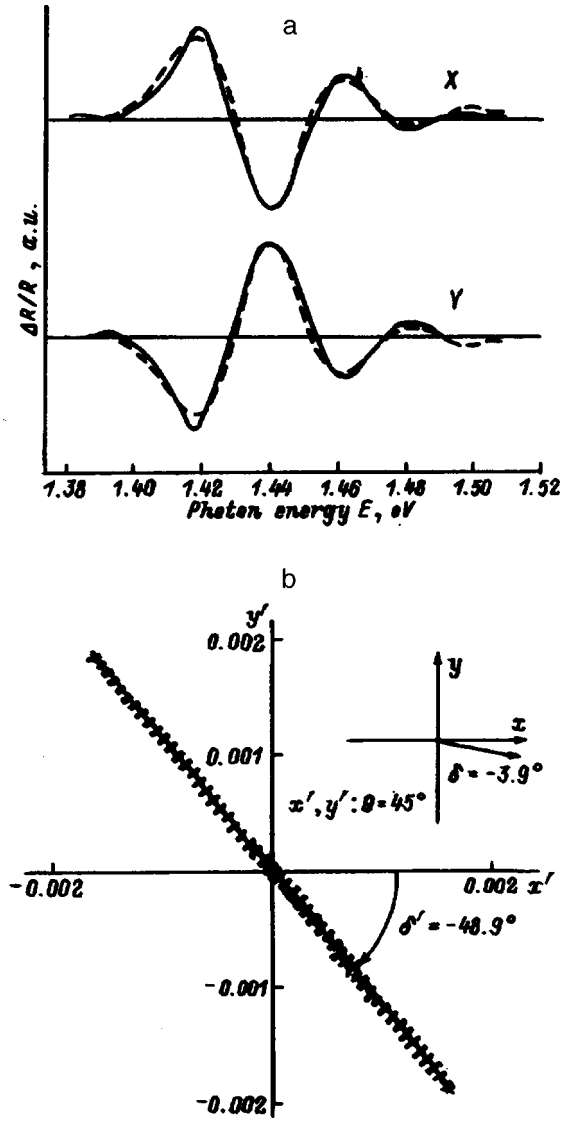

FIG. 3. a—Experimental photoreflectance spectra in the region of the E_0 transition, recorded for a sample of n-GaAs. Photoreflectance spectra obtained for the X and Y channels of the lock-in amplifier (solid lines) and the corresponding fits (dashed lines) are shown. The fitting parameters ($E_0 = 1.412$ eV, $F = 3.44\times 10^6$ V/m, $\Gamma = 12$ meV) coincide for both channels. b—experimental phase diagram of the photoreflectance spectra shown in Fig. 3a, with preset phase $\theta = 45°$. The shape of the phase diagram and the coincidence of the parameters used to fit the $X(E)$ and $Y(E)$ spectra confirm the single-component character of the photoreflectance signal. The phase angle of the spectrum is shown in the inset by the corresponding phase vector.

procedure leads in what follows to a significant simplification of the analysis of the photoreflectance spectrum. The explicit deviation from a straight line in the corresponding experimental phase diagram (see Fig. 4b) also confirms the multicomponent character of this spectrum.

As a result of an analysis of the shape of the spectrum, we separated out the mean-field contribution (Fig. 4a, dashed line). The phase delay of the given component can be easily determined from the preset measurement phase ($\delta = -1°$). The magnitude of the phase delay of the second component is determined with the help of the components $X(E)$ and $Y(E)$ of the experimental spectrum, obtained by analysis of the shape of the spectrum, and the phase diagram constructed

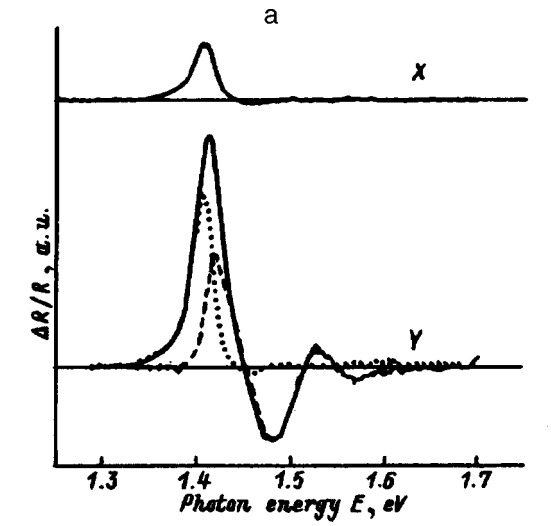

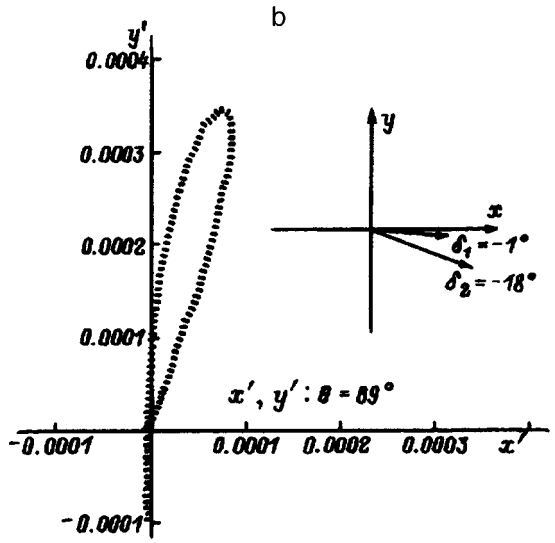

FIG. 4. a—Experimental photoreflectance spectra (solid curves), obtained for the X and Y channels from a sample of n-GaAs. The mean-field component (dashed curve) and impurity component (dotted curve) of the photoreflectance, separated by spectral analysis, are shown for the Y spectrum. The difference ΔE between the transition energy $E_0 = 1.423$ eV, determined by fitting the MF/FKO structure, and the energy position of the peak of the second structure E_i is 17 meV; b—experimental phase diagram of the photoreflectance spectra shown in Fig. 4a for the preset phase $\theta = 89°$. The shape of the phase diagram is an indication of the complex character of the photoreflectance signal. Phase angles of the spectral components are shown in the inset by the corresponding phase vectors.

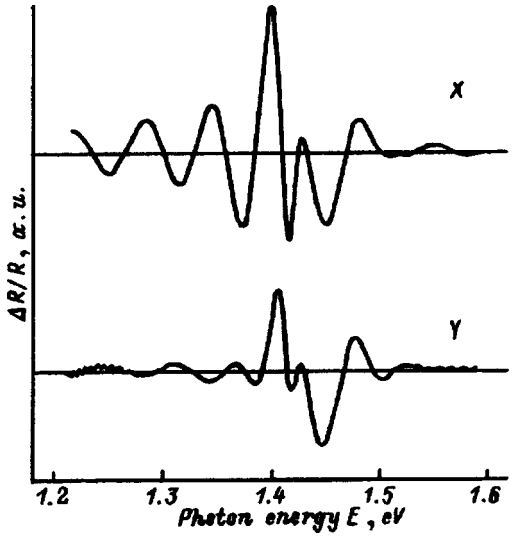

FIG. 5. Experimental photoreflectance spectra obtained for the X and Y channels on a homoepitaxial GaAs/GaAs sample.

with their help. Each of the components has its own linear phase diagram. The phase angles of the spectral components are shown in the inset (Fig. 4b) with the help of the corresponding phase vectors.

Taking the modulation frequency $f = 2500$ Hz into account and using Eqs. (4) and (6), we obtained the values of the corresponding time constants given in Table I. The second component of the photoreflectance was identified along with the mean-field contribution. Its main peak is seen to lie 17 meV below that of the first contribution. The corresponding optical transitions should apparently be linked with modulation of the optical transitions on defects or dopant impurities.

As a third example of multicomponent structures, we chose a photoreflectance spectrum obtained from a sample of the homoepitaxial structure n-GaAs/ n^+-GaAs [n(Si) $= 1\times10^{16}\text{cm}^{-3}/n^+(\text{Si}) = 1\times10^{18}\text{cm}^{-3}$; Figs. 5–7]. The experimental phase diagram, constructed from the $X(E)$ and $Y(E)$ spectra shown in Fig. 5, has a highly complex structure (see Fig. 7), from which we may conclude that this is a multicomponent spectrum.

The photoreflectance structure obtained from this homoepitaxial sample clearly consists of more than two com-

TABLE I. Phase delays δ and characteristic time constants τ of the spectral components of the photoreflectance in the region of the transition E_0.

PR component		GaAs substrate, naturally oxidized ($f = 167$ Hz)	GaAs, surface treated in $ZrOCl_2\times8H_2O+O_2$ ($f = 2500$ Hz)	n-GaAs/n^+-GaAs ($f = 2500$ Hz)
MF/FKO	δ, °	−4	−1	−12
	τ, μs	59.5	1.1	13.3
Exciton	δ, °	–	–	−11
	τ, μs	–	–	12.2
Defects	δ, °	–	−18	–
or impurities	τ, μs	–	21	–
LEIO	δ, °	–	–	−65
	τ, μs	–	–	110

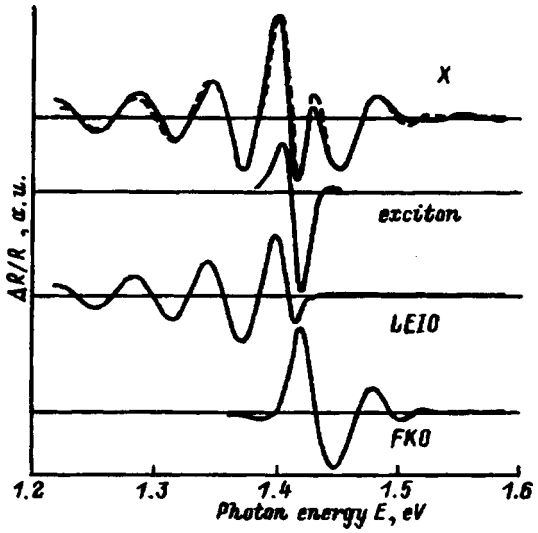

FIG. 6. Results of spectral analysis of the $X(E)$ photoreflectance spectrum from Fig. 5. For comparison, the best fit to the experimental spectrum, obtained by summing the three spectral components shown below and depicted by the dashed curve, is shown for comparison. Fitting parameters: a—(exciton) $E_{\text{exc}}=1.416$ eV, $\Gamma=23.6$ meV; b—(LEIO) $d_{\text{layer}}=2345$ nm; c—(FKO) $E_0=1.432$ eV, $F=7.31\times10^7$ V/m, $\Gamma=20.5$ meV.

ponents. A phase analysis indicates three energy regions, in each of which its own spectral component dominates. In contrast to the example considered above, the experimental separation of each of the spectral contributions to the photoreflectance is not possible and their separation is possible only with the help of a complete mathematical–theoretical analysis.

Figure 6 shows fits to the spectrum which allowed us to identify all three components. The first component corresponds to the mean-field contribution (MF/FKO). The second component corresponds to the so-called low-energy interference oscillations (LEIO),[9–11] which are the result of interference of the photoreflectance signal from the interface in the thin ($d=2.3$ μm) homoepitaxial layer. In the region of the transition energy E_0 we identified the exciton structure (the observation of exciton structures in the photoreflectance at room temperature was also reported in Refs. 12–14). For each of the three spectral components, the corresponding linear phase diagram can be constructed. From the single-component phase diagrams shown in the lower part of Fig. 7 the phase delays of the individual spectral components can be clearly identified.

The experimental phase diagram, shown in the upper half of Fig. 7, has the typical loop structure characteristic of a multicomponent spectrum. By fitting the photoreflectance spectra obtained for the X and Y channels of the lock-in amplifier we obtained a reconstructed phase diagram that agrees well with the experimental phase diagram.

Experimental values of the phase delays and the characteristic time constants, determined from them, of the identified spectral components of the photoreflectance are given collectively in Table I. From our analysis of extensive experimental data we may conclude that the exciton components have the smallest time constants in each spectrum. In contrast, the photoreflectance components, which correspond to optical transitions involving the participation of defects or dopant impurities and to low-energy interference oscillations, have the largest time constants relative to the other components of the corresponding spectra.

Further studies should show how the relatively large values of the time constants can be linked with recharging processes in the skin layer of the considered semiconductor structures. Such studies may prove to be an interesting area of application of phase-sensitive photoreflectance spectroscopy.

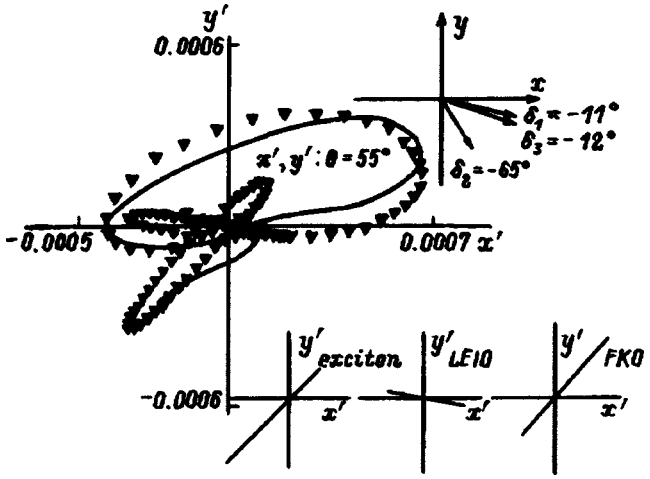

FIG. 7. Reconstruction (solid curve) of the experimental phase diagram (inverted triangles) constructed from the spectra shown in Fig. 6. The lower part of the figure presents the phase diagrams of each of the three spectral components.

Fax: 049-345-55-25-158
E-mail: gansha physik.uni-halle.dee5caf mlucom.urz.uni-halle.de

[1] E. G. Seebauer, J. Appl. Phys. **66**, 4963 (1989).
[2] H. Shen, M. Dutta, R. Lux, W. Buchwald, L. Fotiadis, and R. N. Sacks, Appl. Phys. Lett. **59**, 321 (1991).
[3] W. Zhou, M. Dutta, H. Shen, J. Pamulapati, B. R. Bennett, C. H. Perry, and D. W. Weyburn, J. Appl. Phys. **73**, 1266 (1993).
[4] V. L. Alperovich, A. S. Jaroshevich, H. E. Scheibler, and A. S. Terekhov, Solid-State Electron. **37**, 657 (1994).
[5] D. E. Aspnes, Surf. Sci. **37**, 418 (1973).
[6] M. Cardona, in *Solid State Physics*, Suppl. 11 (Academic Press, New York, 1969) [''Modulation Spectroscopy''].
[7] H. Shen, Z. Hang, S. H. Pan, F. H. Pollak, and J. M. Woodall, Appl. Phys. Lett. **52**, 2058 (1988).
[8] T. Kanata, M. Matsunaga, H. Takakura, Y. Hamakawa, and T. Nishino, J. Appl. Phys. **66**, 358 (1989).
[9] D. Huang, D. Mui, and H. Morkoc, J. Appl. Phys. **66**, 358 (1989).
[10] N. Kallergi, B. Roughani, J. Aubel, and S. Sundaram, J. Appl. Phys. **68**, 4656 (1990).
[11] H. K. Lipsanen and V. M. Airaksinen, Appl. Phys. Lett. **63**, 2863 (1993).
[12] S. Adachi, Phys. Rev. B **41**, 1003 (1990).
[13] D. Nolte and M. Melloch, MRS Bull. (March 1994), p. 44.
[14] R. Wang and Desheng Jiang, J. Appl. Phys. **72**, 3826 (1992).

Translated by Paul F. Schippnick

Electrical properties of GaSb-based solid solutions (GaInAsSb, GaAlSb, GaAlAsSb) and their compositional dependence

T. I. Voronina, B. E. Dzhurtanov, T. S. Lagunova, M. A. Sipovskaya, V. V. Sherstnev, and Yu. P. Yakovlev

A. F. Ioffe Physicotechnical Institute, Russian Academy of Sciences, 194021 St. Petersburg, Russia
(Submitted August 6, 1997; accepted for publication September 15, 1997)
Fiz. Tekh. Poluprovodn. **32**, 278–284 (March 1998)

The electrical properties of GaSb and solid solutions based on it (GaInAsSb, GaAlSb, GaAlAsSb) have been investigated. It is shown that the current-carrier concentration and mobility in all these materials are determined mainly by $V_{Ga}Ga_{Sb}$ structural defects, with their concentration decreasing almost linearly with decrease of the GaSb content of the solid solution. The dependence of the parameters of the solid solutions on the concentration of these structural defects is determined. The possibility of reducing their concentration by using the neutral solvent Pb and rare-earth elements is demonstrated. © *1998 American Institute of Physics.* [S1063-7826(98)00403-7]

Interest in GaSb and isoperiodic solid solutions based on it is due to the fact that these materials are widely used in the construction of optoelectronic devices operating in the infrared (1.3–2.5 μm), including lasers, light-emitting diodes, fast-response photodiodes, avalanche photodiodes, etc. Our earlier comprehensive study of the galvanomagnetic and photoelectric properties of GaSb and solid solutions similar in composition to GaSb ($GaIn_xAsSb$ ($x=0.1-0.2$), $GaAl_xSb$ ($x=0.1$), $GaAl_xAsSb$ ($x=0.34$), (Refs. 1–6) has made it possible to reveal for each material the main factors controlling its quality and level of perfection of the crystals, the nature of the charge carriers in them, their concentration, mobility, and activation energy. The present work has as its goal to uncover the general trends of all the investigated compounds, the relevant electrical and photoelectric properties of these materials, and also their dynamics as a function of the composition of the solid solution and some specific details of their synthesis. This paper also includes completely new experimental data on these solid solutions over a wide range of variation of their composition. Thus, we have investigated $GaAl_xSb$ for $x=0.34$ and $GaAl_xAsSb$ for $x=0.5$. We hope that the results of this study will make it possible to correctly approach the various problems involved in obtaining higher-quality materials with required band gap and given concentration and mobility of the current carriers.

All of the materials we have investigated, both the binary compound GaSb and the ternary and quaternary solid solutions, were prepared by liquid-phase epitaxy at temperatures of 550–650 °C on GaSb substrates. The conductivity, Hall effect, mobility, and magnetoresistance were measured in the GaSb epitaxial layers and solid solutions by the compensation method, and the acceptor and donor concentrations, activation energy of the impurities were determined; the width of the band gap was also determined from photoconductivity and electroluminescence data. Studies of galvanomagnetic effects were carried out on samples of rectangular shape with indium contacts on the surface of the epitaxial film in the temperature interval $T=77-300$ K and in magnetic fields up to 10 kOe.

GALLIUM ANTIMONIDE

Let us first consider the electrical properties of GaSb, which, as it turns out, in many ways determine the parameters of the solid solutions based on this binary material.

As a result of our studies of epitaxial layers of GaSb, grown on p-GaSb substrates 80–200 μm thick (the substrate was later removed), we found that epitaxial GaSb, in which special precautions were taken to keep the level of dopant impurities to a minimum, grown by liquid-phase epitaxy, just like bulk GaSb grown by the Czochralski or Bridgman method, always has p-type conductivity with hole concentration $p=(1-2)\times10^{17}$ cm^{-3} and mobility $\mu=600-700$ cm^2/(V·s) at $T=300$ K and $p=(2-3)\times10^{16}$ cm^{-3} and $\mu=2000-3000$ cm^2/(V·s) at $T=77$ K (see Tables I and II). The width of the band gap in GaSb at $T=77$ K is $E_g=0.78$ eV.

From the temperature dependence of the Hall coefficient R, the conductivity σ, and the hole concentration p, determined by cyclotron resonance, and also from photoelectric measurements in GaSb we established the existence of three acceptor levels: a shallow level with activation energy $E_{A1}=0.011-0.017$ eV due to uncontrolled impurities in the initial ingredients, and two deep levels $E_{A2}=0.03-0.035$ eV and $E_{A3}=0.07-0.09$ eV, which we assign to a doubly charged structural defect. These results agree with earlier data, obtained in Refs. 7 and 8, where it was shown that in GaSb crystals the dominant scattering center is a natural structural defect of the crystal lattice, namely, gallium vacancies with the gallium substituting for antimony ($V_{Ga}Ga_{Sb}$). The concentration of these structural defects determines the hole concentration and mobility in GaSb.

We were faced with a problem: to find an efficient means of lowering the concentration of these structural defects thereby enhancing the quality of these crystals.

It seemed reasonable to assume that the concentration of natural structural defects associated with stoichiometry depends on the relative numbers of antimony and gallium atoms in the solution–melt from which the epitaxial film is grown. We have proposed a method of varying this ratio by

TABLE I.

Sample No.	Composition $Ga_{1-x}In_xAs_{1-y}Sb_y$ x	y	Initial ingredients	p, 10^{16} cm^{-3} 300 K	77 K	μ, cm2/(V·s) 300 K	77 K	E_A, eV E_{A1}	E_{A2}	E_{A3}	E_{A4}	$\{N_D, N_A\}$, 10^{16} cm^{-3} N_D	N_{A1}	NA2	E_g, eV 77 K
1	0	100	Ga, GaSb	17	4	550	2250	0.015	0.03	0.07	–	0.1	1	27	0.79
2	0.11	0.93	In, Sb, GaSb, InAs	6.2	1.5	465	1870	0.008	0.03	–	–	1.7	4.4	2.5	0.65
3	0.155	0.863	In, Sb, GaSb, InAs	9.4	0.59	365	1950	0.008	0.035	0.073	–	3.3	4.3	1.3	0.605
4	0.22	0.81	InSb, GaSb, InAs	3	0.6	500	2850	0.01	0.03	0.07	–	1.4	2.5	1.9	0.565
5*	0.092	0.93	In, Sb, GaSb, InAs	6.6	1.2	370	1100	0.009	0.038	–	–	3	5.7	2.5	0.64
6*	0.156	0.864	In, Sb, GaSb, InAs	70	3.4	118	377	0.003	0.038	–	0.1	8.5	12	3	0.605
7*	0.217	0.836	In, Sb, Ga, InAs	30	17	187	304	0.0014	–	–	0.1	20	40	–	0.57

[a]*Remark.* n-GaSb:Te substrate without intermediate insulating layer.

introducing lead into the solution–melt as a neutral solvent. As a result, it was possible to vary the reduced antimony concentration in the melt $X^*_{Sb}=[Sb]/[Sb+Ga]$ from $X^*_{Sb}=0.125$ (without lead) to $X^*_{Sb}=0.875$. This led to striking results. Figure 1 plots the dependence of the hole concentration at $T=300$ K and the mobility at $T=77$ K on the reduced antimony concentration. It can be seen that the hole concentration falls abruptly with growth of X^*_{Sb}, reaching a minimum at $X^*_{Sb}=0.8$ (in a number of cases in this region we even obtained samples with n-type conductivity), and then rises back up. The mobility has its maximum at $X^*_{Sb}\simeq 0.6$, falls abruptly near $X^*_{Sb}=0.8$, and then rises again.

To determine the donor and acceptor concentrations in GaSb crystals grown from solution–melts with different values of X^*_{Sb}, we used the temperature dependences of the concentration and mobility of the current carriers. Assuming that the mobility is determined by scattering from impurity ions and lattice vibrations, using the Brooks–Herring formula for the dependence of the mobility on the impurity ion concentration, we calculated the concentrations of the deep and shallow acceptors, and also the concentration of donors. We found that the concentration of structural defects with $E_{A2}=0.033$ eV falls continuously from 2.7×10^{17} cm^{-3} in the initial sample with $X^*_{Sb}=0.125$ to 2×10^{15} cm^{-3} for $X^*_{Sb}=0.8$ (see Fig. 1). With further increase of the antimony concentration in the solution–melt, the hole concentration again grows abruptly, but now because of shallow impurities ($E_{A1}\simeq 0.017$ eV), while the concentration of deep structural defects remains quite low as before, $\sim 2\times10^{16}$ cm^{-3}. The authors of Ref. 1 succeeded in obtaining samples of GaSb, grown from a highly antimony-enriched solution–melt ($X^*_{Sb}=0.875$) under conditions which prevented fine impurities from getting into the crystal during epitaxial growth (they used a white-sapphire cassette and antimony of purity 99.9999%). As a result, they obtained GaSb with $p=6.8\times10^{15}$ cm^{-3} and $\mu=6770$ cm^2/(V·s) at 77 K. The concentration of deep acceptors fell to 5×10^{15} cm^{-3}, and the concentration of shallow acceptors was 3×10^{16} cm^{-3}. Thus, by varying the ratio of gallium to antimony in the solution–melt it is possible to obtain pure GaSb crystals and also insulating GaSb (in the region of $X^*_{Sb}=0.8$) with very low current-carrier concentration down to $p=10^{13}$ cm^{-3} at 77 K, which is used as a buffer layer in production applications.

We also achieved the result of decreasing the number of structural defects in GaSb by doping the solution–melt with rare-earths (Gd, Yb).[1] The concentration of deep acceptors was lowered from 1×10^{17} to 4×10^{16} cm^{-3}; granted, in the process the concentration of fine impurities grew. It may be assumed that gallium vacancies diffuse to the rare-earth atom, and that a small vacancy cluster forms around it, blocking the formation of $V_{Ga}Ga_{Sb}$ structural defects and lowering their concentration.

TABLE II.

Composition	p, 10^{16} cm^{-3} 300 K	77 K	μ, cm^2/(V·s) 300 K	77 K	E_A, eV E_{A1}	E_{A2}	E_{A3}	E_{A4}	$\{N_D, N_A\}$, 10^{16} cm^{-3} N_D	N_{A1}	NA2	E_g, eV 77 K
GaSb	17	4.0	550	2250	0.015	0.035	0.07	–	0.1	1.0	27	0.79
$GaAl_{0.1}Sb$	5.6	0.82	670	2600	0.015	0.03	–	–	1.0	1.7	6.2	0.9
$GaAl_{0.34}Sb$	4.0	0.29	320	1300	0.009	0.034	–	–	0.15	0.8	4.0	–
$GaAl_{0.34}AsSb$	6.0	1.5	300	1130	0.009	0.03	–	–	1.3	5.7	6.9	1.2
$GaAl_{0.5}AsSb$	97	0.8	420	1600	0.009	0.034	–	0.15	0.67	1.5	5.0	1.35

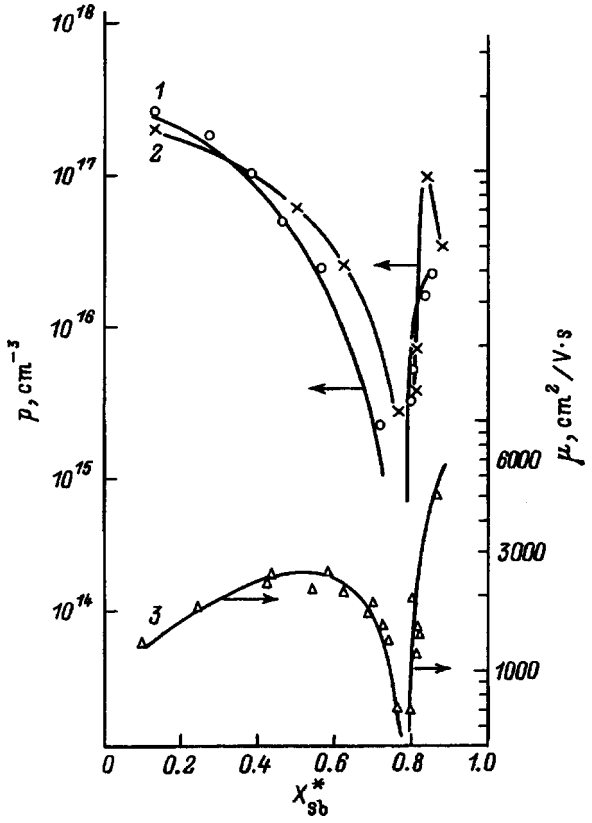

FIG. 1. The hole concentration p at 300 K (*1*), mobility μ at 77 K (*3*), and the concentration of structural defects N_{A2} (*2*) as functions of the reduced antimony concentration X^*_{Sb}.

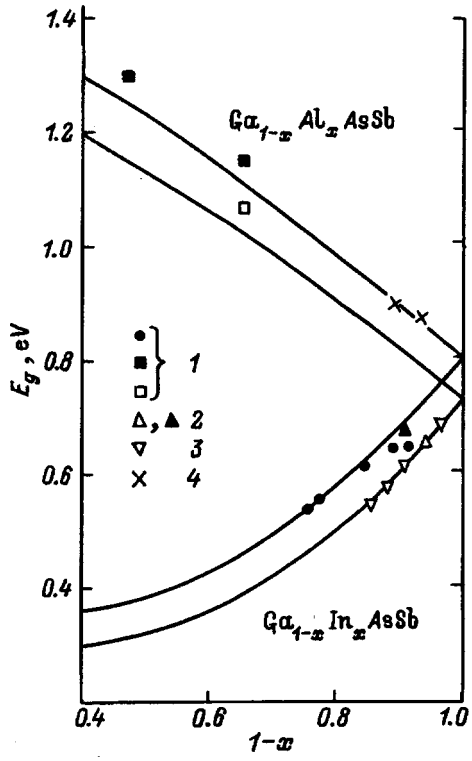

FIG. 2. Dependence of the width of the band gap E_g on the composition of the solid solution at 77 (*a*) and 300 (*b*) K. Data: *1*—our work, *2*—Ref. 11, *3*—Ref. 9, *4*—Ref. 14.

SOLID SOLUTIONS BASED ON GaSb

In order to extend the optical range of devices operating in the infrared, ternary and quaternary solid solutions based on GaSb are widely used: GaInAsSb, GaAlAsSb, GaAlSb, and others.

The calculated width of the band gap E_g in the solid solutions $GaIn_xAsSb$ and $GaIn_xAsSb$, which are isoperiodic with the GaSb substrate, is plotted in Fig. 2 by the solid lines as a function of the composition of the solid solution: $E_g = F(1-x)$. The calculation was based on empirical formulas and data taken from Refs. 9 and 10. As follows from the curves, as x grows, the width of the band gap in the solid solutions $GaIn_xAsSb$ decreases from its value for GaSb (0.79 eV), while in $GaAl_xAsSb$ it increases significantly.

THE SOLID SOLUTION GaInAsSb

It is well known that the solid solution $GaIn_xAsSb$ can be isoperiodic with GaSb ($x \leqslant 0.25$) and isoperiodic with InAs ($x \geqslant 0.7$). The immiscibility region lies at intermediate values of x. We examined the properties of GaInAsSb over the entire existence region of the solid solution isoperiodic with GaSb, i.e., for $x < 0.25$, specifically for $x = 0.1$, 0.15, and 0.22. It can be expected that their electrical properties do not greatly differ from those of GaSb.

With the aim of refining the energy structure and determining the width of the band gap E_g in the investigated solid solutions GaInAsSb, we examined the spectral characteristics of the photoconductivity. The width of the band gap, determined from the half-fall of the long-wavelength edge of the intrinsic photoconductivity is given in Table I and plotted in Fig. 2 (dots) for solid solutions of different compositions. The experimental results are in rather good agreement with the calculated values and reveal a falloff of E_g at $T = 77$ K from 0.79 eV (in GaSb) to 0.565 eV in $GaIn_xAsSb$ with $x = 0.22$. For illustration, Fig. 2 also plots experimental data for E_g in GaInAsSb, taken from Ref. 11.

The thickness of the investigated epitaxial layers of solid solution depend on their indium composition: the layer with $x \simeq 0.1$ are thick (~ 100 μm) and can be removed from the substrate, while for $x = 0.15-0.22$ the thickness of the layers is 5 μm. It was impossible to grind off the substrate. The measurements therefore were carried out on samples with an n-type substrate (GaSb:Te), and also on substrates with an intermediate insulating layer of GaSb grown in the presence of a neutral solvent—lead (see above).

It can be expected that with increasing substitution of the lattice gallium atoms by indium atoms the probability of formation of structural defects $V_{Ga}Ga_{Sb}$ decreases, and the concentration of deep acceptors in the crystals is lowered.

From the temperature dependence of the Hall coefficient, the conductivity, and the mobility, and also from the spectral dependence of the photoconductivity we determined the main parameters of the material: the concentrations of shallow (N_{A1}) and deep (N_{A2}) acceptors, the donor concentration (N_D), activation energies of the impurities (E_{A1}, E_{A2}, E_{A3}, E_{A4}), and the width of the band gap E_g, all of which are listed in Table I. The main result here is that we detected the same deep acceptors in the solid solution, with activation

energies $E_{A2} \simeq 0.03$ and $E_{A3} \simeq 0.07$ eV, that exist in GaSb, and also shallow acceptors with $E_{A1} = 0.008 - 0.014$ eV. The concentration of deep acceptors N_{A2}, as expected, always falls with growth of x in the solid solution $GaIn_xAsSb$. Unfortunately, this does not lead to vigorous growth of the current-carrier mobility since in the samples with an intermediate insulating layer and the samples on an n-type GaSb:Te substrate the concentration of shallow acceptors increases with increasing x as the number of deep acceptors decreases. Analyzing their nature, we note that the background of shallow impurity levels depends on the weighed amounts used in the melt. The lowest content of donors and acceptors N_{A1} is found in epitaxial layers grown from a melt prepared from the binary components InAs and GaSb. The concentration of shallow acceptors increases as the result of uncontrolled impurities in In, Ga, and Sb.

Until now, we have spoken of the properties of GaInAsSb solid solutions in which special precautions have been taken to keep the level of dopant impurities to a minimum. In practice, the necessity frequently arises to dope them with various donor or acceptor impurities. We have investigated the behavior of Ge, Cd, Zn, and Te impurities which were introduced into the solid solution $GaIn_{0.1}AsSb$ during growth from doped liquid phase. The thickness of the layers was ~ 100 μm and the substrate was removed. When the material was doped by Ge, Cd, and Zn, it retained its p-type conductivity. The greatest hole concentration was achieved for doping with germanium ($p > 10^{19}$ cm^{-3}). It is interesting that in this case the donor and acceptor concentrations grew simultaneously, i.e., Ge revealed amphoteric properties with incorporation into the lattice as an acceptor impurity predominating. For Cd and Zn doping, only the acceptor concentration grows, and the limiting hole concentration is $\sim 5 \times 10^{17}$ cm^{-3}.

The behavior of Te in GaInAsSb is very interesting. Usually tellurium is a donor that can be a compensating impurity in semiconductors with p-type conductivity. However, in the solid solution GaInAsSb the behavior of tellurium turns out to be more complicated. During growth of thin (5 μm) epitaxial layers of GaInAsSb solid solution on Te-doped GaSb substrates, tellurium diffuses into the layer, which becomes lightly doped with Te, altering the electrical properties of the epitaxial layer of solid solution. In layers grown on tellurium-doped substrates without a buffer layer, the mobility falls severalfold and both the donor and acceptor concentrations grow. Besides the acceptor structural defects with activation energy $E_{A2} = 0.38$ eV, a new acceptor level appears with $E_{A4} = 0.1$ eV (see Table I). We believe that this deep acceptor is created by tellurium that has diffused out of the substrate, in combination with a gallium vacancy in the lattice of the solid solution (V_{Ga}Te). The possibility for the existence of such a center in GaSb crystals was analyzed in Ref. 12, and a level with such an energy was observed in the luminescence spectra of Te-compensated GaSb layers.[13] Thus, tellurium has a double effect: first, it enters the solid-solution lattice as a compensating donor, and second, it forms a new deep structural defect.

The mobility in layers of these solid solutions had the same temperature dependence as in the undoped samples grown on substrates with a buffer layer, but its values were strongly depressed over the entire temperature interval (see Table I). This speaks not only of the large number of impurities in these samples, but also of the existence of some additional mechanism of hole scattering which suppresses the mobility. The detection in these samples of a longitudinal magnetoresistance and a negative photoconductivity can be explained by the existence in the material of nonuniformly distributed charged centers, in our case apparently bound with tellurium that has diffused into the solid solution. The measured mobility in such samples is therefore governed not only by scattering from impurity ions μ_I and lattice vibrations μ_L, but also by this additional scattering mechanism which contributes to the mobility μ_S:

$$1/\mu = 1/\mu_I + 1/\mu_L + 1/\mu_S . \tag{1}$$

According to the effective medium theory,[14] for a longitudinal magnetoresistance $(\Delta\rho/\rho)^{\parallel}$ in crystals containing clusters of impurities or point defects, we can write

$$(\Delta\rho/\rho)^{\parallel} = 0.3 f (\mu_0 H/c)^2, \tag{2}$$

$$\mu = \mu_0 \left[\left(1 - \frac{3}{2} f \right) \Big/ \left(1 - \frac{3}{4} f \right) \right], \tag{3}$$

where μ_0 is the true mobility in the crystal matrix, and f is the volume fraction occupied by the inhomogeneities. Calculating for the mobility and longitudinal magnetoresistance, measured in all the samples grown on GaSb:Te without a buffer layer, showed that the volume fraction occupied by the inhomogeneities is $f = 0.4$–0.56, while in the samples on an insulating substrate $f \simeq 0.15$. Finding μ_0 from Eqs. (2) and (3), it is possible to determine μ_1 from the relation

$$1/\mu_0 = 1/\mu_I + 1/\mu_L ,$$

and, consequently, N_A and N_D, and also μ_S from Eq. (1). We determined the radius of the space charge region of the clusters $R_{cl} = 630$ Å and their concentration $N_{cl} = 5.6 \times 10^{14}$ cm^{-3} for $GaIn_{0.15}AsSb$ grown without a buffer layer. Thus, tellurium diffusing from the substrate into thin epitaxial layers can strongly impact the quality of the solid solutions and be a deciding factor in the construction of devices. Of course, as Te diffuses from the substrate, the Te concentration in the solid solution is not large and can only poorly be monitored. When Te is specially introduced into the solid solution during epitaxial growth, its concentration can be significantly increased. At tellurium concentrations $> 10^{-3}$ at. %, overcompensation of the holes occurs and the solid solution acquires n-type conductivity. The electron concentration in it subsequently increases appreciably with increasing tellurium concentration, reaching 5×10^{18} cm^{-3}. We have for the first time determined the segregation coefficients for Te, Zn, Ge, and Cd in the solid solution GaInAsSb: $C_{Ge} = 0.2$, $C_{Cd} = 0.03$, $C_{Zn} = 0.04$, $C_{Te} \simeq 0.7$.

After examining the electrical properties of GaInAsSb solid solutions and determining that they are in many ways analogous to the electrical properties of GaSb, we came to the conclusion that the methods we have used to reduce the concentration of structural defects in GaSb, to increase the

mobility, and to obtain a material with the required electrical properties can also be applied to solid solutions.

With this aim in mind, we examined the effect of doping GaInAsSb with rare-earth metals (ytterbium) on the photoluminescence spectra. We found that the introduction of a fairly large quantity of ytterbium (~ 0.01 at. %) leads to the disappearance in the photoconductivity spectra of the maximum associated with photoionization of the 0.1-eV center and closing up of the (V_{Ga}Te) structural defect. In this case the mobility of the current carriers is increased by an order of magnitude and for the holes with a concentration of $p=(1-2)\times 10^{16}$ cm^{-3} amounts to $\mu = 1.5\times 10^3$cm^2/(V·s) at $T=77$ K. The GaInAsSb solid solutions grown in a lead solution are now being studied with the goal of reducing the concentration of structural defects. The results of this study will be published separately.

THE SOLID SOLUTIONS GaAlSb AND GaAlAsSb

Having considered the properties of narrow-band solid solutions based on GaSb in the previous section, we will now consider wide-band solid solutions.

As was said above, compounds similar in composition to GaSb, but having a wide band gap include ternary and quaternary solid solutions containing aluminum, in particular, GaAlSb and GaAlSbAs.

Data on the width of the band gap in GaAl$_x$AsSb obtained from the electroluminescence spectrum confirm the theoretically expected result: multicomponent solid solutions containing aluminum have wider band gaps than GaSb, and the width of the band gap grows linearly with aluminum concentration (see Fig. 2). We found that at $T=77$ K $E_g=1.15$ eV for $x=0.34$ and $E_g=1.33$ eV for $x=0.5$. The experimental values are plotted (points) in Fig. 2. For illustration, this figure also plots the experimental values of E_g for the ternary solid solution GaAlSb, obtained from the photoluminescence and electroluminescence spectra in Ref. 15. In both compounds almost linear growth of E_g with x is observed.

We investigated the galvanomagnetic properties (σ, R, μ) of GaAlSb for two compositions (GaAl$_{0.1}$Sb and GaAl$_{0.34}$Sb) and GaAlAsSb also for two compositions GaAl$_{0.34}$SbAs and GaAl$_{0.5}$SbAs). The solid solutions were grown by liquid-phase epitaxy on n-GaSb substrates. The thickness of the GaAlAsSb films was ~ 7 μm, and that of the GaAlSb films was up to 100 μm. In the first case, the film was insulated from the substrate by a potential barrier, and in the case of GaAlSb the substrate was removed. The parameters were measured in the temperature interval 77–300 K, both in undoped solid solutions and in germanium-doped samples.

Note that while GaAlAsSb was isoperiodic with the GaSb substrate (lattice constant $a=6.09$ Å) in the entire range of variation of the aluminum concentration, in the ternary solid solution GaAlSb the mismatch with the substrate increased with increasing aluminum concentration (the lattice constant of the solid solution grew from 6.09 Å at $x=0.1$ to 6.13 Å at $x=0.34$).

All of the undoped samples had p-type conductivity and at $T=300$ K current-carrier concentration $p=5.6\times 10^{16}-9.7\times 10^{17}$ cm^{-3} and mobility $\mu = 420-670$ cm^2/(V·s), while at $T=77$ K $p=3\times 10^{15}-1.5\times 10^{16}$ cm^{-3} and $\mu = 1130-2600$ cm^2/(V·s) (see Table II).

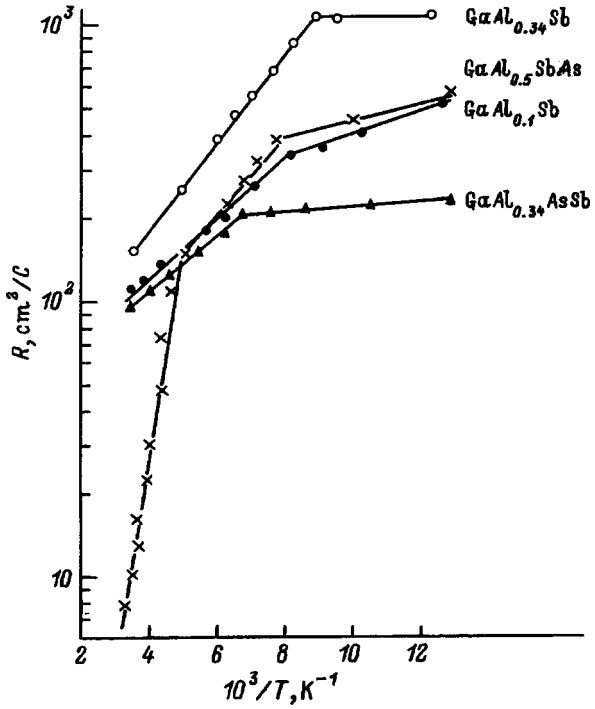

FIG. 3. Temperature dependence of the Hall coefficient for the solid solutions GaAl$_x$Sb and GaAl$_x$AsSb.

Figure 3 plots the temperature dependence of the Hall coefficient for two samples of the ternary solid solutions: GaAl$_{0.1}$Sb and GaAl$_{0.34}$Sb, and two samples of the quaternary solid solutions: GaAl$_{0.34}$SbAs and GaAl$_{0.5}$SbAs. The exponential slopes are clearly visible, indicating the existence of two or three types of acceptor levels. As was already mentioned, in GaSb these are shallow acceptors with $E_{A1}=0.009-0.01$ eV and deep acceptors with $E_{A2}=0.03-0.034$ eV. In all the ternary and quaternary solid solutions these slopes are preserved, whereas in the solid solution with higher aluminum content GaAl$_{0.5}$AsSb a new level with activation energy $E_{A3}=0.15$ eV appears. This is probably a level produced by tellurium diffusing from the substrate. It shows up when the concentration of the main structural defects is lower and the film thickness is small. This level was also observed earlier in GaSb and GaInAsSb. To determine the donor and acceptor concentrations, we utilized the temperature dependence of the mobility in the interval 77–300 K (see Fig. 4). Employing the same calculational technique as for GaInAsSb, we find the total concentration of impurity ions in the solid solution, and also the donor and acceptor concentrations.

The results for the samples examined are presented in Table II. The table also gives the parameters for GaSb grown by the standard technique.

Let us first consider GaAlSb. It can be seen that in comparison with GaSb, in GaAlSb the concentration of shallow impurities N_{A1} is somewhat greater, but with growth of the aluminum concentration, their concentration grows slightly, remaining about 10^{16} cm^{-3}. The concentration of structural

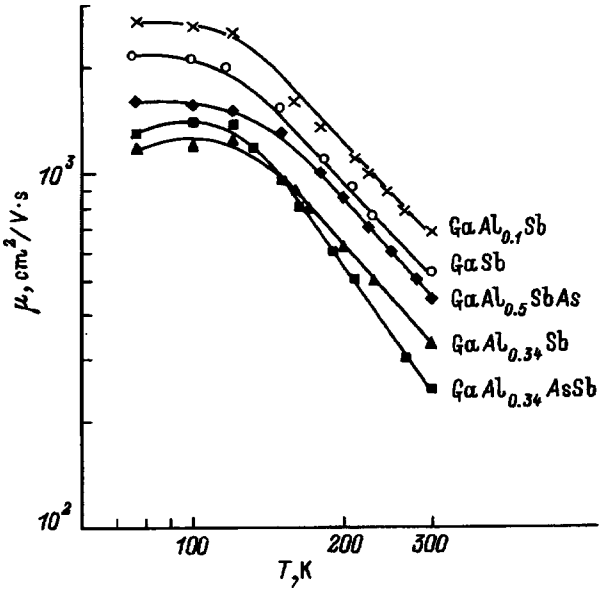

FIG. 4. Temperature dependence of the mobility for the solid solutions $GaAl_xSb$ and $GaAl_xAsSb$.

defects N_{A2} with $E_2=0.034$ eV falls monotonically as the aluminum concentration is increased from 2×10^{17} cm^{-3} in GaSb to 4×10^{16} cm^{-3} in $GaAl_{0.34}Sb$. This could also have been expected since Al replaces Ga in the crystal lattice and thereby blocks the formation of $V_{Ga}Ga_{Sb}$ structural defects. It is interesting that in the solid solution with composition $GaAl_{0.1}Sb$ the mobility at $T=300$ K and $T=77$ K, because of this circumstance, grows in comparison with GaSb. When the aluminum concentration is increased (such as in $GaAl_{0.34}Sb$), the mobility falls abruptly over the entire temperature interval, which indicates the appearance of an additional scattering mechanism, possibly due to an increase in the lattice mismatch since neither the concentration of the deep acceptors nor that of the shallow acceptors grows. In GaAlAsSb the picture is similar: the number of shallow levels in this solid solution is somewhat larger than in GaSb, but with growth of the aluminum concentration it falls. The concentration of structural defects with $E_{A2}=0.034$ eV decreases considerably with increasing aluminum concentration (from 2.7×10^{17} cm^{-3} in GaSb to 5×10^{16} cm^{-3} in $GaAl_{0.5}SbAs$). In this case, growth of the mobility is not observed since it is limited by the appearance of additional scattering from the clusters of point defects possibly associated with diffusion of tellurium into the solid solution and with the appearance of one more deep acceptor, with $E_{A4}=0.15$ eV, which is clearly visible in the temperature dependence of the Hall constant R in the samples of $GaAl_{0.5}Sb$.

Thus, the improvement in the quality of crystals of solid solutions afforded by the decrease in the concentration of structural defects resulting from the substitution of gallium atoms by aluminum atoms is possible only at low aluminum concentrations, when x is no greater than $x=0.1$. Further growth of the aluminum concentration leads to a fall in the mobility due to scattering from clusters of defects.

Let us take a brief look at the possibility of doping the solid solutions containing aluminum with germanium. We investigated in detail the doping of the solid solutions $GaAl_{0.1}Sb$ and $GaAl_{0.34}Sb$. The hole concentration grew with the level of germanium doping: in $GaAl_{0.1}Sb$ it grew from $p=5.6\times10^{16}$ to 1.3×10^{19} cm^{-3} and in $GaAl_{0.34}AsSb$ it grew from $p=6\times10^{16}$ to 6.7×10^{18} cm^{-3} at $T=300$ K. The current-carrier mobility decreased in this case. From the temperature dependence of the mobility we determined the donor and acceptor concentrations in the manner described above. It is interesting that germanium in these solid solutions manifests amphoteric properties: The donor concentration grows simultaneously with the stronger growth of the acceptor concentration. Only upon heavy doping ($p>10^{18}$ cm^{-3}) does the growth of the donor concentration begin to slow down. The same behavior of germanium was also observed in the quaternary solid solution p-GaInAsSb. The segregation coefficient of germanium in GaAlSb and GaAlAsSb was calculated. It turned out to be equal to $0.15-0.2$ and was close in value to its value in GaInAsSb, which again points to the commonality of the electrical properties of ternary and quaternary solid solutions similar in composition to GaSb.

The main results of our study are as follows:

1. We have found that in GaSb and in the isoperiodic solid solutions based on it: $GaIn_xAsSb$ ($x=0.1-0.22$), $GaAl_xAs$ ($x=0.1-0.34$), and $GaAl_xAsSb$ ($x=0.34-0.5$) the conductivity is determined mainly by doubly charged acceptors, which are natural structural defects $V_{Ga}Ga_{Sb}$ (gallium vacancy and gallium replacing antimony) with activation energies $E_{A2}=0.035$ eV and $E_{A3}=0.07$ eV.

2. We have shown that the number of $V_{Ga}Ga_{Sb}$ structural defects in the solid solutions $GaIn_xAsSb$, $GaAl_xSb$, and $GaAl_xAsSb$ decreases with increasing x as the Ga atoms are replaced respectively by indium or aluminum; the hole concentration decreases in this case and the mobility increases. For $x>0.22$ in $GaIn_xAsSb$ and for $x>0.1$ in $GaAl_xSb$ and $GaAl_xAsSb$ we see a clustering of point defects, which lowers the mobility.

3. We were able to reduce the concentration of structural defects in GaSb by two orders of magnitude (from 2.8×10^{17} to 2×10^{15} cm^{-3}) by introducing the neutral solvent lead into the solution–melt, altering the ratio of group-III and V elements in the solution–melt.

4. The concentration of shallow acceptor impurities in the solid solutions was controlled by the purity of the starting ingredients and was significantly lower in solid solutions obtained from binary compounds.

5. Doping of GaSb and the solid solutions GaInAsSb by rare-earth impurities (Gd, Yb) made it possible to increase the mobility of the current carriers by lowering the concentration of natural structural defects: $V_{Ga}Ga_{Sb}$ in GaSb and the acceptor structural defect $V_{Ga}Te$, formed in the solid solution GaInAsSb by diffusion of tellurium from the GaSb:Te substrate.

6. We have demonstrated the possibility of doping GaSb and solid solutions isoperiodic with it with donor and acceptor impurities and have determined the segregation coefficients of Te, Zn, Cd, and Ge.

[1] N. T. Bagraev, A. N. Baranov, T. I. Voronina, Yu. N. Tolparov, and Yu. P. Yakovlev, Pis'ma Zh. Tekh. Fiz. **11**, No. 2, 117 (1985)[Tech. Phys. Lett. **11**, 47 (1985)].
[2] A. N. Baranov, T. I. Voronina, T. S. Lagunova, I. N. Timchenko, Z. I. Chugueva, V. V. Sherstnev, and Yu. P. Yakovlev, Fiz. Tekh. Poluprovodn. **23**, 780 (1989) [Sov. Phys. Semicond. **23**, 490 (1989)].
[3] A. N. Baranov, A. N. Dakhno, B. E. Dzhurtanov, T. S. Lagunova, M. A. Sipovskaya, and Yu. P. Yakovlev, Fiz. Tekh. Poluprovodn. **24**, 98 (1990) [Sov. Phys. Semicond. **24**, 670 (1990)].
[4] A. N. Baranov, T. I. Voronina, A. N. Dakhno, B. E. Dzhurtanov, T. S. Lagunova, M. A. Sipovskaya, and Yu. P. Yakovlev, FIz. Tekh. Poluprovodn. **24**, 1072 (1990) [Sov. Phys. Semicond. **24**, 676 (1990)].
[5] T. I. Voronina, A. N. Dakhno, B. E. Dzhurtanov, T. S. Lagunova, M. A. Sipovskaya, and Yu. P. Yakovlev, FIz. Tekh. Poluprovodn. **24**, 1072 (1990) [Sov. Phys. Semicond. **24**, 676 (1990)].
[6] T. I. Voronina, B. E. Dzhurtanov, T. S. Lagunova, and Yu. P. Yakovlev, Fiz. Tekh. Poluprovodn. **28**, 2001 (1994) [Semiconductors **28**, 1103 (1994)].
[7] D. E. Effer and P. J. Effer, J. Phys. Chem. Solids **25**, 451 (1964).
[8] Kenshiro Nakashima, Jpn. J. Appl. Phys. **20**, 1085 (1981).
[9] T. C. De Winter, M. A. Pollack, A. K. Strivastava, and J. L. Zuskind, J. Electron. Mater. **4**, 729 (1985).
[10] P. G. Eliseev, Élektron. Promst., No. 8, 49 (1980).
[11] A. N. Baranov, A. N. Imenkov, A. A. Rogachev, V. V. Sherstnev, and Yu. P. Yakovlev, Fiz. Tekh. Poluprovodn. **20**, 2217 (1986) [Sov. Phys. Semicond. **20**, 1385 (1986)].
[12] A. S. Kyuregyan, I. K. Lazareva, V. M. Stuchebnikov, A. É. Yunovich, Fiz. Tekh. Poluprovodn. **6**, 242 (1972) [Sov. Phys. Semicond. **6**, 208 (1972)].
[13] A. N. Baranov, T. I. Voronina, N. S. Zimogorova, L. M. Kanskaya, and Yu. P. Yakovlev, Fiz. Tekh. Poluprovodn. **19**, 1672 (1985) [Sov. Phys. Semicond. **19**, 1026 (1985)].
[14] M. H. Cohen, Phys. Rev. Lett. **30**, 694 (1973).
[15] A. N. Baranov, Author's Abstract of Candidate's Dissertation (A. F. Ioffe Physicotechnical Institute, Russ. Acad. Sci., Leningrad, 1984).

Translated by Paul F. Schippnick

Low-frequency noise in *n*-GaN

N. V. D'yakonova and M. E. Levinshteĭn

A. F. Ioffe Physicotechnical Institute, Russian Academy of Sciences, 194021 St. Petersburg, Russia

S. Contreras and W. Knap

G.E.S., UMR-CNRS 5650, cc074, Université Montpellier II, F-34095 Montpellier, France

B. Beaumont and P. Gibart

CRHEA, rue Bernard Gregory, F-06560 Valbonne, France

(Submitted September 9, 1997; accepted for publication September 15, 1997)
Fiz. Tekh. Poluprovodn. **32**, 285–289 (March 1998)

Low-frequency noise has been investigated in the hexagonal polytype of *n*-type gallium nitride (GaN) with equilibrium electron concentration at 300 K $n_0 \simeq 7\times10^{17}$ cm^{-3}. The frequency and temperature dependence of the noise spectral density S_I/I^2 was studied in the range of analysis frequencies f from 20 Hz to 20 kHz in the temperature range from 80 to 400 K. Over the entire temperature range the frequency dependence of the dark noise is close to $S_I/I^2 \sim 1/f$ (flicker noise). The rather weak temperature dependence of the noise level is characterized by very high values of the Hooge constant $\alpha \simeq 5-7$. These large α values indicate a rather low level of structural quality of the material. The effects of infrared and band-to-band illumination on low-frequency noise in GaN are studied here for the first time. The noise level is unaffected by illumination with photon energy $E_{\rm ph} < E_g$ (E_g is the band gap) even for a relatively high value of the photoconductivity $\Delta\sigma/\sigma \simeq 50\%$. Band-to-band illumination ($E_{\rm ph} \geqslant E_g$) influences the low-frequency noise level over the entire investigated temperature range. At relatively high temperatures the influence of illumination is qualitatively similar to that of band-to-band illumination on low-frequency noise in Si and GaAs. At relatively low temperatures the influence of illumination on the noise in GaN is qualitatively different from the results obtained earlier for Si and GaAs. © *1998 American Institute of Physics.* [S1063-7826(98)00503-1]

1. INTRODUCTION

Gallium nitride (GaN) is one of the semiconductor materials that has been studied intensively in recent years. Progress in the technology of this direct-band semiconductor having a wide band gap ($E_g = 3.4$ eV) has demonstrated its potential for use in the fabrication of blue and violet light-emitting diodes and lasers,[1,2] ultraviolet photodetectors, and devices using surface acoustic waves, etc. (see, e.g., the series of review articles[1–3] in the MRS Bulletin, No. 2, February 1997). The high value of the maximum electron velocity $v_{\max}$ and the saturated velocity v_s ($v_{\max} \simeq 2.7\times10^7$ cm/s, $v_s \simeq 1.5\times10^7$ cm/s; Refs. 4 and 5) in combination with the large width of its band gap make GaN a uniquely promising material for use in high-temperature, high-frequency electronics. Gallium nitride (GaN) and compounds based on it have already been used to build field transistors with generation frequencies exceeding 70 GHz (Ref. 6).

It is well known that the low-frequency noise level is one of the most important parameters of any microwave generator or photodetector, and often determines the possibility of practical use of the device. In addition, the low-frequency noise level allows one to judge the degree of structural perfection of the material,[7,8] and measurements of the surface noise and contact noise can be used for nondestructive testing of the quality of individual manufacturing operations as well as the finished devices.[9,10] This is especially important for GaN since, despite the impressive technological progress of the last few years, the level of structural perfection as well as methods of surface processing and fabrication of contacts are in need of substantial improvement.[11,12] Nevertheless, data on the low-frequency noise level in GaN are, to the best of our knowledge, not available in the literature. In this study we have investigated the low-frequency noise in samples of gallium nitride with *n*-type conductivity and room-temperature electron concentration $n_0 = 7\times10^{17}$ cm^{-3}.

2. CONDITIONS OF THE EXPERIMENT

We examined samples of the hexagonal polytype of *n*-GaN, obtained by epitaxy on a sapphire substrate. A buffer layer of GaN of 250-Å thickness were grown on the substrate at 600 °C followed by a layer of GaN of 0.8-μm thickness at 1080 °C, followed by a layer of AlN of 200-Å thickness, also at 1080 °C. A 1.0-μm-thick layer of GaN with room-temperature electron concentration $n_0 = 7\times10^{17}$ cm^{-3} was grown on top of the AlN layer at 1080 °C. Ni–Au contacts were deposited on the surface of the film. The distance between the current contacts L was 2240 μm, and the distance between the potential contacts l was 140 μm. The two pairs of potential contacts and two pairs of current contacts made it possible to judge the degree of homogeneity of the electrical parameters of the sample.

The mean value of the Hall mobility at $T = 300$ K was $\mu_H \simeq 45$ cm^2/(V·s). As the temperature is lowered, μ_H grows and reaches the maximum value $\mu_H \simeq 60$ cm^2/(V·s)

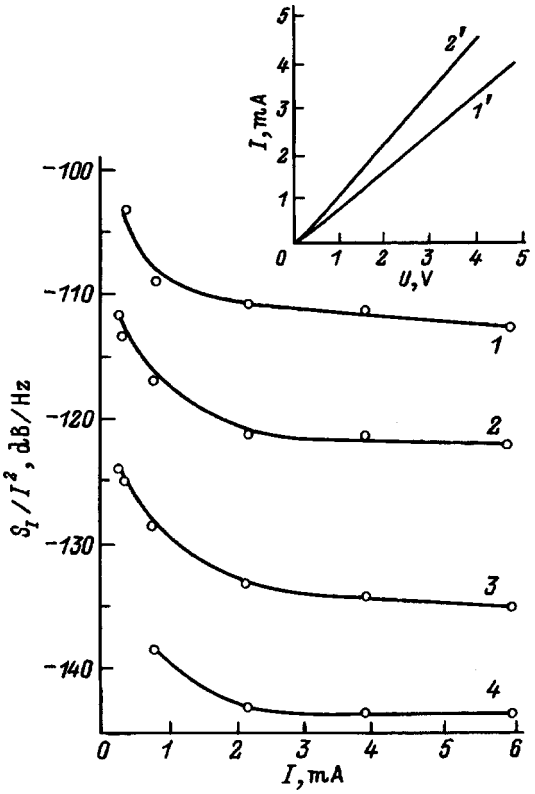

FIG. 1. Dependence of the relative spectral density of the noise S_I/I^2 on the current flowing through the sample I for different analysis frequencies f, Hz: *1*—20, *2*—160, *3*—2560, *4*—20 000. $T=300$ K. T, K: *1′*—300, *2′*—77.

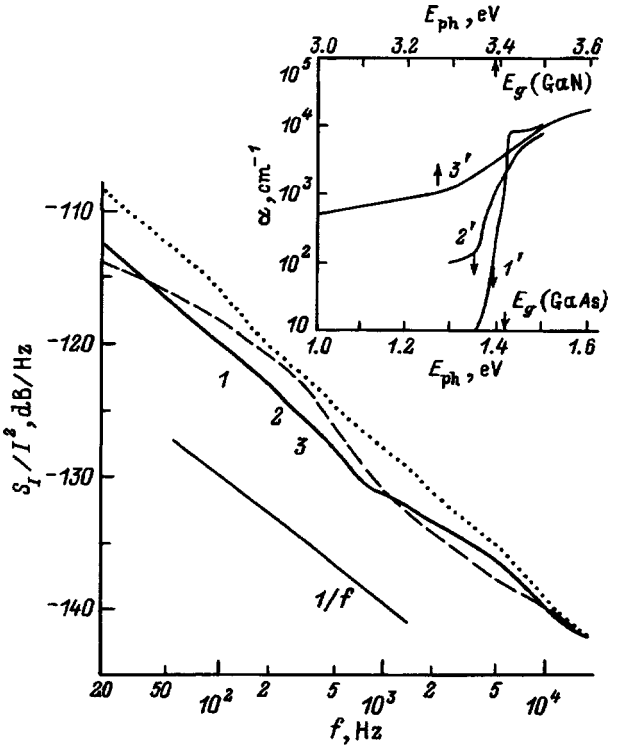

FIG. 2. Frequency dependence of the relative spectral density of the noise S_I/I^2 at temperatures T, K: *1*—77, *2*—293, *3*—387. The inset plots the dependence of the absorption coefficient α on the photon energy E_{ph} for pure GaAs with doping level $N_d \simeq 5\times10^{13}$ cm^{-3} (*1′*), doped GaAs with $N_d \simeq 6.7\times10^{18}$ cm^{-3} (*2′*), and pure GaN with $N_d \simeq 2\times10^{16}$ cm^{-3} (*3′*) at $T=300$ K; the arrows pointing at the horizontal axes show the width of the band gap E_g for GaAs and GaN at 300 K.

at $T \simeq 100$ K. The depth of the donor level, calculated from the Hall measurements, was $\Delta E_d \simeq 260$ meV.

The measured value of the mobility at 300 K and the weak temperature dependence of the mobility are evidence of a significant level of compensation of the material.[13] Measurements carried out on various pairs of Hall and potential contacts indicate substantial inhomogeneity of the electrical parameters.

3. RESULTS AND DISCUSSION

A. The role of contacts

The inset in Fig. 1 shows the current–voltage characteristics (CVC's) of the sample at 77 and 300 K. At voltages $V \lesssim 0.7$ V precise measurements indicate weak superlinearity of the CVC's. At voltages $V \gtrsim 1.5-2$ V the current–voltage characteristic is essentially linear. The level of non-ohmicity, defined as the ratio of the resistance of the sample R_c at $V < kT$ (~ 10 mV) to the resistance R_0 at $V \gtrsim 2$ V, is essentially constant over the entire investigated temperature range $77-400$ K and is equal to $R_{1c}/R_0 \simeq 1.15-1.20$. The value of the resistance, calculated on the basis of the geometrical dimensions of the sample, the values of the mobility, and the measured values of the concentration, coincides with the measured value of R_0. All this indicates high-quality contacts and a relatively low potential barrier in the near-contact region.[14]

It is well known, however, that even relatively weak non-ohmicity of the contacts can lead to an abrupt growth of the low-frequency noise[15] and a deviation from the ''classical'' dependence of the spectral density of the noise (S_I) on the current through the sample (I): $S_I \sim I^2$ (Ref. 16).

Figure 1 plots the dependence of the relative spectral density of the noise S_I/I^2 on the current through the sample I for measurements on the same contacts through which the current passes. It can be seen that at small currents ($I \lesssim 2$ mA), which corresponds to voltages on the sample $V \lesssim 2$ V, the quantity S_I/I^2 grows as the current is decreased. This is a direct indication of the defining contribution of the contact noise to the total noise. In contrast, for $I \gtrsim 2$ mA the quantity S_I/I^2 does not depend on I. It thus follows that the contribution of the contact noise can probably be ignored. Noise measurements on a four-point (potential) scheme, when the sample is fed from a current generator and the input resistance of the measurement scheme exceeds the resistance between the potential contacts by many orders of magnitude, revealed complete coincidence with the results of two-point measurements at high voltages ($V \gtrsim 2$ V).

The noted trends are characteristic of the entire temperature range $77 \leqslant T \leqslant 400$ K.

B. Low-frequency dark noise

Figure 2 plots the frequency dependence of the relative spectral density of the noise at $T=77$ K (curve *1*), at room temperature (curve *2*), and at $T=387$ K (curve *3*), measured on the potential contacts. It can be seen that at all tempera-

tures the slope of the dependence $S(f)$ is close to $S\sim 1/f$. The dependence of the noise level on the temperature is weak and nonmonotonic.

The noise properties of various materials are often characterized by the dimensionless Hooge parameter α (Ref. 17):

$$\alpha = \frac{S_I}{I^2} fN, \tag{1}$$

where f is the analysis frequency, and N is the total number of carriers.

For the same material, depending on the level of structural perfection of the material, the presence of internal stresses, the dislocation density, etc. the values of α can differ by many orders of magnitude. For silicon, for example, the measured values of α lie between 10^{-8} and 10^{-1} (see the bibliography in Ref. 8), for GaAs—between 10^{-8} and 10^{-1} (Ref. 18), and for SiC—between 10^{-6} and 1 (Refs. 19 and 20). The higher the level of structural perfection, the lower the value of α.

The volume of the GaN sample between the potential contacts V was $140\times 700\times 1$ μm$^3\simeq 10^{-7}$ cm^{-3}, which corresponds to total number of carriers in the measured volume $N=n_0V\simeq 7\times 10^{10}$. Thus, the measured room-temperature value of α is $\alpha\simeq 5-7$. This value is an order of magnitude greater than that found for SiC in Ref. 19. Nevertheless, such a large value of the Hooge constant, considering the present level of GaN technology, is not unexpected. Even for better samples of GaN the dislocation density lies in the range 10^8-10^9 cm^{-2}. For samples of gallium nitride a high level of internal stresses, significant inhomogeneities, etc. is characteristic.

One more parameter, sensitive to the level of structural perfection of the material, is the density of states $\rho(E)$ in the tails of the density of states in the band gap of the semiconductor near the edges of the conduction band and the valence band. Moreover, there exists a direct connection between the level of volume noise $1/f$ in semiconductors and $\rho(E)$ (Ref. 8). The density of states $\rho(E)$ can be inferred from the absorption coefficient of light, whose photon energy $E_{\rm ph}$ is somewhat less than the width of the semiconductor band gap E_g. The inset in Fig. 2 plots the absorption coefficient as a function of the photon energy, $\alpha(E_{\rm ph})$, for pure and doped GaAs (Ref. 21) and pure GaN (Ref. 22). It can be seen that even in pure GaN with residual impurity concentration $N_d\simeq 2\times 10^{16}$ cm^{-3} the density of states near the edge of the conduction band is substantially higher than in GaAs with doping level $N_d\simeq 7\times 10^{18}$ cm^{-3}.

C. Low-frequency noise under conditions of illumination

To determine the nature of the $1/f$ noise in Si and GaAs, Hooge and Tacano[18] successfully applied the technique of recharging the levels forming the tail of the density of states with minority carriers (holes). Holes were created in Si and GaAs with the help of band-to-band illumination (see Ref. 18, for example).

In the present work we have examined for the first time the effect of infrared and band-to-band illumination on low-frequency noise in GaN.

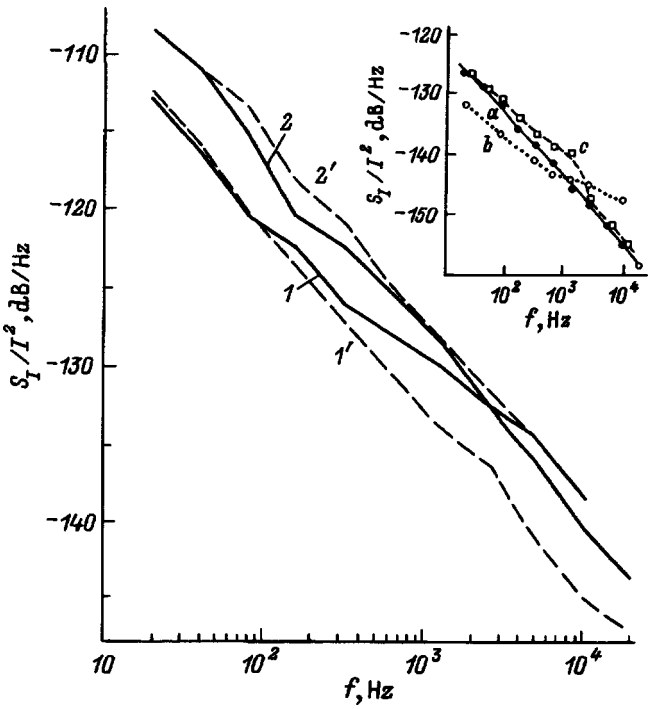

FIG. 3. Frequency dependence of the relative spectral density of the noise in darkness (solid curves) and the noise under conditions of band-to-band illumination (dashed curves) at $T=102$ (*1,1′*) and 370 K (*2,2′*). The inset plots analogous dependences for GaAs with doping level $N_d=10^{15}$ cm^{-3} at 300 K (Ref. 24); a—in darkness, b—at maximum illumination intensity $J=J_0$, c—for the illumination intensity $J=10^{-3}J_0$.

Illumination by a point-source incandescent lamp with 100 W power led to noticeable photoconductivity ($\Delta\sigma/\sigma\simeq 25\%$ at 300 K); however, it had no effect on the low-frequency noise in GaN in the temperature range from 77 to 400 K.

Band-to-band illumination was realized with the help of a GKL-100 halogen lamp with a quartz bulb, which allowed us to record transmission spectra all the way down to wavelengths ~ 0.31 μm ($E_{\rm ph}\simeq 4$ eV). SZS-25+UFS-5 filters were positioned between the lamp and the sample. The UFS-5 filter absorbs radiation almost completely in the wavelength interval $0.42-0.65$ μm; the SZS-25 filter absorbs quite efficiently in the wavelength region $\lambda\gtrsim 0.7$ μm. Under such conditions the main illumination component consists of photons with energy close to the width of the GaN band gap ($E_g\simeq 3.4$ eV, $\lambda\simeq 0.36$ μm).

Figure 3 plots the frequency dependence of the relative spectral density of the noise in darkness and under conditions of band-to-band illumination at $T=102$ and 370 K. The photoconductivity at $T=102$ K was $\Delta\sigma/\sigma\simeq 37\%$. In this case, according to Eq. (1) the noise level should be lowered at all analysis frequencies by approximately 1.4 dB simply because of the increase in the number of carriers N. In the construction of curve *1′* the values of S_I/I^2 were increased by 1.4 dB at all analysis frequencies, i.e., curve *1′* is reduced to the initial dark carrier concentration. At $T=370$ K $\Delta\sigma/\sigma\simeq 9\%$. At such a value of $\Delta\sigma/\sigma$ the error due to the increase in the number of carriers is less than the noise measurement accuracy (± 5 dB).

The main qualitative result of this study is that band-to-

band illumination noticeably changes the low-frequency noise level and that the nature of the effect of illumination depends strongly on temperature. On the basis of this result we may conclude that, as in Si and GaAs, the noise observed in GaN is generated by fluctuations of the population of some groups of closely lying levels or bands of the density of states in the band gap.

However, the available data do not make it possible to come to any conclusions about the nature of these bands or about their localization.

In the case in which fluctuations of levels forming the exponential tail of the density of states (exponentially falling into the band gap) are responsible for the $1/f$ noise, the theory[23] (see also Ref. 8) predicts a nonmonotonic dependence of the noise level on the illumination intensity. At each analysis frequency, as the intensity is increased, the noise at first grows, then reaches a maximum, and then with further increase of the intensity falls to a level below the dark level. Also, the lower the analysis frequency, the weaker the illumination intensities at which the noise reaches its maximum and begins to decrease. This prediction of the theory accords well with the experimental results for Si and GaAs.[8]

The inset in Fig. 3 shows the experimental results for GaAs obtained in Ref. 24. The effect of illumination on the noise at high temperatures in GaN (Fig. 3, curve *2′*) is qualitatively similar to the analogous effect of band-to-band illumination in GaAs (compare curve *c* of the inset). The fact that noise suppression upon illumination is not observed in GaN at $T=370$ K is probably explained simply by the fact that the flux intensity of photons with $E_{\mathrm{ph}} \geqslant E_g$ is too small.

At low temperatures (curves *1* and *1′*) the experimental results for GaN are qualitatively at variance with the theory.[23] It can be seen that at high frequencies band-to-band illumination suppresses noise while at high analysis frequencies light has no effect on the noise. Such a situation is incompatible with the prediction of the theory.[23]

CONCLUSIONS

This study of low-frequency noise in GaN testifies to the low level of structural perfection of the material. A study of low-frequency noise, including $1/f$ noise, in samples with different doping levels and mobility is extraordinarily urgent. The first experiments on the effect of band-to-band illumination on low-frequency noise in GaN with *n*-type conductivity are indicative of the substantial difference between such behavior in GaN and in silicon and GaAs.

We are grateful to V. Bugrov and I. A. Khrebtov for assistance with this work and to S. Rumyantsev for a discussion of the results.

This work was supported by the Russian Fund for Fundamental Research (Grant No. 06-02-18563).

E-mail: melev@nimis.ioffe.rssi.ru
[a]E-mail: sylvie.jarrixcem2.univ-montp2.fr
[†]E-mail: bbcrheal.unice.fr

[1] S. J. Pearton and C. Kuo, MRS Bull. (February, 1997), p. 17
[2] S. Nakamura, MRS Bull. (February, 1997), p. 29.
[3] M. S. Shur and M. A. Khan, MRS Bull. (February, 1997), p. 44.
[4] M. A. Littlejohn, J. R. Hauser, and T. H. Glisson, Appl. Phys. Lett. **26**, 625 (1975).
[5] B. Gelmont, K. S. Kim, and M. Shur, J. Appl. Phys. **74**, 1818 (1993).
[6] M. A. Khan, M. S. Shur, J. N. Kuznia, J. Burn, and W. Shaff, Appl. Phys. Lett. **66**, 283 (1995).
[7] L. K. J. Vandamme and S. Oosterhoff, J. Appl. Phys. **59**, 3169 (1986).
[8] N. V. D'yakonova, M. E. Levinshteĭn, and S. L. Rumyantsev, Fiz. Tekh. Poluprovodn. **25**, 2065 (1991) [Sov. Phys. Semicond. **25**, 1241 (1991)].
[9] L. K. J. Vandamme, IEEE Trans. Electron Devices **41**, 2176 (1994).
[10] D. Ursutiu and B. K. Jones, Semicond. Sci. Technol. **11**, 1133 (1996).
[11] F. A. Ponce, MRS Bull. (February, 1997), p. 51.
[12] D. B. Ingerly, J. A. Chang, N. R. Perkins, and T. F. Keuch, Appl. Phys. Lett. **70**, 108 (1996).
[13] D. K. Gaskill, L. B. Rowland, and K. Doverprike, in *Properties of Group-III Nitrides*, edited by J. H. Edgar [EMIS Data Reviews Ser. (INSPEC Publication, 1994) N 11].
[14] Yu. A. Gol'dberg, Fiz. Tekh. Poluprovodn. **28**, 1681 (1994) [Semiconductors **28**, 935 (1994)].
[15] R. D. Black, M. B. Weissman, and P. J. Restle, Appl. Phys. Lett. **53**, 6280 (1982).
[16] R. F. Voss and J. Clark, Phys. Rev. B **13**, 556 (1976).
[17] F. N. Hooge, T. G. M. Kleinpenning, and L. K. J. Vandamme, Rep. Prog. Phys. **44**, 479 (1981).
[18] F. N. Hooge and M. Tacano, Physica B **190**, 145 (1993).
[19] S. Tehrani, L. L. Hench, C. M. Van Vliet, and G. S. Bosman, J. Appl. Phys. **58**, 1571 (1985).
[20] J. V. Palmour, M. E. Levinshtein, S. L. Rumyantsev, and G. S. Simin, Appl. Phys. Lett. **68**, 2669 (1996).
[21] H. C. Casey, D. D. Sell, and K. W. Weight, J. Appl. Phys. **46**, 250 (1975).
[22] O. Ambacher, W. Rieger, and M. Stutzman, in *Abstract Book Topical Workshop on III-V Nitrides* (Nagoya, Japan, September 1995), p. F-5.
[23] G. V. D'yakonova and M. E. Levinshteĭn, Fiz. Tekh. Poluprovodn. **23**, 283 (1989) [Sov. Phys. Semicond. **23**, 175 (1989)].
[24] G. V. D'yakonova, Fiz. Tekh. Poluprovodn. **25**, 358 (1991) [Sov. Phys. Semicond. **25**, 219 (1991)].

Translated by Paul F. Schippnick

Equation of state of an electron gas and theory of the thermal voltage in a quantizing magnetic field

B. M. Askerov, M. M. Machmudov, and Kh. A. Gasanov

Baku State University, 370073 Baku, Azerbaijan
(Submitted September 23, 1997; accepted for publication October 2, 1997)
Fiz. Tekh. Poluprovodn. **32**, 290–291 (March 1998)

[S1063-7826(98)00603-6]

In a quantizing magnetic field the kinetic equation is inapplicable. Therefore, a consistent quantum theory of thermomagnetic phenomena, in particular, the thermal emf, does not exist. There are only various approaches. The first attempt to construct a quantum theory of the thermoelectric voltage was undertaken in Ref. 1, where the thermomagnetic current was calculated; however, the expression obtained there does not satisfy the Einstein relation. An account of the diamagnetism of the electron gas eliminated this shortcoming and made it possible to show that the thermoelectric voltage in a quantizing magnetic field can be expressed in terms of the entropy.[2] Such an approach is quite cumbersome and less intuitive.

In the present paper we calculate the thermoelectric voltage in a quantizing magnetic field on the basis of a more intuitive approach. Since this voltage in a strong magnetic field is a nondissipative effect, i.e., it does not depend on the mechanisms of current carrier scattering, it can be related to the equation of state and other thermodynamic functions. If we start with a valid definition of the thermoelectric field,[3]

$$E=-\nabla\left(\varphi-\frac{\xi}{e}\right)=\alpha\nabla T, \tag{1}$$

as the gradient of the electrochemical potential, where e is the electron charge, ξ is the chemical potential, and α is the thermoelectric voltage, we obtain

$$\alpha\nabla T=E_0+\frac{1}{e}\frac{\partial\xi}{\partial T}\nabla T. \tag{2}$$

Here $E_0=-\nabla\varphi$ is the electric field. In the presence of a steady-state temperature gradient in the sample the following condition should be satisfied:

$$-enE_0=\frac{\partial P}{\partial T}\nabla T, \tag{3}$$

where n is the free electron concentration, and P is the pressure of the electron gas. The right-hand side of condition (3) is a statistical force associated with the temperature gradient.

Substituting E_0 from Eq. (3) into Eq. (2), we obtain for the thermoelectric voltage coefficient

$$\alpha=-\frac{1}{en}\frac{\partial P}{\partial T}+\frac{1}{e}\frac{\partial\xi}{\partial T}. \tag{4}$$

It is thus clear that in the nondissipative region, if the equation of state of the electron gas $P=P(T,V,H,\xi)$ in a strong magnetic field is known, it is possible to calculate the thermoelectric voltage. Equation (4) was used to estimate the thermoelectric voltage in the absence of a magnetic field in Ref. 4. However, it should be noted that Eq. (4) is valid only in strong magnetic fields and is inapplicable in the absence of a magnetic field, when the thermoelectric voltage depends strongly on the scattering mechanisms.

To determine the explicit form of the equation of state, we use the grand thermodynamic potential of the electron gas in a quantizing magnetic field[5]

$$\Omega_e=-\frac{2k_0TV}{(2\pi R)^2}\sum_{N,\sigma}\int_{\varepsilon_0(N,\sigma)}^{\infty}\frac{dk_z(\varepsilon,N,\sigma)}{d\varepsilon}\times\ln\left[1+\exp\left(\frac{\xi-\varepsilon}{k_0T}\right)\right]d\varepsilon, \tag{5}$$

where the lower limit of the integral $\varepsilon_0(N,\sigma)$ is the root of the equation $k_z(\varepsilon_0,N,\sigma)=0$, $R=(\hbar c/eH)^{1/2}$ is the magnetic length, $N=0,1,2,\ldots$ is the Landau oscillator quantum number, and $\sigma=\pm1$ is the spin quantum number. We integrate Eq. (5) using integration by parts; we then obtain

$$\Omega_e=-\frac{2V}{(2\pi R)^2}\sum_{N,\sigma}\int_{\varepsilon_0(N,\sigma)}^{\infty}k_z(\varepsilon,N,\sigma)f_0(\varepsilon)d\varepsilon, \tag{6}$$

where $f_0(\varepsilon)=\{1+\exp[(\varepsilon-\xi)/(k_0/T)]\}^{-1}$ is the Fermi distribution function. Knowing Ω_e, we can calculate the pressure $P=-(\partial\Omega_e/\partial V)_{\xi,H,T}$, the concentration $n=-1/V(\partial\Omega_e/\partial\xi)_{T,V,H}$, and the entropy of the electron gas $S=-(\partial\Omega_e/\partial T)_{\xi,H,V}$ on the basis of Eq. (6):

$$P=\frac{2}{(2\pi R)^2}\sum_{N,\sigma}\int_{\varepsilon_0(N,\sigma)}^{\infty}k_z(\varepsilon,N,\sigma)f_0(\varepsilon)d\varepsilon, \tag{7}$$

$$n=\frac{2}{(2\pi R)^2}\sum_{N,\sigma}\int_{\varepsilon_0(N,\sigma)}^{\infty}\left(-\frac{\partial f_0}{\partial\varepsilon}\right)k_z(\varepsilon,N,\sigma)d\varepsilon, \tag{8}$$

$$S=\frac{2}{(2\pi R)^2}\sum_{N,\sigma}\int_{\varepsilon_0(N,\sigma)}^{\infty}k_z(\varepsilon,N,\sigma)\left(\frac{\varepsilon-\xi}{T}\right)\left(-\frac{\partial f_0}{\partial\varepsilon}\right)d\varepsilon. \tag{9}$$

In obtaining the expression for S from Eq. (6) we took into account that

$$\left(\frac{\partial f_0}{\partial T}\right)_{\xi}=\left(\frac{\varepsilon-\xi}{T}\right)\left(-\frac{\partial f_0}{\partial\varepsilon}\right). \tag{10}$$

Substituting P from Eq. (7) into Eq. (4) and noting that

$$\frac{\partial f_0}{\partial T}=\left(\frac{\varepsilon-\xi}{T}+\frac{\partial\xi}{\partial T}\right)\left(-\frac{\partial f_0}{\partial\varepsilon}\right), \tag{11}$$

 1063-7826/98/030261-02$15.00

we obtain for the thermoelectric voltage

$$\alpha = -\frac{1}{en}\frac{2}{(2\pi R)^2}\sum_{N,\sigma}\int_{\varepsilon_0(N,\sigma)}^{\infty} k_z(\varepsilon,N,\sigma) \times\left(\frac{\varepsilon-\xi}{T}\right)\left(-\frac{\partial f_0}{\partial\varepsilon}\right)d\varepsilon, \quad (12)$$

and it follows from a comparison of Eqs. (12) and (9) that $\alpha = -S/en$. This result coincides with that obtained in Ref. 2.

[1] A. I. Ansel'm and B. M. Askerov, Fiz. Tverd. Tela. **2**, 2310 (1960) [Sov. Phys. Solid State **2**, 2060 (1960)].
[2] Yu. N. Obraztsov, Fiz. Tverd. Tela **7**, 573 (1965) [Sov. Phys. Solid State **7**, 455 (1965)].
[3] L. D. Landau and E. M. Lifshitz, *Electrodynamics of Continuous Media* (Pergamon Press, Oxford, 1960).
[4] G. I. Epifanov, *Solid State Physics* (Mir, Moscow, 1979).
[5] B. M. Askerov, *Electron Transport Phenomena in Semiconductors* [in Russian] (Nauka, Moscow, 1985).

Translated by Paul F. Schippnick

Diffusion saturation of nondoped hydrated amorphous silicon by tin impurity

A. N. Kabaldin, V. B. Neĭmash, V. M. Tsmots', and V. S. Shtym

Institute of Physics, Ukrainian National Academy of Sciences, 252650 Kiev, Ukraine
(Submitted June 10, 1997; accepted for publication August 28, 1997)
Fiz. Tekh. Poluprovodn. **32**, 292–295 (March 1998)

The effect of radiation defects on the field and temperature dependences of the magnetic susceptibility of single-crystal Si was studied. A nonlinear magnetic-field-dependence of the magnetic susceptibility of irradiated Si was observed. This behavior can be explained by magnetic ordering of *A* centers. It was concluded that clusters of these centers with a local density of the order of 10^{21} cm^{-3} exist. An explanation of the ''diffusion paradox'' in the formation of oxygen-containing thermal donors was proposed on the basis of micrononuniformities of the spatial distribution of thermal donors and interstitial oxygen in Si. © *1998 American Institute of Physics.* [S1063-7826(98)01803-1]

1. INTRODUCTION

Interstitial oxygen O_i is the main residual technological impurity in commercial Si. A characteristic feature of interstitial oxygen is its nonuniform spatial distribution in crystals. Technological progress in recent years has made it possible to obtain Si crystals whose macroscopic nonuniformity with respect to the O_i distribution on a scale of $(10^{-1}-1)$ cm does not exceed 10%.[1] At the same time, as miniaturization of the components of solid-state electronics proceeds, it becomes important to monitor micrononuniformities of the O_i distribution several and tenths of a micron in size, an indirect manifestation of which are clusters of oxygen-containing thermal donors (TDs).[2,3] However, the question of the uniqueness of the correlation between TD microclusters and oxygen distribution micrononuniformities in the initial material remains open. This is because the nature and mechanism leading to TD formation are not completely understood. Specifically, the so-called TD ''diffusion paradox'' has not been explained: the inconsistency between the value of the O_i diffusion coefficient calculated from the kinetics of generation of TDs viewed as SiO_n complexes distributed uniformly over the crystal and the substantially lower value obtained from direct experiments.[4] If at least one model of accelerated low-temperature O_i diffusion in Si is confirmed,[5–7] then it will impossible to connect existence of clusters of TDs unequivocally with the existence of O_i distribution nonuniformities in the initial Si. For this reason, our objective in the present work is to endeavor to find microclusters of oxygen-containing defects whose formation does not require diffusion of O_i. Such defects could be secondary radiation defects with participation of oxygen atoms.

2. EXPERIMENTAL PROCEDURE

Samples of commercial KÉF-0.3, KÉF-1, and KÉF-45 Si (phosphorus-doped Si; the numbers indicate the resistivity in $\Omega\cdot$cm) with the initial parameters presented in Table I were used in the experiment. The table indicates the electron density n_{300} at $T=300$ K, the oxygen impurity density N_O, and the carbon impurity density N_C.

To introduce radiation defects (RDs) the samples were irradiated with 3.5 MeV electrons at temperature $T<80$ °C in the fluence range $\Phi_e=10^{16}-5\times10^{16}$ cm^{-2}. The accumulation of secondary radiation defects (SRDs) was monitored according to the temperature dependences of the Hall coefficient in the range 80–300 K. The field and temperature dependences of the magnetic susceptibility (MS) of the irradiated and control samples were determined by measuring the static MS, as described in Ref. 8. The relative measurement error did not exceed 3% and the sensitivity was equal to $3\times10^{15}\mu_B$. The total MS, which we shall denote below as χ, was measured.

3. EXPERIMENTAL RESULTS AND DISCUSSION

Figure 1a shows χ versus the magnetic field intensity H for the initial silicon samples (see Table I) at 300 and 80 K. One can see that at these temperatures χ does not depend on H, and for all materials studied as well as in order of magnitude it corresponds to the values characteristic for the MS χ_L of the Si crystal lattice.

Figure 1b shows $\chi(H)$ for the irradiated samples ($\Phi_e=5\times10^{16}$ cm^{-2}). One can see that irradiation has no effect on $\chi(H)$ at 300 K, but it does change $\chi(H)$ in the KÉF-0.3 and KÉF-1 samples at 80 K. In this case, in the first place, a nonlinearity appears in $\chi(H)$ and, in the second place, the diamagnetism of the samples in the region of saturation of $\chi(H)$ at $H=4$ kOe decreases. We denote by χ_p the paramagnetic component responsible for the decrease in the diamagnetism of the irradiated samples and by χ_{or} the component of the MS that is due to magnetic ordering and determines the behavior of $\chi(H)$. In this notation the experimentally measured values of $\chi(H)$ are the sum of three terms:

$$\chi(H)=\chi_L+\chi_p+\chi_{or}(H).$$

The susceptibility χ_p was determined for each experimental sample as the difference

$$\chi_p=\chi(4\ \text{kOe})-\chi_L,$$

and, correspondingly,

$$\chi_{or}=\chi(H)-\chi(4\ \text{kOe}).$$

The values of χ_p and

$$\chi_{or}(0.3)\equiv\chi(0.3)-\chi(4\ \text{kOe})$$

 1063-7826/98/030263-04$15.00

TABLE I.

Sample No.	Material	n_{300}, cm^{-3}	N_O, cm^{-3}	N_C, cm^{-3}
1	KÉF-0.3	1.5×10^{16}	9×10^{17}	$<5\times10^{16}$
2	KÉF-1	5×10^{15}	1×10^{18}	$<5\times10^{16}$
3	KÉF-45	7×10^{13}	8×10^{17}	$<5\times10^{16}$

for each sample are correlated with the initial density of free current carriers.

Figure 2 shows similar curves for the KÉF-0.3 samples irradiated with different fluences: $\Phi_e=5\times10^{16}$ cm^{-2} (*1, 2*) and $\Phi_e=3\times10^{16}$ cm^{-2} (*3, 4*). One can see that the values of χ_p and $\chi_{or}(0.3)$ are correlated with the irradiation flux, i.e., the density of radiation defects.

To determine the type of RDs which are responsible for the change in the MS after irradiation we conducted isochronous annealing of the experimental samples. It was found that when *E* centers are annealed in the temperature interval 120–150 °C the parameter $\chi_{or}(0.3)$ increases by approximately 30%, while the parameter χ_p remains unchanged. One can see from the curves of $n(1/T)$ that negative annealing of *A* centers with their density N_A almost doubling occurs. In the case of the annealing of *A* centers in the interval 330–370°C both χ_p and $\chi_{or}(0.3)$ decrease to zero.

The results obtained can be interpreted as follows. The appearance of a paramagnetic component χ_p can be explained by the paramagnetism of unpaired electrons occupying deep levels of *A* and *E* centers with energies $E_c-0.17$ eV and $E_c-0.44$ eV, respectively. The temperature dependence of the parameter χ_p in this case is explained by the Curie–Weiss law and the freeze-out of electrons onto a level of *A* centers as temperature decreases from 300 to 80 K. The dependence of χ_p on the resistivity of the initial materials (Fig. 1b) is apparently due to the electron occupancy of the levels of *A* and *E* centers at 80 K. For example, in sample No. 3 (see Table I) the free-carrier density, determined by the phosphorus impurity, is too low for recharging a number of RDs that is adequate for the sensitivity of our apparatus. For this reason, in sample No. 3 $\chi_p=0$, while in sample No. 2 $\chi_p=0.3\times10^{-8}$ cm^3g^{-1} and in sample No. 1 $\chi_p=1.1\times10^{-8}$ cm^3g^{-1}. The fact that the parameter χ_p does not change when *E* centers are annealed (accompanied by an increase in N_A) apparently signifies that spins are transferred from *E* to *A* centers, i.e. vacancies *V* which are liberated during annealing of *E* centers are mainly trapped by O_i atoms, resulting in the formation of *A* centers. As a result, the total paramagnetism remains unchanged.

As one can see from Figs. 1b and 2, the field dependences $\chi(H)$ have the form characteristic of ferromagnets and other materials with cooperative-type magnetic ordering.[9] The quantity $\chi_{or}(0.3)$ characterizes the degree of this ordering. For this reason, the correlation of this parameter with the annealing of *A* centers, with the accumulation of *A* centers under irradiation, and with the electronic occupancy of the energy levels of *A* centers (depending on the temperature and the resistivity of the material) is in our view sufficient proof of the fact that *A* centers are responsible for the indicated ordering.

Figure 3 shows the temperature dependences of the parameter $\chi_{or}(0.3)$ (curve *1*) and the electron occupancy of the levels of a *A* center (curve *2*) in an irradiated KÉF-0.3 sample. One can see that the MS becomes temperature-dependent at $T<160$ K, where many electrons are now frozen out on *A* centers with energy $E_c-0.17$ eV, i.e. the presence of electrons on *A* centers is a necessary but not sufficient condition for magnetic ordering of the centers. Evidently, there exists a critical temperature above which ordering of *A* centers does not appear.

We were not able to measure sufficiently accurately the temperature dependence of the parameter χ_p and to determine its conformance to the Curie–Weiss law because the sensitivity of our experimental apparatus was too low.

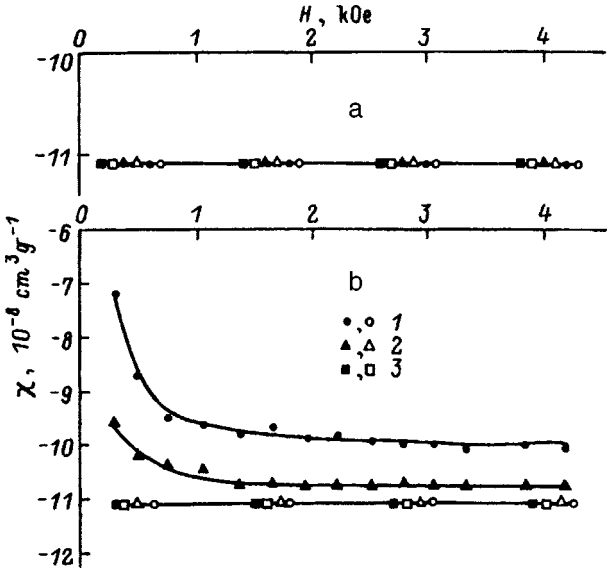

FIG. 1. Field dependences of the magnetic susceptibility χ for the following samples: a — initial, b — irradiated with $\Phi_e=5\times10^{16}$ cm^{-2}; Si brands: *1* — KÉF-0.3, *2* — KÉF-1, *3* — KÉF-45. The open symbols represent measurements at $T=80$ K and the filled symbols represent measurements at $T=300$ K.

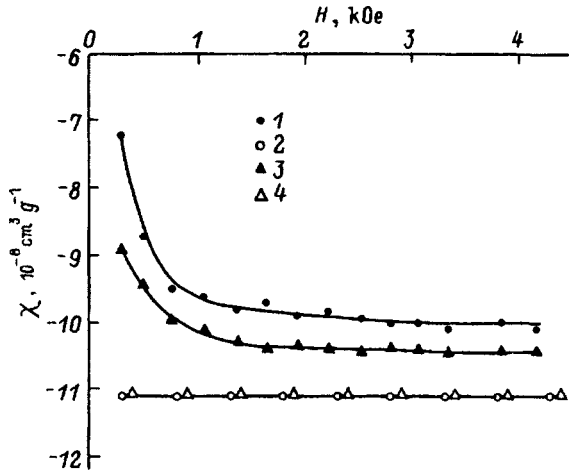

FIG. 2. Magnetic susceptibility χ versus magnetic field intensity *H* for KÉF-0.3 samples irradiated with fluences Φ_e, 10^{16} cm^{-2}: *1, 2* — 5; *3, 4* — 3. The open and filled symbols have the same meaning as in Fig. 1.

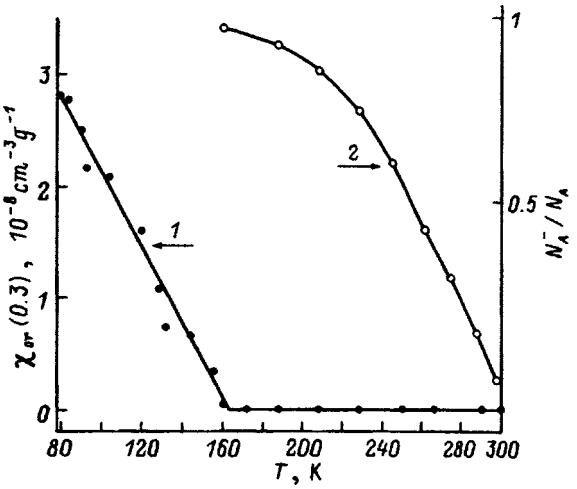

FIG. 3. Temperature dependences of the parameter $\chi_{or}(0.3)$ (curve *1*) and electron occupancy of the levels of *A* centers N_A^-/N_A (curve *2*) in KÉF-0.3 Si.

The main result of the experimental work presented here is the observation in irradiated Si of a nonlinearity in the field-dependence of the MS that correlated with the density and charge state of *A* centers. As we have already mentioned, the nonlinearity of $\chi(H)$ in weak fields is a characteristic indicator of cooperative-type magnetic ordering. According to Ref. 9, the cooperative magnetic state is a consequence of the exchange interaction. Exchange interactions in turn can be divided into two classes:

1. Direct (or contact) exchange between magnetic moments of ions separated by a small enough distance for their wave functions to overlap;

2. Indirect exchange coupling magnetic moments separated by relatively large distances, occurs through mediators, such as delocalized electrons or nonmagnetic ions in the lattice.

Our experimental results are best explained in terms of the hypothesis of magnetic ordering as a result of the direct exchange interaction. This is because the density of impurity atoms ($N_p \approx 10^{16}$ cm^{-3}), which in the Si lattice can be nonmagnetic ions, as well as the conduction electron density ($n_{300} \approx 10^{16}$ cm^{-3}), which are present even in the KÉF-0.3 sample, are inadequate for the indirect exchange interaction to occur.[10]

The following main types of magnetic ordering which are realized by means of the direct exchange interaction are distinguished:[9] a) ferromagnetism, b) antiferromagnetism, c) ferrimagnetism, d) metamagnetism, e) superparamagnetism, f) asperomagnetism, g) helimagnetism, and h) sperimagnetism.

Analysis of the above-indicated mechanisms of magnetic ordering as well as comparison of the field- and temperature-dependences of MS characteristic of them with the experimentally obtained dependences show that our experimental results are best explained by the mechanism of asperomagnetic ordering of *A* centers as a result of a direct exchange interaction. However, to establish an interaction of this type between separate paramagnetic centers their electronic wave functions must partially overlap. According to Ref. 11, the electronic level of an *A* center corresponds to an antibonding orbital of broken Si–Si bonds in the vacancy part of the complex *V*–O closed on one another. Therefore the localization radius of an electron in this level can be assumed to be equal in order of magnitude to the lattice constant. In this case overlapping of the electronic clouds of the *A* centers requires a density N_A of the order of 10^{21} cm^{-3}. Hall measurements show that the density N_A of charged *A* centers does not exceed 10^{16} cm^{-3}. This discrepancy is removed if it is assumed that a definite fraction of *A* centers is located in clusters, where their local density reaches the values required to establish an exchange interaction. These clusters apparently ''follow'' O_i distribution nonuniformities of type ''oxygen clouds'' in the initial Si (the term introduced in Refs. 12 and 13).

The results obtained could signify the existence of smaller but more ''dense'' (concentrated) oxygen clouds than the clouds which are detected indirectly by small-angle light scattering.[12] The results presented here make it possible in our view to answer affirmatively the question, posed at the beginning of the paper, concerning the existence of a spatial correlation between microclusters of thermal donors and nonuniformities of the O_i distribution in the initial Si. Correspondingly, an explanation of the TD ''diffusion paradox'' can be proposed on the basis of the data from Refs. 2 and 3 on the presence of TD microclusters in Si. This explanation reduces essentially to the following. For a sufficiently high local density of O_i atoms in the initial oxygen clouds the distance between the atoms may be sufficient for formation of thermal donor complexes of the type SiO_n even for low values of the O_i diffusion coefficient. The fraction of O_i atoms located in clouds, as estimated from the TD generation kinetics, does not exceed 1–2% of the total oxygen content,[14] so that clusters of these atoms are not seen in other experiments, including electrical. However, they are capable of determining the TD generation rate at the initial stages. In calculations of the O_i diffusion coefficient from the TD generation kinetics the existence of oxygen clouds is neglected, which could be the reason why the paradox arises.

This interpretation is valid if the mean-free path length L_V of a radiation vacancy is comparable to the average distance r between oxygen clouds. Indeed, the above-described behavior of MS is observed even for $N_A \approx 10^{16}$ cm^{-3}, when the formation of *V*–O complexes is determined by the behavior of the minority component. We employed uniform irradiation, so that for $L_V \ll r$ and $N_V \ll N_O$ (where N_V is the total vacancy density during irradiation) the spatial nonuniformity in localization of *A* centers does not depend on the nonuniformity of the oxygen localization. The nonuniformity in the distribution N_O affects the localization of *V*–O complexes (for irradiation fluences such that $N_V < N_O$) only when $L_V \geqslant r$. From this condition we can estimate the density N_{agg} of clusters of *A* centers, using the relation $N_{agg} \sim r^{-3}$. There is no unanimity of opinion in the literature on the value of the parameter L_V. Specifically, in Ref. 15 it is estimated that in crucible Si $L_V \simeq 10^{-4} - 10^{-3}$ cm, which gives $N_{agg} \simeq 10^9 - 10^{12}$ cm^{-3}.

In summary, the following results were obtained in this work.

1. A nonlinear field dependence of the magnetic susceptibility (MS) in irradiated Si was found, and it was interpreted by asperomagnetic-type magnetic ordering of *A* centers.

2. Analysis of the experimental data on the MS in irradiated Si leads to the conclusion that clusters of *A* centers with local density $N_A \simeq 10^{21}$ cm^{-3} exist.

3. An explanation based on micrononuniformities of the spatial localization of TDs and interstitial O_i oxyen atoms in Si was proposed for the diffusion paradox in the formation of thermal donors (TDs).

We thank A. N. Kraĭchinskiĭ for a helpful discussion of the results.

[1] V. A. Il'chishin and V. N. Stepchenkov, Élektron. Tekhn. Ser. Materialy, No. 2, 3 (1983).
[2] V. B. Neĭmash, T. R. Sagan, V. M. Tsmots', V. I. Shakhovtsov, V. S. Shtym *et al.*, Fiz. Tekh. Poluprovodn. **25**, 1864 (1991) [Sov. Phys. Semicond. **25**, 1121 (1991)].
[3] A. N. Kabaldin, V. B. Neĭmash, V. M. Tsmots', V. I. Shakhovtsov, A. V. Batunina *et al.*, Ukr. Fiz. Zh. **38**, 34 (1993).
[4] Y. Itoh and T. Nazaki, Jpn. J. Appl. Phys. **24**, 279 (1985).
[5] R. C. Newman, A. S. Oates, and F. M. Livingston, J. Phys. C.: So. St. Phys. **16**, 667 (1983).
[6] B. Pajot, H. Compain, J. Leroweille, and B. Clerjawd, Physica B & C **117/118**, 110 (1983).
[7] U. Gosele and T. Tan, in *Symposium*, Boston, MA (Nov. 4, 1982) 153 (1983).
[8] V. M. Tsmots', M. Yu. Voĭtusik, V. M. Mel'nik, and V. S. Shtym, Byull. Izobreteniĭ i Otkrytiĭ, No. 185, 138 (1988).
[9] C. M. Hurd, Contemp. Phys. **23**, 469 (1982).
[10] S. Methfessel and D. C. Mattis, in *Handbuch der Physik*, Vol. 18, Part 1, edited by P. J. Wijn, Springer-Verlag, Berlin, 1968, p. 389 [Russian translation, Mir, Moscow, 1972].
[11] L. I. Shpinar, I. I. Yaskovets, and M. I. Klinger, Fiz. Tekh. Poluprovodn. **24**, 1153 (1990) [Sov. Phys. Semicond. **24**, 729 (1990)].
[12] V. V. Voronkov, G. I. Voronkova, B. V. Zubov, V. P. Kalinushkin, E. A. Klimanov *et al.*, Fiz. Tekh. Poluprovodn. **13**, 846 (1979) [Sov. Phys. Semicond. **13**, 498 (1979)].
[13] V. V. Voronkov, G. I. Voronkova, V. P. Kalinushkin, T. Murina, T. Nazarov *et al.*, Fiz. Tekh. Poluprovodn. **17**, 2137 (1983) [Sov. Phys. Semicond. **17**, 1366 (1983)].
[14] D. I. Brinkevich, V. P. Markevich, L. I. Murin, and V. V. Petrov, Fiz. Tekh. Poluprovodn. **26**, 682 (1992) [Sov. Phys. Semicond. **26**, 383 (1992)].
[15] V. L. Vinetskiĭ and G. A. Kholodar', Fiz. Tekh. Poluprovodn. **18**, 362 (1984) [Sov. Phys. Semicond. **18**, 226 (1984)].

Translated by M. E. Alferieff

Role of light fluctuations in the appearance of the bistability of the photocarrier distribution

Yu. V. Gudyma and D. D. Nikirsa

Yu. Fed'kovich Chernovtsy State University, 274012 Chernovtsy, Ukraine
(Submitted May 5, 1997; accepted for publication July 29, 1997)
Fiz. Tekh. Poluprovodn. **32**, 296–298 (March 1998)

The effect of light fluctuations on the light-induced bistability of the photocarrier distribution is studied. The bistability can be explained by the threshold character of interband transitions and narrowing of the band gap of the semiconductor with increasing photocarrier density. The stationary probability density of the states and the mathematical expectation of the transition time between states are calculated. It is shown that external noise induces a strongly absorbing state of the semiconductor below the critical intensity of the incident radiation and suppresses stationary states above this value. © *1998 American Institute of Physics.* [S1063-7826(98)01903-6]

The intrinsic absorption of a semiconductor due to interband electron transitions exhibits a marked threshold character. On the other hand, as the photocarrier density increases, narrowing of the band gap of the semiconductor on account of the Coulomb interaction between the photocarriers is observed in a number of materials.[1] Such a combination of nonlinearity and internal positive feedback should produce a multivalued distribution of the nonequilibrium carriers in semiconductors and the associated cavityless optical bistability[2] (see also the review Ref. 3). After the discovery and first investigations of bistability with increasing light absorption in semiconductors, the latter came to be viewed as a natural optical material for practical bistable devices. It became clear that as a result of the cavityless character and high degree of focusing of beams without substantial losses due to beam divergence, only highly efficient waveguide systems can compete with such semiconductor crystals.[4] Investigations of the intrinsic and hybrid bistability led in a natural manner to the problem of the effect of external noise (fluctuations of the cooperative parameter) on the intensity of transmitted radiation. In a semiconductor with nonlinear threshold interband absorption, as will be seen below, the intensity of the incident laser beam plays the role of a controlling parameter, and the system must be studied relative to the fluctuations of the squared amplitude of this parameter. The problem has not been solved in this formulation, while in the light of what we have said above such an investigation is certainly of interest. The light intensity is assumed to be so high that the electron and hole densities, n and p, are much higher than the equilibrium values (and therefore $n \simeq p$).

In this formulation of the problem the transfer equation for radiation with intensity $I(z)$ and the transport equation for the free-photocarrier density $n(z,t)$ are

$$\frac{dI(z)}{dz} = -\alpha(\omega,n)I(z), \tag{1}$$

$$\frac{\partial n}{\partial t} = D\frac{\partial^2 n}{\partial z^2} + \alpha(\omega,n)I(z) - bn^2, \tag{2}$$

where $\alpha(\omega,n)$, b, and D are the light absorption coefficient and the interband carrier recombination and diffusion coefficients, respectively. We assume that the surface $(z=0)$ of the semiconductor plate of thickness l is illuminated uniformly by light with intensity I_0.

The frequency dependence of the absorption coefficient $\alpha(\omega,n)$ in the case of direct interband absorption is given by the function

$$\alpha(\omega,n) = \alpha_0\sqrt{\frac{\hbar\omega - E_g^*}{E_g}}. \tag{3}$$

The renormalized value of the band gap

$$E_g^* = E_g(1-cn), \tag{4}$$

signifies that a light beam with photon energy greater than the band gap is intense enough so that all lower states of the conduction band are filled more rapidly than they decay. We shall assume that the intraband absorption is constant,

$$\alpha(\omega,n) = \alpha_1, \tag{5}$$

and weak, $\alpha_1 \ll \alpha_0$.

Assuming that the diffusion length is greater than the plate thickness and introducing the thickness-averaged light intensity we obtain a nonlinear generation-recombination balance equation

$$\frac{dn}{dt} = I_0 l^{-1}\{1-\exp[-\alpha(\omega,n)l]\} - bn^2, \tag{6}$$

which has from one to three stationary solutions, depending on the intensity of the incident light.

Fixing the frequency of the incident light, we rewrite Eq. (6) in terms of the dimensionless variables $\eta = n/n_0$, $\theta = bn_0 t$, $\beta = I_0 b^{-1} n_0^{-2} L^{-1}$, $\lambda = \alpha_0 L$, and $\Omega = cn_0$ as

$$\frac{dn}{d\theta} = \beta\{1-\exp[-\lambda(\Omega(1+\eta))^{1/2}]\} - \eta^2, \tag{7}$$

where

$$n_0 = \frac{(\hbar\omega - E_g)}{cE_g}.$$

Let us examine the changes produced in the state of the system by intensity fluctuations of light incident on the face

of the plate ($z=0$). With respect to the photocarrier system this parameter is an external parameter and appears in Eq. (7) as a multiplicative factor. We shall describe the nondeterminate breakdown of light coherence by the process $\beta(t)=\beta+\sigma\xi(t)$, where the external noise $\xi(t)$ is characterized by very rapid, compared with the characteristic evolution time of the system $\tau=(bn_0)^{-1}$, fluctuations (the case of quasiwhite noise). We note that the result depends strongly on the character of the fluctuations. For this reason, the results obtained below are valid only for δ-correlated noise. Approximating the random disturbances by white noise type processes, the variables η should be interpreted as random variables which are described by a stochastic equation in the Stratonovich sense. In this case the Fokker–Planck equation for the probability distribution function $P(\eta,\theta|\eta'\theta')$ of the states has the form

$$\frac{\partial P(\eta,\theta|\eta',\theta')}{\partial\theta}=-\frac{\partial}{\partial\eta}[A(\eta,\theta)P(\eta,\theta|\eta',\theta')]+\frac{1}{2}\frac{\partial^2}{\partial\eta^2}[B(\eta,\theta)P(\eta,\theta|\eta',\theta')], \tag{8}$$

where

$$A(\eta,\theta)=\beta\{1-\exp[-\lambda(1+\eta)]^{1/2}]\}-\eta^2+\frac{\sigma^2}{4}\sqrt{\frac{\lambda^2\Omega}{1+\eta}}\times\exp[-\lambda(1+\eta)]^{1/2}\{1-\exp[-\lambda(1+\eta)^{1/2}]\},$$

$$B(\eta,\theta)=\frac{\sigma^2}{2}\{1-\exp[-\lambda(1+\eta)^{1/2}]\}^2 .$$

The theory of the correspondence between a stochastic differential equation and the Fokker–Planck equation is well developed and is presented in a number of books (see, for example, Ref. 5).

The stationary distribution in a steady-state process is determined by the function

$$\mathrm{PS}(\eta)=\mathrm{N}\{1-\exp[-\lambda(1+\eta)]1/2\}-1\times\exp\left(-\frac{2}{\sigma^2}\int_0^{\eta}\frac{\beta\{1-\exp[-\lambda(1+U)]^{1/2}\}-U^2}{\{1-\exp[-\lambda(1+U)]^{1/2}\}^2}\,dU\right). \tag{9}$$

The integration constant N is obtained from the normalization condition

$$\int_0^b P_S(\eta)\,d\eta=1, \tag{10}$$

where the upper limit is determined by the limitations imposed by the physical conditions of the problem (for example, the maximum possible density of photogenerated carriers). However, we shall confine our attention to the case of the nonnormalized probability density. The solution (9) is of the potential form, i.e., it can be put into the well-known form of the canonical distribution from equilibrium thermodynamics

$$P_S(\eta)=N\exp[-2V(\eta)/\sigma^2]. \tag{11}$$

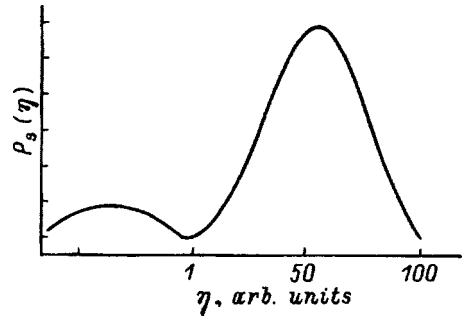

FIG. 1. Stationary probability distribution of the states. Since a nonnormalized probability density is plotted, numbers are not indicated along the ordinate.

Clearly, the maxima of the probability density correspond to stable stationary states, while the minima correspond to unstable stationary states (Fig. 1). Thus, the extrema of the stationary probability density can be identified with macroscopic stationary states of the system.[5] For calculations we chose $\lambda=0.2$ and $\Omega=0.1$. In Fig. 1 the left-hand maximum corresponds to weakly absorbing and the right-hand maximum to strongly absorbing states. For subcritical values of the controlling (bifurcation) parameter, in the absence of external multiplicative noise the system is characterized by one stationary state, but growth of fluctuations of the incident light leads to the appearance of bistability. This effect could be of interest from the practical standpoint, since it attests to external-noise-induced strongly absorbing state below the critical intensity of the incident radiation.

On the other hand, for supercritical values of the controlling parameter the action of the external noise is to shift the region of bistability in the direction of somewhat higher values of the intensity of the incident light (suppression of bistability by noise).

The phenomena described by Eq. (8) occur on two time scales: The fast scale is related with the inverse relaxation to a local minimum of the potential function $V(\eta)$ after the perturbation and the slow scale is related with a transition from a metastable to a global minimum. This is indicated by the presence of two terms on the right-hand side of Eq. (8) — drift and diffusion.

The Fokker–Planck equation method makes it possible to calculate the mathematical expectation of the transition time $T(\eta)$ (average first emission time) of the system from a

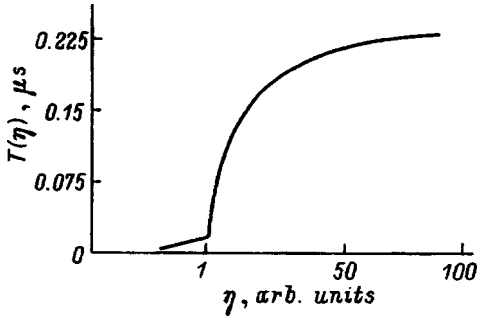

FIG. 2. Mathematical expectation of the transition time of the system from a weakly in to a strongly absorbing state.

weakly into strongly absorbing state, fixing the slow time scale. It is described by an ordinary differential equation[5]

$$\frac{1}{2}\{1-\exp[-\lambda(1+\eta)]^{1/2}\}^2\frac{d^2T}{dx^2}$$

$$+[\beta\{1-\exp[-\lambda(1+\eta)]^{1/2}\}-\eta^2]\frac{dT}{dx}=-1. \quad (12)$$

A plot of the solution (11) (Fig. 2) shows that most of the time the system endeavors to self-overcome the barrier. As the intensity of the fluctuations decreases ($\sigma\to 0$), the memory time of the system increases.

The phenomena occurring as a result of narrowing (renormalization) of the band gap occur in a number of semiconductor crystals, but because of their relatively simple energy structure direct-gap semiconductors of the type CdS, CdSe, or ZnSe are best suited for experimental observation of the stochastically induced effects described above.

[1] M. Wegener, C. Klingshirn, S. W. Koch, and L. Banyai, Semicond. Sci. Technol. **1**, 366 (1986).
[2] V. A. Kochelal, L. Yu. Mel'nikov, and V. N. Sokolov, Fiz. Tekh. Poluprovodn. **16**, 1167 (1982) [Sov. Phys. Semicond. **16**, 746 (1982)].
[3] F. Henneberger, Phys. Status Solidi B **137**, 371 (1986).
[4] H. M. Gibbs, *Optical Bistability: Controlling Light with Light*, Academic Press, Orlando, 1985 [Russian translation, Mir, Moscow, 1988].
[5] N. G. Van Kampen, *Stochastic Processes in Physics and Chemistry*, North-Holland, Amsterdam, 1984 [Russian translation, Vyssh. Shkola, Moscow, 1990].

Translated by M. E. Alferieff

Laser-modulated epitaxy of lead telluride

S. V. Plyatsko

Institute of Semiconductor Physics, Ukrainian National Academy of Sciences, 252028 Kiev, Ukraine

(Submitted February 7, 1997; accepted for publication July 14, 1997)
Fiz. Tekh. Poluprovodn. **32**, 299–302 (March 1998)

The dependences of the density and mobility of free current carriers in PbTe/KCl(KBr) layers, grown by epitaxy modulated by infrared laser radiation, on the power density W of the laser radiation at the target and the substrate temperature T_s were investigated. It is shown that the free-carrier density in the regions of both electronic and hole conductivity ($10^{16}<N$, $P<10^{19}\text{cm}^{-3}$) with mobility at 77 K corresponding to the most perfect crystals can be controlled over wide limits by varying W and T_s. © *1998 American Institute of Physics.* [S1063-7826(98)02003-1]

The possibility of using laser radiation for evaporation of different materials, including PbTe, followed by condensation in the form of thin films was demonstrated back in the mid-1960s.[1–3] In the 1970s[4–8] these investigations became purposeful and integrated from the standpoint of studying both the interaction of laser radiation with a solid and the mechanisms of growth of thin films from vapor-plasma flows. This led to the development of two independent directions in the technology — laser-stimulated transformation of the properties of a solid as well as laser epitaxy (this term is now firmly established, but it essentially does not reflect the physical essence of the method).

Laser-modulated epitaxy (LME) is more versatile than the conventional thermal methods of epitaxial growth of IV–VI semiconductor compounds. In the LME method it is possible to change an entire series of parameters (power density of the laser radiation, pulse duration and repetition frequency, substrate temperature, substrate–target distance) and to obtain within the parameter limits perfect layers with prescribed electrophysical properties.

In thermal growth methods, there exist strictly determined temperature regimes outside of which the layers are not single-crystalline, while the carrier density can be controlled only by additional sources of components, mainly the chalcogen.

The laser radiation employed for sputtering semiconductor sources can be divided according to spectral region of application into two ranges: a) laser photon energy ($\hbar\omega$) greater than the band gap E_g and b) laser photon energy less than the band gap ($\hbar\omega<E_g$). Most works concerning this problem were performed for $\hbar\omega>E_g$. The most important results on laser epitaxy of semiconductor compounds were obtained for epitaxy of CdMnTe,[13] CdHgTe,[9,10] PbCdSe, and PbSe.[11,12] True, in the case of epitaxy of the narrow-gap compounds CdHgTe, together with laser epitaxy, molecular-beam epitaxy (MBE) was was used.

The laser epitaxy results for other semiconductors are more modest. In areas of thin-film technology where MBE and MOS hydride method encounter difficulties, as a rule this stimulates the development of new unconventional methods for obtaining epitaxial layers. This is true in full measure for superconducting materials, where, especially recently, wide application of laser radiation for sputtering the source material has started.[14]

The present paper reports on investigations of the dependence of the electrophysical parameters of PbTe films on the power density of laser radiation at the target ($\hbar\omega<E_g^{\text{PbTe}}$) and on the substrate temperature. The source–target was sputtered with modulated infrared (IR) laser radiation ($\hbar\omega=0.118$ eV), which was introduced through a focusing optical system into the vacuum chamber with a residual vapor pressure $P=10^{-6}$ torr.

The structural perfection of the films was investigated by transmission electron microscopy and x-ray diffraction reflection methods. The half-width of the diffraction reflection peak depended on the layer thickness h. For the thinnest layers ($h\simeq 30$ Å) $\Delta\theta=40$ s, while for the thickest layers ($h=7$ μm) $\Delta\theta$ did not exceed 2 min.

Figure 1 shows the dependence of the current-carrier density and mobility ($T=77$ K) on the power density W of the laser radiation at a single-crystal PbTe target. During epitaxy the temperature of the KCl and KBr substrates with (100) orientation was equal to $T_s=150$ °C. For low power densities ($10^4<W<3\times10^4$ W/cm^2) the films are p-type. In this range of values of W the hole density P decreases by three orders of magnitude in films on KBr substrates and by two orders of magnitude in films on KCl substrates. This could be to the fact that the free surface energy σ of the (001) plane in KBr is lower than for the corresponding plane in KCl ($\sigma^{\text{KBr}}<\sigma^{\text{KCl}}$ (Ref. 19)). For power density $W=(3-3.5)\times10^4$ W/cm^2 an inversion of conduction type occurs, after which the electron density N increases with W. One can see from Fig. 1 that the dependences $P(W)$ and $N(W)$ have a pronounced plateau at the minimum, within which layers with low current-carrier density with both hole and electron conductivity can be obtained reproducibly. The carrier mobility at $T=77$ K corresponds in a quite wide region of W to the most perfect single crystals and films ($\mu_{77}>10^4$ cm^2/V·s). The highest mobility obtained for n-PbTe/KCl(KBr) corresponded to $\mu_{77}=4.5\times10^4$ cm^2/V·s and was observed in films grown on structurally perfect substrates with surface microrelief $\delta<1000$ Å.

The decrease in hole density with increasing power density ($T=$ const) attests to a decrease in the density of accep-

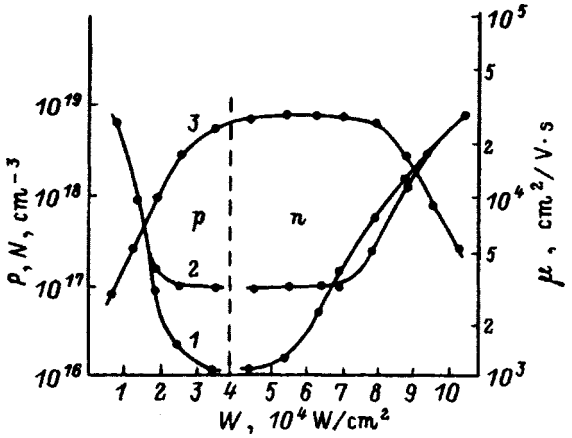

FIG. 1. Current-carrier density (*1*, *2*) and mobility μ (*3*) at $T=77$ K versus the laser power density on the target–source for different samples: *1* — PbTe/KBr and *2* — PbTe/KCl.

tor centers. They cannot be thermal Pb vacancies directly, since their density should be much lower at such epitaxy temperatures.[15] Moreover, it is difficult to imagine that the number of thermal vacancies decreased as W increased. On the other hand, acceptors of a different nature have not been shown to exist in nondoped crystals. Therefore the behavior of $P(W)$ (Fig. 1) can be explained by taking into account the characteristics of the growth technology which stem from the laser sputtering of the source material.

On account of the strong intramolecular bonds and the ''inert electron pair'' effect, IV–VI compounds vaporize mainly in the form of molecules. But the minority components from decomposition of the vapors M, X, X_2, MX_2, and M_2X_2 are also nevertheless observed in small quantities. Investigation of the mass spectra of the modulated beam formed by Knudsen evaporation of PbTe showed that the components in the beam are distributed as follows:[20]

$$\mathrm{PbTe} : \mathrm{Pb} : \mathrm{Te_2} : \mathrm{PbTe_2} : \mathrm{Pb_2Te_2}$$
$$= 100 : 13 : 1.0 : 0.14 \ (<0.03).$$

The dissociation energies of PbTe and Te_2 molecules are quite high ($E^{\mathrm{PbTe}}=246$ kJ/mole (Ref. 20) and $E^{\mathrm{Te_2}}=219$ kJ/mole (Ref. 21)). For this reason, the main source of chalcogen during sputtering or thermal annealing is apparently the chalcogen that is present in the crystal in the form X_2 and does not form with lead strong intramolecular bonds. As shown in Refs. 23 and 24, there are more than enough such formations in narrow-gap IV–VI compounds.

Dureing laser sputtering of a material evaporation occurs only from the zone of action of the radiation without formation of a liquid phase and in consequence without the spraying effect. Under these conditions the composition of the vapor flux will remain unchanged during deposition (during depostion the source undergoes a rotational-translational motion) and is displaced in the direction of enrichment by the chalcogen not only near the source but also on the substrate. This happens because of the high temperature of the material in the zone of action of the laser radiation ($T^{\mathrm{PbTe}}\simeq 2500$ K), at which the vapor pressure of the main material as well as of the metal and chalcogen exceeds 10^3 Torr. The chalcogen content in the film, however, will not be determined only by the source temperature, but it will be equally determined by the substrate temperature or, more accurately, the ratio of the chalcogen reaching the substrate and re-evaporating from it. This mechanism provides the basis for controlling the electrophysical properties of epitaxial structures of lead chalcogenides.[22]

However, when laser radiation is used to sputter semiconductor sources it is necessary to take into account the fact that the growth process occurs under conditions far from equilibrium, and this can result in the formation of new defects of a different nature, including interstitial. Their density and arrangement will be determined by many external factors, primarily the power density of the laser radiation and the epitaxy temperature. Unfortunately, these contributions are difficult to distinguish, especially at low epitaxy temperatures, since besides the stationary substrate temperature T_s there exists a correction ΔT_{pul}, which at high power densities W can be comparable to T_s. The correction ΔT_{pul} arises because energy is exchanged between the substrate and the products of the sputtering, and it will depend on both W and the duration τ_{pul} of the laser pulse.

In our case $\tau_{\mathrm{pul}}=$ const. Therefore, since the values of W employed are much lower than the values at which ''dry etching'' and implantation occur, an increase of power density W will give rise only to an increase of the substrate temperature in a pulse. This will decrease the attachment coefficient of tellurium ($k_{\mathrm{Te}}<k_{\mathrm{Pb}}$, k_{PbTe}). This will show up in the dependences $P,N(W)$ as a decrease in the hole density, subsequent inversion of conduction type, and an increase of electron density. This behavior of $P,N(W)$ shows that donor and acceptor mechanisms of defect formation in the films compete with one another when IR laser radiation is used for sputtering the source material with $T_s=150$ °C. Investigations of the temperature dependence of the Hall constant in the region of electronic conductivity show that interstitial Pb can play the role of the donors.

On the other hand, on the basis of what we have said above, increasing the epitaxy temperature (W, $\Delta T=$ const) likewise should result in a change in the current-carrier density in the film, but now because the attachment coefficients of Pb and Te and formation enthalpies of thermal vacancies of the intrinsic components are different.

Figure 2 shows the current-carrier density and mobility as a function of the temperature of the KCl substrate with constant laser power density at the target $W=8.5\times10^4$ W/cm^2 and pulse duration $\tau_{\mathrm{pul}}=3\times10^{-3}$ s.

These deposition conditions corresponded to an effective growth rate $V_{eff}=160$ Å/s. Just as in the first case, stoichiometric Czochralski p-PbTe single crystals with hole density $P_{77}=2.5\times10^{16}$ cm^{-3} and mobility $\mu_{77}=1.2\times10^4$ cm^2/V·s at $T=77$ K were used as the target–source. During deposition the target executed a rotational-translational motion.

The electron density in the film $N=1.1\times10^{18}$ cm^{-3} remains practically unchanged up to the deposition temperature $T_s=180$ °C (Fig. 2). A further increase of the substrate temperature ($180<T_s<280$ °C) results in a quite sharp decrease of the electron density followed by inversion of the conduction type ($280<T_s<330$ °C), after which the conduc-

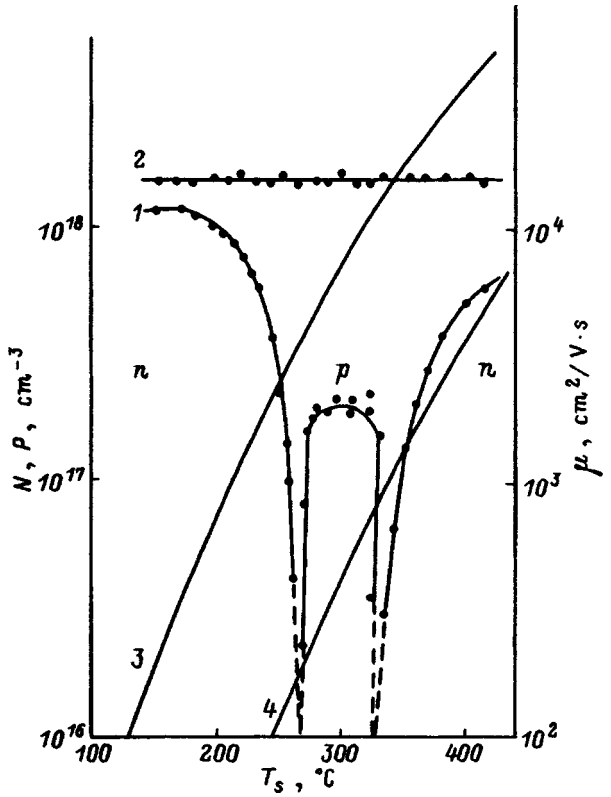

FIG. 2. Current-carrier density (*1*) and mobility (*2*) at $T=77$ K versus KCl substrate temperature T_s with a constant laser power density $W=8.5\times10^4$ W/cm^2 on the target. *3, 4* — Hole and electron densities due to Pb and Te vacancies versus the temperature T_s.[15]

tion type reverts back at the epitaxy temperature $T_s\simeq330$ °C. The carrier mobility in this range of growth temperatures is virtually temperature-independent (Fig. 2, curve *2*).

It is known that the attachment coefficient of Pb atoms decreases with increasing temperature, approaching zero at $T_s\simeq310$ °C.[16] Figure 2 shows that indeed near $T_s\simeq300$ °C the electron density decreases rapidly, reaching the region of inversion of conduction type. In this temperature range $280<T_s<330$ °C the PbTe films exhibit stable hole-type conduction ($P_{77}=10^{16}-10^{17}$ cm^{-3}). The existence of repeated inversion with increasing epitaxy temperature T_s indicates that the hole density in this temperature range will be determined by the resulting density of acceptors, which decreases with temperature, and by the generation of new donor centers. The density of these centers is close to the density of thermal Te vacancies, but still does not correspond to it and has a tendency to saturate, while the density of vacancies grows exponentially with temperature (Fig. 2, curve *4*). Furthermore, the experimentally obtained dependence $P,N(T_s)$ with $W,\Delta T=$ const shows that the region of hole-type conduction is not related with Pb vacancies, whose density, just as that of Te vacancies, should grow with temperature and predominate in the entire range of epitaxy temperature T_s (Fig. 2, curve *3*).

Since the composition of the vapor phase remains constant during the deposition process ($W=$ const), the results obtained suggest that in LME-grown PbTe films the mechanism leading to the formation of electrically active defects is complicated and depends on the technological conditions under which the films are obtained. The role of acceptors in this case can apparently be attributed to the tellurium enrichment of the vapor flow produced by the laser radiation. Thermal Te vacancies and interstitial Pb most likely appear as donors. This latter conjecture is also confirmed by an investigation of the ESR of *n*PbTe:Mn films grown with $W=(7-10)\times10^4$ W/cm^2 and $T_s=150$ °C, in which only the hyperfine structure of the Mn^{+2} ions corresponding to Mn ions in interstices was observed.

As far as the production of doped PbTe layers with impurities distributed uniformly over the sites of the metal sublattice is concerned, it was shown earlier that PbTe can be grown from sources doped with Mn and Eu, whose vapor pressure is much lower than that of the main material.[18] But in the case of substitution for the metal component Mn and Eu are pseudodonor impurities and therefore do not affect the electrical properties of the films.[18] It is also known that group-I and -III impurities manifest their electroactive properties at densities above $(1-3)\times10^{19}$ cm^{-3}, since they have a tendency to cluster,[17] on account of which the density of the impurity introduced is almost always much higher than the current-carrier density. In the case of congruent evaporation this difference should be eliminated and the current-carrier density should correspond to the density of the impurity introduced. The results concerning the use of In, Tl, Na, and Cr doped single crystals as sources are presented in Table I.

TABLE I.

Impurity and type of conduction in the source	Impurity density in target–source, 10^{18}, cm^{-3}	Laser power density, 10^4 W/cm^2	Type of conduction and carrier density in the film, 10^{18} cm^{-3}	Substrate material
Tl, *p*	4.8	4.5	*p*, 3.42	KBr
Tl, *p*	4.8	5.1	*p*, 1.42	KCl
Tl, *p*	9.6	8.8	*p*, 11.7	KCl
Tl, *p*	9.6	8.8	*p*, 13.6	KBr
Tl, *p*	4.8	9.1	*n*, 1.55	KBr
Na, *p*	15.0	9.1	*p*, 11.8	KBr
Na, *p*	15.0	4.3	*p*, 15.2	KCl
In, *p*	8.6	9.2	*n*, 13.4	KCl
In, *p*	8.6	2.1	*n*, 7.15	KBr
Cr, *n*	6.0	1.2	*n*, 4.45	KCl

In summary, the application of modulated IR laser radiation for sputtering of a PbTe source-target followed by condensation of the vapor flux on dielectric substrates has shown that it is possible to obtain structurally perfect PbTe layers in a wide range of substrate temperatures T_s and laser power densities on the target. The electrophysical properties of *p*- and *n*-type PbTe are determined by the intrinsic point defects, whose density depends on the technological conditions of growth. The films obtained from doped sources are characterized by the type of conduction and the current-carrier density, determined by the nature of the impurity and its density in the source, respectively.

[1] H. M. Smith and A. F. Turner, Appl. Opt. **4**, 147 (1965).
[2] P. D. Zavitsanos and W. E. Saver, J. Electrochem. Soc. **115**, 109 (1968).
[3] H. Schwartz and H. A. Tourtellotte, J. Vac. Sci. Technol. **6**, 373 (1969).
[4] V. S. Ban and D. A. Krumer, J. Mater. Sci. **5**, 978 (1970).
[5] Z. P. Beketova, S. V. Gaponov, B. S. Kaverin, B. A. Nesterova, and N. N. Salashchenko, Izv. Vyssh. Uchebn. Zaved. Radiofiz. No. 6, 908 (1975).
[6] O. K. Filatov, N. N. Salashchenko, and M. M. Kochchev, Fiz. Tverd. Tela (Leningrad) **17**, 2105 (1975) [Sov. Phys. Solid State **17**, 1378 (1975)].
[7] S. V. Gaponov, B. M. Luskin, and N. N. Salashchenko, Pis'ma Zh. Tekh. Fiz. **9**, 516 (1979).
[8] J. K. Klimer, J. Appl. Phys. **44**, 490 (1973).
[9] J. T. Cheung and J.-S. Chen, Appl. Phys. Lett. **55**, 2191 (1988).
[10] J. T. Cheung and H. Sankur, CRC Crit. Rev. Sol. St. Mater. Sci. **15**, 63 (1988).
[11] M. Baleva and E. Meteeva, J. Phys.: Condens. Matter **5**, 7959 (1993).
[12] M. Baleva and E. Meteeva, J. Phys.: Condens. Matter **5**, 7971 (1993).
[13] J. M. Wrobel and J. J. Dubovski, Appl. Phys. Lett. **55**, 469 (1989).
[14] H. Tabata, T. Kawai, and S. Kawai, Appl. Phys. Lett. **58**, 1443 (1991).
[15] F. F. Sizov and S. V. Plyatsko, J. Cryst. Growth **92**, 571 (1988).
[16] A. G. Mikolaĭchuk, D. M. Freĭk, and V. M. Shperun, *Physical and Technological Principles of the Synthesis of Semiconductor Films* [in Russian], Naukova Dumka, L'vov, 1978.
[17] Yu. S. Gromovoj, S. V. Plyatsko, and F. F. Sizov, Mater. Lett. **8**, 495 (1989).
[18] S. V. Plyatsko, Yu. S. Gromovoĭ, and G. E. Kostyunin, Fiz. Tekh. Poluprovodn. **25**, 427 (1991) [Sov. Phys. Semicond. **25**, 259 (1991)].
[19] I. K. Kikoin [Ed.], *Reference Data on Physical Quantities* [in Russian], Atomizdat, Moscow, 1970.
[20] *Molecular-Beam Epitaxy and Heterostructures* [Russian translation], Mir, Moscow, 1989.
[21] E. Rutner, P. Goldfinger, and J. P. Hirth, *Condensation and Solids*, Gordon and Breach Sci. Pub., N. Y., 1964.
[22] B. É. Gol'tsman, Z. M. Dashevskiĭ, V. I. Kaĭdanov, and N. V. Kolomoets, *Film Termoelements* [in Russian], Nauka, Moscow, 1985.
[23] R. Breschi, A. Camanzi, and V. Fano, J. Cryst. Growth **58**, 399 (1982).
[24] V. Fano, Prog. Cryst. Growth Charact. **3**, 287 (1981).

Translated by M. E. Alferieff

Optical properties of crystals of the solid solutions $(InSb)_{1-x}(CdTe)_x$

V. A. Brodovoĭ, N. G. Vyalyĭ, and L. M. Knorozok

Taras Shevchenko Kiev State University, 252022 Kiev, Ukraine
(Submitted February 3, 1997; accepted for publication July 14, 1997)
Fiz. Tekh. Poluprovodn. **32**, 303–306 (March 1998)

The reflection and absorption spectra of crystals of the solid solutions $(InSb)_{1-x}(CdTe)_x$ in the wavelength interval 2.5–25 μm were measured within the limits of solubility of CdTe in InSb ($x \leqslant 0.05$) at room temperature. Analysis of the experimental results confirmed the applicability of the Kane theory for all compositions investigated. The variation of the optical band gap $\mathcal{E}_g^{\text{opt}}$ and the effective mass m_c at the Fermi level as a function of composition was determined. It is shown that the minimum values $m_c = 0.8\times 10^{-2} m_0$ and $\mathcal{E}_g^{\text{opt}} = 0.07$ eV are reached for $x = 0.02-0.03$. Information about the predominant mechanism of scattering for each alloy is obtained from the absorption curves in the region of absorption by free charge carriers. X-Ray crystallographic investigations were performed and the change $\Delta a(x)$ in the lattice constant of the solid solutions relative to pure InSb was determined. It is shown that the behavior of $m_c(x)$ and $\mathcal{E}_g^{\text{opt}}$ is uniquely determined by $\Delta a(x)$. In turn, $\Delta a(x)$ is determined by the complicated character of the interaction of the dopants with one another and with the InSb lattice. © *1998 American Institute of Physics.* [S1063-7826(98)02103-6]

It is well known that any deviations from an ideal crystal structure in narrow-gap semiconductors can have an appreciable effect on the formation of the energy spectrum of charge carriers if the fluctuations of the potential energy of the electrons and holes are comparable to the band gap, since the band gap is small. An example of such disordered systems, where configurational disorder is realized in one or several crystal sublattices, are solid solutions (SSs) of semiconductors.

In the present work, the reflection and absorption spectra of $(InSb)_{1-x}(CdTe)_x$ crystals, forming a continuous series of SSs for $x \leqslant 0.05$,[1–3] were investigated for the purpose of obtaining information about the effect of composition on the band structure parameter of the alloys.

Single crystals of the SSs obtained by directed crystallization of InSb melt containing Cd and Te impurities in an equiatomic ratio were investigated. The total impurity density varied from 3.75×10^{19} cm^{-3} ($x = 0.0025$) to 7.5×10^{20} cm^{-3} ($x = 0.05$). Synthesis was conducted in quartz ampuls evacuated to 10^{-3} Pa. The melt was homogenized at 1100 °C for at least 100 h. The composition and homogeneity of the alloys were monitored by x-ray crystallographic and microchemical analyses. After mechanical polishing, the samples were worked with a SR-4A polishing etchant. The dimensions of the wafers were $0.8\times 0.4\times 0.3$ cm^{-3}. To measure absorption the wafer thickness d was decreased to 70 μm. All crystals were n-type. The free-electron density n and mobility μ_n were calculated as a function of the composition from measurements of the conductivity σ and the Hall coefficient R_H.

The reflection and absorption spectra were measured in a SPEKORD two-beam spectrometer at room temperature in the wavelength interval from 2.5 to 25 μm.

Nine groups of samples, whose parameters are presented in Table I, were investigated. In each group the reflection spectra were measured as a function of the electron density n. The absorption coefficient K was found from the optical transmission spectra $T(\hbar\omega)$ according to the formula

$$T = \frac{(1-R)^2 e^{-Kd}}{1-R^{2Kd}}. \tag{1}$$

The transmission spectra were measured in the phonon energy interval 0.1–0.5 eV, where the reflection coefficient R was constant and equal to 0.36.

Figure 1a shows the reflection coefficient as a function of the energy $\hbar\omega$ of the incident photons for a series of solid solutions with different composition. All curves had a pronounced characteristic minimum corresponding to resonance absorption by free charge carriers. The effective mass m_c of the charge carriers at the Fermi level was determined from the position $\omega_{\min}$ of the minima for different values of x. According to Ref. 4

$$m_c = e^2 n/\varepsilon_0 \omega_{\min}^2 (\varepsilon_\infty - 1). \tag{2}$$

The value of ε_∞ for each composition was calculated by the method described in Ref. 4. It is well known that at frequencies close to $\mathcal{E}_g/\hbar$, where $\mathcal{E}_g$ is the band gap of the experimental material, the coefficient of normal reflection R equals $R = (\sqrt{\varepsilon_\infty}-1)^2/(\sqrt{\varepsilon_\infty}+1)^2$. One can see from the curves in Fig. 1a that as the energy increases, for all compositions R approaches 36%, which gives $\varepsilon_\infty = 16$. We note that according to Ref. 4 the error in determining m_c and ε_∞ by the methods indicated does not exceed 10–15%, if the electron gas is strongly degenerate, which was always so in our case. The values of m_c/m_0 calculated from Eq. (2) are presented in Fig. 1b.

Assuming a Kane dispersion law, the relation between m_c and n can be represented in the form[5]

$$\left(\frac{m_c/m_0}{1-m_c/m_0}\right)^2 = 32.5\times 10^{-32}\frac{\mathcal{E}_g}{P^4} + 8.25\times 10^{-30}\frac{n^{2/3}}{P^2}, \tag{3}$$

 1063-7826/98/030274-03$15.00

TABLE I. Electron density and Hall mobility in $(InSb)_{1-x}(CdTe)_x$ crystals at $T=300$ K.

Sample group No.	Composition, x	Electronic density in a group n, cm^{-3}	Electron mobility in a group μ_n, $cm^2/V\cdot s$
1	0	$(7.2\pm4.6)\times10^{16}$	$(2.3\pm1.1)\times10^4$
2	0.0025	$(3.5\pm1.2)\times10^{18}$	$(6.2\pm3.8)\times10^3$
3	0.005	$(8.4\pm7.3)\times10^{18}$	$(8.2\pm7.1)\times10^3$
4	0.0075	$(6.4\pm1.9)\times10^{18}$	$(3.2\pm2.4)\times10^3$
5	0.01	$(2.8\pm0.8)\times10^{18}$	$(3.5\pm1.8)\times10^3$
6	0.02	$(7.2\pm1.6)\times10^{17}$	$(6.6\pm5.4)\times10^3$
7	0.03	$(6.6\pm2.1)\times10^{17}$	$(6.4\pm5.2)\times10^3$
8	0.04	$(7.7\pm3.4)\times10^{17}$	$(6.0\pm4.3)\times10^3$
9	0.05	$(1.1\pm0.7)\times10^{19}$	$(8.7\pm6.3)\times10^2$

where the matrix element of the momentum operator P for InSb and other III–V compounds equals 8.7×10^{-8} eV·cm to within 20%.

Figure 2a shows the experimental dependences $[(m_c/m_0)(1-m_c/m_0)]^2=f(n^{2/3})$. One can see that the experimental points fall on a straight line, confirming the applicability of the Kane theory for all compositions investigated. The band gap $\mathcal{E}_g^{\rm opt}$ for each composition was determined from the intercepts of straight lines on the ordinate (Fig. 2c).

Figure 3b shows typical curves $K(\hbar\omega)$ for three crystals with different Cd and Te content. Two rising sections can be distinguished in the absorption curves in the regions of high and low energies, characterizing interband transitions and absorption by free charge carriers, respectively. Using at low energies ($\hbar\omega<0.3$ eV) the well-known relation between K and the wavelength λ of the incident radiation in the form

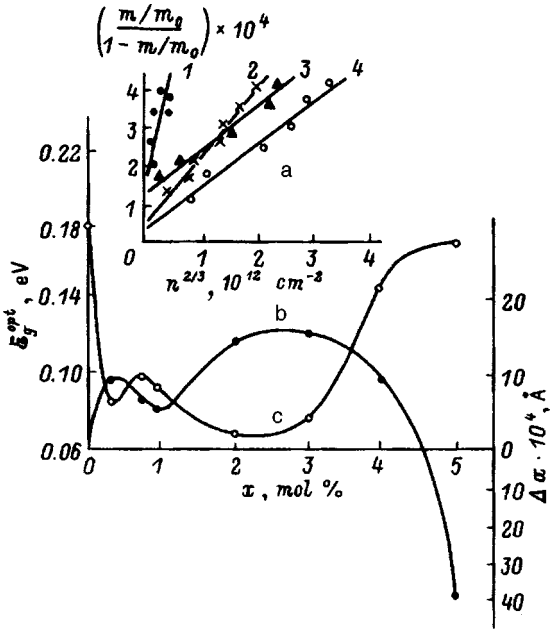

FIG. 2. a — Electron effective mass at the Fermi level versus electron density for different x: *1* — 0.05, *2* — 0.01, *3* — 0.04, *4* — 0.0025. b — Lattice parameter of the solid solutions versus composition. c — Optical band gap $\mathcal{E}_g^{\rm opt}$ of the solid solutions versus composition.

$K=A\lambda^{\alpha}$, where the exponent a depends on the mechanism of scattering of the charge carriers, information can be obtained about the predominant mechanism of scattering for each alloy. The curves $K(\hbar\omega)$ plotted in double-logarithmic coordinates were straight lines, which made it possible to determine the parameter α. Calculations gave $\alpha=2$ for $x=0.0025$, $\alpha=1.94$ for $x=0.05$, $\alpha=3.6$ for $x=0.02$, and $\alpha=3.5$ for $x=0.01$. Values of α close to 2 are characteristic for strongly degenerate materials. For the same SSs the elec-

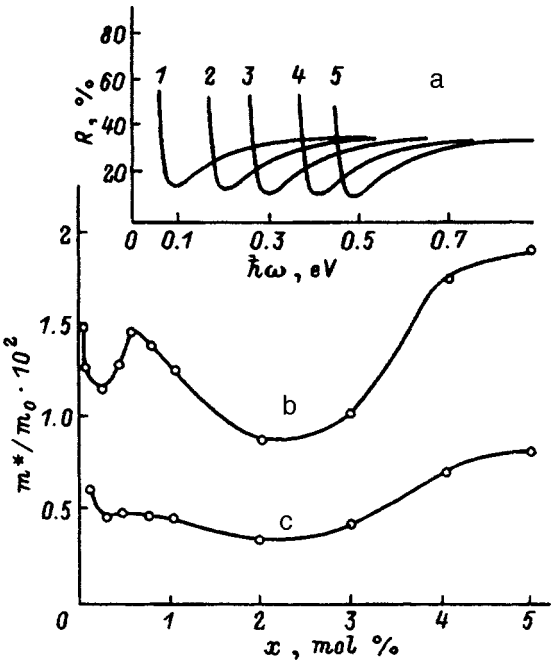

FIG. 1. a — Reflection coefficient R versus photon energy for $(InSb)_{1-x}(CdTe)_x$ crystals. x: *1* — 0.03, *2* — 0.02, *3* — 0.01, *4* — 0.04, *5* — 0.05. Composition dependence of the effective mass: b — at the Fermi level, c — at the conduction-band bottom.

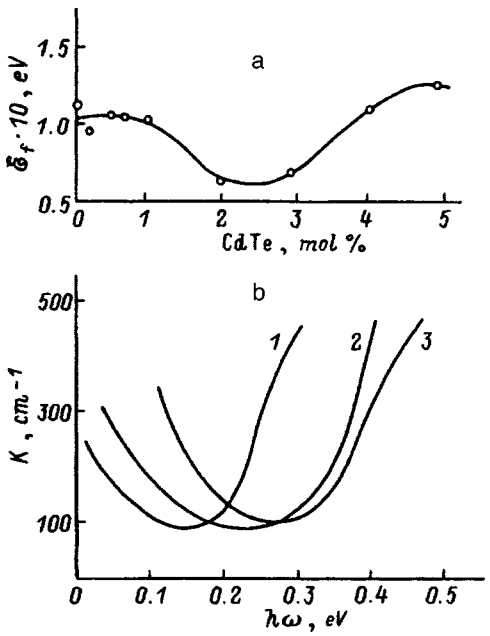

FIG. 3. a — Position of the Fermi level relative to the conduction-band bottom versus composition. b — Typical absorption curves for crystals of the solid solutions $(InSb)_{1-x}(CdTe)_x$. x: *1* — 0.0025, *2* — 0.05, *3* – 0.01.

tron mobility $\mu_n = R_x\sigma$ is virtually independent of temperature in a wide temperature interval 100–400 K.[3] The exponents $\alpha = 3-3.5$ are observed if the carriers are scattered by ionic impurities. This result also follows from analysis of the temperature dependence of the mobility. In the temperature interval 100–400 K $\mu_n \sim T^{\gamma}$, where γ is close to 1.5.[3]

At higher energies ($\hbar\omega > 0.3$ eV) it is difficult to analyze the form of the long-wavelength intrinsic absorption edge for a number of reasons, including the fact that absorption with the participation of the tails of the density of states can be superposed on absorption accompanying direct transitions between corresponding states in bands with the same wave number. Another substantial complication is that under strong degeneracy conditions absorption by free charge carriers is superposed on absorption near the long-wavelength edge. Analysis showed that $K^2 \sim \hbar\omega$ starting with $K \geqslant 200$ cm^{-1}. This is characteristic for direct transitions. The optical band gap $\mathcal{E}_g^{\text{opt}}$ was found from the intercepts by straight lines $K^2 \sim \hbar\omega$ on the energy axis taking account of the position of the Fermi level in the conduction band. The latter was estimated using the experimental values of the effective mass m_c at the Fermi level. According to Ref. 6, the relation between the effective masses at the Fermi level and at the conduction-band bottom is given by the expression

$$m_c = m_c(0)\left(1 + 2\frac{\mathcal{E}_f}{\mathcal{E}_g}\right). \tag{4}$$

The value of $m_c(0)$ was found from the formula[6]

$$1/m_c(0) = \frac{1}{m_0}\left(1 + \frac{\mathcal{E}_p}{\mathcal{E}_g}\right). \tag{5}$$

For all crystals with diamond and zinc blende structure $\mathcal{E}_P = 20$ eV to within 20%.[6] The values obtained in this manner for $\mathcal{E}_f$ and $m_c(0)$ are presented in Figs. 1c and 3a. The value obtained for $\mathcal{E}_g^{\text{opt}}$ by analyzing the absorption curves was virtually identical with respect to the character of the energy dependence and the absolute values to values presented in Fig. 2c.

It follows from Figs. 1c and 2c that the composition dependence of the effective mass and optical band gap is of a complicated, nonmonotonic character. The minimum values $m_c = 0.8\times 10^{-2} m_0$ and $\mathcal{E}_g^{\text{opt}} = 0.07$ eV are reached in the region $x = 0.02-0.03$. To determine the reasons for the observed features we performed x-ray crystallographic investigations and determined the change in the lattice parameter of the solid solutions $\Delta a(x) = a_x - a_0$, where a_x and a_0 are, respectively, the lattice parameters of the alloys and of pure InSb (Fig. 2b). Comparing the curves in Figs. 1c, 2c, and 2b shows that the behavior of $m_c(x)$ and $\mathcal{E}_g^{\text{opt}}(x)$ is determined uniquely by $\Delta a(x)$. It can be conjectured in turn that the dependence $\Delta a(x)$ is due to the complicated character of the interaction of the dopants with one another and with the InSb lattice.

It is known that Te atoms replace Sb atoms in the InSb lattice and determine the *n*-type conductivity of the crystals and that the Cd atoms at In sites play the role of acceptors. The tetrahedral and ionic radii of the interacting atoms are, respectively, $R_{\text{Sb}} = 1.36$ Å, $R_{\text{Te}} = 1.32$ Å, $R_{\text{Te}^+} = 0.5$ Å, $R_{\text{In}} = 1.44$ Å, $R_{\text{Cd}} = 1.48$ Å, and $R_{\text{Cd}} = 1.8$ Å.[7] Under these conditions replacement of Sb atoms by positive Te^+ ions will result in a stretching of the lattice and an increase in Δa. The minimum at $x = 0.01$ can be explained by an increase in the Cd content in solution in the form of Cd^- ions and a decrease in the amount of Te^+ as a result of Coulomb attraction and formation of neutral complexes $(CdTe)^0$ with lattice constant close to that of InSb ($a_{\text{CdTe}} = 6.4822$ Å). The increase in Δa ($0.01 < x < 0.03$) is apparently due to the production of high concentrations of the neutral complexes of the type In_2Te_3, consisting of three Te^+ ions at Sb sites, two In atoms, and a negatively charged In vacancy, in the melt. Since for In_2Te_3 two cubic modifications with lattice constants $a = 6.15$ Å and $a = 18.40$ Å are characteristic,[8] it can be expected that in the first case the lattice of the SS will expand because $a_{\text{InSb}} > a_{\text{In}_2\text{Te}_3}$, while in the second case the lattice of the SS will contract, since $a_{\text{In}_2\text{Te}_3} > a_{\text{InSb}}$. The effect will occur if the density of complexes with a large lattice constant in the SS increases with increasing degree of doping.

In conclusion, it should be noted that in samples specially saturated with Cd during preparation the maximum in the curve $\Delta a(x)$ and the minima in the curves $\mathcal{E}_g^{\text{opt}}(x)$ and $m_c(x)$ at $x = 0.0025$ were not observed.

This work showed that in solid solutions an interaction exists between donors and acceptors. This interaction substantial changes the lattice structure and physical properties of the corresponding materials.

[1] É. N. Khabarov and P. V. Sharovskiĭ, Dokl. Akad. Nauk SSSR **155**, 542 (1964) [Sov. Phys. Dokl. **9**, 225 (1964)].
[2] L. A. Skorobogatova and É. N. Khabarov, Fiz. Tekh. Poluprovodn. **8**, 401 (1974) [Sov. Phys. Semicond. **8**, 257 (1974)].
[3] V. A. Anishchenko, V. A. Brodovoĭ, N. G. Vyalyĭ, V. A. Vikulov, and L. M. Knorozok, Neorg. Mater. **29**, 332 (1993).
[4] Yu. I. Ukhanov, *Optical Properties of Semiconductors* [in Russian], Nauka, Moscow, 1977.
[5] I. M. Tsidil'kovskiĭ, *Electrons and Holes in Semiconductors* [in Russian], Nauka, Moscow, 1972.
[6] I. M. Tsidil'kovskiĭ, *Gapless Semiconductors* [in Russian], Nauka, Moscow, 1986.
[7] P. I. Baranskiĭ, V. P. Klochkov, and I. V. Potykevich, *Handbook of Semiconductor Electronics* [in Russian], Naukova Dumka, Kiev, 1975.
[8] *Reference Data on the Physical and Chemical Properties of Semiconductors* [in Russian], Nauka, Moscow, 1979, Sec. 2. p. 70.

Translated by M. E. Alferieff

Effect of metastable states on the de-excitation of excitons in *n*-GaAs

V. V. Krivolapchuk[a] and N. K. Poletaev

A. F. Ioffe Physicotechnical Institute, Russian Academy of Sciences, 194021 St. Petersburg, Russia
(Submitted June 30, 1997; accepted for publication July 14, 1997)
Fiz. Tekh. Poluprovodn. **32**, 307–310 (March 1998)

The decay of the spontaneous emission of excitons in *n*-GaAs was investigated as a function of temperature and excitation intensity. We report the first experimental observation of the effect of a metastable state in resonance with the conduction band on the exciton de-excitation process. © *1998 American Institute of Physics.* [S1063-7826(98)02203-0]

The luminescence and photoelectric properties of GaAs are determined, first and foremost, by the characteristics of the recombination of photoexcited carriers. At low temperatures the main recombination channel in perfect epitaxial *n*-GaAs layers with a low compensation is the formation (followed by annihilation) of free excitons (X) and excitons bound on shallow donors (D^0,x) as well as the recombination of an electron of a shallow donor and a valence-band hole (D^0,h). The characteristic times of these processes fall in the range $10^{-9}-10^{-8}$ s.[1] In many cases the probability of recombination of a carrier trapped in a localized state is small. Then the lifetime of a carrier in this state becomes long ($\tau_e>10^{-6}$ s), which means that the carrier is in a metastable state. Metastable states in GaAs are of a very diverse nature and they appear in investigations of different phenomena. An interesting and important type of metastability of states are states which are in resonance with the conduction band. The great progress made in the study of such states is due to the investigation of DX centers.[2] The main results for DX centers have been obtained in investigations of the photoconductivity and relaxation spectra of deep levels (DLTS) in the compounds AlGaAs and strongly doped GaAs layers.[3,4]

The purpose of the present work is to investigate experimentally the manifestation of metastable electronic states in spontaneous edge photoluminescence (PL) of nondoped epitaxial *n*-GaAs layers.

The samples consisted of 10–100 μm thick epitaxial *n*-GaAs layers grown by vapor-phase epitaxy (VPE). The impurity density was $N_d-N_a<10^{14}$ cm^{-3}. We investigated the PL spectra with continuous excitation by a He–Ne laser (632.8 nm) and the PL decay kinetics with pulsed excitation by semiconductor (804.4 nm), YAG (530 nm), and nitrogen (337.1 nm) lasers. Detection was performed by the time-correlated photon-count method. The temperature was varied in the interval 2–25 K. The PL decay time in the micro- and nanosecond ranges (the half-width of the instrumental function was equal to 1.3 ns) as well as the total intensity of the lines of a free exciton and an exciton bound on a shallow neutral donor were measured as a function of the temperature and the excitation intensity.

The method employed in the present work is based on studying the characteristic features of the decay of edge photoluminescence. In Ref. 5 it was shown in an investigation of the decay of photoluminescence (PL) that local metastable states (E^h_{ms}) which effectively trap minority carriers (holes) are present in *n*-GaAs. The anomalously long decay ($>10^{-6}$ s) of PL observed in the D^0,h line is due to the time for nonactivational transfer of holes from metastable states into the valence band, after which these holes are bound with electrons of shallow donors and the D^0,h line is formed in the delayed PL spectra as a result. Moreover, the delayed spectra contain a line of an exciton bound on a shallow donor — D^0,x as well as a line of a free exciton. It is obvious that in order to observe excitonic lines in substantially delayed (>2 μs) spectra long-lived electrons must be present in addition to long-lived holes.[6] The purpose of the present work is to study the effect of long-lived electronic states — the process of excitonic emission.

The decay curve $I(t)$ of the D_0,x line at 2 K is displayed in Fig. 1. As one can see from the figure, a rapid dropoff (the section a–b) is observed in the decay of the PL. This dropoff reflects the characteristic radiative decay of the corresponding impurity complexes and for the indicated lines it lies in the range $(9-54)\times10^{-9}$ s. Next follows a slow tail (the section b–c), reflecting the liberation of holes from a metastable state ($>10^{-6}$ s).

The slow-decay time and the area under the decay curve (Fig. 1) were determined from the luminescence kinetics. It should be noted that the slow decay is not exponential, so that an adjustable parameter which can be interpreted as the decay time is determined by mathematical analysis of a collection of points. This parameter reflects the hole transfer time into the valence band from metastable hole states (MS_h).

The integral of $I(t)$ is determined by the expression $I_t=\int_{t_1}^{t_2}I(t)dt$ and reflects the quantum yield of delayed PL, which is proportional to the density of holes trapped in metastable states and therefore is a good measure of the process of slow depopulation of hole states E^h_{ms}.

As one can see from Fig. 2b, the integral $I(t,T)$ exhibits unusual behavior with increasing temperature. A pronounced minimum is observed at a temperature near 6 K (0.51 meV) against the background of a monotonic decrease of this integral. Moreover, at a definite intensity of continuous excitation the total intensity of the lines of a free exciton on a shallow donor (D^0,x) likewise has a minimum at temperature $T=6$ K (Fig. 2c). This minimum is observed comparatively far from the edge of thermally activated decay of the complex (D^0,x).

As shown in Ref. 5, since the hole transfer time from a

 1063-7826/98/030277-03$15.00

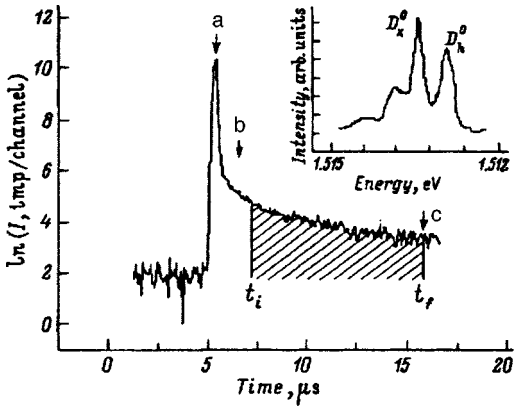

FIG. 1. Kinetics of the photoluminescence $I_0(t)$ of the line D^0,x on a semilogarithmic scale with $E=2$ K. The hatched region represents the integral of $I(t)$, where t_i and t_r are the limits of integration (equal to 3 and 10 μs, respectively) measured from the end of the excitation pulse (point a). Inset: Typical PL spectrum of the experimental GaAs samples at $T=2$ K.

metastable state E_{ms}^h ($\tau_h=10^{-6}$ s) is several orders of magnitude longer than the radiative decay time of the impurity complexes D^0,x and D^0,h ($10^{-8}-10^{-9}$ s), the time t_h characterizes the hole contribution to the process leading to the formation of the line in delayed spectra. We underscore that the hole transfer time determined from the PL decay curve (section b–c in Fig. 1) is virtually temperature-independent (Fig. 2a). This suggests that the temperature dependence $I(t,T)$ is due to the contribution of not holes but electrons.

Let us see how the temperature can influence the behavior of the exciton bound on a shallow donor — D^0,x. The temperature dependence of the intensity of the D^0,x line corresponding to thermally activated decay of the corresponding impurity complex is described by the expression[7]

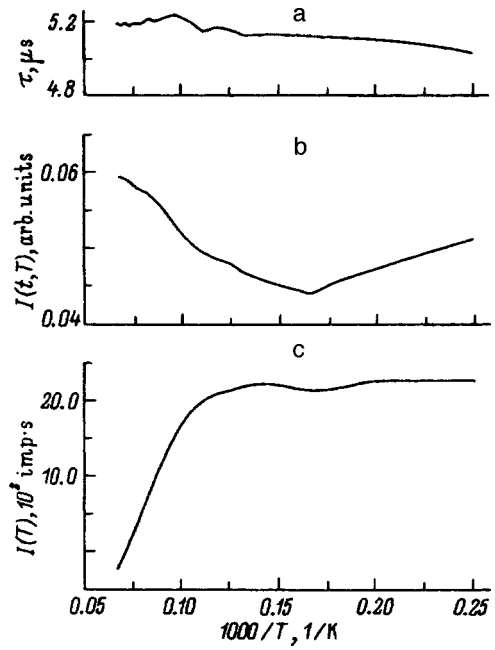

FIG. 2. Temperature dependences of a — slow hole transfer time τ_h out of a metastable hole state, b — the value of the area $I(t,T)$ under the curve of the slow decay of the PL of the D^0,x line, and c — the total intensity $I(T)$ of the D^0,x line with continuous excitation by a He–Ne laser.

$$I(T)=I_0/\{1+C\exp(-E/T)\},$$

where E is the thermal activation energy of the level and C is the temperature-independent constant. It is obvious that this expression can be used to describe the continuous decrease of the quantum yield but it cannot explain the existence of a minimum. Phenomenologically, the existence of a minimum in this case can be explained by the fact that at temperature $T=6$ K electrons do not participate in the formation of excitonic lines. For electrons not to participate in the formation of excitonic lines they must be transferred as a result of heating into a state that does not contribute to radiation. Taking into consideration the energy imparted to the electrons (0.51 eV), this state can be an excited state of a shallow donor.

In this case the electrons can leave the donor nonradiatively by an Auger process.[8] The characteristic time of this process ($<10^{-10}$ s) is much shorter than the radiative recombination time. For this reason, there is a high probability that electrons will be transferred into a band and as a result, together with a decrease of the PL intensity, the free-carrier density will increase, as was observed in Ref. 7. However, investigations showed that the expected increase in the free-carrier density, an indicator of which is the free-exciton line, does not occur. Moreover, an increase in the excitation intensity and therefore the carrier density causes the minimum to vanish with both continuous and pulsed excitation. On the basis of known mechanisms of exciton formation (see below) and the totality of experimental facts the Auger process (the case of a short time) must be ruled out as the main process. Moreover, in this case it is difficult to explain the decrease at $T=6$ K of the intensity of the free-exciton line. This latter circumstance is very important, since it indicates that the electrons are trapped in a state whose energy lies near the conduction-band edge and as a result they do not participate in radiative recombination. In this case this should be manifested not only in a slow kinetics but also in rapid decay of excitons. To prove this we investigated the decay of the D^0,x line in the nanosecond range. To increase the accuracy of the analysis of the experimental results we employed the convolution operation $S(\tau)=\int_0^\infty f(t)F(\tau-t)dt$. For $f(t)$ we used the experimentally obtained laser pulse, and we took for $F(\tau-t)$ the function $\exp-\{(t-t_0/\tau)\}^2$, since such a function best describes the decay of the PL. The result of analyzing the PL decay curve in this manner for one value of T is displayed in Fig. 3. The inset shows the variation of the decay time τ obtained in this manner versus temperature. As one can see from the figure, the decay time of a bound exciton decreases rapidly at $T\cong 6$ K.

Let us consider the explanation of such a temperature dependence of the decay time. Under our experimental conditions a free exciton is formed from free carriers[9] A bound exciton (D^0,x) is formed by trapping of either a free exciton as a whole or free carriers by a donor. The lifetime of free excitons and electrons in high-quality n-GaAs samples is longer than the radiative recombination time of a bound exciton D^0,x. For this reason, the probability of de-excitation (and therefore the radiative lifetime) of an exciton (D^0,x)

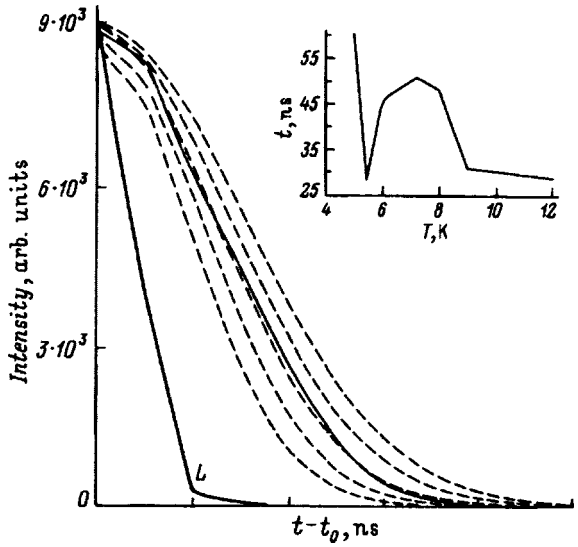

FIG. 3. Decay of the PL of the line D^0,x in the nanosecond range. L — laser pulse. The solid line shows the experimental decay curve at $T=7$ K. The dashed lines show the computational results obtained for the convolution with different values of the parameter τ. Inset: Temperature dependence of the decay.

reflects the lifetime of free excitons; this is confirmed by the large value of the decay time of the radiation in the line D^0,x as compared with the known value $\tau_{ex}=(0.8-1)\times10^{-9}$ s.[10] The sharp decrease of the decay time of the D^0,x line in the nanosecond range indicates a decrease in the lifetime of a free exciton at the thermostat temperature $T\cong6$ K. This is also indicated by the decrease in the intensity of the radiation of a free exciton with increasing temperature up to 6 K in the case of continuous weak excitation. As a result of the mechanism of formation of a bound exciton (D^0,x), this should result in a decrease of the decay time of the latter. As one can see from Fig. 3), we have indeed observed a decrease in the decay time of the PL in the line of a bound exciton (D^0,x). This attests to the fact that, just as the decrease in the intensity of the radiation of a free exciton at this temperature, the decay of the integral $I(t,T)$ as the temperature 6 K is approached from below is determined by the thermally stimulated trapping of electrons (excitons) in a state with a long lifetime relative to recombination; this is equivalent to a metastable state. The increase in the value of the integral for $T>6$ K can be explained as follows. As one can see from the figure (Fig. 2c), the depth of the minimum on a comparable scale is small. This indicates that the number of electrons trapped in the state E^e_{ms} is also small. In this case the small increase in $I(t,T)$ near $T>6$ K (condition of a minimum), just as the vanishing of the minimum at high excitation intensities, is explained by the fact that heated electrons with energy $E>E^e_{ms}$ do not decay into this state and the de-excitation process proceeds in the conventional manner.

In summary, it can be concluded from the totality of the experimental data presented that an electronic metastable state E^e_{ms} has an appreciable effect on the de-excitation of excitons in n-GaAs. Since free excitons are formed from itinerant carriers, it must be assumed that the state E^e_{ms} is in resonance with the conduction band. We can say the following about the nature of this state. Since the energy of thermally stimulated trapping in the state E^e_{ms} (0.51 meV) is much less than the value obtained for DX centers,[3] it is unlikely that this state can be associated with these centers. It can be conjectured that the state E^e_{ms} could be due to the content of the residual transition-metal impurities (for example, Cr), which can give rise to a resonance state in the conduction band.[11] However, taking into consideration the low degree of compensation and the high quality of the epitaxial layers of gallium arsenide, we assume that the state E^e_{ms} is due to the presence of D centers.[12]

In closing, it is our pleasant duty to thank V. V. Travnikov and A. V. Akimov for fruitful discussions.

[a)]E-mail: lumkin@krivol.ioffe.rssi.ru

[1] D. Bimberg, H. Munzel, A. Steckenborn, and J. Cristen, Phys. Rev. B **31**, 7788 (1985).
[2] P. M. Mooney, J. Appl. Phys. **67**, R1 (1990).
[3] T. N. Theis, P. M. Mooney, and S. L. Wright, Phys. Rev. Lett. **60**, 361 (1988).
[4] G. Brunhaler, K. Ploog, and W. Juntsch, Phys. Rev. Lett. **63**, 2276 (1989).
[5] A. V. Akimov, A. A. Kaplyanskiĭ, V. V. Krivolapchuk, and E. V. Moskalenko, JETP Lett. **46**, 42 (1987).
[6] A. V. Akimov, V. V. Krivolapchuk, N. K. Poletaev, and V. G. Shofman, Fiz. Tekh. Poluprovodn. **27**, 310 (1993) [Semiconductors **27**, 171 (1993)].
[7] E. H. Bogardus and H. B. Bebb, Phys. Rev. **176**, 993 (1968).
[8] B. L. Gel'mont, N. N. Zinov'ev, D. I. Kovalev, V. A. Kharchenko, I. D. Yaroshetskiĭ, and I. N. Yassievich, Zh. Éksp. Teor. Fiz. **94**, 332 (1988) [Sov. Phys. JETP **67**, 613 (1988)].
[9] C. Weisbuch, Solid-State Electron. **21**, 179 (1978).
[10] C. J. Hwang, Phys. Rev. B **8**, 646 (1973).
[11] A. É. Vasil'ev, N. P. Il'in, and V. F. Masterov, Fiz. Tekh. Poluprovodn. **23**, 804 (1989) [Sov. Phys. Semicond. **23**, 506 (1989)].
[12] C. J. Armistead, S. P. Najda, R. A. Stradling, and J. C. Maan, Solid State Commun. **53**, 1109 (1985).

Translated by M. E. Alferieff

Transport phenomena in the solid solution $(Pb_{0.78}Sn_{0.22})_{0.97}In_{0.03}Te$ in the hopping conduction region

S. A. Nemov, Yu. I. Ravich, V. I. Proshin, and T. G. Abaĭdulina

St. Petersburg State Technical University, 195251 St. Petersburg, Russia
(Submitted October 15, 1997; accepted for publication October 20, 1997)
Fiz. Tekh. Poluprovodn. **32**, 311–314 (March 1998)

Data on the electrical conductivity, the thermoelectric power, and the Hall and Nernst–Ettingshausen effects in the temperature range from 77 to 400 K for the a solid solution PbTe–SnTe with a high In content (3 at. %) and additional doping with chlorine and thallium are presented. Specifically, the Nernst–Ettingshausen coefficient exhibits properties which are unusual for IV–VI semiconductors: It is positive and decreases rapidly with increasing temperature. The experimental data are discussed on the basis of a model in which the main transport mechanism is hopping conduction along strongly localized electronic states of the In impurity. Conduction along delocalized states of the conduction band makes a substantial contribution to the effects observed in a transverse magnetic field. The model gives satisfactory agreement with experiment, including the sign, magnitude, and temperature dependence of the Nernst–Ettingshausen coefficient.
[S1063-7826(98)02303-5]

In lead telluride and its solid solutions with a high indium impurity content, hopping conduction has been observed along strongly localized In states[1–4] lying near the edge of the band gap. The double-doping method was used to study in greater detail the mechanisms of hopping conduction and the density of localized states in $(Pb_{0.78}Sn_{0.22})_{0.97}In_{0.03}Te$.[5,6] In the double-doping method, localized or resonance levels appear on account of one impurity, in this case In, while the other additional impurity, which does not produce energy levels near the chemical potential, makes it possible to change the position of the chemical potential and thereby probe the existing electron energy spectrum. In Ref. 5 the additional impurity was Cl, which is a donor and increases the chemical potential, and the acceptor impurity was Tl, which does not produce levels in the conduction band or in the top part of the band gap.

In Ref. 5 experimental data mainly on the thermoelectric power in $Pb_{0.78}Sm_{0.22}Te$ with 3 at. % In and with additional impurities at temperatures 100–400 K were presented and analyzed. In the present paper we present and discuss experimental results for four transport coefficients (the electrical conductivity, the thermoelectric power, and the Hall and Nernst–Ettingshausen coefficients) in the same materials and in the same temperature range.

Figures 1–3 show the temperature dependences of the electrical conductivity σ, the Hall coefficient R, and the Nernst–Ettingshausen coefficient Q for different amounts of the additional impurity. Similar curves for the thermoelectric power S have been published earlier[5] and will also be brought into the analysis of our experimental data.

In the temperature interval 150–400 K the electrical conductivity of the materials investigated grows exponentially. It was concluded earlier[2,3] on the basis of all experimental data that the electrical conduction is mainly of a hopping character, i.e., the hopping conductivity σ_h is much larger than the band component σ_b and $\sigma \approx \sigma_h$. At temperatures T above approximately 150 K the curve of $\ln\sigma$ versus $1/T$ is a straight line. The activation energy ε_h of hopping conduction is independent of the content of the additional impurity Cl and equal to approximately 35 ± 3 meV. Since the activation energy is determined by the spread of the localized levels, this means that the impurity Cl does not influence the energy spectrum of the levels produced by the In impurity atoms. Additional doping with thallium somewhat increases the activation energy, up to 50 meV with 1.5 at. % Tl. This could be explained by the shift of the chemical potential into the energy range where the spread of the levels is larger.

With the exception of the sample with the highest Tl concentration (2 at. %), the thermoelectric power for the In content studied in the present work (3 at. %) is negative ($S<0$) in the entire temperature range 100–400 K. As we have already mentioned, the dependences of the thermoelectric power on the temperature and the concentration of additional impurities was discussed earlier[5] on the basis of the assumption that the processes determining the thermoelectric power are of a hopping character so that $S \approx S_h$.

The Hall coefficient is negative ($R<0$) and decreases rapidly in absolute magnitude as a function of temperature. Therefore it can be stated that the Hall electron density grows exponentially with temperature. This behavior can be explained by assuming that hopping conduction increases with temperature more rapidly than conduction along delocalized band states. As is well known,[7,8] the Hall coefficient, which is proportional to the off-diagonal component σ_{xy} of the electrical conductivity tensor in a magnetic field, is negligibly small in the case of purely hopping conduction. Since the probability of a hop between two sites does not depend on the magnetic field in weak magnetic fields, to calculate σ_{xy} it is insufficient to study the two-site problem, the problem of hops between three and more sites must be solved. The fact that R_h is small while the electrical conductivity σ_h is relatively high makes it necessary to calculate the Hall

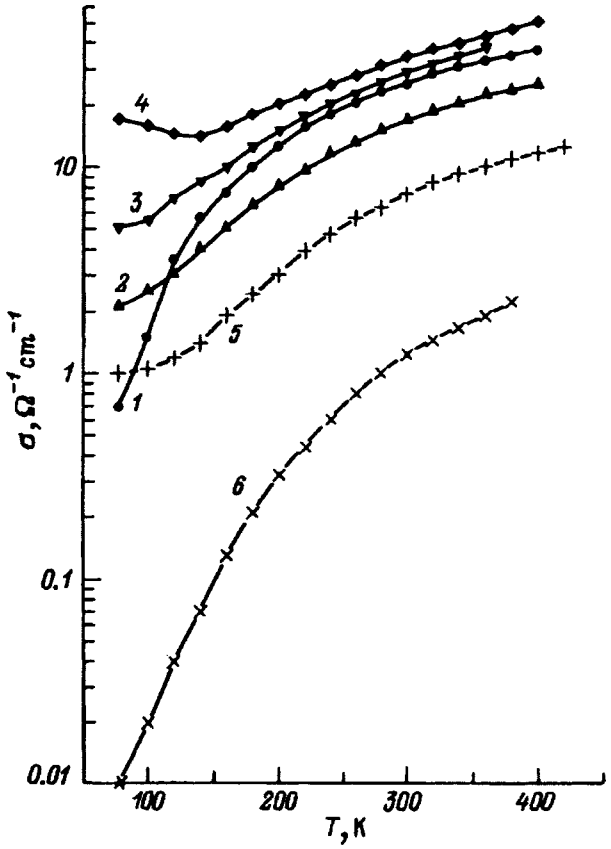

FIG. 1. Temperature dependence of the electrical conductivity σ in $Pb_{0.78}Sm_{0.22}Te$ samples doped with 3 at. % In and additional Cl or Tl impurity. Additional impurity content N_{ad}, at.%: *1*—0, *2*—1, *3*—2, *4*—3, *5*—1, *6*—1.5. Type of additional impurity: *2–4* — Cl, *5–6* — Tl.

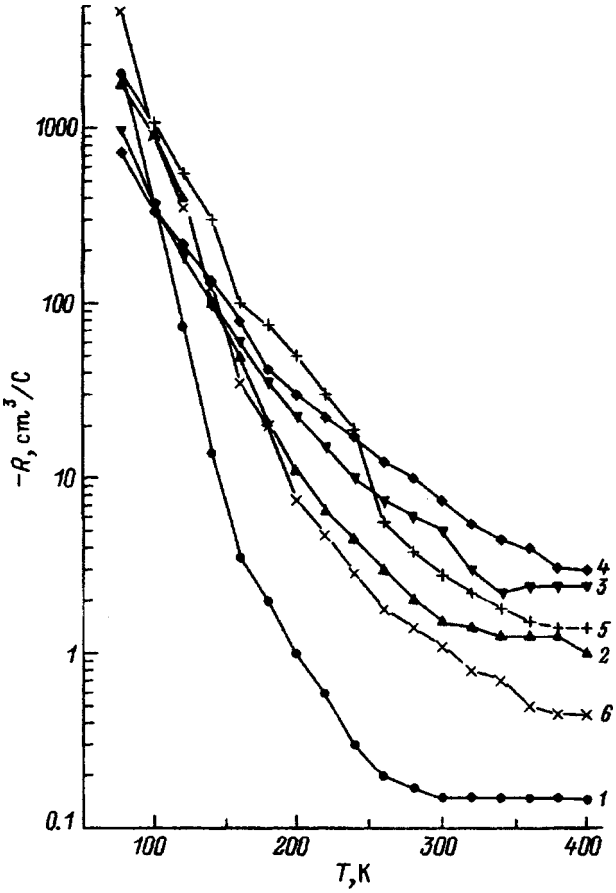

FIG. 2. Temperature dependence of the Hall coefficient R in $(Pb_{0.78}Sn_{0.22})_{0.97}In_{0.03}Te$ samples additionally doped with Cl or Tl. The numbers on the curves have the same meaning as in Fig. 1.

coefficient R using a model similar to the diffusion model for semiconductors.[7] This model takes into account both the hopping component σ_h of the conductivity and the band conductivity σ_b, which is due to electrons with energies above the mobility threshold ε_c. As a result, we have for the Hall coefficient

$$R=\frac{R_b\sigma_b^2+R_h\sigma_h^2}{(\sigma_b+\sigma_h)^2}\,. \tag{1}$$

Since R_h is small and $\sigma_h \gg \sigma_b$, we obtain

$$R\approx R_b\left(\frac{\sigma_b}{\sigma_h}\right)^2\,. \tag{2}$$

Assuming that the electron density in the conduction band above the mobility threshold increases with temperature with activation energy ε_b, we obtain that the activation energy of the Hall density $1/e|R|$ equals $\varepsilon_R=2\varepsilon_h-\varepsilon_b$.[7] According to our experimental data, the activation energy ε_R is approximately twice the conduction activation energy ε_h. The accuracy with which the parameters ε_h and ε_R are determined does not permit finding the activation energy ε_b of the band conductivity according to the difference $2\varepsilon_h-\varepsilon_b$; one can only conclude that this quantity is relatively small or the band conductivity is not of an activational character at all.

The formula for the Hall mobility $R\sigma$ will be helpful for what follows. According to Eq. (1)

$$R\sigma=R_b\sigma_b\,\frac{\sigma_b}{\sigma} \tag{3}$$

and is much smaller in absolute magnitude than the Hall mobility for the band conductivity $R_b\sigma_b$. From what we have said above about the activation energies for conduction and Hall density, it follows that $|R\sigma|$ decreases rapidly with increasing temperature.

We shall now discuss a different effect in a transverse magnetic field — the Nernst–Ettingshausen effect (NEE). In contrast to the conventional NEE with single-band conduction in lead chalcogenides, the NEE coefficient Q in the solid solutions $(Pb_{0.78}Sn_{0.22})_{0.97}In_{0.03}Te$ is positive ($Q>0$) and decreases rapidly with increasing temperature over the entire range 100–400 K. This temperature dependence of the NEE occurs for the same reason as the analogous dependence of the Hall coefficient. Indeed, the expression for the NEE coefficient contains two terms, one of which is proportional to the term σ_{xy} mentioned above in connection with the discussion of the Hall coefficient, while the other is the off-diagonal tensor component b_{xy}. Just as the Hall component σ_{xy}, the quantity b_{xy} gives a current component along the x axis with a generalized force directed along the y axis. The quantity σ_{xy} can be represented as an integral over the energy

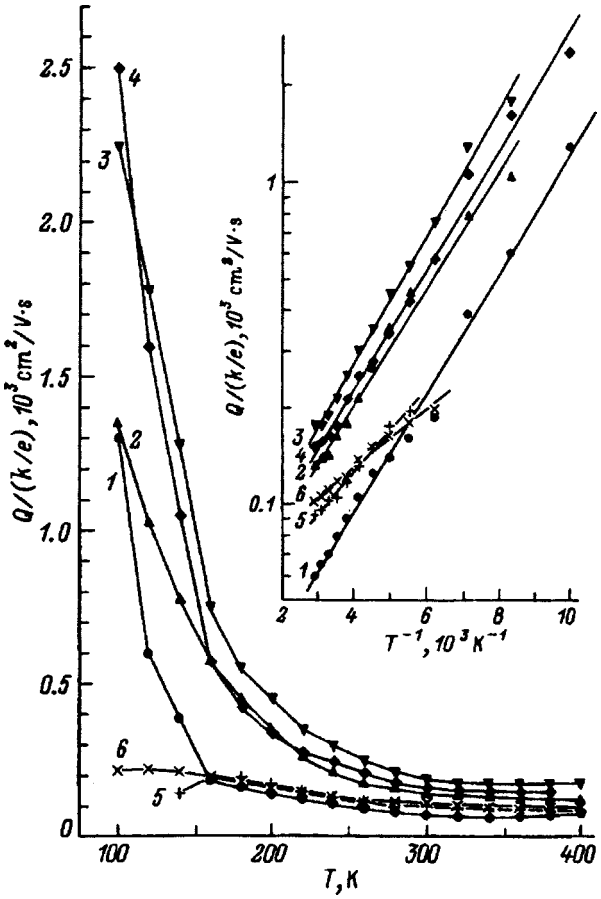

FIG. 3. Temperature dependence of the transverse Nernst–Ettingshausen effect coefficient Q in $(Pb_{0.78}Sn_{0.22})_{0.97}In_{0.03}Te$ samples additionally doped with Cl or Tl. The numbers on the curves have the same meaning as in Fig. 1. Inset: $\ln[Q/(e/k)]$ as a function of $10^3/T$.

$$\sigma_{xy}=\int \left(-\frac{\partial f}{\partial \varepsilon}\right)\sigma_{xy}(\varepsilon)d\varepsilon, \tag{4}$$

and the smallness of σ_{xy} in the case of hopping conduction is due to the smallness of the function $\sigma_{xy}(\varepsilon)$. The component b_{xy} can be expressed in the similar form

$$b_{xy}=\frac{1}{eT}\int \left(-\frac{\partial f}{\partial \mathrm{E}}\right)(\varepsilon-\mu)\sigma_{xy}(\varepsilon)d\varepsilon, \tag{5}$$

where μ is the chemical potential. As a result of the smallness of the function $\sigma_{xy}(\varepsilon)$, b_{xy} and therefore the NEE coefficient are small. Despite the approximate character of the formulas (4) and (5),[9] they can be used to draw the qualitative conclusion that the Nernst–Ettingshausen coefficient Q_h for hopping conduction is small.

In summary, to calculate the measured coefficient Q, just as R, it is necessary to use a model with two types of conduction. This gives the formula

$$Q=Q_b\frac{\sigma_b}{\sigma}+Q_h\frac{\sigma_h}{\sigma}+\frac{\sigma_b\sigma_h}{\sigma^2}(S_b-S_h)(R_b\sigma_b-R_h\sigma_h). \tag{6}$$

Eliminating R_h and Q_h from the relation (6) and using Eq. (3), we obtain

$$Q\approx Q_b\frac{\sigma_b}{\sigma}+(S_b-S_h)R\sigma. \tag{7}$$

The quantity Q in Eq. (7) consists of three terms, $Q=Q_1+Q_2+Q_3$. Since $S_h\approx S$, we shall express the third term as a product of three directly measured quantities

$$Q_3=-SR\sigma. \tag{8}$$

This negative term is lower in absolute magnitude for all compositions than the measured coefficient Q. Table I gives as an example the experimentally measured transport coefficients in a sample with no additional impurities.

Next, we shall estimate the first and second terms in Eq. (7). To estimate electronic transport phenomena, we shall regard the mobility threshold as the edge of an allowed band and we shall employ for Q_b and S_b the standard formulas obtained for semiconductors in the absence of statistical degeneracy

$$Q_b\approx-\frac{k}{e}rR_b\sigma_b, \tag{9}$$

$$S_b\approx-\frac{k}{e}\left(\frac{5}{2}+r+\frac{\varepsilon_c-\mu}{kT}\right). \tag{10}$$

The formulas (9) and (10) include the scatter parameter r. It can be expected that as energy increases above the mobility threshold, $\sigma(\varepsilon)$ will increase and the quantity

$$r\approx\frac{d\ln\sigma(\varepsilon)}{d\ln\varepsilon},$$

will be positive. Since the Hall coefficients R and R_b are negative, we conclude the terms Q_1 and Q_2 are positive.

The materials investigated are apparently strongly nonuniform, and the mobility threshold is associated with the percolation level. At the percolation level $\sigma(\varepsilon_c)=0$, while above it current flows along percolation channels[10,11] so that the function $\sigma(\varepsilon)$ increases as $(\varepsilon-\varepsilon_c)^t$, where t is the critical exponent for electrical conductivity and equals 1.6.[7] Measuring energy from the percolation level, we can use this number as an estimate of the parameter r. The quantity ε_c

TABLE I. Results of measurements of the transport coefficients and theoretical estimates of terms in the relation (7) for a $(Pb_{0.78}Sn_{0.22})_{0.97}In_{0.03}Te$ sample without additional impurity.

T, K	σ, $\Omega^{-1}\mathrm{cm}^{-1}$	S, μV/K	R, cm^3/C	$\lvert R\sigma\rvert$, $\mathrm{cm}^3/\mathrm{V}\cdot\mathrm{s}$	$Q/(k/e)$, $\mathrm{cm}^2/\mathrm{V}\cdot\mathrm{s}$	$Q_1/(k/e)$, $\mathrm{cm}^2/\mathrm{V}\cdot\mathrm{s}$	$Q_2/(k/e)$, $\mathrm{cm}^2/\mathrm{V}\cdot\mathrm{s}$	$Q_3/(k/e)$, $\mathrm{cm}^2/\mathrm{V}\cdot\mathrm{s}$	$(Q_1+Q_2+Q_3)/(k/e)$, $\mathrm{cm}^2/\mathrm{V}\cdot\mathrm{s}$
150	5	−80	−17	85	300	140	340	−80	400
200	12	−41	−2.1	25	150	40	100	−12	130
300	28	−45	−0.35	10	80	16	40	−5	50

$-\mu$ equals the activation energy ε_b of band conduction. As noted above, according to the experimental data, this parameter is small and the third term in Eq. (10) can be neglected in a rough estimate. Using the formulas and parameters presented above, we obtain for Q_1 and Q_2

$$Q_1 \approx 1.6 \frac{k}{e} |R\sigma|, \tag{11}$$

$$Q_2 \approx 4.1 \frac{k}{e} |R\sigma|. \tag{12}$$

The estimates (11) and (12) show that the positive terms Q_1 and Q_2 are greater in absolute magnitude than $|Q_3|$ (see Table I). As a result of these terms, the total Nernst–Ettingshausen coefficient Q is positive and close to the experimental value. The decrease in the Hall mobility $|R\sigma|$ with temperature results in a corresponding decrease in Q.

In summary, the positive sign, the order of magnitude, and the temperature dependence of the Nernst–Ettingshausen coefficient, just as the other electrophysical properties studied, can be explained on the basis of the assumption that hopping conduction plays a dominant role and that band states with energies above the mobility threshold participate in the formation of transport effects in a transverse magnetic field.

[1] S. N. Lykov, Yu. I. Ravich, and I. A. Chernik, Fiz. Tekh. Poluprovodn. **11**, 1731 (1977) [Sov. Phys. Semicond. **11**, 1016 (1977)].
[2] S. A. Nemov, Yu. I. Ravich, A. V. Berezin, V. É. Gasumyants, M. K. Zhitinskaya, and V. I. Proshin, Fiz. Tekh. Poluprovodn. **27**, 299 (1993) [Semiconductors **27**, 165 (1993)].
[3] Yu. I. Ravich, S. A. Nemov, and V. I. Proshin, Fiz. Tekh. Poluprovodn. **29**, 1448 (1996) [Semiconductors **29**, 754 (1996)].
[4] S. A. Nemov, V. I. Proshin, and Yu. I. Ravich, Fiz. Tekh. Poluprovodn. **30**, 2164 (1996) [Semiconductors **30** 1128 (1996)].
[5] T. G. Abaĭdulina, S. A. Nemov, V. I. Proshin, and Yu. I. Ravich, Fiz. Tekh. Poluprovodn. **30**, 2173 (1996) [Semiconductors **30**, 1133 (1996)].
[6] V. I. Kaĭdanov and Yu. I. Ravich, Usp. Fiz. Nauk **145**, 51 (1985) [Sov. Phys. Usp. **28**, 31 (1985)].
[7] B. I. Shklovskiĭ and A. L. Éfros, *Electronic Properties of Doped Semiconductors*, Springer-Verlag, N. Y., 1984 [Russian original, Nauka, Moscow, 1979].
[8] H. Böttger and V. V. Bryskin, *Hopping Conduction in Solids*, Akademie Verlag, Berlin, 1985.
[9] I. P. Zvyagin, in *Hopping Transport in Solids*, edited by B. Shklovskii and M. Polak, Elsevier Science Publishers V. B., 1991, p. 143.
[10] M. H. Cohen and J. Jortner, Phys. Rev. Lett. **30**, 699 (1973).
[11] N. F. Mott, in *Proceedings of 4th International Conference on Non-Crystalline Solids*, Clausthal-Zellerfeld, 1976, edited by G. H. Frishche, Trans. Tech. Publications, 1977, p. 3.

Translated by M. E. Alferieff

Local neutrality and pinning of the chemical potential in III–V solid solutions: interfaces and radiation effects

V. N. Brudnyi and S. N. Grinyev

V. D. Kuznetsov Siberian Physicotechnical Institute, 634050 Tomsk, Russia
(Submitted March 6, 1997; accepted for publication June 30, 1997)
Fiz. Tekh. Poluprovodn. **32**, 315–318 (March 1998)

In the virtual crystal approximation the mole fraction (X) of the local neutrality level E_{lnl}: $E_{lnl}(X)^{\mathrm{ABC}}=XE_{lnl}^{\mathrm{AC}}+(1-X)E_{lnl}^{\mathrm{BC}}-C_{\mathrm{ABC}}X(1-X)$ has been calculated in ABC solid solutions for 18 pairs of III–V semiconductors. An interpolation formula is proposed for the nonlinear coefficient C_{ABC} (in eV): $C_{\mathrm{ABC}}=-0.03+0.04|\Delta a|+1.4|\Delta a|^2$ as a function of the lattice mismatch $|\Delta a|$ (in Å) for boundary compositions of the solid solutions. It is shown that the numerical values of E_{lnl} obtained provide good agreement with the experimental values of the heights of the Schottky barriers (F_{bS}) and the limiting Fermi level positions (F_{lim}) in irradiated III–V solid solutions. © *1998 American Institute of Physics.* [S1063-7826(98)00703-0]

Local neutrality in semiconductors is manifested in pinning of the chemical potential (Fermi level) on the metal–semiconductor interface of a heteropair, on the surface, and also on its stabilization in the ''limiting'' position F_{lim} in a semiconductor irradiated by high-energy particles. It is assumed here that pinning of the chemical potential on interfaces and in bulk defect-containing material occurs near the level of local neutrality E_{lnl}, a concept that was formulated by the authors of Ref. 1. Therefore, calculations of the energy level E_{lnl} in semiconductors take on a level of importance for applied purposes, and the quantity E_{lnl} itself is one of the fundamental characteristics of a crystal.

A model for estimating E_{lnl} in semiconductors has now been used extensively.[2] In this model the value of E_{lnl} is found from the condition that the Green's function of the crystal averaged over the unit cell vanish:

$$\left|\sum_{n_c\mathbf{k}}\frac{\exp(i\mathbf{k}\cdot\mathbf{R}_m)}{[E_{n_c}(\mathbf{k})-E_{lnl}]}\right|=\left|\sum_{n_v\mathbf{k}}\frac{\exp(i\mathbf{k}\cdot\mathbf{R}_m)}{[E_{n_v}(\mathbf{k})-E_{lnl}]}\right|. \tag{1}$$

Here $\mathbf{k}$ is the Bloch wave vector, n is the number of the energy band, $\mathbf{R}_m=(1/2)ma(110)$, $m=1,2,3\ldots$, a is the lattice constant, and $E_{n_c}(\mathbf{k})$ and $E_{n_v}(\mathbf{k})$ are the energies of the conduction band and the valence band, respectively. Equation (1) is widely used to estimate the height of the Schottky barrier F_{bS} and the band discontinuity in heteropairs

$$\Delta E_v=E_v^{\mathrm{AC}}-E_v^{\mathrm{BC}}.$$

Here E_v^{AC} and E_v^{BC} are the energies of the tops of the valence bands of the semiconductors AC and BC, respectively. In the model of rigid pinning of the Fermi level to an interface, which is characteristic of semiconductors with diamond structure and III–V compounds, it is assumed that $F_{bS}=E_{lnl}$ and

$$\Delta E_v=E_{lnl}^{\mathrm{AC}}-E_{lnl}^{\mathrm{BC}},$$

where the energy is reckoned from the level Γ_{8v}. It is significant here that the quantity E_{lnl} is completely determined by the band spectra of the crystal and does not depend on the work function of the metal or the nature of damage on the interface. Despite the large number of assumptions made in the derivation of expression (1) and in subsequent numerical calculations of E_{lnl}, the accuracy of the metal–semiconductor barrier heights and band discontinuities for heteropairs in this model is several times higher than in the classical models of Schottky and Anderson.

A more rigorous expression for estimating the energy level E_{lnl}, which coincide with the chemical potential of the electrons (holes) localized on the levels of the defect states in the band gap of the crystal and which is based on the standard approach for determining the chemical potential in statistical physics, was proposed in Ref. 3. Accordingly, the standard condition for electron balance

$$E(N)-E(N-1)=E(N+1)-E(N)$$

was modified to the case where the total energies $E(N\pm1)$ are found from the local electron and hole states located in the band gap. The above relation corresponds to the condition of global neutrality in a solid body, where $E(N)$ is the total energy of a system of N electrons, in accordance with the Bloch nature of the wave functions of free electrons. This allows one to obtain a new equation for determining the level of local neutrality in a semiconductor, which is different from Eq. (1)

$$\sum_{n_c\mathbf{k}}[E_{n_c}(\mathbf{k})-E_{lnl}]^{-2}=\sum_{n_v\mathbf{k}}[E_{n_v}(\mathbf{k})-E_{lnl}]^{-2}. \tag{2}$$

We used Eq. (2) to estimate values of $F_{\mathrm{lim}}(\cong E_{lnl})$ in irradiated bulk semiconductors which are in good agreement with the corresponding experimental data for a large group of materials.[4] The calculated values of E_{lnl} obtained on the basis of Eqs. (1) and (2) are in good agreement with each other (Table I).[4,5]

The present work addresses the problem of estimating the dependence $E_{lnl}(X)$ in III–V semiconductor solid solutions; here X is the mole fraction of the solid solution. Such

TABLE I. Calculated values of the level of local neutrality E_{lnl}, the width of the band gap E_g, and experimental values of $F_{\lim}$ and F_{bS} in C, Si, Ge and in III–V semiconductors. Values reckoned from the top of the valence band (the level Γ_{8v}).

Semiconductor	E_g, eV	E_{lnl}, eV	E_{lnl}^T, eV	E_{lnl}^S, eV	$F_{\lim}$, eV	F_{bS}, eV
C	5.45	2.11	–	1.96	–	1.71
Si	1.20	0.41	0.36	0.39	0.39	0.32–0.4
Ge	0.78	0.09	0.18	0.18	0.13	0.07–0.18
BN	7.99	4.18	–	4.34	–	3.10
BP	1.99	0.89	–	0.81	–	0.87
BAs	1.82	0.23	–	0.00	–	–
AlP	2.48	1.10	1.27	1.20	–	–
AlAs	2.24	0.83	1.05	0.88	–	0.96
AlSb	1.60	0.42	0.45	0.47	0.5	0.55
GaP	2.37	0.86	0.81	1.00	1.0+0.2	0.94–1.17
GaAs	1.51	0.51	0.50	0.63	0.6	0.52–0.62
GaSb	0.87	0.05	0.07	0.14	0.02–0.05	0.07–0.1
InP	1.43	0.72	0.76	0.89	1.0	0.76–0.98
InAs	0.39	0.55	0.50	0.50	0.51	0.47
InSb	0.14	0.03	0.01	0.15	0.0	0.00

[a]*Remark*. E_{lnl}^T—our calculations based on expression (1) using the (100)–spin–orbit functions obtained by the EMP method; E_{lnl}^S—the same, but based on expression (2); see Ref. 4. Experimental values: E_{lnl}—data of Refs. 2 and 5 obtained using expression (1) and energy bands calculated by the SPW method; $F_{\lim}$—limiting position of the Fermi level in the irradiated semiconductors;[4,9] F_{bS}—height of the Schottky barrier (Al and Au).[2,5,8]

calculations have not yet been carried out and to estimate $E_{lnl}(X)$ the linear approximation is typically used together with boundary compositions of the solid solutions.

We used Eq. (1) to calculate E_{lnl} in semiconductors, but recalculated the values of E_{lnl} for the investigated materials since the authors of Ref. 2 used insufficiently accurate crystal band spectra, obtained by the method of summed plane waves (SPW), for which the error in the calculation of the interband gaps reaches about 1 eV. This necessitated subsequent ''improvement'' of resulting values by rigidly shifting the conduction bands relative to the valence bands until reasonable values of the interband gaps were obtained. This procedure is not unique and is realized by fitting the calculated values to the experimental values. In addition, the spin–orbit splitting of the valence band was taken into account in this work semi-empirically. All this puts in doubt the predicted capability of using Eq. (1) to estimate E_{lnl} in semiconductors.

In our calculations we used band spectra obtained by the empirical model pseudopotential (EMP) method, which provides accurate estimates of the energy of interband gaps on average not worse than 0.1 eV (Ref. 4), which enables us to obtain values of E_{lnl} in the investigated materials without any subsequent fitting procedures. In the calculations of E_{lnl} we allowed for 100 spin–orbit interactions, and in the calculation of the integrals over the Brillouin zone we used the method of special points.[6] For semiconductors in which the level of local neutrality falls in the band gap we used 10 special points to calculate E_{lnl}. To monitor the accuracy of the results so obtained, we compared them for the case of GaAs with the results of a calculation based on the band structure calculated on a fine grid in **k**-space (about 150 points in the irreducible part of the Brillouin zone) and found good agreement (at the level of 0.02 eV) with the value of E_{lnl} calculated using 10 special points. The dependence of E_{lnl} on the lattice vector is quite weak. For example, for GaAs the value $E_{lnl}(m=2)=0.52$ eV and $E_{lnl}(m=3)=0.50$ eV; therefore, for the final value of E_{lnl} we took their mean value (Table I).

For InAs the energy level E_{lnl} falls in the continuum of the conduction band; therefore, to enhance the accuracy of the calculations we used 29 special points generated by the extended unit cell method.[7] We applied the procedure of smoothing the Green's function with a Lorentzian with broadening equal to 0.2 eV.

Our values of E_{lnl} and also the values from Refs. 2, 4, and 5, together with experimental data for the heights of Schottky barriers F_{bS} based on Al and Au[5,8] and values of $F_{\lim}$ in irradiated bulk semiconductors,[4,9] and also calculated values of the minimum width of the band gap E_g for the investigated materials, which illustrate the goodness of the band spectra used in the calculations of E_{lnl}, are presented in Table I. The energy levels are reckoned from the top of the valence band (the level Γ_{8v}) since in the investigated materials these bands are similar. The experimental values of $F_{\lim}$ and F_{bS} were obtained at temperatures near room temperature, with the exception of InAs and InSb, and the calculated values of E_{lnl}—at 0 K. To adapt the theoretical to the experimental data, we calculated the temperature dependence of E_{lnl} for two compounds: InAs and GaAs. We showed that in the temperature interval 0–300 K the temperature derivative $(\partial E_{lnl}/\partial T) \leqslant -10^{-4}$ eV/K; i.e., the temperature correction is found within the limits of accuracy of the calculations of E_{lnl} itself and, consequently, the level of local neutrality is essentially ''stuck'' to the top of the valence band as the temperature of the material varies. This allows us to use the obtained calculated values for comparison with the experimental values (Table I). When necessary, in the case of small values of E_{lnl}, as in InSb and GaSb, temperature corrections can be taken into account.

TABLE II. Calculated values of the nonlinearity coefficient C_{ABC} [eV] in expression (3) for III–V solid solutions.

Semiconductor	AlAs	GaAs	InAs	AlP	GaP	InP	AlSb	GaSb	InSb
AlAs	0	−0.02	0.22	−0.02	–	–	0.44	–	–
GaAs	−0.02	0	0.20	–	−0.02	–	–	0.22	–
InAs	0.22	0.20	0	–	–	0.04	–	–	0.24
AlP	−0.02	–	–	0	−0.10	0.24	0.62	–	–
GaP	–	−0.02	–	−0.10	0	0.22	–	–	
InP	–	–	0.04	0.24	0.22	0	–	–	0.52
AlSb	0.44	–	–	0.62	–	–	0	0.00	0.26
GaSb	–	0.22	–	–	0.52	–	0.00	0.00	0.10
InSb	–	–	0.24	–	–	0.52	0.26	0.10	0

We used values of E_{lnl} for boundary compositions of the solid solutions in calculations of the dependence $E_{lnl}(X)$ in III–V semiconductor solid solutions. Various interpolation schemes are widely used to describe the dependence of various parameters on the mole fraction (X) of the solid solutions. In this context such parameters as the lattice constant, the density of the material, the elastic constants, and the dielectric constant obey Végard's rule, whereas the energy parameters of the band spectrum, such as the width of the band gap and the ionization energy of the impurity levels, are characterized by a quadratic dependence on the mole fraction.[10] The dependence $E_{lnl}(X)$ for solid solutions has so far not been examined; therefore, besides the boundary compositions of the solid solutions we also calculated E_{lnl} for equimolar concentrations $(X=0.5)$ in the virtual crystal approximation using Végard's law for the lattice constant. For solutions with isovalent substitution the virtual crystal model provides a satisfactory description of the concentration dependence of the band spectrum.[11] On the basis of the obtained data we propose a quadratic interpolation formula for the dependence $E_{lnl}^{\mathrm{ABC}}(X)$ in the investigated solid solutions

$$E_{lnl}^{\mathrm{ABC}}(X)=XE_{lnl}^{\mathrm{AC}}+(1-X)E_{lnl}^{\mathrm{BC}}-C_{\mathrm{ABC}}X(1-X). \qquad (3)$$

Here C_{ABC} [eV] is the nonlinearity parameter, whose values for the investigated pairs of solid solutions are given in Table II. A direct check of Eq. (3) for intermediate values of X against exact calculations shows that the quadratic dependence with the coefficient C_{ABC} from Table II describes $E_{lnl}(X)$ in the entire region of compositions with an error not greater than 0.02 eV. From this table it follows that the linear approximation can be used for a limited number of solid solutions, such as (GaAl)As, Al(AsP), Ga(AsP), (AlGa)Sb, and some others, while in the remaining cases it is necessary to use the general expression (3).

We analyzed the connection between the nonlinear coefficient C_{ABC} and the lattice mismatch parameter $|\Delta a|$ for the boundary conditions in the investigated solid solutions and obtained the following interpolation formula:

$$C_{\mathrm{ABC}}=-0.03+0.04|\Delta a|+1.4|\Delta a|^2, \qquad (4)$$

which can be used for approximate estimates of $E_{lnl}(X)$ from the boundary values of E_{lnl} and for other pairs of solid solutions of the given group of compounds (see Fig. 1); here $|\Delta a|$ is in Å. Expression (4) agrees qualitatively with a similar calculational formula for the energy gaps of the band structure of the solid solutions of III–V compounds (Ref. 12).

The results of our calculations, presented in Tables I–III and expressed in Eqs. (3) and (4) can be used to estimate F_{bS} and ΔE_v in solid solutions of the investigated semiconductors. For example, a comparison of the calculated values of $E_{lnl}(X)$ and the experimental data $F_{bS}(X)$ for the well-studied solution (GaAl)As, in which the level of local neutrality is found in the band gap for all values of X, and for a solution with peculiarities, $\mathrm{In}_x\mathrm{Ga}_{1-x}\mathrm{As}$, in which E_{lnl} falls in the region of allowed energies of the conduction band for $X<0.25$ (at 300 K), shows reasonable agreement between theory and experiment.[13]

The calculated values of $E_{lnl}(X)$ can also be used to estimate $F_{\mathrm{lim}}(X)$ in irradiated solid solutions and, consequently, to predict their electronic properties after irradiation with high-energy particles. Thus, according to the model data, $\mathrm{In}_x\mathrm{Ga}_{1-x}\mathrm{As}$ solid solutions upon radiation treatment should acquire n^+-type conductivity for $X<0.25$ and become highly resistive for $X>0.25$, while (GaAl)As-based solution becomes an insulator over the entire composition range. Note that despite the large number of studies of radiation effects in semiconductors, there are practically no direct

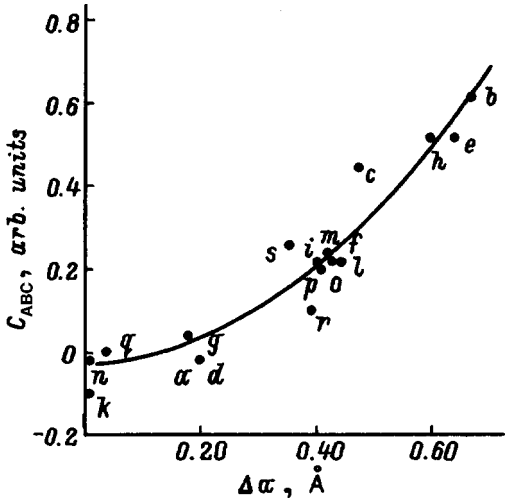

FIG. 1. Correlation between the nonlinearity coefficient C_{ABC} (eV) (Table II) and the lattice mismatch parameter $|\Delta a|$ (Å) for the boundary compositions of the III–V solid solutions. The solid curve corresponds to Eq. (4).

TABLE III. The notation is given in Fig. 1.

Semiconductor	Symbol
Al(AsP)	*a*
Al(PSb)	*b*
Al(AsSb)	*c*
Ga(AsP)	*d*
Ga(PSb)	*e*
Ga(AsSb)	*f*
In(PAs)	*g*
In(PSb)	*h*
In(AsSb)	*i*
(AlGa)P	*k*
(GaIn)P	*l*
(AlIn)P	*m*
(AlGa)As	*n*
(GaIn)As	*o*
(AlIn)As	*p*
(AlGa)Sb	*q*
(GaIn)Sb	*r*
(AlIn)Sb	*s*

experimental studies of $F_{\lim}$ in their solid solutions at present; therefore, the above calculations of $E_{lnl}(X)$ are of great practical importance.

In conclusion, we note that studies presented here can find use in predictive estimates of the electronic properties of irradiated semiconductors and their solid solutions, and also in the construction of energy diagrams of the Schottky barriers and heteropairs, including quantum wells based on solid solutions of III–V semiconductors. Here the corrections associated with charge redistribution on the interface should be taken into account, as well as deformation effects for semiconductor pairs with large values of $|\Delta a|$.

This work was carried out with the partial support of the grants ''Universities of Russia'' and ''Basic Research in Nuclear Engineering and the Physics of Ionizing Radiation Beams.''

[1] C. Tejedor, F. Flores, and E. Louis, J. Phys. C **10**, 2163 (1977).
[2] J. Tersoff, Surf. Sci. **168**, 275 (1986).
[3] V. E. Stepanov, in *New Materials for Electronics Technology* [in Russian], ed. by F. A. Kuznetsov (Nauka, Siberian Branch Acad. Sci. USSR, Novosibirsk, 1990), p. 26.
[4] V. N. Brudnyi, S. N. Grinyev, and V. E. Stenanov, Physica B **212**, 429 (1995).
[5] J. Tersoff, J. Vac. Sci. Technol. B **4**, 1066 (1986).
[6] D. J. Ċhadi and M. L. Cohen, Phys. Rev. B **8**, 5747 (1973).
[7] R. A. Évarestov, *Quantum-Chemistry Methods in Solid State Theory* (Leningrad University Press, Leningrad, 1982).
[8] S. M. Sze, *Physics of Semiconductor Devices* (Wiley, New York, 1969).
[9] V. N. Brudnyĭ, Izv. Vuzov. Fizika **29**, 84 (1986).
[10] S. Adachi, J. Appl. Phys. **58**, R1 (1985).
[11] S. N. Grinyaev, S. G. Kataev, and V. A. Chaldyshev, Izv. Vuzov. Fizika **29**, 15 (1986).
[12] V. A. Chaldyshev and S. N. Grinyaev, Izv. Vuzov. Fizika **26**, 38 (1983).
[13] P. Vogl, Adv. Electron. Electron Phys. **62**, 101 (1984).

Translated by Paul F. Schippnick

Two- and three-dimensional conduction channels at block boundaries in (CdHg)Te mosaic crystals

V. A. Pogrebnyak,[a] D. D. Khalameĭda, and V. M. Yakovenko

Institute of Radio Physics and Electronics, Ukrainian National Academy of Sciences, 310085 Khar'kov, Ukraine

I. M. Rarenko

Chernovtsy State University, 274012 Chernovtsy, Ukraine

(Submitted June 2, 1997; accepted for publication September 9, 1997)
Fiz. Tekh. Poluprovodn. **32**, 319–325 (March 1998)

Additional electronic conduction has been observed along the block boundaries in mosaic *n*-type $Cd_xHg_{1-x}Te$ crystals. Conduction along block boundaries is two-dimensional (2D) in one group of samples and three-dimensional (3D) in another group. The main parameters of the 2D and 3D channels—electron density cyclotron mass, relaxation time, and mobility—were determined by analyzing the Shubnikov–de Haas oscillations. In strong magnetic fields at liquid-helium temperatures conduction occurs mainly along a network of conducting channels at block boundaries. The resistance of such a network of 2D channels in a $6\times1.5\times0.5$ mm^3 sample equals approximately 110 Ω and is virtually temperature-independent. © *1998 American Institute of Physics.* [S1063-7826(98)00803-5]

1. INTRODUCTION

$Cd_xHg_{1-x}Te$ (CMT) narrow-gap semiconductors are widely used for fabricating infrared photodetectors. Aside from their importance for applications, the low effective mass of these crystals makes them unique objects for investigating the fundamental physical properties of electrons in a crystal. The electronic energy spectrum of CMT is quite complicated. The study of transport phenomena is an important method for determining the electronic energy spectrum. However, the investigation of transport phenomena in CMT is far from a simple problem because of the presence of a large number of electrically active intrinsic point defects due to deviation from the stoichiometric composition, which in turn largely depends on the technological process used to grow the CMT. In this connection, a great deal of attention has been devoted in the literature to the study of the properties of point defects in these crystals and the effect of these defects on transport phenomena.[1–4] Their electronic properties of extended defects, such as small-angle and block boundaries, have received less attention. The important role of block boundaries in the mechanism of conduction in CMT was first pointed out in Ref. 5, after which investigations in this direction were elaborated in Refs. 6 and 7, where it is shown that conduction along block boundaries in *p*-type samples can lead to anomalous transport phenomena. However, it should be noted that the conductivity along block boundaries in *p*-type crystals was determined indirectly. This is because in *p*-type samples, which the indicated studies involved, the conduction channels are only slightly filled with electrons and it is impossible to observe them directly. However, in *n*-type samples the conduction channels at the block boundaries are completely filled and the electron gas in them is degenerate, so that measurements can be performed directly, for example, according to the Shubnikov–de Haas (SdH) oscillations.[8]

In the present work, direct measurements confirming the existence of conducting electronic channels at block boundaries were performed by means of an analysis of SdH oscillations. The parameters of the electronic channels—electron density, cyclotron mass, and mobility—were determined and the character of the conduction was also established—in some cases conduction along the block boundaries is of a two-dimensional (2D) character and in other cases it is of a three-dimensional (3D) character. It is shown that the conductivity along the channels is comparable to the volume conductivity of the crystal at liquid-helium temperatures.

2. SAMPLE PREPARATION. X-RAY AND METALLOGRAPHIC INVESTIGATIONS

It is well known that CMT single crystals have a large number of small-angle boundaries, forming the mosaic structure of the crystal. The presence of block boundaries is due to the characteristic features of the technology used to grow CMT single crystals and the specific nature of the physicochemical properties of CMT alloys. The volatility of mercury plays an important role. The excess Cd or Te arising for this reason can lead to concentration supercooling near the crystallization front and to the formation of cellular or mosaic structure. The appearance of dislocations and a mosaic structure in a crystal gives rise to a low value of the critical shear stress for the appearance of dislocations in CMT. This leads to the generation of dislocations by the thermoelastic stress field near the crystallization front.[9]

$Cd_xHg_{1-x}Te$ ingots were grown by a modified vertical zone melting method[10,11] from prepurified components of the solid solution. The modification consisted of the fact that the cell with the growing crystal was rotated at a rate of 2–60 rpm and was tilted at an angle of 0–60 °C. The growth rate was equal to 0.035 mm/h with temperature stability of no worse than ±0.25 °C. The grown single crystals were cut

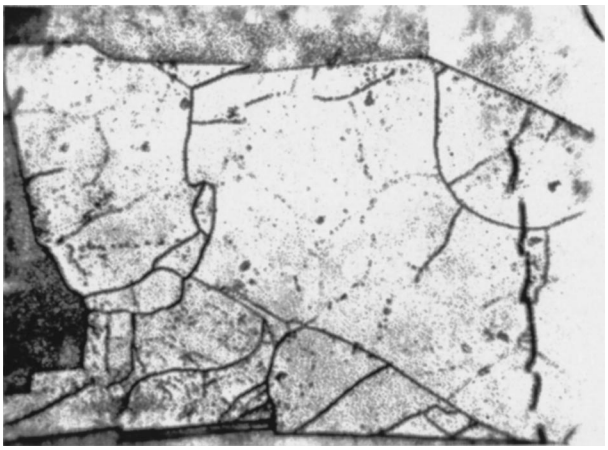

FIG. 1. Mosaic structure of $Cd_xHg_{1-x}Te$ crystal. Photograph of a surface pretreated by selective etching; ×67 magnification.

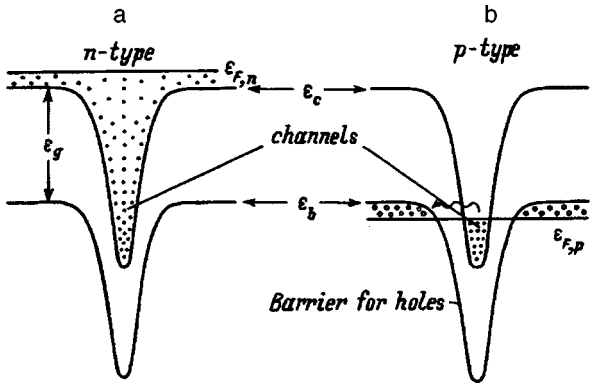

FIG. 2. Band diagram of electronic states at a block boundary. In the *n*-type semiconductor (a) the electrons completely fill the potential well; in the *p*-type sample (b) there are very few electrons in the conduction channel.

into disks perpendicular to the direction of growth. After mechanical and chemical polishing the disks were annealed in mercury vapor for 15–20 days in order to approach stoichiometry. The annealing regimes were selected in accordance with the composition of the disks, which was determined from measurements of the transmittance near the intrinsic absorption edge or by x-ray microprobe analysis. After annealing the disks were again checked for uniformity of composition along the diameter. Samples in the form of $6\times1.5\times0.5$ mm^3 parallelepipeds were cut out of the central regions of the disks, which were subjected beforehand to preliminary galvanomagnetic measurements by the van der Pauw method at 296 and 77 K.

To reveal the structural features of the material, such as the dislocation density and the presence of blocks and small-angle boundaries, the crystals were subjected to x-ray crystallographic and metallographic investigations. The x-ray crystallographic investigations were conducted by the Berg–Barret topographic analysis method. The topograms made it possible to reveal small-angle boundaries and blocks, the disorientation angles between which ranged from several angular minutes to 10 angular seconds. The arrangement of the angular boundaries depends on the direction of growth of the ingot. In (CdHg)Te crystals grown in the [111] direction the small-angle boundaries lie in three {100} planes parallel to the growth axis of the crystal. Ordinarily, mosaic structure arises in single crystals possessing a high dislocation density of the order of 10^5 cm^{-2}. The dislocation density was determined by counting etch pits. Figure 1 shows photographs of the surface of a crystal, preetched with a selective etchant, with (111) orientation. The dislocation density was equal to approximately 10^5 cm^{-2} within the confines of the blocks. The dimensions of the blocks lie in the range 50–400 μm. A rough calculation of the number of dislocations per unit length gives $N_D\simeq10^4$ cm^{-1}. The value of N_D is related to the disorientation angle θ by the relation[12] $N_D=1/D=(2/b)\sin\theta/2$, where b is Burgers vector, and D is the distance between the dislocations. For our crystals this relation is satisfied with $\theta\approx10'$, i.e., for the maximum angles obtained from the x-ray crystallographic investigations.

The samples possessed current and two pairs of potential contacts. The ohmic contacts were deposited with a low-temperature solder based on Bi and In. Au from a water solution of gold chloride was deposited beforehand on the contact pads. The pads were 0.1 mm in size. We investigated $Cd_xHg_{1-x}Te$ samples with $x=0.13-0.19$ in semimetallic and semiconductor phases with electron density $n=10^{14}-10^{16}$ cm^{-3} at liquid-helium temperatures and with mobility $\mu=10^5-10^6$ cm^2/(V·s).

It is well known[12] that small-angle boundaries and block boundaries are dislocation walls. In crystals with a partially ionic bond, which CMT alloys are, the dislocations become charged. The charge of a dislocation is determined by which type of bond is unsaturated in a specific case. Experimental investigations[13,14] indicate that dislocations in CMT crystals form donor-type levels. The accumulation of charge dislocations on block boundaries leads to the formation of two-dimensional space-charge layers and to bending of the conduction band bottom, as well as to the possibility of formation of conducting channels on the block boundaries. The degree of bending of the conduction band bottom or, in other words, the depth of the potential well on a block boundary depends on the dislocation charge and on the disorientation angle between neighboring blocks. Depending on the values of these parameters, 3D[15] or 2D[16] conduction channels can arise on the block boundaries in the crystals. The experimental samples can be divided into two groups accordingly: with 2D or 3D conduction along block boundaries. The character of the conduction and also the density of both groups of electrons can be determined by analyzing the SdH oscillations in bulk and thin samples.[8] For such investigations *n*-type samples are most suitable, since the Fermi level $\varepsilon_{F,n}$ in these samples lies above the conduction band bottom. In this case both 2D and 3D channels are completely filled with conduction electrons (see Fig. 2a). Conduction channels in *p*-type samples are much less filled with electrons, since the Fermi level $\varepsilon_{F,p}$ in this case lies below the valence band top (Fig. 2b). In the latter case the block boundaries become potential barriers for holes, the sample becomes strongly nonuniform, and conduction is of a percolation character.[17]

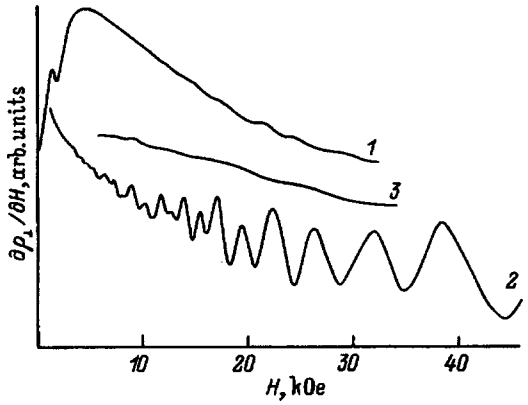

FIG. 3. Derivative $\partial\rho_\perp/\partial H$ versus the transverse magnetic field versus the magnetic field H for $Cd_xHg_{1-x}Te$ samples: *1*—bulk, 2, 3—thin layer. **H** orientation: *2*—parallel to the surface of the layer, *3*—perpendicular to the surface. Layer thickness 65 μm, $x=0.185$, $T=4.2$ K.

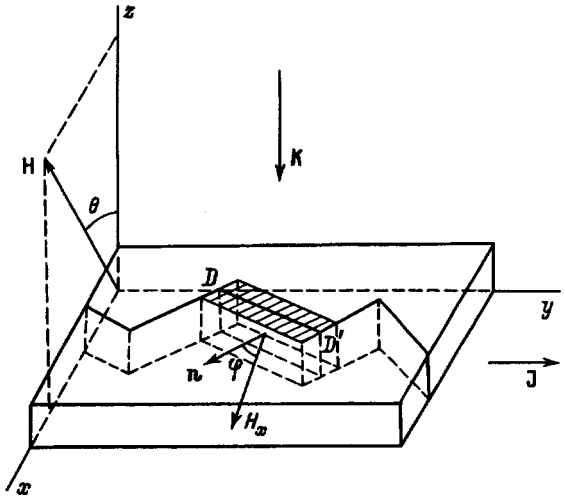

FIG. 4. Schematic diagram of 2D and 3D electronic channels on the block boundary DD' in a thin layer of $Cd_xHg_{1-x}Te$: **n**—normal to the plane of a 2D channel. The hatched region represents the cross section of a 3D channel; φ—angle between the normal and the x axis; **J**—direction of current flow.

3. TWO-DIMENSIONAL CONDUCTION ALONG BLOCK BOUNDARIES

Samples exhibiting 2D conduction along block boundaries were prepared from crystals with the minimum volume electron density $n=1.4\times10^{14}$ cm^{-3} and with a relatively low electron mobility $\mu=1.05\times10^5$ cm^2/(V·s) at $T=4.2$ K.

The density of both groups of electrons (3D and 2D) in a n-type sample can be determined and the two-dimensionality of conduction along block boundaries can be ascertained by analyzing the SdH oscillations.[8] Figure 3 (curve *1*) shows a curve of the derivative of the transverse magnetoresistance $\partial\rho_\perp/\partial H$ for samples with $x=0.185$. The SdH oscillations at $H\simeq1.5$ kOe correspond to the bulk value of the electron density $n=1.4\times10^{14}$ cm^{-3}. Oscillations of $\partial\rho_\perp/\partial H$, barely distinguishable at the maximum sensitivity of the apparatus, can be seen in fields $H>10$ kOe (curve *1*). These oscillations are due to quantization of the electron gas in the 2D channels at the block boundaries. The very small amplitude of these oscillations is explained by the fact that only relatively few boundaries are perpendicular to the given direction of the magnetic field and quantization of electron motion occurs in them. Twice as many boundaries are oriented parallel to **H**; quantization along the magnetic field does not occur in them, they possess a lower resistance, and they shunt the channels that give oscillations of $\rho_\perp(H)$. The shunting effect of the indicated portion of the channels can be eliminated by decreasing the thickness of the samples to less than the average block size.

Curve *2* in Fig. 3 shows a tracing of $\partial\rho_\perp/\partial H$ for a 65 μm-thick layer obtained from a bulk sample, which had been mechanically polished and chemically etched. Curve *2* corresponds to the case where **H** is parallel to the surface of a thin layer, and curve *3* was obtained for a perpendicular orientation. The oscillations in curve *2* have the characteristic form for the magnetoresistance of 2D channels, where electrons fill several quantum-well subbands. The anisotropy of the oscillatory pattern as a function of the orientation of **H** and the appearance of the oscillations can be explained as follows. When the thickness of the sample decreases to a monolayer with respect to the blocks, almost all boundaries will be oriented perpendicular to the film surface. This is because the sample is oriented, as was mentioned in the first section, in a manner so that the plane of the film is perpendicular to the direction of growth [111] and the extended boundaries are arranged mainly parallel to [111] (see Fig. 4), but they are oriented in a arbitrary manner in the xy plane (the angle φ in Fig. 4). If the magnetic field is oriented perpendicular to the surface of the film, then it will not give rise to quantization in the channels, since in this case the channels are oriented parallel to **H** (curve *3*). However, if the magnetic field is directed parallel to the surface of the film, then for a random orientation of block boundaries, some boundaries will be oriented perpendicular to the fixed direction of the magnetic field and they will make a contribution to the oscillatory pattern, whereas the oscillations from the remaining channels, which are tilted at different angles φ, will extinguish one another. This can be easily verified by averaging the oscillatory part of the 2D magnetoresistance $\sim\cos(2\pi\varepsilon_F/\hbar\omega_c)$ over the angle φ. This procedure is similar to integrating over the longitudinal quasimomentum when calculating $\rho_\perp(H)$ in the 3D case.[18] Averaging gives the expression

$$\langle\rho_\perp\rangle_\varphi=\rho_\perp^0\left[1-8\pi^{3/2}\sqrt{\frac{\hbar\omega_c}{2\pi\varepsilon_F}}\times\frac{\cos\left(\frac{2\pi\varepsilon_F}{\hbar\omega_c}+\frac{\pi}{4}\right)}{\sinh\left(\frac{2\pi^2T}{\hbar\omega_c}\right)}\exp\left(-\frac{\pi}{\omega_c\tau}\right)\right], \tag{1}$$

where ε_F is the Fermi level of the 2D gas, $\rho_\perp^0$ is the monotonic component of the magnetoresistance, τ is the 2D-electron pulse relaxation time, and $\omega_c=eH/mc$. As one can see from the expression (1), averaging has decreased the am-

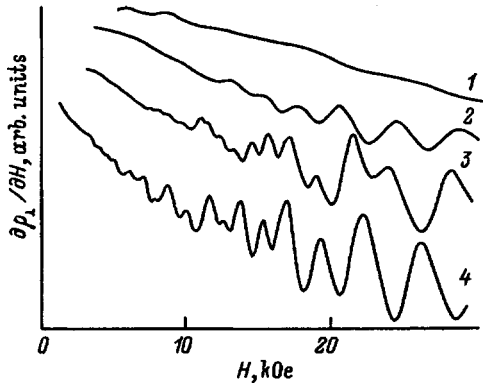

FIG. 5. Amplitude of SdH oscillations in a thin layer of $Cd_xHg_{1-x}Te$ (same as in Fig. 3) for different angles θ: *1*—0°, *2*—52°, *3*—62°, *4*—90°.

plitude of the oscillations, just as in the 3D case, by the factor $\sqrt{2\pi\varepsilon_F/\hbar\omega_c}$. Thus, it follows from Eq. (1) that, as observed in the experiment, the oscillation picture for identical 2D channels remains unchanged as the direction of the magnetic field varies in the plane of the film.

The dependence of the frequency of the SdH oscillations on the angle θ (Fig. 5) between the normal to the surface of the layer and the direction of the magnetic field **H** serves as proof of the two-dimensionality of the electron gas at the block boundaries. The frequency of the SdH oscillations depends on the angle θ in accordance with the variation of the normal component, with respect to the 2D channel, of the magnetic field $H\sin\theta$, confirming the two-dimensional character of electron motion on the block boundaries.

Analysis of the oscillation pattern makes it possible to determine the main parameters of a 2D channel. The electron density in the 2D subbands can be found[19] from the period of the oscillations of $\partial\rho/\partial H$ in terms of the reciprocal of the magnetic field $\Delta_i(1/H)$:

$$n_i = e/\pi c\hbar\Delta_i . \tag{2}$$

Analysis of the oscillations gives the value of n_i: $n_g = 8.2\times10^{11}$ cm^{-2} in the main subband and $n_1 = 4\times10^{11}$ cm^{-2} in the first subband. The oscillations from higher subbands are smeared, making it impossible to find the corresponding densities. The electron cyclotron masses in the subbands can be found from the ratio of the amplitudes of the oscillations for fixed values of the magnetic field but different values of the temperatures. At $T=4.2$ K, in addition to the dependence (curve *2* in Fig. 3), measured at $T=4.2$K, we have accordingly measured the dependences $\partial\rho_\perp/\partial H$ at $T=2.5$ and 1.67 K. Calculation gives the cyclotron masses $m_g = 0.046m_0$ and $m_1 = 0.041m_0$, where m_0 is the free-electron mass. The relaxation time (ratio of the amplitudes at different values of H) $\tau\approx1.5\times10^{-12}$ s was also determined by analyzing the SdH oscillations. The parameters obtained make it possible to calculate the electron mobility in a channel $\mu = 6\times10^4$ cm^2/(V·s) and the resistivity of a 2D channel $\rho_\square = 83\ \Omega$. From these data it is possible to estimate the resistance of the network consisting of 2D channels (along which current flows) in a $6\times1.5\times0.5$ mm^3 sample with an average block size of 200 μm. Assuming that the blocks in the sample are cubic, the resistance of a such a network equals 110 Ω, which is comparable to the volume resistance 50 Ω of the sample. It is obvious that the resistance of the network depends strongly on the average block size. As the latter quantity decreases, the resistance of the network also decreases, since the number of 2D channels connected in parallel increases. For example, if the characteristic block size is 100 μm, then the resistance of a network consisting of 2D channels will equal 39 Ω.

A real sample is not such an ideal model with cubic blocks. The network consisting of the block boundaries comprises a structure consisting of flat channels with joints and random discontinuities of the planes. The conductivity of such a structure is described by percolation theory. This explains the static character in the observation of the anomalous properties of CMT crystals for different samples as well as the dependence of these properties on the geometric dimensions, as was observed in Ref. 20. As the thickness of the sample decreases, the three-dimensional network transforms into a two-dimensional network. Since the critical exponent of the appearance of a connected conducting cluster is higher in the 3D case than in the 2D case,[21] as the dimensions of the sample decrease, a discontinuity can appear in a conducting cluster. As a result, the conductivity can decrease abruptly[20] or it can change from *n*- into *p*-type or vice versa.

4. PHOTOTHERMOMAGNETIC EFFECT IN 2D CHANNELS

Two-dimensional channels in CMT crystals can be observed and investigated not only according to the SdH oscillations but also by a different, independent method—according to oscillations of the photothermomagnetic (PTM) emf.

Let microwave radiation be incident on the top boundary of a thin layer in manner so that the wave vector **k** is parallel to the *z* axis (see Fig. 4). The damping of the electromagnetic wave in the sample results in the appearance of a gradient $\nabla_z\theta$ of the electron temperature in the 2D channels. If the magnetic field **H** is directed perpendicular to the plane of a 2D channel and therefore also to the gradient of the electron temperature, then a photothermomagnetic field E_y and a corresponding emf appear in a direction perpendicular to $\nabla_z\theta$ and **H**.[22] Physically, this is the Nernst–Ettingshausen effect on hot electrons. Just as in the case of the SdH oscillations, a random orientation of the channels in the *xy* plane (the angle φ in Fig. 4) decreases the amplitude of the oscillations by a factor of $\sqrt{2\pi\varepsilon_F/\hbar\omega_c}$. The oscillations of the PTM emf are of the same nature as the SdH oscillations. However, in contrast to the latter, the PTM emf does not have a constant component (at $H=0$ the PTM emf likewise equals zero). For this reason, the PTM effect is a more sensitive method for investigating the electronic properties of a crystal.

The experimental thin sample of *n*-$Cd_xHG_{1-x}Te$, cut into disks with $x=0.185$, was inserted into a waveguide in a manner so that the wave vector **k** of the electromagnetic wave was oriented perpendicular to the surface of the thin layer (see Fig. 4). The frequency of the incident radiation was $f=136$ GHz and the power $P\simeq10$ mV. The sample was irradiated in a pulsed regime in order to avoid heating the crystal lattice of the sample. Figure 6 shows the photother-

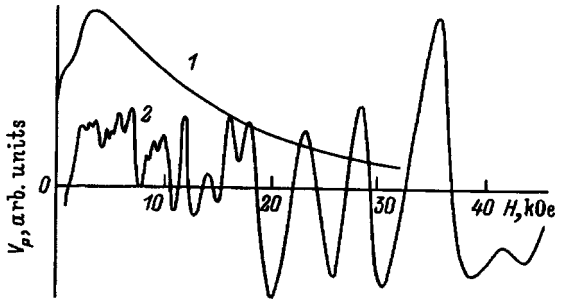

FIG. 6. Photothermomagnetic emf V_p versus magnetic field H for $Cd_xHg_{1-x}Te$ samples: *1*—bulk, *2*—thin layer with 2D channels. Layer thickness 65 μm, $x=0.185$, $T=4.2$ K.

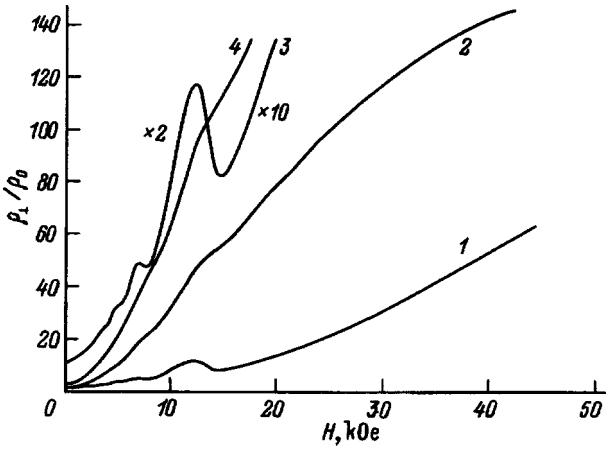

FIG. 7. Transverse magnetoresistance $\rho_\perp$ versus magnetic field H for a thin layer of $Cd_xHg_{1-x}Te$ with 3D channels for magnetic field orientations **H** relative to the direction of the normal **n** to the plane of the layer: *1, 3*—$\mathbf{H}\perp\mathbf{n}$; *2, 4*—$\mathbf{H}\parallel\mathbf{n}$. Curves *3* and *4*—initial sections of the curves *1* and *2*, respectively. Layer thickness 100 μm, $x=0.13$, $n=2.1\times10^{15}$ cm^{-3}, $m=5.4\times10^{-2}m_0$, $T=4.2$ K.

momagnetic emf signal $V_P=E_y l$ versus the magnetic field (l is the length of the sample). The oscillations of V_P have the typical form for 2D systems in which electrons fill several subbands. Theoretical analysis of the photothermomagnetic effect (Nernst–Ettingshausen effect) shows[18] that the oscillations of V_P are determined by the oscillations of the derivative of the density of states of the 2D gas with respect to the Fermi energy in a magnetic field $V_p\sim\partial g/\partial\varepsilon_F\approx g_0\sin(2\pi\varepsilon_F/\hbar\omega_c)$. The oscillations of V_P in Fig. 6 are more informative than curve *2* in Fig. 3. This makes it possible to determine the electron density in all subbands. Using Eq. (2), we find the electron density in the 2D channels in the ground and three excited subbands: $n_g=0.7n_s$, $n_1=0.19n_s$, $n_2=0.07n_s$, and $n_3=0.04n_s$, where $n_s=2.7\times10^{12}$ cm^{-2} is the total surface density of electrons.

Thus, the existence of 2D channels can be confirmed independently by investigating the PTM emf.

5. THREE-DIMENSIONAL CHANNELS AT THE BLOCK BOUNDARIES

In more perfect $Cd_xHg_{1-x}Te$ crystals, not only are fewer small-angle boundaries observed but the disorientation angle between neighboring blocks is also smaller. The depth of the potential well, which determines the character of the localization of electrons at the block boundary, depends on many parameters that characterize the dislocation structure of the boundary and the corresponding Cottrell atmosphere.[23] However, the main parameter is the disorientation angle between neighboring blocks forming a boundary. The depth and width of the potential well increase with the disorientation angle between the blocks.[12] This gives rise to a variance in the parameters of the potential wells. This results, first and foremost, in the broadening of the SdH oscillations in the 2D channels and, second, in the fact that for small disorientation angles (the most perfect crystals) the depths of the potential wells may not be sufficient for a 2D gas to form. In this case enriched three-dimensional conduction channels will arise along the block boundaries. The width of a channel depends on the majority carrier density in the semiconductor, the disorientation angle between the blocks, and the degree of filling of the unsaturated bonds of edge dislocations, forming the block boundaries. In view of the fact that the linear density of unsaturated bonds of dislocations is much higher than the donor density per unit length N_D, the well width can reach the size of a block.[15]

Thus, in more perfect crystals charge carriers will accumulate in the potential wells (3D channels), forming a nonuniform conducting medium. Just as in the case of 2D channels, a unique classical magnetoresistance size-effect should be expected to appear as the thickness of the sample decreases to dimensions less than the average size of the blocks. Indeed, for bulk samples the transverse magnetoresistance does not depend on the orientation of the magnetic field **H** in a plane perpendicular to the current. Magnetoresistance anisotropy arises as the sample thickness decreases to sizes less than the average block size (see Fig. 7). This is because in a thin sample an isotropic three-dimensional conducting cluster becomes a two-dimensional cluster. For **H** oriented perpendicular to the plane of the thin layer, the magnetic field will be directed perpendicular to the current in all sections of current flow; i.e., $\mathbf{H}\perp\mathbf{J}$ everywhere. However, if **H** is oriented parallel to the plane of the layer, then for an equally probable distribution of directions of the block boundaries in the plane of the film the case $\mathbf{H}\perp\mathbf{J}$ materializes in approximately half of the current flow paths and the case $\mathbf{H}\parallel\mathbf{J}$ materializes in the other half. For this reason, a magnetoresistance anisotropy $\Delta\rho_\perp/\Delta\rho_\parallel\simeq2$ will be present in strong magnetic fields, $\omega_c\tau\gg1$, as happens in the experiment (Fig. 7, curves *1* and *2*).

It should be underscored that the 3D channels forming along dislocation walls (block boundaries) possess an intrinsic conductivity anisotropy in the case of current flow along and across a dislocation wall.[12] An enriched 3D channel is shown on the section DD' in Fig. 4. The conductivity anisotropy is due to the nonuniform structure of the channel. The dislocation wall DD' separates the channel into two symmetric parts in the direction of the vector **n** (normal to the surface of the channel). The effect of such a channel structure is that the properties of the channel are isotropic in a plane perpendicular to **n**, whereas the channel is strongly

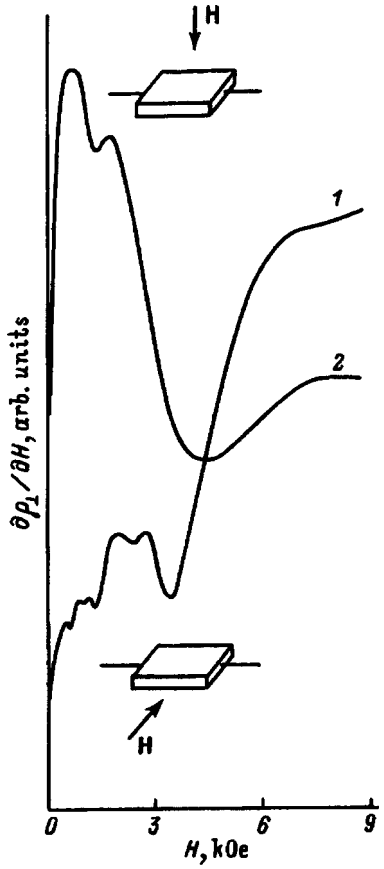

FIG. 8. Anisotropy of SdH oscillations in a thin layer of $Cd_xHg_{1-x}Te$ with 3D channels for magnetic field orientations **H** relative to the direction of the normal **n** to the plane of the layer: 1—$\mathbf{H}\perp\mathbf{n}$; 2—$\mathbf{H}\parallel\mathbf{n}$. Layer thickness 30 μm, $x=0.14$, $n=5.4\times10^{14}$ cm^{-3}, $m=4\times10^{-3}m_0$, $\mu\simeq10^6$ cm^2/(V·s), $T=4.2$ K.

nonuniform along **n** as a result of the nonuniform distribution of the potential in this direction. In addition, an electron moving along **n** crosses the dislocation wall. As a result of the indicated channel nonuniformity, a relaxation time anisotropy arises for electron motion along and across a dislocation wall (DW). The relaxation time $\tau_\perp$ for electron motion perpendicular to a DW is shorter than the relaxation time $\tau_\parallel$ for electron motion along the DW.[24] This anisotropy of τ is manifested in different values of the Dingle temperature, which determines the different broadening of the SdH oscillations in the two cases of orientation of the magnetic field $\mathbf{H}\perp\mathbf{n}$ and $\mathbf{H}\parallel\mathbf{n}$. This is clearly seen by comparing the curves *3* and *4* in Fig. 7 and the curves *1* and *2* in Fig. 8.

6. CONCLUSIONS

Our investigations show that conductivity in mosaic $Cd_xHg_{1-x}Te$ (CMT) crystals is made up of p- of n-type 3D conductivity and an additional electronic 2D or 3D conductivity along block boundaries. The 3D electronic conductivity can be substantially diminished at liquid-helium temperatures in strong magnetic fields. In crystals with volume density $n\simeq10^{14}$ cm^{-3} electron localization in the wells of the fluctuation potential appears in fields $H>1$ kOe.[25] In this case conduction will occur primarily along 2D or 3D electronic channels along the block boundaries. In a bulk sample such a structure consisting of conducting channels is isotropic with respect to the direction of the magnetic field in a plane perpendicular to the current. Anisotropy of the transport and high-frequency properties as a function of the direction of the magnetic field appears in samples with thickness less than the average block size.

In closing, we note that the conduction channels on block boundaries can strongly influence not only the transport properties of CMT crystals but also other properties, such as the photoelectric properties. Specifically, we call attention to studies of the relaxation time of photoconductivity in CMT. As note in Refs. 17 and 26, besides the usual characteristic relaxation time τ_0, photoelectrons with lifetimes 100 times longer than τ_0 were also observed. Such transitions in all probability could be associated with photoelectrons that became localized in a 2D well and then tunnel into the valence band (recombine), overcoming a substantial potential barrier of the order of ε_g, as shown by the wavy line in Fig. 2b. This barrier is the factor that substantially increases the recombination time of photoelectrons.

We express our appreciation to É. Tal'yanskiĭ for preparing the samples and for participating in the investigation of their structure.

[a)]pogrebnyak@ire.kharkov.ua; fax: (0572)44115

[1] *Narrow-Gap Semiconductors and Their Applications* [Russian translation], Mir, Moscow, 1969.
[2] R. Dornhaus and G. Nimtz, Springer Tracts in Mod. Phys. **98**, 119 (1983).
[3] I. M. Tsidilkovski, G. I. Harus, and N. G. Shelushina, Adv. Phys. **34**, 43 (1985).
[4] L. A. Bovina and V. I. Stafeev, in *The Physics of II–V Compounds* [in Russian], edited by A. N. Georgobiani and M. K. Sheĭnkman, Nauka, Moscow, 1986, p. 246.
[5] V. I. Ivanov-Omskiĭ, B. I. Ivanov, V. K. Ogorodnikov, and K. P. Smekalova, in *Proceedings of the 1st All-Union Symposium on Narrow-Gap Semiconductors and Semimetals* [in Russian], L'vov State University, L'vov, 1975, Part 3, p. 47.
[6] A. I. Elizarov, V. I. Ivanov-Omskiĭ, V. I. Korniyash, and V. A. Petryakov, Fiz. Tekh. Poluprovodn. **18**, 201 (1984)[Sov. Phys. Semicond. **18**, 125 (1984)].
[7] V. Ivanov-Omskiĭ, N. Berchenko, and A. Elizarov, Phys. Status Solidi A **103**, 11 (1987).
[8] V. A. Pogrebnyak, D. D. Khalameĭda, and V. M. Yakovenko, JETP Lett. **46**, 210 (1987).
[9] M. G. Mil'vidskiĭ and V. B. Osvenskiĭ, *Structural Defects in Semiconductor Single-Crystals* [in Russian], Metallurgiua, Moscow, 1984.
[10] K. Shinohara, R. Ueda, O. Ohtsuki, and I. Ueda, Jpn. J. Appl. Phys. **11**, 273 (1972).
[11] R. Triboulet, Rev. Phys. Appl. **12**, 123 (1977).
[12] H. F. Matare, *Defect Electronics in Semiconductors*, Wiley–Interscience Publishers, N. Y., 1971 [Russian translation, Mir, Moscow, 1974].
[13] J. Hirth and H. Ehrenreich, J. Vac. Sci. Technol. A **3**, 367 (1985).
[14] S. G. Gasan-zade, E. A. Sal'kov, and G. A. Shepel'skiĭ, Fiz. Tekh. Poluprovodn. **17**, 1913 (1983) [Sov. Phys. Semicond. **17**, 1225 (1983)].
[15] H. F. Matare, J. Appl. Phys. **56**, 2605 (1984).
[16] B. M. Vul and É. I. Zavaritskaya, Zh. Éksp. Teor. Fiz. **76**, 1089 (1979) [Sov. Phys. JETP **49**, 551 (1979)].
[17] N. L. Bazhenov, V. I. Ivanov-Omskiĭ, and V. K. Ogorodnikov, Fiz. Tekh. Poluprovodn. **18**, 1458 (1984) [Sov. Phys. Semicond. **18**, 911 (1984)].
[18] V. A. Pogrebnyak, D. Khalameida, and V. Yakovenko, Solid State Commun. **68**, 811 (1988).
[19] D. Shoenberg, *Magnetic Oscillations in Metals*, Cambridge Univ. Press., N. Y., 1984 [Russian translation, Mir, Moscow, 1986].
[20] A. I. Elizarov, V. I. Ivanov-Omskiĭ, and K. R. Kurbanov, Pim'ma Zh. Tekh. Fiz. **7**, 1089 (1981) [Sov. Tech. Phys. Lett. **7**, 466 (1981)].

[21] B. I. Shklovskiĭ and A. A. Éfros, *Electronic Properties of Doped Semiconductors* [Springer-Verlag, N. Y., 1984, Nauka, Moscow, 1979], p. 166.
[22] A. N. Vystavkin, Sh. M. Kogan, T. M. Lifshitz, and P. G. Mel'nik, Radiotekh. Élektron. **8**, 999 (1963).
[23] A. Cottrell, *Dislocation and Plastic Flow in Crystals*, Clarendon Press, Oxford, 1951 [Russian translation, Metallurgizdat, Moscow, 1968].
[24] P. N. Gorleĭ, L. A. Korachevtseva, K. R. Kurbatov, N. Ya. Kushnir, and É. A. Malovichko, Ukr. Fiz. Zh. **38**, 1067 (1993).
[25] I. M. Tsidil'kovskiĭ, Usp. Fiz. Nauk **152**, 583 (1987) [Sov. Phys. Usp. **30**, 676 (1987)].
[26] S. G. Gasan-zade, I. P. Zhad'ko, É. A. Zinchenko, V. A. Romanov, E. A. Sal'kov, and G. A. Shepel'skiĭ, Fiz. Tekh. Poluprovodn. **23**, 85 (1989) [Sov. Phys. Semicond. **23**, 53 (1989)].

Translated by M. E. Alferieff

Preparation and photosensitivity of heterostructures based on anodized silicon carbide

A. A. Lebedev, A. A. Lebedev, and Yu. V. Rud'

A. F. Ioffe Physicotechnical Institute, Russian Academy of Sciences, 194021 St. Petersburg, Russia

V. Yu. Rud'

St. Petersburg State Technical University, 195251 St. Petersburg, Russia
(Submitted February 24, 1997; accepted for publication March 5, 1997)
Fiz. Tekh. Poluprovodn. **32**, 326–328 (March 1998)

Heterojunctions were obained by mechanical clamping of anodized 6*H*-SiC wafers to wafers of layered III–VI semiconductors (InSe and GaSe) at 300 K. On account of the high degree of perfection of the cleavage surfaces, a strong and quite perfect electrical contact is formed. The photo-emf spectrum of the heterojunctions has the form of a wide band. The long-wavelength edge of this band is due to the narrow-gap component and the short-wavelength edge is due to the narrow-gap component and the short-wavelength edge is due to absorption in SiC. © *1998 American Institute of Physics.* [S1063-7826(98)02403-X]

During a study of the possibilities of anodic etching of silicon carbide it was discovered that under certain conditions layers cleaving in the (0001) plane in the form of thin wafers with mirror-smooth surfaces and lattice parameters corresponding to the initial material are formed on the surface of 6*H*-SiC wafers.[1] However, even the first investigations showed that the physical properties of these layers are different from those of the initial bulk crystal. Specifically, it was established in Ref. 2 that, just as in the case of porous silicon,[3] layers obtained in this manner (layers of anodized silicon carbide) are characterized by a reproducible increase (by up to a factor of 30) in the efficiency of photoluminescence without large changes in its spectral distribution. This can be used in devices for short-wavelength luminescence electronics. In the present paper we report the results of the first investigations of the photosensitivity of heterostructures produced by joining via an optical contact wafers of anodized SiC with the cleavage surfaces of layered III–VI semiconductors — InSe and GaSe.

Wafers of 6*H*-SiC, grown by the Lely method,[4] with (0001) crystalline orientation and free electron density of the order of 10^{18} cm^{-3} at $T=300$ K were used to obtain the anodized silicon carbide. The initial crystals possessed a high hardness typical for SiC; scratching with corundum did not leave any tracks on their surface. After these crystals were etched[1] in the mixture $2HF + 3C_2H_5OH + 0.1HNO_3$ (the volume fractions are indicated) for 40–120 min with current densities 20–120 mA/cm^2 at room temperature, a gold-colored region formed on their surface. In some cases separation of the anodized layer was observed and transparent colorless wafers floated up to the surface of the etchant. In most cases, however, after etching wafers with perfect mirror faces and average dimensions of $4\times4\times0.05$ mm^3 could be cleaved from the surface of the bulk crystal with a metal needle. The thicknesses of these wafers were further decreased by splitting them under a microscope with a sharp blade. In this manner we were able to obtain a wafer down to 10 μm thick withno microcleavages anywhere on the surface. The preparation of silicon carbide wafers with very perfect surfaces served as a prerequisite for studying the possibility of producing heterostructures by putting these wafers in direct contact with layered III–VI semiconductors — InSe and GaSe. For these substances, the property of forming perfect cleavage surfaces has been known for a long time and is attributed to the fact that van-der-Waals forces act between the layers.[5] This made it possible to obtain thin wafers with perfect (0001) surfaces for heterostructures of InSe and GaSe crystals.[6,7]

Electrically homogeneous *n*-InSe single crystals (resistivity perpendicular to the layers $\rho_\perp \simeq 10-10^3\ \Omega\cdot$cm, electron density $n\simeq 10^{13}-10^{14}$ cm^{-3} at 300 K) and *n*-GaSe ($\rho_\perp \simeq 10^4-10^5\ \Omega\cdot$cm, electron density $n\simeq 10^{13}$ cm^{-3} at 300 K), which were specially not doped and were grown by the method of directed crystallization from nearly stoichiometric melts with a vertical arrangement of the quartz crucible, were used to produce the heterostructures. The wafers, obtained by cleaving in air, with mirror (0001) surfaces were 20–50 μm thick. To produce heterostructures from the III–VI material and SiC, each wafer was fitted with an ohmic contact on one side while the other side was used to make a contact with another wafer. A special holder was used to obtain uniform mechanical clamping of the wafers to one another over the entire area. After the pressure was removed, the InSe or GaSe wafer remained in close contact with SiC and approximately the same force as that for cleaving the III–VI wafers themselves from the ingot was required to separate them. This shows that quite stable InSe/SiC and GaSe/SiC contacts were obtained. Crystallographic polarity had no effect on the procedure for forming such a contact.

A photovoltaic effect is produced when the heterostructures are illuminated. The effect is stronger when the SiC side is illuminated. The sign of the photovoltage does not depend on either the energy of the incident photons or the location of the light probe (1 mm in diameter) on the surface of the structures. This shows that the photoeffect is due to the fact that in such structures there exists only one active region separating the nonequilibrium carriers. To determine the relative quantum efficiency η of the structures the photovoltage was measured on the linear section of the voltage–illumination characteristic and the values obtained were normalized to the number of incident photons. Typical spectral dependences $\eta(h\nu)$ at 300 K with SiC side illumination are

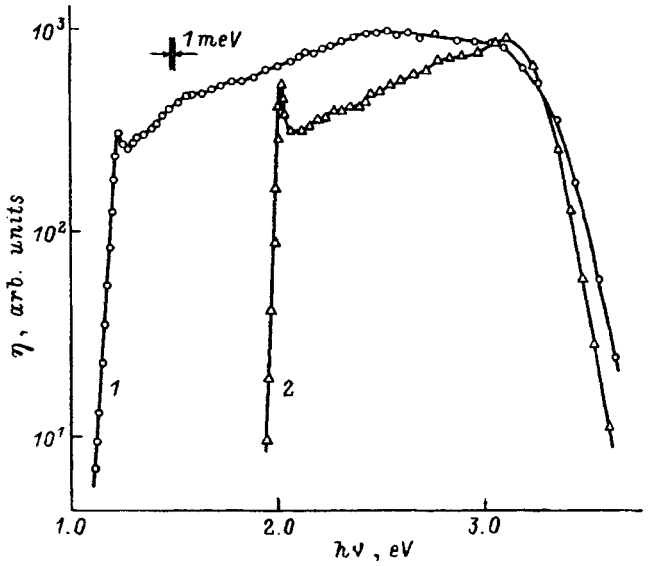

FIG. 1. Spectral dependence of the relative photoconversion quantum efficiency of InSe/SiC (*1*) and GaSe/SiC (*2*) heterostructures. The structures were illuminated with unpolarized radiation on the SiC side. Wafer thicknesses (in mm): InSe — 0.05, GaSe — 0.02, SiC — 0.015 (*1*) and 0.02 (*2*).

presented in Fig. 1, while some parameters of the structure are presented in Table I. The main characteristics observed in the investigations can be summarized as follows.

As follows from Fig. 1, a wide-band photovoltaic effect appears when the heterostructures are illuminated from the SiC side.[8] The exponential behavior of $\eta(h\nu)$, the spectral position of the long-wavelength photosensitivity edge, and the slope $s=d(\ln\eta)/d(h\nu)$ of the edge can be attributed to direct interband transitions in the narrow-gap components of the heterostructures. The presence of a narrow peak on the long-wavelength edge of the spectral dependences of η for both heterostructures is interesting. Such peaks have been observed in the photosensitivity spectra of InSe and GaSe and have been attributed to excitonic absorption.[9] The fact that excitonic peaks appear in the photosensitivity spectra of the heterostructures itself shows that putting layered III–VI semiconductors into mechanical contact with SiC does not result in any appreciable damage to their structures near the heteroboundary. Therefore, there are grounds for believing that the well-known conditions for the formation of perfect heterojunctions can be substantially ''weakened'' by putting semiconductors with high quality surfaces in contact with one another,[10] while the differences in the type and parameters of the crystal lattice is not critical for producing efficient phototransducers.

TABLE I. Photoelectric parameters of heterostructures based on anodized silicon carbide wafers at 300 K. .

	Δa, %	Δc,%	s, eV^{-1}	S_u^m, V/W	$\delta_{1/2}$, eV	$h\nu_m$, eV
InSe/SiC	27	−11.2	40	10	1.7	2.2–2.9
GaSe/SiC	19.9	−5.3	115	100	0.8	3.1

Note. $\Delta a,\Delta c$ — mismatch of the lattice parameters for conditions of epitaxial formation of a heteroboundaryaccording to Ref. 8; $h\nu_m$ — energy of maximum photosensitivity

Wide-band photosensitivity obtains when the heterostructures are illuminated on the SiC side. This indicates the existence of a quite perfect, with respect to recombination processes, heteroboundary. The width $\delta_{1/2}$ at half-height of the photosensitivity spectra of the heterostructures is larger in InSe/SiC structures (see Fig. 1 and Table I) and smaller in GaSe/SiC, where the band gap of the narrow-gap component is larger. The maximum value of η is obtained at the fundamental absorption depth of III–VI crystals. The short-wavelength dropoff of η in both heterostructures starts at $h\nu\simeq 3.1$ eV. This dropoff could be due to an increase in the optical absorption in the bulk of the SiC wafer. As one can see from the figure, the photoconversion efficiency of the heterostructures obtained drops practically to zero when the photon energy reaches ~ 3.7 eV. This quantity can be viewed as an estimate, obtained for the first time, of the band gap for SiC wafers obtained by anodized etching.

Since directed deformations can arise in the SiC anodized layers when the layers are formed, we also performed polarization measurements of the photosensitivity of heterostructures illuminated in a direction normal to the plane of the SiC wafers. Natural photopleochroism was not observed in this case. This is because the linearly polarized radiation propagated along the isotropic direction of the media in contact and it attests to the absence of large deformations in the plane of the layers.[11]

In summary, putting SiC wafers in direct optical contact with III–VI semiconductors makes it possible to obtain a wide-band photovoltaic effect with maximum sensitivity $S_u^m\simeq 10-100$ V/W at 300 K. The long-wavelength photosensitivity edge of these heterostructures is determined by direct optical transitions in the III–VI crystals, while the short-wavelength edge is determined by the band gap of the anodized silicon carbide.

This work was performed as part of the program ''Physics of solid-state of nanostructures'' (Project No. 1-079/5) and with the partial support of the University of Arizona (USA).

[1] A. A. Lebedev, A. A. Lebedev, V. Yu. Rud', Yu. V. Rud', and A. M. Strel'chuk, Pis'ma Zh. Tekh. Fiz. **22**, 59 (1996) [Tech. Phys. Lett. **22**, 715 (1996)].
[2] A. A. Lebedev, A. A. Lebedev, and Yu. V. Rud', Pis'ma Zh. Tekh. Fiz. **21**, 64 (1995) [Tech. Phys. Lett. **22**, 117 (1995)].
[3] L. T. Canham, Appl. Phys. Lett. **57**, 1046 (1990).
[4] J. A. Lely, Ber. Deut. Ceram. Soc. **32**, 229 (1955).
[5] V. L. Bakumenko and V. F. Chishko, Fiz. Tekh. Poluprovodn. **11**, 2000 (1977) [Sov. Phys. Semicond. **11**, 1171 (1977)].
[6] V. L. Bakumenko, Z. D. Kovalyuk, L. N. Kurbatov, V. G. Tagiev, and V. F. Chishko, Fiz. Tekh. Poluprovodn. **12**, 374 (1978) [Sov. Phys. Semicond. **12**, 216 (1978)].
[7] N. N. Konstantinova, I. A. Magomedov, V. Yu. Rud', and Yu. V. Rud', Fiz. Tekh. Poluprovodn. **26**, 558 (1992) [Sov. Phys. Semicond. **26**, 317 (1992)].
[8] *Reference Data on the Physical and Chemical Properties of Semiconductor Materials* [in Russian], Nauka, Moscow, 1978.
[9] N. M. Metkhiev, *Author's Abstract of Doctoral Dissertation* [in Russian], Institute of Physics, Azerbaĭdzhan Academy of Sciences, Baku, 1991.
[10] A. G. Milnes and D. L. Feucht, *Heterojunctions and Metal–Semiconductor Junctions*, Academic Press, N. Y., 1972.
[11] Yu. V. Rud', Izv. Vyssh. Uchebn. Zaved. Fiz. **29**, 68 (1986).

Translated by M. E. Alferieff

Properties of periodic α-Si:H/a-SiN$_x$:H structures obtained by nitridization of amorphous-silicon layers

D. I. Bilenko, O. Ya. Belobrovaya, Yu. N. Galishnikova, É. A. Zharkova, N. P. Kazanova, O. Yu. Koldobanova, and E. I. Khasina

Scientific-Research Institute of Mechanics and Physics, N. G. Chernyshevskiĭ Saratov State University, 410026 Saratov, Russia

(Submitted July 18, 1996; accepted for publication July 3, 1997)
Fiz. Tekh. Poluprovodn. **32**, 329–333 (March 1998)

The kinetics of nitridization of a-Si:H layers, the properties of the structures that are formed and a-Si:H in them have been investigated. The changes occurring in the resistance of the a-Si:H layers in the course of nitridization are described in terms of the competition between doping, transport, and change in the thickness of the remaining a-Si:H layer. The experimental data on the band spectrum of superlattices with a-Si:H and a-SiN$_x$:H layer thicknesses $\sim$35 Å and $\sim$5 Å, respectively, are in agreement with calculations in a model of interacting quantum wells with $m^*=(0.36\pm0.1)m_0$. Comparison of the properties of superlattices obtained by deposition of successive layers and nitridization of the a-Si:H layers showed that the latter can have a higher ''structural perfection.'' © *1998 American Institute of Physics.* [S1063-7826(98)00903-X]

The properties of periodic structures are determined not only by the composition and thickness of the layers but also by the properties of the interfaces between the layers.[1–4] Ordinarily, the methods used to produce periodic structures are based on successive deposition of layers of different materials.[5,6] It is of interest to look for and study new possibilities for producing periodic structures by obtaining a new material by modification of the composition of a previously deposited layer. This could be especially helpful for obtaining structures with low dimension, specifically, superlattices (SLs). The possibility of obtaining a-Si:H/a-SiN$_x$:H multilayer structures by layerwise nitridization of a-Si:H in a NH_3 plasma has been demonstrated in Ref. 7 . However, the kinetics of nitridized-layer formation as well as the optical, electric, and photoelectric properties of structures with such layers have virtually been ignored.

In the present paper we report the results of an experimental study of the processes leading to the formation of and the properties of nitridized a-Si:H layers, as well as periodic structures of the type a-Si:H/a-SiN$_x$:H obtained by layerwise partial nitridization of a-Si:H.

The structures were fabricated by alternating plasma-chemical deposition of amorphous silicon followed by modification of the silicon in the plasma of highly pure ammonia gas. The substrate temperature during nitridization was of the order of 300–320 °C, the ammonia flow rate was equal to 2 liters/h, and the pressure in the reaction chamber was equal to 25 Pa. The microwave power was varied from 15 to 30 W. Helium served as a diluent gas. The nitridization time was varied from 1 to 60 min, and 10 to 22 pairs of the layers were produced. As substrates we used single-crystal silicon wafers and optically polished quartz and glass, coated with plasma-chemically deposited a-SiN$_x$:H, with comb-shaped electrodes consisting of deposited layers of chromium. The samples for investigating the room-temperature electric and photoelectric properties possessed additional Al and Ni contacts deposited successively in a comb-shaped pattern on top of the layers or with overlapping in specially produced channels passing through the entire structure.

The less than 50-Å thickness of the amorphous-silicon layers in the periodic structures was found from the deposition rate which in turn was determined, while growing layers of the order of 400–1200 Å, from *in situ* measurements of the a-Si:H thickness according to the interference of $\lambda=0.6328$ μm laser radiation. The accuracy of this method was confirmed by studying the a-Si:H deposition kinetics and by the fact that the layer thicknesses in the lattices were virtually identical (to within ±2 Å) at the level 80–130 Å, as determined from the deposition rate and from x-ray analysis by the total external reflection method.

The optical properties (spectral dependences of the refractive index n_s, absorption index χ_s, and the absorption coefficient α), the parameters of the band structure of the a-Si:H layers, and the thickness d_N of the nitridized layer obtained in multilayer periodic structures were determined in the region of the fundamental absorption band according to the spectral dependences of the reflection and transmission coefficients.

The problem of determining n_s and χ_s was complicated by the fact that in order to find them it is necessary to know the insulating layer thicknesses d_N, which in the experimental structures can equal several angstroms.[7] For this purpose, a procedure based on a computational experiment using the direct-optimization method was developed.[8] The sum of the squared deviations of the experimentally obtained values of the reflection and transmission coefficients from the computed values was chosen as the target function. The search region for the parameter d_N was determined from additional

physical considerations imposed on the quantities n_s and χ_s in the short-wavelength region of the fundamental absorption band.

This method makes it possible to determine the refractive and absorption indices of a-Si:H layers and the thickness of the nitridized layer in periodic structures to within $\pm 5\%$ and ± 1 Å, respectively, and to correct the value obtained for the thickness of the a-Si:H layer from the deposition rate. The discrepancies between the a-Si:H layer thicknesses determined in the course of the process and on the basis of calculations of the optical properties were equal to several angstroms.

The band structure parameters of the a-Si:H layers in lattices with nitridized layers—the band gap E_g and the Urbach parameter E_0 characterizing the smearing of the band edges—were calculated from the spectral dependences obtained for the refractive index and the absorption coefficient. The density of SiH, SiN, NH, and SiO bonds and the total concentration C_H of bound hydrogen in structures with a-Si:H layer thickness greater than 1000 Å were determined from the corresponding IR absorption bands, taking into account the absorption cross sections for the corresponding bonds.[9] The hydrogen concentration for structures with a-Si:H layer thicknesses less than 1000 Å was found from the dependence $E_g(C_H)$ obtained in Ref. 10 .

The time dependence of the resistance of a structure was measured in the course of the formation of the structures. Measurements of the resistance R were performed after a definite time intervals during deposition and nitridization of the a-Si:H layers with the microwave generator switched off. For the arrangement employed for the contacts on the substrate, the resistance in the plane of the structure is determined not only by the resistance along the a-Si:H layers but also by the resistance R_{N} of the nitridized silicon layers in the transverse direction. The parameters of the multilayer periodic structure—the height $e\varphi_0$ of the potential barrier at the boundary with the substrate, the conductivity σ_0 of the structure with an infinitely large number of pairs, the effective thickness x_N of the depletion layer and the nitridized layers, and the resistance R_{N}—were found from the dependence of the resistance R of the structure on the number M of pairs of layers, using the conductivity model that takes into account the transport doping and a recurrence relation which relates R and the resistances of the a-Si:H layers and R_{N}.[11]

The field and time dependences of the dark conductivity and photoconductivity, according to which the ratio $\sigma_{d,\mathrm{ph}}/\sigma_d$ and the residual photoconductivity (RPC) were determined, were measured on the finished structures in which the electrodes short-circuited the a-Si:H layers. The quantity $Q=(\sigma_{p,\mathrm{ph}}-\sigma_{d0})/\sigma_{d0}$ was used as a measure of the RPC; here, σ_{d0} is the dark conductivity prior to photoexcitation and $\sigma_{d,\mathrm{ph}}$ is the dark conductivity after photoexcitation when the long-time stable value is reached.[10] The radiation used for photoexcitation was close to the radiation from an AM-1 type source.

New information about the nitridization kinetics and the properties of the nitridized silicon layers was obtained by conducting the processes in a controlled manner and by investigating the prepared layers.

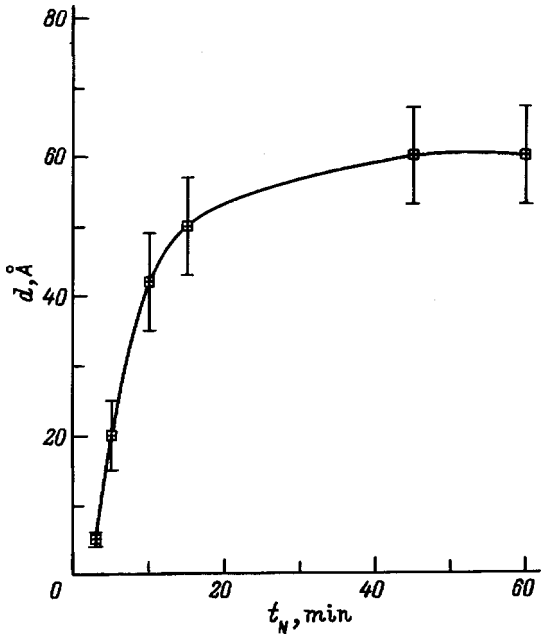

FIG. 1. Thickness of a-SiN_x:H layer formed versus nitridization time.

1. The kinetics of nitridization of amorphous silicon can be approximated at the initial stage by a parabolic law with an initial delay time (Fig. 1). We obtained the empirical relation

$$d_{\mathrm{N}}^2 = 210 t_{\mathrm{N}} - 600, \tag{1}$$

where d_{N} is the thickness of the a-SiN_x:H layer (in Å), and t_{N} is the nitridization time (in min). The relation (1) holds for silicon nitride thicknesses less than 50 Å, which corresponds to a nitridization time of less than 15 min. The relative error in describing the kinetics by the relation (1) in this range is less than 10%. Subsequently, the rate of nitridization of amorphous silicon decreases and the thickness of the silicon nitride layer formed saturates.

The data obtained attest to the fact that the rate of nitridization of the amorphous silicon is determined by the rate of mass transfer of nitrogen-containing particles or the initial material in the volume of the nitride layer formed. As it grows, the silicon nitride film becomes an obstacle to the motion of the particles, and when a definite thickness is reached the nitridization process virtually stops. The nature of the time delay in the formation of silicon nitride in the process of nitridization is still not clear.

2. It was established that nitridization can change the properties of the remaining layer of amorphous silicon. These changes are all the greater, the more prolonged nitridization and the smaller the thickness of the remaining layer are. This is manifested in a number of properties associated with disordering and losses of hydrogen. The a-Si:H layer thicknesses prior to nitridization varied from 70 to 300 Å. As the nitridization time increases, all properties of a-Si:H change: The amplitude of the maximum of the reflection coefficient decreases in the region of interband transitions and in the process the reflection maximum shifts into the

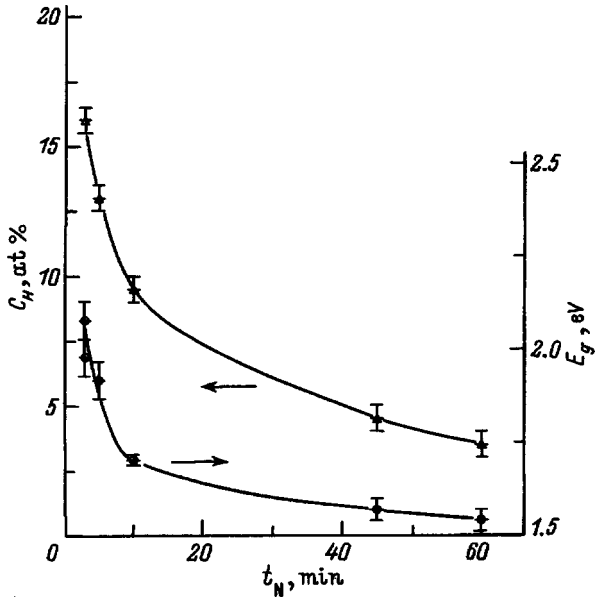

FIG. 2. Hydrogen concentration and band gap in the *a*-Si:H layer remaining after nitridization versus nitridization time.

region of low frequencies; the parameter E_0 increases and E_g decreases. The dependence $E_g(t_N)$ is displayed in Fig. 2, which also gives the dependence of the hydrogen concentration in the *a*-Si:H layers on the nitridization time. As one can see, C_H in *a*-Si:H decreases from 15 to 3–4% after 45 minutes of nitridization, and the properties of the material approach those of nonhydrated amorphous silicon. Loss of hydrogen leads to disordering of the *a*-Si:H network. This is manifested as an increase in E_0 (up to $\sim$0.22 eV) and, correspondingly, an increase in the concentration of broken bonds.

3. A characteristic feature of the time dependence of the resistance R of the *a*-Si:H layer measured *in situ* in the process of nitridization is that the resistance passes through a minimum, increases, and then saturates (Fig. 3). A sharp decrease (by 1–2 orders of magnitude) of the resistance of the structure is observed when a second *a*-Si:H layer is deposited on the nitridized first layer.

One possible explanation of the observed minimum of the resistance of the structure accompanying nitridization could be competition between two phenomena: a decrease of the resistance of the *a*-Si:H layer as a result of doping of the layer by transport from the silicon nitride formed[5] and an increase of the resistance of the *a*-Si:H layer as a result of a decrease of the layer thickness accompanying conversion of part of the *a*-Si:H layer into silicon nitride. Taking this factor into account and using the expression for the conductivity of a periodic structure,[5,11] we can represent the time dependence of the conductivity σ of one *a*-Si:H layer in the course of nitridization of the layer in the form

$$\sigma=\sigma_0\exp(-e\varphi_0/kT)\times\exp\left(-\frac{d_N^{1/2}(t_N)[d_n(t_N)+d_s(t_N)\varepsilon_N/\varepsilon_s]^{1/2}}{x_N}\right),$$

$$d_s(t_N)=d_{s0}-d_N(t_N), \qquad (2)$$

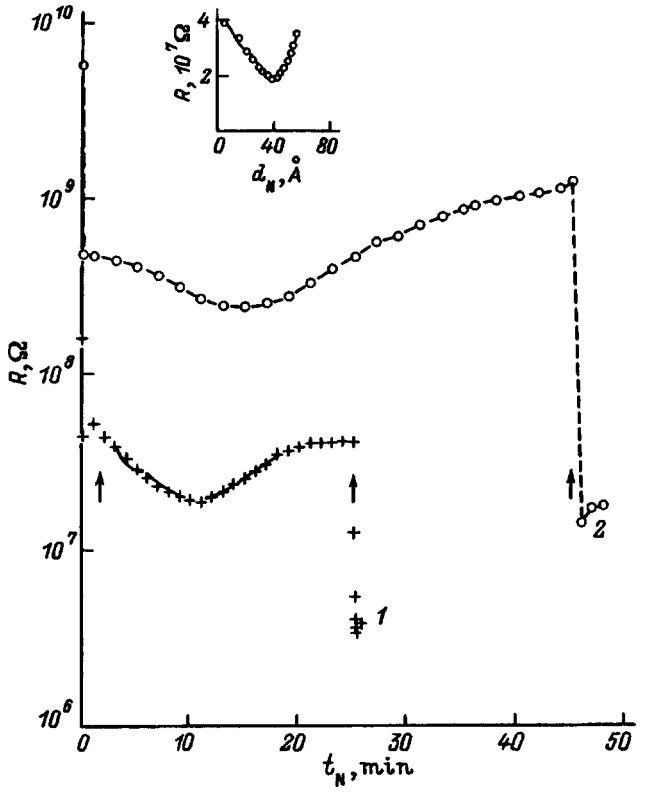

FIG. 3. Resistance of *a*-Si:H/nitridized layer/*a*-Si:H structure versus time in the process of deposition and nitridization of the layers. Thicknesses d_{s0} of the first and second *a*-Si:H layers: *1*—70 Å/300 Å; *2*—70 Å/1600 Å. The arrows mark the start and end of nitridization. Inset: Resistance of a *a*-Si:H/nitridized layer bilayer structure versus d_N according to (1); the solid line was computed.

where $d_s(t_N)$ and $d_N(t_N)$ are the thicknesses of the *a*-Si:H layers and silicon nitride during nitridization in accordance with Eq. (1), d_{s0} is the initial thickness of the *a*-Si:H layer prior to nitridization, and ε_N and ε_s are the dielectric constants of the silicon nitride and amorphous silicon.

The relations (1) and (2) made it possible to determine the values of the parameters $e\varphi_0$, x_N, and σ_0 from the experimental time dependences of the resistance of *a*-Si:H in the course of its nitridization. The calculation was performed according to the least-squares criterion for the relative deviations of the experimental values of the resistance from the computed values with the values of the desired parameters varying over a wide range. Figure 3 shows together with the experimental time dependences the computed time dependences of the resistance of *a*-Si:H in the course of nitridization. The inset in Fig. 3 shows the dependence of the resistance of a two-layer structure on the thickness of the growing layer of silicon nitride. The rms relative deviations of the experimental values from the computed values do not exceed 9.5%, which attests to a good correspondence of the model adopted to the real process. Thus, the following values were obtained for the parameters of the structure: $e\varphi_0=(0.20\pm0.01)$ eV, $x_N=(50\pm1)$ Å, and $\sigma_0=(8.6\pm0.1)\times10^{-3}\ \Omega^{-1}\cdot\mathrm{cm}^{-1}$.

4. The room-temperature data showed that in *a*-Si:H/*a*-SiN_x:H bilayer structures perfect boundaries were obtained between the layers with nitridization durations for the

first a-Si:H layer not exceeding 10 min. In these structures the average resistivity $\rho_T \simeq 7\times10^8\ \Omega\cdot$cm, the photoconductivity $\sigma_{\rm ph}/\sigma_d \simeq 10^5$ with an AM=1 source, and the residual photoconductivity is virtually zero ($Q \simeq 0.01$). Increasing the nitridization time of the first a-Si:H layer probably results in disordering of the boundary and changes the properties of the material. This is manifested as an increase in the residual photoconductivity to $Q=1-2$ and agrees with the increase of the Urbach parameter $E_0 \simeq 0.2-0.25$ eV compared with $E_0 \simeq 0.1-0.15$ with $t_{\rm N} \simeq 3$ min.

Studying the nitridization kinetics of a-Si:H layers made it possible to choose regimes for obtaining multilayer periodic structures with layerwise partial nitridization of a-Si:H.

Investigations of the optical and electrical properties of the periodic structures in the course of and after the formation of the structures allowed us to draw the following conclusions:

1. The thickness of the nitridized interlayers in periodic structures as determined from the transmission and reflection spectra equals 5–6 Å with 3-min nitridization.

2. The optical properties of multilayer periodic structures with a-Si:H layer thickness less than 40 Å are described by the model of a superlattice with interacting quantum wells. The computational results obtained using models of isolated quantum wells taking into account the collective interaction by the Kronig–Penney method[11–13] were compared with the experimental data for structures with dielectric barrier thicknesses 5–10 Å and a-Si:H layer thicknesses 35 Å. Kinks corresponding to transition energies E_i and characteristic of superlattices are observed in the experimental curves of the absorption coefficient α, described by a piecewise-linear function, in the coordinates $\alpha\cdot\hbar\omega$ versus $\hbar\omega$.[14] Very good agreement between the calculations and the experimental data was obtained by varying the effective mass m^* and the barrier height V. For $m^*=(0.36\pm0.1)m_0$ and $V=(1.20\pm0.05)$ eV the computed values of E_i are 1.98, 2.3, and 2.6 eV and the experimental values are 1.98, 2.26, and 2.64 eV, respectively.

3. Transport doping, manifested as a change in the resistance *in situ* (Fig. 4), is observed in a-Si:H/a-SiN$_x$:H lattices with nitridized amorphous-silicon layers $(\mathrm{SL})_N$, just as in lattices with plasma-chemical deposition of the layers $(\mathrm{SL})_p$ (Ref. 6). Upon formation of a-Si:Ha-SiN$_x$:H superlattices in which the silicon nitride layers were obtained by nitridization of a-Si:H or plasma-chemical deposition of the layers, the resistance of the structure decreases monotonically (Fig. 4, curves *1* and *4*). When the silicon nitride layers are produced alternately by plasma-chemical deposition and nitridization of a-Si:H, nonmonotonic variation of the resistance of the growing structure arises (Fig. 4, curves *2* and *3*). This could be due to the fact that the combination of different methods of obtaining silicon nitride in the superlattice results in the appearance of a different built-in-field asymmetry on neighboring interfaces than in the case of identical layers of silicon nitride. As we showed earlier,[4] a change in the asymmetry of the interface charge can result in a substantial (by several orders of magnitude) change in the resistance of the a-Si:H layers. In addition, the transport doping effects change and the thickness of the a-Si:H layer decreases as the

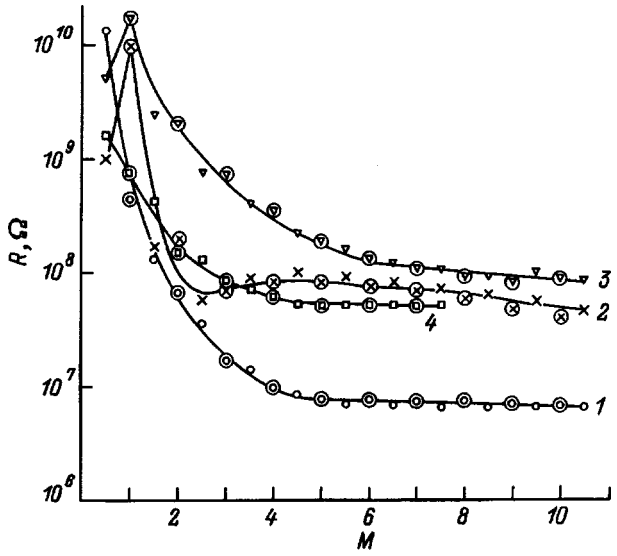

FIG. 4. Resistance of a-Si:H/a-SiN$_x$:H superlattices versus the number of pairs of layers in the process of formation of the layers. The circles mark the a-SiN$_x$:H layers. Structures: *1*—quartz/$(\mathrm{CL})_{\rm N}$ ($d_s=55$ Å, $d_{\rm N}=5$ Å); *2*—glass/$(a\text{-SiN}_x\text{:H})_p/(\mathrm{SL})_{\rm N}$ ($d_s=35$ Å, $d_{\rm N}=5$ Å); *3*—quartz/$(a\text{-SiN}_x\text{:H})_p/(\mathrm{CL})_{\rm N}$ ($d_s=35$ Å, $d_{\rm N}=5$ Å); *4*—quartz/$(\mathrm{CL})_p$ ($d_s=30$ Å, $d_{\rm N}=50$ Å).

layer is nitridized. These phenomena collectively could be responsible for the resistance jumps observed at the start of growth.

4. The resistance of the structure measured after each process of growth and nitridization of the a-Si:H layer made it possible to determine the parameters of the structure. The following sets of parameters at the deposition temperature with nitridization over the first six pairs of layers were obtained for the structures whose dependences $R(M)$ are presented in Fig. 4: $e\varphi_0=1.02$, 0.84, 0.45 eV; $\sigma_0=1.2\times10^{-2}$, 2.2×10^{-2}, 2×10^{-3} $\Omega^{-1}\cdot\mathrm{cm}^{-1}$; $x_{\rm N}=12$, 11, 19 Å; $R_{\rm N}=5.3\times10^5$, 1.6×10^7, and $5.2\times10^6\ \Omega$. The rms relative deviations of the experimental values of R from the values computed using these parameters equal 4–9%. The conductivity of the nitridized silicon interlayers, calculated according to the parameter $R_{\rm N}$, under nitridization conditions corresponds to $\sigma_{\rm N}\simeq4.5\times10^{-10}-1.5\times10^{-11}\ \Omega^{-1}\cdot\ \mathrm{cm}^{-1}$, in agreement with the results of Ref. 15 on the temperature dependence of the electrical conductivity of silicon nitride. The electrical conductivity of the obtained dielectric interlayers is four to five orders of magnitude lower than that of the first, highest-resistance a-Si:H layer in the structure: $\sigma_{s1}\sim5\times10^{-6}\ \Omega^{-1}\cdot\ \mathrm{cm}^{-1}$.

Therefore the measurements of the resistance of the structure confirm the formation of a periodic structure with insulating layers during layerwise nitridization of a-Si:H.

5. At room temperature the superlattices with a-Si:H nitridization with 10 pairs of layers and a total thickness of the a-Si:H layers of approximately 400 Å possessed an average resistivity $\rho_T\sim10^7-10^8\ \Omega\cdot$ cm, which is approximately 100 times lower than ρ_T in a homogeneous a-Si:H layer of the same thickness. The $(\mathrm{SL})_N$ obtained possess a very low residual photoconductivity $Q\simeq0.05-0.2$ compared with Q from 0.2 up to several units for $(\mathrm{SL})_p$.[6] Together with the low values of E_0, this shows that superlattices obtained by

nitridization of alternating a-Si:H layers have a higher degree of structural perfection than superlattices obtained by conventional sequential deposition of layers.

In summary, nitridization of a-Si:H layers makes it possible to obtain superlattices in which the thickness of the layers is less than the electron wavelength, resulting in collective interaction effects. The degree of structural perfection can be quite high, as is reflected in the fact that the experimental data can be described on the basis of the effective-mass approximation. The results obtained expand the possibilities for obtaining superlattices with different functional and physical properties.

We thank N. V. Lykova and V. Yu. Smirnov for assisting in the experiments.

[1] R. A. Street, M. J. Thompson, and N. M. Jonson, Philos. Mag. B **51**, 1 (1985).
[2] C. B. Roxlo, B. Abeles, and P. D. Persans, J. Vac. Sci. Technol. B **4**, 1430 (1986).
[3] P. V. Santos, M. Hundhausen, L. Ley, and C. Viczian, J. Appl. Phys. **69**, 778 (1991).
[4] D. Bilenko, Y. Galishnikova, A. Jarkova, O. Coldobanova, and E. Khasina, in *Proceedings International Semiconductors Dev. Res. Symp., Charlottesville, 1995.*
[5] T. Thedje and B. Abeles, Appl. Phys. Lett. **45**, 179 (1984).
[6] D. I. Bilenko, Yu. N. Galishnikova, É. A. Zharkova, O. Yu. Koldobanova, and E. I. Khasina, Fiz. Tekh. Poluprovodn. **28**, 2179 (1994) Semiconductors **28**, 1197 (1994).
[7] Y. Hazama, K. Yamada, S. Miyazaki, and M. Hirose, J. Non-Cryst. Solids **114**, 777 (1989).
[8] T. Schule, *Solving Engineering Problems on a Computer* [Russian translation], Mir, Moscow, 1982.
[9] L. A. Balagurov, Fiz. Tekh. Poluprovodn. **20**, 45 (1986) [*sic*].
[10] V. V. Krasnopevtsev, Itogi Nauki i Tekhniki, Ser. Élektronika **14**, 213 (1982).
[11] D. I. Bilenko, Yu. N. Galishnikova, É. A. Zharkova, O. Yu. Koldobanova, and I. I. Nikolaeva, Pis'ma Zh. Tekh. Fiz. **15**, 64 (1989) [Sov. Tech. Phys. Lett. **15**, 607 (1989)].
[12] T. Ando, A. Fowler, and F. Stern, Rev. Mod. Phys. **54**, 437 (1982) [Russian translation, Mir, Moscow, 1985].
[13] K. Seeger, *Semiconductor Physics*, Springer-Verlag, N. Y., 1982 [Russian translation, Mir, Moscow, 1977].
[14] K. Hattori and T. Mori, Phys. Rev. Lett. **80**, 825 (1988).
[15] B. Dunnett, D. L. Jones, and A. D. Stewart, Philos. Mag. B **53**, 159 (1986).

Translated by M. E. Alferieff

Ionization of impurity centers in a semiconductor quantum superlattice by nonlinear electromagnetic waves

S. V. Kryuchkov and K. A. Popov

Pedagogical University, 400013 Volgograd, Russia
(Submitted June 26, 1996; accepted for publication September 9, 1997)
Fiz. Tekh. Poluprovodn. **32**, 334–337 (March 1998)

The ionization of impurity centers in a semiconductor superlattice by nonlinear electromagnetic waves, which are the most general solution of the sine-Gordon equation and can be expressed in terms of the Jacobi elliptic functions, is investigated. The problem is solved in a quasiclassical approximation for arbitrary ratio of V (depth of the impurity energy level) and Δ (half-width of the conduction miniband). Results in agreement with those for solitary waves and sinusoidal (linear) electromagnetic waves are obtained in limiting cases. The effect of a uniform high-frequency electric field on the processes leading to the ionization of impurities by solitary waves is also investigated.
[S1063-7826(98)01003-5]

1. In recent years quantum semiconductor superlattices (SLs) have been used as working components in optoelectronics devices (filters, polarizers, IR photodetectors, and others). The unique properties (including optical) of the superlattice are determined by the presence of an additional periodic potential along one of the axes, which results in the formation of a miniband structure of the energy spectrum of the charge carriers. A review of the main experimental studies of the optical properties of regular type-I, -II, and -III semiconductor superlattices, formed by AlGaAs/GaAs, InAs/GaAs, and HgTe/CdTe heterostructures, respectively, was published by Voos.[1]. The absorption and indirect-luminescence spectra of strained GaAs/AlAs-based superlattices with layers of different thicknesses were investigated experimentally in Ref. 2. Many important properties of superlattices are due to the presence of impurity centers and defects of different types. For example, impurity centers produce peaks in the photoluminescence spectrum of superlattices with smooth heteroboundaries,[3] and they also lead to the appearance of bands in the absorption spectrum of GaAs.[4] Experiments studying the photoluminescence of the materials used in the production of superlattices are described in Refs. 5 and 6.

A characteristic feature of semiconductor superlattices is their capability to exhibit nonlinear optical properties even in the presence of weak electromagnetic (EM) signals. In addition, the relaxation times of the nonlinear effects are found to be short.[7] A possible nonlinear optical effect—two-photon absorption of EM radiation—was investigated experimentally in Ref. 8.

Nonlinear EM waves propagating through a superlattice can give rise to ionization of impurity centers, which in turn can be manifested in the damping of the EM waves and luminescence. The equation describing an EM wave in a superlattice is the well-known sine-Gordon (SG) equation. The simplest particular solutions of the SG equation are solitons and breathers. The ionization of impurities in a superlattice by solitons and breathers has been investigated theoretically in Refs. 9–11. The most general solution of the SG equation can be expressed in terms of the Jacobi elliptic functions $\mathrm{sn}(x)$, $\mathrm{cn}(x)$, and $\mathrm{dn}(x)$. In the present paper we investigate the ionization of impurity centers by nonlinear EM waves expressed in terms of the Jacobi elliptic functions. The problem is solved in the quasiclassical approximation, when multiphoton processes are important, with an arbitrary ratio of V (the depth of the impurity energy level) and Δ (the half-width of the conduction miniband). Results in agreement with those for solitary waves and sinusoidal (linear) EM waves are obtained in limiting cases. The effect of an uniform rf electric field on the processes leading to the ionization of impurities by solitary waves is also investigated.

2. Let the electronic energy spectrum be described by the expression

$$\epsilon_p=\frac{p_y^2+p_z^2}{2m}+\Delta[1-\cos(p_x d)], \quad \hbar=1, \tag{1}$$

where d is the period of the superlattice. Then, according to Ref. 12, the propagation of an EM wave in the collisionless regime is described by the unperturbed SG equation, whose most general solution can be expressed in terms of the Jacobi elliptical functions: $\mathrm{cn}(x)$, $\mathrm{sn}(x)$, and $\mathrm{dn}(x)$.

For fast waves [$\beta=(U/c)>1$, where U is the propagation velocity of the electromagnetic wave, and c is the velocity in the absence of electrons] the solutions are

$$\varphi(z,t)=2\sin^{-1}\left\{\varkappa\,\mathrm{sn}\left[\frac{2K\omega_0}{\pi}\left(t-\frac{z}{U}\right),\varkappa\right]\right\},$$

$$0<\varkappa\leqslant 1, \tag{2}$$

$$\varphi(z,t)=2\sin^{-1}\left\{\mathrm{sn}\left[\frac{2K\varkappa\omega_0}{\pi}\left(t-\frac{z}{U}\right),\varkappa^{-1}\right]\right\},$$

$$\varkappa>1. \tag{3}$$

For slow waves ($\beta<1$) we have

$$\varphi(z,t)=2\sin^{-1}\left\{\mathrm{dn}\left[\frac{2K\omega_0}{\pi}\left(t-\frac{z}{U}\right),\varkappa\right]\right\},$$

$$0<\varkappa\leqslant 1, \tag{4}$$

$$\varphi(z,t)=2\sin^{-1}\left\{\mathrm{cn}\left[\frac{2K\varkappa\omega_0}{\pi}\left(t-\frac{z}{U}\right),\varkappa^{-1}\right]\right\},$$

$$\varkappa>1, \tag{5}$$

where

$$\varphi=ed\int_{-\infty}^{t}E_x(t)dt,\quad \omega_0=\frac{\pi\omega_{pl}}{2K(\varkappa)}\frac{\beta}{|1-\beta^2|^{1/2}},$$

$$\varkappa=\frac{edE_0}{2\omega_{pl}}\frac{|1-\beta^2|^{1/2}}{\beta},$$

$K=K(\varkappa)$ is the complete elliptic integral of the first kind, ω_{pl} is the generalized plasma frequency of the electrons in the miniband,[12] and E_0 is the amplitude of the electric field of the EM wave. The collisionless regime presupposes that $\nu\ll\omega_{pl}$ (ν is the frequency of collisions between the electrons and the irregularities of the crystal lattice).

We assume that the wavelength of the EM wave is large compared to the period of the superlattice and the impurity localization radius. We can then ignore spatial dispersion in the expression for the field of the nonlinear wave, setting $z=0$ in Eqs. (2)–(5).

In the case of deep impurity ($V\gg\hbar\omega_0$) the ionization process consists of tunneling of an electron through the potential barrier and is of a quasiclassical character. The ionization probability in this approximation can be written, to exponential accuracy, as

$$W=\exp[-2\mathrm{Im}(S)], \tag{6}$$

where

$$S=\int_0^{t_0}[\epsilon(t)+V]dt, \tag{7}$$

S is the classical action acquired by the particle during the subbarrier motion, and the moment t_0 at which tunneling starts is determined by the condition

$$\epsilon(t_0)=-V. \tag{8}$$

To find the function $\epsilon(t)$ it is sufficient to study the one-dimensional classical equation of motion[10]

$$\frac{dp_x}{dt}=eE_x(t) \tag{9}$$

with the initial condition

$$p_x(0)=0. \tag{10}$$

We shall now find the ionization probability for a wave, which is described by the expression (6). The electric field intensity for it is

$$E_x(t)=E_0\mathrm{cn}\left(\frac{2K\omega_0}{\pi}t,\varkappa\right). \tag{11}$$

We find from Eq. (9)

$$p_x=\frac{2}{d}\sin^{-1}\left\{\varkappa\mathrm{sn}\left[\frac{2K\omega_0}{\pi}t,\varkappa\right]\right\}, \tag{12}$$

and therefore

$$\epsilon(t)=\epsilon[p_x(t)]=2\Delta\varkappa^2\mathrm{sn}^2\left(\frac{2K\omega_0}{\pi}t,\varkappa\right). \tag{13}$$

Solving simultaneously Eqs. (8) and (13) using the equations from Ref. 13, we obtain the time t_0

$$t_0=\frac{i\pi}{2K\omega_0}F\left[\tan^{-1}\left(\frac{1}{\varkappa}\sqrt{\frac{V}{2\Delta}}\right),\varkappa'\right], \tag{14}$$

where $F(\varphi,\varkappa)$ is an elliptic integral of the first kind, and $\varkappa'=\sqrt{1-\varkappa^2}$. We note that t_0 is a purely imaginary quantity.

Integrating Eq. (7), we obtain the following expression for the action:

$$S=\frac{i\pi V}{2K\omega_0}\left\{F\left[\tan^{-1}\left(\frac{1}{\varkappa}\sqrt{\frac{V}{2\Delta}}\right),\varkappa'\right]+\frac{2\Delta}{V}E\left[\tan^{-1}\left(\frac{1}{\varkappa}\sqrt{\frac{V}{2\Delta}}\right),\varkappa'\right]-\sqrt{\frac{2\Delta}{V}}\sqrt{\frac{V+2\Delta}{V+2\Delta\varkappa^2}}\right\}, \tag{15}$$

where $E(\varphi,\varkappa)$ is an elliptic integral of the second kind.

The ionization probability can be written to exponential accuracy in the form

$$W=\exp[-\theta f(\gamma)], \tag{16}$$

where

$$\theta=\frac{\pi V}{2K\omega_0},\quad \gamma=\sqrt{\frac{V}{2\Delta}},$$

$$f(\gamma)=F\left[\tan^{-1}\frac{\gamma}{\varkappa},\varkappa'\right]+\gamma^{-2}E\left[\tan^{-1}\frac{\gamma}{\varkappa},\varkappa'\right]-\gamma^{-1}\sqrt{\frac{\gamma^2+1}{\gamma^2+\varkappa^2}}.$$

For $\varkappa=1$ Eq. (15) passes into the formula for the action in the case of ionization of an impurity by a soliton.[10]

For fast waves with $\varkappa>1$, after similar transformations we obtain t_0

$$t_0=\frac{i\pi}{2\varkappa K\omega_0}F\left[\tan^{-1}\sqrt{\frac{V}{2\Delta}},\frac{\sqrt{\varkappa^2-1}}{\varkappa}\right], \tag{17}$$

and the action S

$$S=\frac{i\pi V}{2\varkappa K\omega_0}\left\{F\left[\tan^{-1}\sqrt{\frac{V}{2\Delta}},\frac{\sqrt{\varkappa^2-1}}{\varkappa}\right]+\varkappa^2\frac{2\Delta}{V}E\left[\tan^{-1}\sqrt{\frac{V}{2\Delta}},\frac{\sqrt{\varkappa^2-1}}{\varkappa}\right]-\varkappa\sqrt{\frac{2\Delta}{V}}\sqrt{\frac{V+2\Delta\varkappa^2}{V+2\Delta}}\right\}. \tag{18}$$

We can see that for $\varkappa=1$ the expression (17) passes into the expression (14) and the expression (18) passes into the expression (15).

Curves of the imaginary part $\mathrm{Im}(S)$ of the action versus the ratio V/Δ are presented in Fig. 1 for waves propagating

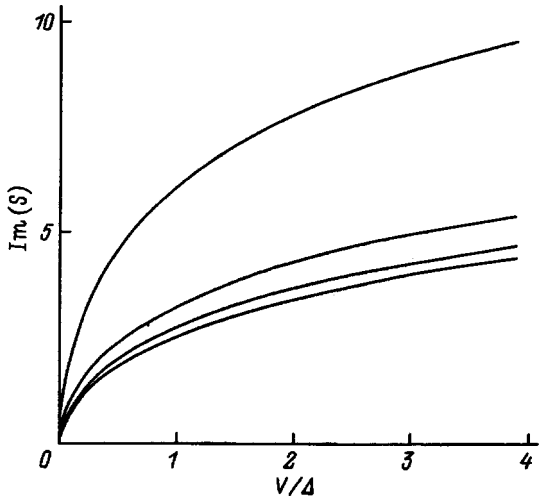

FIG. 1. Imaginary part of the action versus ratio V/Δ with $V=0.1$ eV and $\omega_0=10^{13}$ s^{-1} for different values of $\varkappa$: *1*—0.6, *2*—0.9, *3*—1.2, *4*—1.5.

with the same velocity but different amplitudes and correspondingly different ''nonlinearity coefficients'' $\varkappa$. We see that for the same value of V/Δ the action decreases with increasing $\varkappa$; i.e., the ionization probability increases. In addition, since for $\varkappa \ll 1$ a wave of the type (11) passes into a linear wave, one can see that the probability of ionization of an impurity by a nonlinear wave is higher than the probability for a transition to occur under the action of a linear perturbation.

The use of this quasiclassical method to calculate the ionization probability for impurity centers is limited by the condition imposed on the argument of the exponential in Eq. (16), $\theta f \ll 1$, which holds if the inequality $V > \hbar\omega_{pl}$ is satisfied.

For slow waves, described by the expressions (4) and (5), we obtain in a similar manner the expressions for the action (15) and (18), respectively.

Let us now make a numerical estimate of the absorption coefficient α for an electromagnetic wave. The absorption coefficient can be written as the ratio of the energy absorbed per 1 cm^3 of matter per 1 s

$$NWV/\tau_0$$

[N is the density of impurity atoms, $\tau_0=\mathrm{Im}(t_0)$] to the incident energy flux density

$$\frac{c}{\varepsilon}\frac{E_0^2}{4\pi}$$

(ε is the dielectric constant of the superlattice). Thus, we have

$$\alpha=\frac{4\pi\varepsilon NV}{c\tau_0 E_0^2}\exp[-2\mathrm{Im}(S)]. \tag{19}$$

For $N=10^{15}$ cm^{-3} (Ref. 4), $\varepsilon=3$, $V=0.1$ eV (Ref. 4). $\Delta=0.025$ eV, $\omega_0=10^{13}$ s^{-1}, $\varkappa=0.5$, and $E=20$ cgs units (6×10^3 V/cm), we obtain for the absorption coefficient $\alpha\approx 3\times10^3$ cm^{-1} in order of magnitude, which is accessible to measurement.

3. It is shown in Ref. 14 that a time-varying perturbation sharply increases the probability of quasiclassical tunneling processes. We shall examine in greater detail the effect of an uniform rf field on the ionization of an impurity by a solitary wave (soliton), which is a particular case of a nonlinear wave corresponding to $\varkappa=1$. The importance of this problem is determined, among other things, by the fact that the effect of a rf field on a semiconductor superlattice is, as shown in Refs. 15 and 16, to stabilize the shape of solitons, which decay very rapidly in the absence of variable perturbation due to the electron collision.

In the case of a sufficiently low intensity E_1 of the alternating field, the value of $\mathrm{Im}(S)$ can be found analytically using the procedure from Ref. 14. According to this procedure, the action can be written as

$$S=S_0+S_1, \tag{20}$$

where S_0 is the action in the case of ionization of an impurity by a soliton,[10]

$$S_0=\frac{4i\Delta}{eE_0 d}\left[\left(\frac{V}{2\Delta}+1\right)\tan^{-1}\sqrt{\frac{V}{2\Delta}}-\sqrt{\frac{V}{2\Delta}}\right], \tag{21}$$

and S_1 has the form

$$S_1=-2eE_1\int_0^{t_0}x(t)\,\cos(\omega t)dt, \tag{22}$$

where $t_0=(iL/U)\tan^{-1}\sqrt{V/2\Delta}$, and $x(t)$ is a trajectory in the absence of a rf field. From Eq. (9) we find the momentum

$$p_x=\frac{2}{d}\tan^{-1}\left[\sinh\left(\frac{Ut}{L}\right)\right],$$

acquired by an electron under the action of the soliton field, and the velocity component of the electron along the x axis has the form

$$v_x=2\Delta d\,\mathrm{sech}^2\left(\frac{Ut}{L}\right)\sinh\left(\frac{Ut}{L}\right).$$

We thus find the unperturbed trajectory

$$x(t)=\frac{2\Delta dL}{U}\left(\mathrm{sech}\frac{Ut_0}{L}-\mathrm{sech}\frac{Ut}{L}\right). \tag{23}$$

Substituting the expression (23) into Eq. (22) ,we obtain for S_1

$$S_1=-\frac{4ieE_1\Delta dL}{U\omega}\sqrt{1+\frac{V}{2\Delta}}\sinh\left(\frac{\omega L}{U}\tan^{-1}\left[\sqrt{\frac{V}{2\Delta}}\right]\right)$$
$$+\frac{4ieE_1\Delta dL^2}{U^2}\int_0^{\psi}\frac{\cosh(\omega L t' U^{-1})}{\cos(t')}dt', \tag{24}$$

where $\psi=\tan^{-1}\sqrt{V/2\Delta}$.

Let us now examine the limiting cases. For a shallow impurity ($V\ll 2\Delta$) it follows from Eq. (24) that

$$S_1=-\frac{2ieE_1 dVL}{U\omega}\sinh\left(\frac{\omega L}{U}\sqrt{\frac{V}{2\Delta}}\right). \tag{25}$$

In the case of a deep impurity ($V\gg 2\Delta$) and $U/L\gg\omega$ the integration in Eq. (24) gives the expression

$$S_1 = -\frac{4ieE_1\Delta dL}{U\omega}\sqrt{\frac{V}{2\Delta}}\sinh\left(\frac{\omega L}{U}\tan^{-1}\left[\sqrt{\frac{V}{2\Delta}}\right]\right)$$

$$+\frac{4ieE_1\Delta dL^2}{U^2}\ln\left(\frac{\pi}{2}+\frac{1}{2}\tan^{-1}\left[\sqrt{\frac{V}{2\Delta}}\right]\right). \qquad (26)$$

It follows from the expressions (25) and (26) that the effect of the rf field leads to an exponential increase in the ionization probability. By increasing the electron density and hence the plasma frequency ω_{pl}, which determines the parameters of the soliton, this increase in turn can undermine the stabilization of the shape of the soliton by the external alternating field. The latter circumstance must be taken into account in attempts to stabilize soliton motion by applying a uniform rf field to a doped superlattice.

Let us now estimate the transit time of a soliton, with allowance for the rf perturbation, determined by the formula[10]

$$t^* = \frac{E_0^2 L}{4\pi NUVW} \qquad (27)$$

For the soliton amplitude $E_0 = 19$ cgs units (5.7×10^3 V/cm) and the superlattice parameters presented above, the transit time reaches, in order of magnitude, $t^* \approx 10^{-10}$ s. Over this time a soliton traverses a distance of 1 cm. Changing the amplitude of the rf field from 2 to 4 cgs units, with the frequency of the external field $\omega = 10^{13}$ s^{-1}, decreases the transit time by an order of magnitude. This agrees with the conclusion reached in Ref. 14 that even a weak rf field can increase exponentially the probability of overcoming potential barriers in a quasiclassical situation.

[1] M. Voos, Ann. Telecommun. **43**, 357 (1988).
[2] G. R. Olbright, J. Klem, A. Owyong, T. M. Brennan, R. Binder, and S. W. Koch, J. Opt. Soc. Am. B **7**, 1473 (1990).
[3] R. Fischer, W. T. Masselink, Y. L. Sun *et al.*, J. Vac. Sci. Technol. B **2**, 170 (1984).
[4] H. Ch. Alt, Appl. Phys. Lett. **54**, 1445 (1989).
[5] V. A. Bykovskiĭ and V. I. Utenko, Fiz. Tekh. Poluprovodn. **23**, 1767 (1989) [Sov. Phys. Semicond. **23**, 1093 (1989)].
[6] V. A. Bogdanova and N. A. Semikolenova, Fiz. Tekh. Poluprovodn. **26**, 818 (1992) [Sov. Phys. Semicond. **26**, 460 (1992)].
[7] W. Cheng Uli, Physics **15**, 345 (1986).
[8] I. B. Catalano, A. Cingolani, M. Lepore, R. Congolani, and K. Ploog, Nuovo Cimento D **12**, 1465 (1990).
[9] É. M. Épshteĭn, Izv. Vyssh. Uchebn. Zaved. Radiofiz. **25**, 3 (1982).
[10] S. V. Kryuchkov, Fiz. Tekh. Poluprovodn. **23**, 1314 (1989) [Sov. Phys. Semicond. **23**, 819 (1989)].
[11] S. V. Kryuchkov and G. A. Syrodoev, Fiz. Tekh. Poluprovodn. **24**, 913 (1990) [Sov. Phys. Semicond. **24**, 573 (1990)].
[12] F. G. Bass, A. A. Bulgakov, and A. P. Tetervov, *High-Frequency Properties of Semiconductors with Superlattices* [in Russian], Nauka, Moscow, 1989.
[13] M. Abramowitz and I. Stegun [Eds.], *Handbook of Mathematical Functions*, Dover, N. Y., 1965 [Russian translation, Nauka, Moscow, 1979].
[14] B. I. Ivlev and V. I. Mel'nikov, Zh. Éksp. Teor. Fiz. **90**, 2208 (1986) [Sov. Phys. JETP **63**, 1295 (1986)].
[15] F. G. Bass, S. V. Kryuchkov, and A. I. Shapovalov, Fiz. Tekh. Poluprovodn. **29**, 19 (1995) [Semiconductors **29**, 9 (1995)].
[16] S. V. Kryuchkov and G. A. Syrodoev, Fiz. Tekh. Poluprovodn. **23**, 857 (1989) [Sov. Phys. Semicond. **23**, 537 (1989)].

Translated by M. E. Alferieff

Harmonics generation in quantum-size structures in a strong electromagnetic field

V. V. Kapaev[a] and A. E. Tyurin

P. M. Lebedev Physical Institute, Russian Academy of Sciences, 117924 Moscow, Russia
(Submitted May 25, 1997; accepted for publication September 9, 1997)
Fiz. Tekh. Poluprovodn. **32**, 338–344 (March 1998)

Harmonics generation in a system of tunneling-coupled quantum wells is investigated by solving numerically the nonstationary Schrödinger equation, without using perturbation theory, in an external electromagnetic field. The time-dependence of the dipole moment is calculated and a method is proposed for calculating the radiation intensity at a fixed frequency. For systems containing three equidistant energy levels, it is shown that the effect of the field on the energy spectrum becomes substantial at intensities of several hundreds V/cm; the system falls out of resonance. The field-dependence of the second harmonic amplitude becomes nonquadratic, in contrast to the dependence predicted by perturbation theory, and the system passes into a stable level. In the quasienergy-crossing regime, it is shown that even-harmonics generation is possible in a symmetric system in a strong field. The amplitude of the harmonics is largely determined by the initial state of the system. It is possible to have a situation where the amplitude of the generated harmonic can even be greater than in structures with a resonance configuration of energy levels (three equidistant levels for the second harmonic). © *1998 American Institute of Physics.* [S1063-7826(98)02503-4]

1. INTRODUCTION

In the last few years substantial progress has been made in the theoretical and experimental investigation of the nonlinear optical properties of quantum-size structures.[1–3] Quantum-size structures make it possible to study a wide spectrum of quantum effects without turning to natural atomic and ionic systems.[4] This could serve as a basis for producing new optoelectronic devices, and it can also be used for developing and implementing new information processing and transmission methods.

As a rule, perturbation theory is used to describe optical nonlinearities in quantum-size heterostructures.[1,3,5] The criterion for applicability of perturbation theory is that in an expansion in terms of a small parameter (amplitude of the external perturbation) each subsequent correction to the wave function must be small compared with the preceding correction: $|a_k^{n+1}| \ll |a_k^n|$. The field amplitude obtained from this condition can range from ~ 10 up $\sim 10^3$ V/cm, depending on the parameters of the system. Optical nonlinearities in quantum-size structures are intensified compared with the bulk material. This was first predicted in Ref. 6 for an asymmetric structure based on $GaAs/Al_xGa_{1-x}As$. This is due to, first and foremost, the fact that the region of localization of the wave functions in quantum-size structures is tens of nanometers in size instead of several picometers in atomic and ionic systems. The matrix elements of intersubband transitions are of the same order of magnitude as the width of the structure.

For clarity and simplicity, second harmonic generation is studied most often. In this case the nonlinear permeabilities in the perturbation theory are cubic functions of the dipole matrix elements, so that there is no effect if the system is invariant under inversion.[5] The maximum second harmonic generation obtains in a system with three equidistant energy levels, where absorption of two photons with energy equal to the splitting between the levels occurs as resonance is approached and the radiation is subsequently re-emitted at the doubled frequency — the so-called ''double resonance'' regime. As shown in Ref. 1, in this regime the magnitude of the second-order nonlinear permeability is more than three orders of magnitude greater than that in a bulk material. The intensities of the radiation sources used in experiments on quantum-size structures are such that the formal criterion for applicability of perturbation theory may not be satisfied. In this connection it is of interest to calculate the intensities of the generated harmonics without using perturbation theory. In the literature a number of schemes have been proposed to solve the nonstationary Schrödinger equation in the presence of an external periodic field.[4,7,8] In Refs. 9 and 10 an analytical method is proposed for investigating harmonics generation, including at low frequencies, for a two-level system with no restrictions on the amplitude of the perturbation. In the present paper we shall employ the temporal analog of the Kronig–Penney model, proposed in Ref. 7, to calculate the electronic wave functions. The advantage of this method for calculating the radiation intensity at one or another frequency without limit on the number of quasienergy levels will be indicated in Sec. 2. We shall compare in the same section the intensities of the second harmonic of dipole radiation that could be achieved in a strong field with the intensity that is observed in the above-mentioned double-resonance regime in a system with three equidistant energy levels.

In Sec. 3 a calculation and quantitative analysis of the radiation harmonics generated in a strong field in a system consisting of two tunneling-coupled quantum wells in the quasienergy-crossing regime are performed. It is shown that generation of one or another radiation frequency is possible in a strong field, depending on the initial state and parameters of the structure. It is noted that even-harmonics generation can be observed in the case of symmetric structures,

which in weak fields is impossible in principle. It is shown that an optical rectification regime can be realized in a strong field for a special choice of the relative position of several quasienergy levels and the initial state of the system.

2. SECOND HARMONIC GENERATION

Let us consider a heterostructure consisting of two quantum wells separated by a tunneling-transparent barrier and subjected to an external periodic perturbation. We shall make a direct calculation of the total radiation intensity and frequency ω using the spectral decomposition[11,12]

$$dE_\omega = \frac{4}{3c^3}\left|\frac{d^2P_\omega(t)}{dt^2}\right|^2 \frac{d\omega}{2\pi}. \tag{1}$$

We shall calculate the time-dependence of the dipole moment of the structure on the basis of the temporal analog of the Kronig–Penney method.[7] This method is based on the assumption that a periodic sequence of rectangular pulses acts on the system

$$U(t) = \begin{cases} U_1, & nT < t < nT + \tau_1, \\ U_2, & nT + \tau_1 < t < (n+1)T, \end{cases} \tag{2}$$

where n is an integer and $T = \tau_1 + \tau_2$ is the period of the external perturbation. This model has the advantage that the computational methods are simpler than in the case when a potential of the form $U(t) = U_0 \sin(\omega t)$ is used, and the basic results obtained are similar. If the quasienergy spectrum is known,[10] then it is possible to perform a qualitative analysis of the behavior of the system at any moment in time. In the case when two size-quantization levels play the main role, this method makes it possible to perform the analysis analytically. The wave function of the system in an external field can be represented in the form

$$\Psi(x,t) = \sum_{m=1}^{\infty} g_m \exp(-i\epsilon_m t/\hbar)\Phi_m(x,t), \tag{3}$$

where ε_m is the quasienergy, $\Phi_m(x,t)$ is the corresponding Floquet function and is periodic in time $\Phi_m(x,t) = \Phi_m(x,t+T)$, and g_m are the expansion coefficients of the initial state of the system $\Psi(x,0)$ in the basis $\Phi_m(x,0)$. Substituting the expansion (3) into the expression for the dipole moment $P(t) = e\int \Psi^*(x,t)x\Psi(x,t)dx$ and expanding $\Phi_m(x,t)$ in a Fourier series, we obtain

$$P(t) = e \sum_{m,n_\infty} g_m^* g_n \exp[-i(\epsilon_n - \epsilon_m)t/\hbar] \times \sum_{k=1}^{\infty} a_k^{mn} \exp(-i\omega k t), \tag{4}$$

where

$$a_k^{mn} = 2/T \int_{-T/2}^{-T/2} dt \int \exp(i\omega k t)\Phi_m^*(x,t)x\Phi_n(x,t)dx.$$

As one can see from Eq. (4), in the case when only two quasienergy levels play the main role and $\varepsilon_1 = \varepsilon_2$, the behavior of the dipole moment in time becomes periodic, while the amplitude of the k-th harmonic is simply determined by the coefficient of $\exp(-i\omega k t)$ in the expansion (4). When several quasienergy levels play a role in the expansion (3), the Fourier integral expansion of $P(t)$ on a finite time interval T_0 can be used to calculate the amplitudes of the harmonics.

In the general case the wave functions of the size-quantization levels in the well may not form a complete orthonormal system. Then the wave functions of the continuous spectrum must be taken into account. We shall employ the model of a quasicontinuous spectrum produced by infinite potential barriers at a definite distance from the edges of the structure. This distance is chosen so as to obtain convergent results.

When the number of quasienergy levels is large, difficulties arise in choosing an appropriate time interval T_0 on account of the fact that the quasienergies are incommensurate. To circumvent this difficulty we shall use as the response of the structure at a given frequency $n\omega_0$ a convolution of the spectral density from Eq. (1) with the function

$$\sigma(\omega) = 1/\sqrt{2\pi\Delta\omega^0}_2 \exp[-(\omega - n\omega_0)^2/2\Delta\omega_0^2], \tag{5}$$

where $\Delta\omega_0$ is the spectral width of the line of the detecting device, n is the harmonic order of the radiation, and ω_0 is the frequency of the external perturbation. It is reasonable to choose the spectral width of the detector line to be of the order of the ''natural widths'' Γ of the energy levels. The total intensity of the radiation at frequency $n\omega_0$ is obtained by substituting the second time derivative of the dipole moment $P(t)$ in Eq. (1), premultiplying the expression obtained by the expression (5), and integrating over the entire frequency range. The result for the intensity is

$$I = \sum_{m,n,k}^{\infty} |\omega_{n,m,k}^2 g_m^* g_n a_k^{n,m}|^2 \sigma^*(\omega_{n,m,k}), \tag{6}$$

where

$$\sigma^*(\omega_{n,m,k}) = \sigma(\psi_{n,m,k}) \Big/ \sum_{m',n',k'}^{\infty} \sigma(\omega_{n',m',k'}),$$

$$\omega_{n,m,k} = (1/\hbar)(\epsilon_n - \epsilon_m) + \omega k.$$

We shall employ one or another computational method, depending on the conditions of the problem. To decrease the number of parameters in the numerical calculation we introduce the dimensionless coordinate and time: $x^* = x/\lambda$, where $\lambda = (2\pi\hbar^2/m^*\Delta E_c)^2$ and $t^* = t/t_0$, where $t_0 = 2\pi\hbar/\Delta E_c$. For GaAs/$Al_xGa_{1-x}$As-based structures $t_0 \simeq 0.041$ ps for $x = 0.1$ and $\lambda \simeq 15$ nm and $t_0 \simeq 0.016$ ps for $x = 0.3$ and $\lambda \simeq 9$ nm.

We shall examine first a two-well structure with three equidistant energy levels: $a_1 = 0.4\lambda$, $a_2 = 0.88\lambda$, and $b = 0.2\lambda$, where a_1 is the width of the left-hand well, a_2 is the width of the right-hand well, and b is the width of the barrier. For such a structure $E_2 - E_1 = E_3 - E_2 = \Delta E$, and the period of the perturbation, corresponding to $\hbar\omega = \Delta E$, equals $T = 3.75t_0$. The expression for the second-order nonlinear permeability, obtained in perturbation theory taking account of relaxation processes, has the form[1]

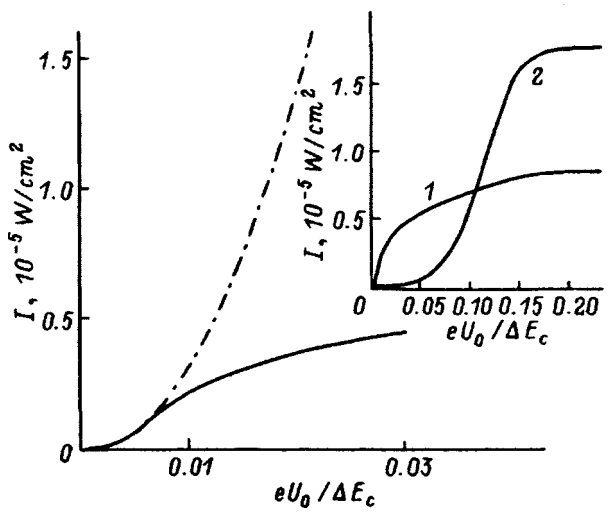

FIG. 1. Second harmonic intensity I versus the amplitude of the field for a double-well structure with three equidistant levels. Solid line — calculation with Eq. (6) (see text); dot-dashed line — perturbation theory calculation. Inset: Second harmonic intensity as a function of the amplitude of the field for a structure with three equidistant levels ($a_1=0.4\lambda$, $a_2=0.8821\lambda$, $b=0.2\lambda$) (*1*) and for a structure with the parameters $a_1=0.4\lambda$, $a_2=0.8\lambda$, and $b=0.6\lambda$ (*2*). The period of the perturbation is $T=3.74t_0$.

$$\chi_{2\omega}^{(2)}=\frac{e^3Z_{12}Z_{23}Z_{31}}{\hbar^2(\omega_{12}-\omega-i\Gamma_{21})(2w_{23}-2w-i\Gamma_{32})}, \tag{7}$$

where e is the electron charge, Z_{12}, Z_{23}, and Z_{31} are the dipole transition matrix elements, and $\Gamma_{ij}=\hbar/T_{ij}$ is the relaxation time. Ordinarily, it is assumed[13] that $\Gamma_{21}=\Gamma_{32}=\hbar/T_{\text{offdiag}}$, where $T_{\text{offdiag}}\sim 10^{-12}$ s.

It is difficult to make a direct quantitative comparison of our results with Eq. (7), since we neglect relaxation processes. This situation corresponds to $\Gamma_{ij}=0$ in Eq. (7). Then the expression (7) will be valid for any detuning of the frequency ω from resonance. In the region where perturbation theory and Eq. (7) are applicable, the quadratic dependence of the dipole moment $P_{2\omega}$ on the amplitude of the field should remain. Our calculation is valid for any $\omega-\omega_{12}$. For a small perturbation amplitude our computational result should agree with Eq. (7). Just as in the case of Eq. (7), for a small detuning $\omega-\omega_{12}$ from resonance the amplitude of the second harmonic is large, and even for low amplitudes $P(E)$ differs substantially from a quadratic law. When comparing with the results of perturbation theory, it is reasonable to choose $\Delta\omega_0$ to be of the order of magnitude of $\Gamma_{ij}/\hbar$, where Γ_{ij} is the width of the energy levels and is proportional to the reciprocal $1/T_{\text{offdiag}}$ of the relaxation time. Thus, our calculations make it possible to refine the criterion for applicability of perturbation theory for calculating the amplitude of the second harmonic.

To take account of the quasicontinuous spectrum we shall employ a convolution of the spectral density with the transfer function (5). Figure 1 shows the dependence of the intensity of the second harmonic on the amplitude of the external perturbation (solid line). We took for the initial state $\Psi(x,0)=|1\rangle^0$ in the absence of an external perturbation. Estimating the limits of applicability according to the formulas of perturbation theory we obtain the field $\sim 10^3$ V/cm ($\sim 0.01\Delta E_c$). The dot-dashed curve in Fig. 1 corresponds to the second-harmonic intensity calculated in perturbation theory. Above some value of the field the second-harmonic dependence (solid line) deviates from the dot-dashed curve. The value of the field at which this dependence no longer reflects the quadratic dependence of the dipole moment of the structure on the field intensity is $\sim 7\times 10^2$ V/cm. As the field amplitude increases further, the second-harmonic intensity reaches a stable level. The formula (6) agrees well with the experimental results presented in Ref. 1. The experiment was performed in a field $\sim 10^3$ V/cm, which corresponds to the theoretical limit of applicability of perturbation theory. The system falls out of resonance (and the dependence deviates from a quadratic dependence) because the distance between the quasienergy levels depends on the amplitude of the field and because the matrix elements $a_k^{n,m}$ change as a result of the field-dependence of the Floquet functions.

Thus, a three-level system falls out of resonance at a finite amplitude of the external perturbation. This suggests choosing the parameters of the system so that resonance will be achieved at a fixed amplitude of the perturbation.

Such a situation can be realized in a structure with the parameters $a_1=0.4\lambda$, $a_2=0.8\lambda$, and $b=0.6\lambda$ at the same frequency of the perturbation.

The inset in Fig. 1 shows the second-harmonic intensity for a system with three equidistant levels (curve *1*) and for the structure $a_1=0.4\lambda$, $a_2=0.8\lambda$, and $b=0.6\lambda$ (curve *2*). Curve *1* is a continuation of the solid line in Fig. 1 into the region of high fields. As expected, for small perturbations the intensity of the radiation of the system with three equidistant levels is much higher than that of the second harmonic generated by a structure which is ''nonresonant'' in this region. However, as the amplitude of the field increases, there appears a region of amplitudes where the intensity of the second harmonic of this structure is higher than the intensity in the system of three equidistant levels.

Thus, there exists a two-well structure in which the second harmonic generation is intensified in a strong field even compared with the resonance regime in a system with three equidistant levels. A similar calculation can be used for nonlinear effects of a higher order, for which a similar kind of amplification can also be expected.

It should be noted that the use of square pulses instead of a sinusoidal perturbation can affect the final result, since higher-order harmonics are present in the perturbation itself. However, for a pulse period-to-pulse duration ratio of 1 for electromagnetic radiation, the second Fourier component of the initial signal equals zero. To obtain additional confirmation of the validity of this model we performed calculations with a sinusoidal perturbation, for which the qualitative dependence of the second-harmonic amplitude on the field is similar.

3. HARMONICS GENERATION IN A DOUBLE-WELL SYSTEM

Let us analyze in greater detail harmonics generation in structures containing two spatial-quantization levels. In this case, as a rule, only the first two terms play the main role in the expansion (3). This is the clearest situation, and the same

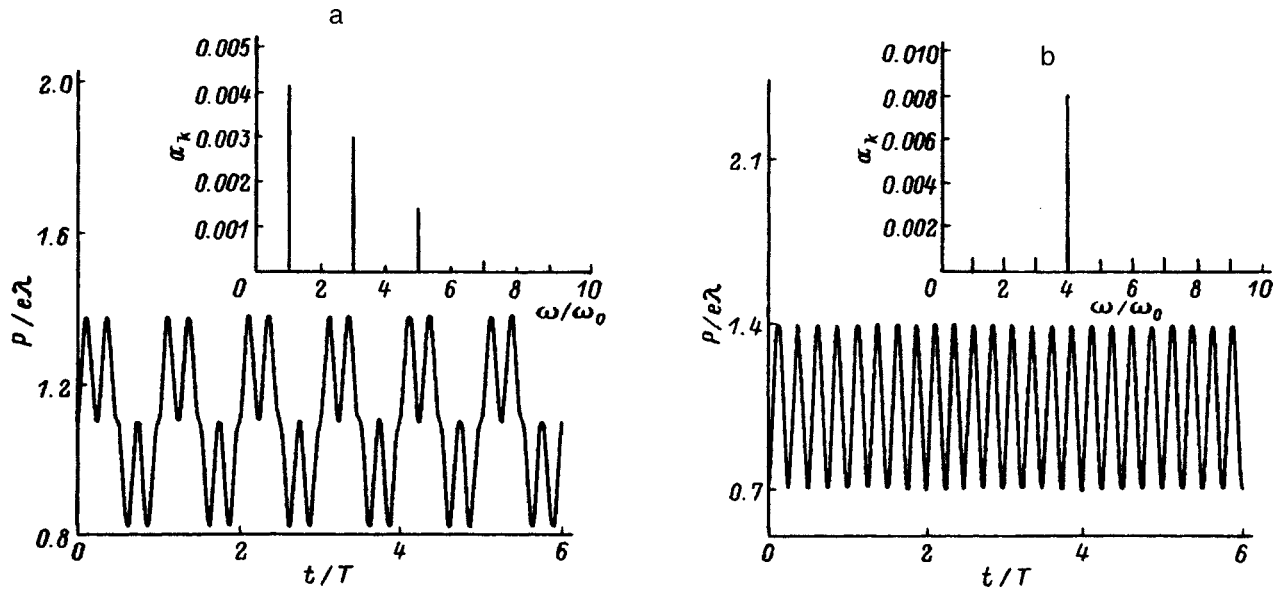

FIG. 2. Dipole moment P versus time t for a symmetric structure with parameters $a_1=0.4\lambda$, $a_2=0.4\lambda$, and $b=0.4\lambda$ with $T=46t_0$ and $eU_0=0.05\Delta E_c$. Initial state: a — $\Psi(x,0)=|1\rangle^0$, b — $\Psi(x,0)=(|1\rangle^0+|2\rangle^0)/\sqrt{2}$. Insets: Fourier coefficients in the expansion of the corresponding dipole moments.

general approach can be used when studying a large number of Floquet modes. The analysis simplifies substantially if it is assumed that the system is in a quasienergy-crossing regime, since the behavior of the dipole moment as a function of time becomes periodic, as mentioned earlier, while the amplitude of the generated harmonic is determined by the coefficient of the corresponding exponential in Eq. (4).

Let us examine as an example a symmetric double-well structure with well width $a_1=a_2=0.4\lambda$ and barrier width $b=0.4\lambda$. For a symmetric structure under a symmetric periodic perturbation the condition for crossing of two quasienergy levels can be found analytically:[7]

$$\Delta_1=\Delta_2=2m\hbar\omega, \tag{8}$$

$$\Delta_1=E_2^{(1)}-E_1^{(1)}, \quad \Delta_2=E_2^{(2)}-E_1^{(2)},$$

where $\omega=2\pi/T$ is the frequency of the external perturbation and $E_i^{(j)}$ is the corresponding value of the energy level (i) in the first and second half-periods of the perturbation (j). Thus, the crossing of energy levels can be associated to a $2m$-quantum process, in which over each half-period of the perturbation the system undergoes an identical number m of complete oscillations, i.e., generation of a harmonic with frequency $2m\omega$ can be expected. Since the Fourier expansion $P(\omega)$ is determined by the coefficients g_i, the result will depend on the initial conditions.

So as not to limit the analysis to second harmonic generation only, let us consider the case of the generation of a harmonic with frequency 4ω. The parameters of the perturbation $T=46t_0$ and $l_0=0.05\Delta E_c$ correspond to a four-quantum process. Figure 2a shows the time-dependence of the dipole moment with $\Psi(x,0)=|1\rangle^0$ as the initial state in the absence of the external perturbation. The same dependence but with the initial state $\Psi(x,0)=(|1\rangle^0+|2\rangle^0)/\sqrt{2}$ is shown in Fig. 2b. The insets in Figs. 2a and b show the expansion of the dipole moment in a Fourier series. Only odd harmonics are present in the radiation in one case and only even harmonics are present in the other; in addition, the fourth harmonic will be strongest.

To explain the presence of even or odd harmonics in a symmetric structure we note that the problem is symmetric under the transformation $C=T\sigma_z$, where T is the shift in time by a half-period of the external perturbation and σ_z is the spatial parity operator,[14] i.e., the problem exhibits so-called generalized parity.[15] The Floquet functions are orthogonal to one another. In our case they were constructed in a manner so that the first Floquet function corresponds to the ground state of the system in the absence of an external perturbation, and the second function corresponds to the first excited state. The wave function of the ground state is even and that of the first excited state is odd. Both functions are antisymmetric under a displacement by a half-period, and the temporal oscillations of $\Phi_1(x,t)$ and $\Phi_2(x,t)$ are in antiphase. Thus, we have two states with a different generalized parity. Hence it follows that when the ground or first excited state is taken as the initial state, only odd harmonics of the radiation are present. If the initial state is a linear combination of two of these states with equal coefficients, one Floquet function is subtracted from the other, as a result of which all odd harmonics vanish and only an even harmonic, determined by the quantum number m in Eq., (8), appears. A linear combination of the Floquet functions gives a wave function which is delocalized over the entire structure. This is reflected in a large increase of the amplitude of the even harmonics relative to the odd harmonics.

Let us now consider an asymmetric structure with the parameters $a_1=0.5\lambda$, $a_2=0.4\lambda$, and $b=0.6\lambda$. The condition of crossing of the quasienergy levels for an asymmetric structure is satisfied when the ratio Δ_1/Δ_2 of the energies of the stationary states in the first and second half-wave equals the ratio l/m of integers.[7] Then the period of the perturbation should equal $T=4\pi\hbar l/\Delta_1$. As an example let us take eU_0

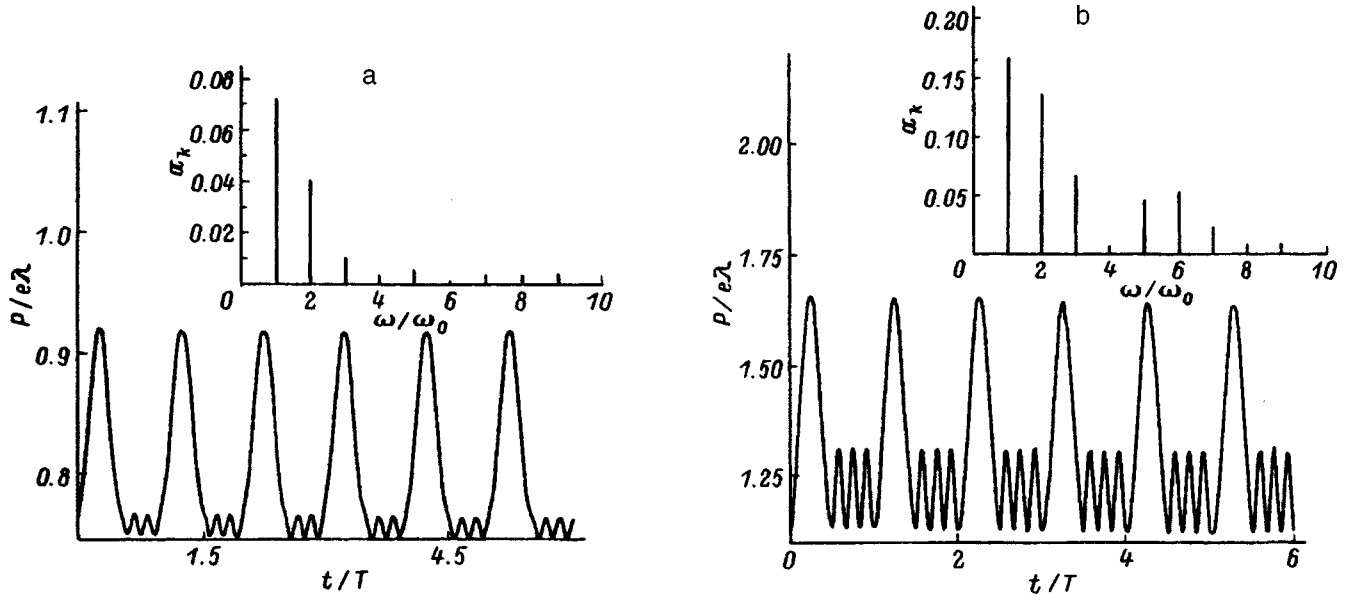

FIG. 3. Dipole moment P versus time t for an asymmetric structure with parameters $a_1=0.5\lambda$, $a_2=0.4\lambda$, and $b=0.6\lambda$ with $T=40.6t_0$ and $eU_0=0.075\Delta E_c$. Initial state: a — $\Psi(x,0)=|1\rangle^0$, b — $\Psi(x,0)=(|1\rangle^0+|2\rangle^0)/\sqrt{2}$. Insets: Fourier coefficients in the expansion of the corresponding dipole moments.

$=0.075\Delta E_c$ and $T=40.6t_0$. Then the ratio of the energies will be $\Delta_2/\Delta_1=3$. Just as in the case of a symmetric structure, we shall perform the calculation for different initial conditions $\Psi(x,0)=|1\rangle^0$ and $\Psi(x,0)=(|1\rangle^0+|2\rangle^0)/\sqrt{2}$. The computational results are presented in Fig. 3. As we can see from Fig. 3a, for $\Psi(x,0)=|1\rangle^0$ the system completes one oscillation during the first half-period and three over the second half-period; this corresponds to quantum numbers $l=1$ and $m=3$, respectively. The inset in Fig. 3a shows the expansion of the dipole moment in a Fourier series, in which the first, second, and third harmonics of the oscillations are present. For the initial state $\Psi(x,0)=(|1\rangle^0+|2\rangle^0)/\sqrt{2}$ the amplitudes of the Fourier coefficients are much larger and the even harmonics are more intense (Fig. 3b). This is explained by the fact that, as already mentioned above, the wave function is delocalized over the structure when the initial state is a linear combination of stationary states. This increases the dipole moment and results in a large participation of even harmonics.

Thus, symmetric systems in a strong field are a good object for producing even harmonics of radiation with a quite large amplitude, ''distinguished'' against the background of all other frequencies. The structure becomes asymmetric during each half-period of the perturbation. This results in a loss of the spatial center of inversion. In the case when the field does not strongly affect the energy level of a symmetric structure, the product of the transition dipole matrix elements in Eq. (7) vanishes, so that generation of a second (even) harmonic is impossible. The frequency spectrum in the case of asymmetric structures is richer than that of symmetric structures, which makes it possible to use asymmetric structures for generating a wider spectrum of harmonics. The required frequency distribution with distinguished harmonics corresponding to quantum numbers l and m can be obtained in a controllable manner by choosing structures with different values of the ratio Δ_2/Δ_1.

We have examined a regime with behavior of the wave functions is periodic, which obtains under conditions when the first two quasienergy levels cross. The analysis performed above shows that in this case integer harmonics are distinguished in the spectrum. Although in practice the required initial state is quite difficult to obtain, the case when for a specially chosen relative arrangement of several quasienergy levels and a definite choice of an initial state it is possible to obtain a regime with generation of low frequencies (optical rectification regime) is also of interest. The dynamics of the wave functions is determined by the relative arrangement of the quasienergy levels, so that by controlling the splitting between them it is also possible to achieve generation of frequencies which are lower by an integer number of times than the frequency of the external perturbation. A structure in which for an amplitude of the external perturbation $eU_0=0.05\Delta E_c$ only the first three terms make the main contribution to the expansion (3) was chosen for the calculation: $a_1=0.7\lambda$, $a_2=0.5\lambda$, and $b=0.3\lambda$. In this case, since the number of quasienergy levels is small, it is convenient to use a Fourier integral expansion of the dipole moment. The regime which we require should be realized when two of the three quasienergy levels considered converged toward one another substantially. The first such convergence occurs for a period of the perturbation $T=2.06t_0$. A special choice of the initial state gives a large value of the coefficient of the exponential with a low oscillation frequency and a small value of the coefficient of terms with frequencies $k\omega$, where k is an integer. Such a situation obtains if the first excited state $\Psi(x,0)=|2\rangle^0$ in the absence of an external field is taken as the initial state. The computational results are displayed in Fig. 4. An electron initially localized in the right-hand well

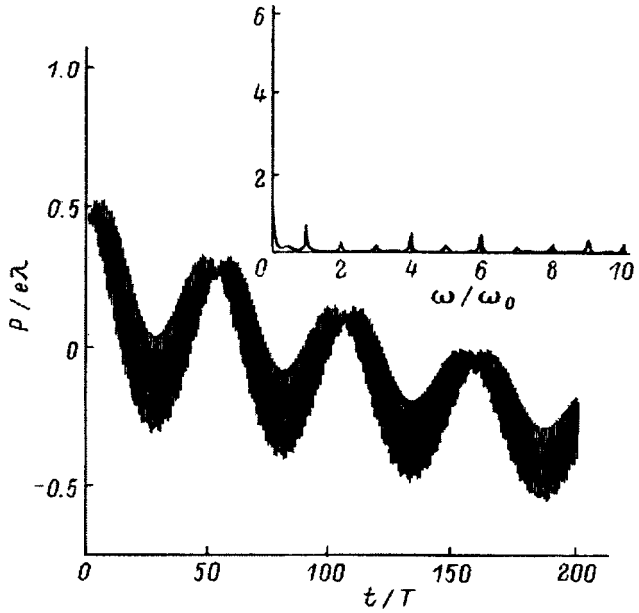

FIG. 4. Dipole moment versus time for an asymmetric structure with parameters $a_1=0.7\lambda$, $a_2=0.5\lambda$, and $b=0.3\lambda$ with $T=2.06t_0$ and $eU_0=0.05\Delta E_c$. Initial state: $\Psi(x,0)=|2\rangle^0$. Inset: Spectral density of the dipole moment.

undergoes a continuous relocation from one well into another with very small oscillations at integer-valued frequencies. The period of continuous relocation is determined by the relative arrangement of the quasienergy levels. The distance between the quasienergies equals $0.21\Delta E_c$, which corresponds to $T=96.82t_0$.

4. CONCLUSIONS

In the present paper the generation of harmonics of dipole radiation by a strong external electromagnetic field in the case of two tunnelling-coupled quantum wells was studied by solving the nonstationary Schrödinger equation numerically. The total intensity of the radiation was calculated by means of the temporal analog of the Kronig–Penney model for the example of second harmonic generation. The magnitude of the second harmonic generation effect in a system in a strong field in a resonance tunneling regime was compared to the ''double resonance'' effect in a system of three equidistant levels, where the maximum radiation obtains at frequency 2ω with small perturbations. It was noted that second harmonic generation in a strong field can be much stronger than in the case of a resonance radiation regime.

Harmonics generated in a two-level system in a strong field in a quasienergy level crossing regime was analyzed. It was established that the generation of the required harmonic of dipole radiation can be achieved in a controllable manner by using a controllable evolution of the electronic states in quantum-size structures. It was shown that symmetric structures in a strong field can serve as a good object for generation of even harmonics of radiation, which is in principle impossible with weak perturbations. It was noted that an optical rectification regime can be obtained with a special relative arrangement of three quasienergy levels and a definite choice of the initial state.

This work was supported by the Russian Fund for Fundamental Research and INTAS.

[a)]e-mail: kapaev@sci.lpi.ru

[1] E. Rosencher and Ph. Bois, Phys. Rev. B **44**, 11315 (1991).
[2] J. Z. Kaminski, J. Phys.: Condens. Matter **6**, 1577 (1994).
[3] H. Kuwatsuka and H. Ishikawa, Phys. Rev. B **50**, 5323 (1994).
[4] F. Kachar, H. Heinrich, and G. Bauer [Eds.], *Localization and Confinement of Electrons in Semiconductors*, Springer-Verlag, Berlin, 1990.
[5] N. Bloembergen *Nonlinear Optics*, Benjamin, N. Y., 1965 [Russian translation, Mir, Moscow, 1966].
[6] M. K. Gurnik and T. A. DeTemple, IEEE J. Quantum Electron. **QE-19**, 791 (1983).
[7] A. A. Gorbatsevich, V. V. Kapaev, and Yu. V. Kopaev, Zh. Éksp. Teor. Fiz. **107**, 1320 (1995) [J. Exp. Theor. Phys. **80**, 734 (1995)].
[8] Ya. Kousuke, F. Shechao, and Qing Hu, Phys. Rev. B **54**, 7987 (1996).
[9] Y. Dakhnovksii and R. Bavli, Phys. Rev. B **48**, 11020 (1993).
[10] Y. Dakhnovksii and R. Bavli, Phys. Rev. B **48**, 11010 (1993).
[11] Ya. Zel'dovich, Zh. Éksp. Teor. Fiz. **51**, 1492 (1966) [Sov. Phys. JETP **24**, 1006 (1967)].
[12] L. D. Landau and E. M. Lifshitz, *The Classical Theory of Fields*, Pergamon Press, N. Y. [Russian original, Nauka, Moscow, 1988].
[13] E. Rosencher, P. Bois, and J. Nagle, SPIE Proc. **1273**, 138 (1990).
[14] Opt. Spektrosk. **49**, 1024 (1980).
[15] R. Bavli and N. Metiu, Phys. Rev. A **47**, 3299 (1993).

Translated by M. E. Alferieff

Effect of the charge state of defects on the light-induced kinetics of the photoconductivity of amorphous hydrated silicon

O. A. Golikova

A. F. Ioffe Physicotechnical Institute, Russian Academy of Sciences, 194021 St. Petersburg, Russia
(Submitted May 29, 1997; accepted for publication June 7, 1997)
Fiz. Tekh. Poluprovodn. **32**, 345–348 (March 1998)

The photoconductivity and defect density in films of nondoped *a*-Si:H soaked with light ($W=114$ mW/cm^2, $\lambda<0.9$ μm) for 5 h were investigated. It is shown that $\sigma_{ph}\sim t^{-\gamma}$ and $N_D\sim t^{\beta}$, where $\gamma>\beta$ or $\gamma\approx\beta$, depending on the position of the Fermi level prior to light soaking, i.e., depending on the charge state of the defects: D^- and D^0 or D^+ and D^0. It is also shown that the light-induced kinetics of σ_{ph} is affected by a transition of the defects into the D^0 state because of a corresponding shift of the Fermi level during light soaking. © *1998 American Institute of Physics.* [S1063-7826(98)01103-X]

1. INTRODUCTION

The stability of the photoelectric parameters of amorphous hydrated silicon *a*-Si:H subjected to an external perturbation (light, electric field, and others) remains a key problem concerning device applications of this material. The Staebler–Wronski effect (SWE), discovered 20 years ago, consists of a drop in both the dark photoconductivity σ_d and the photoconductivity σ_{ph} of *a*-Si:H under exposure to intense illumination, i.e., degradation of σ_{ph} accompanying a shift of the Fermi level ε_F toward the center of the mobility gap occurs. Later it was established that the density of defects—broken Si–Si bonds (N_D)—increases under illumination. Since the ESR method was used, it was concluded that the light-induced defects are in the D^0 state and the degration of σ_{ph} is due to an increase in N_D.

Despite the very large number of studies on the SWE, the nature of this effect remains unclear. The literature contains ambiguous and sometimes even contradictory data on the role of different structural characteristics for the SWE. Even the role of hydrogen is still being debated.

It has recently been pointed out again that under illumination σ_{ph} decreases at a much higher rate than N_D increases; i.e., the light-induced kinetics of σ_{ph} is different from that of N_D.[1] Therefore, it is natural to assume that, aside from an increase in N_D, other changes influencing σ_{ph} occur in the structure of an *a*-Si:H film. Indeed, some light-induced changes in the structure of *a*-Si:H have been observed, but their influence on σ_{ph} remains unknown. For example, in Ref. 2 it was established that the SWE is accompanied by a decrease in the entropy of *a*-Si:H; it is assumed that short-range ordering of the structure occurs. Moreover, in Ref. 3 it was concluded on the basis of NMR data that the SWE is accompanied by changes in the structure of the film at the level of midrange ordering; it is assumed that this occurs as a result of a change in the charge state of defects. In Ref. 5 the characteristic features of the light-induced kinetics of σ_{ph} of nondoped *a*-Si:H films with different microstructure, determined by the deposition temperature ($T_s=133-267$ °C), were explained on the basis of a model of light-induced charge transfer on defects.[4]

In the present study we investigated the light-induced kinetics of σ_{ph} and N_D of *a*-Si:H films, which were deposited at $T_s=300$ °C and described in detail in Ref. 6. The position of the Fermi level of nondoped *a*-Si:H was varied in the limits $\varepsilon_c-\varepsilon_F=0.45-0.85$ eV (ε_c is the conduction band edge). The charge state of the defects was varied correspondingly: in the direction from D^- to D^0 and then to D^+.[7] The objective of the present work is to determine the effect of the charge state of the defects on the light-induced kinetics of σ_{ph} of *a*-Si:H.

2. EXPERIMENT

The films were soaked at room temperature for 5 h by light from a source with $W=114$ mV/cm^2 and $\lambda<0.9$ μm. The conductivity σ_{ph} measured as a function of the light-soaking time was approximated by a power-law function $\sigma_{ph}\sim t^{-\gamma}$, where γ characterizes the degradation rate.[8] The photoconductivity was measured at room temperature. The charge carrier generation rate was $G=10^{19}$ cm$^{-3}\cdot$s^{-1} and the photon energy was $h\nu=2$ eV. The defect density was also approximated by a power-law function: $N_D\sim t^{\beta}$. The defect density N_D was measured by the constant-photocurrent method, which in contrast to ESR yields information about the density of defects, irrespective of their charge state. The dark conductivity was measured in order to determine the light-induced shift of the Fermi level: $\varepsilon_c-\varepsilon_F=kT\ln\sigma_0/\sigma_d$, where $T=300$ K and $\sigma_0=150$ $\Omega^{-1}\cdot$cm^{-1}.

3. EXPERIMENTAL RESULTS AND DISCUSSION

Figure 1 shows curves of $N_D/N_D(0)$ versus the light-soaking time for a series of experimental *a*-Si:H films [here $N_D(0)$ is the presoaking defect density]. The parameter β, characterizing the rate of growth of N_D, was determined as a function of the position of the Fermi level $\varepsilon_c-\varepsilon_F$ (Fig. 2) on the basis of these data. We see that as $\varepsilon_c-\varepsilon_F$ increases, β at first increases and then decreases somewhat. The maximum

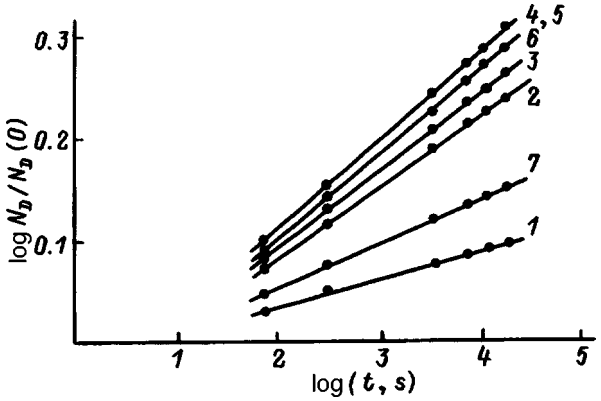

FIG. 1. Light-induced kinetics of defect density in a-Si:H films. $\varepsilon_c-\varepsilon_F$, eV: *1*—0.45, *2*—0.55, *3*—0.65, *4*—0.70, *5*—0.76, *6*—0.82, *7*—0.85.

value of β is attained for ''intrinsic'' a-Si:H ($\varepsilon_c-\varepsilon_F=0.70$ eV), which prior to soaking has the minimum defect density.[6] It should be noted that on this segment of the soaking time β does not exceed 0.1, i.e., N_D grows very slowly. One would expect that the rate of growth of N_D should increase with a further large increase in the soaking time, as in, for example, Ref. 9. However, in most cases, $N_D(t)$ can no longer be approximated by a simple power-law function [$N_D(t)$ is represented in the form of a so-called ''extended'' exponential]. The is also true for $\sigma_{\rm ph}(t)$. We will therefore confine our attention to a comparatively short light-soaking time, for which the rates of change of $\sigma_{\rm ph}$ and N_D (the quantities γ and β) can be conveniently compared.

Figure 3 shows $\sigma_{\rm ph}/\sigma_{\rm ph}(0)$ versus the light-soaking time for a series of experimental films [$\sigma_{\rm ph}(0)$ is the presoaking photoconductivity]. Figure 4 shows γ as a function of $\varepsilon_c-\varepsilon_F$. We see that two regions can be distinguished in Fig. 4: $\gamma=0.6-0.4$ in region I, after which γ is observed to drop rapidly, and $\gamma<0.1$ in region II. Thus, $\gamma>\beta$ in region I and $\gamma\simeq\beta$ in region II; i.e., a large disparity between the rate of growth of the defect density and the rate of decrease of the photoconductivity is observed only for region I.

The ''boundary'' between the regions I and II corresponds to the value of $\varepsilon_c-\varepsilon_F$ in intrinsic a-Si:H. This is the ''singular'' point on the curves showing nonmonotonic behavior of a number of structural parameters as a function of $\varepsilon_c-\varepsilon_F$ (Fig. 5): the density of defects, the content of bound hydrogen in the film, the Urbach parameter, the Raman frequency ω_{TO}, and the width $\Delta\omega_{TO}$ of the corresponding

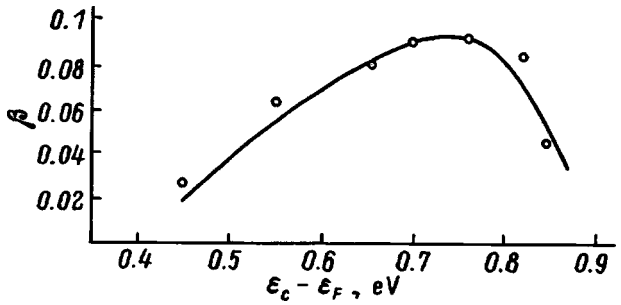

FIG. 2. The parameter β ($N_D\sim t^{\beta}$) versus the position of the Fermi level ($\varepsilon_c-\varepsilon_F$).

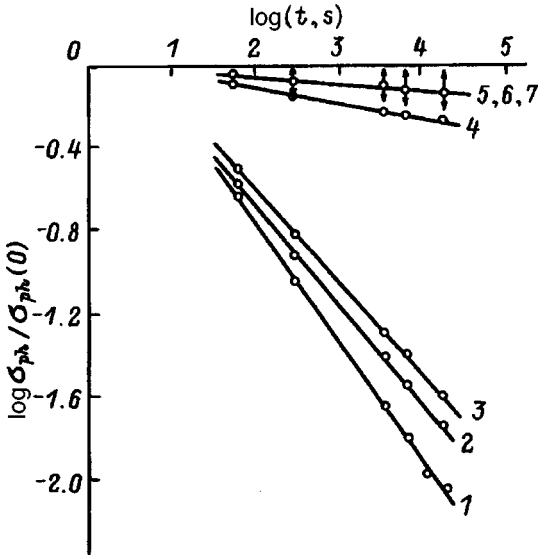

FIG. 3. Light-induced kinetics of the photoconductivity of a-Si:H films. The numbers of the films and the corresponding values of $\varepsilon_c-\varepsilon_F$ are the same as in Fig. 1. The arrows mark the limits of the changes in $\log\sigma_{\rm ph}/\sigma_{\rm ph}(0)$ for films Nos. 5–7.

band. Differences are also observed in the values of the microstructural parameter, R, and the optical mobility gap, E_G. Furthermore, as analysis of infrared and Raman spectra showed, region-II films are distinguished from region-I films by a larger scale of the structural nonuniformities. Nonetheless, the photoconductivity decreases monotonically as $\varepsilon_c-\varepsilon_F$ increases.[6] In the region I it drops together with the defect density and in region II it drops with increasing defect density. It is obvious that in the regions indicated the defects are in different charge states: In ''intrinsic'' a-Si:H ($\varepsilon_c-\varepsilon_F=0.70$ eV) defects are in the neutral state D^0, whereas as ε_F shifts toward ε_c or ε_v, an increasingly larger fraction of the defects is in the charge states D^- or D^+, just as in a-Si:H doped with donor or acceptor impurities.[10]

Indeed, the photoconductivity in region I is determined not by all defects (D^- and D^0) but rather only by the defects with a larger electron trapping cross section—D^0, whose relative fraction increases rapidly as $\varepsilon_c-\varepsilon_F=0.70$ eV is ap-

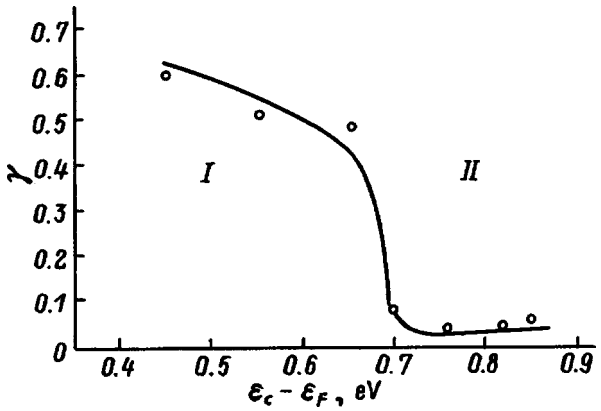

FIG. 4. The parameter γ ($\sigma_{\rm ph}\sim t^{-\gamma}$) versus the position of the Fermi level ($\varepsilon_c-\varepsilon_F$). The regions I and II are shown in the figure (see text for explanation).

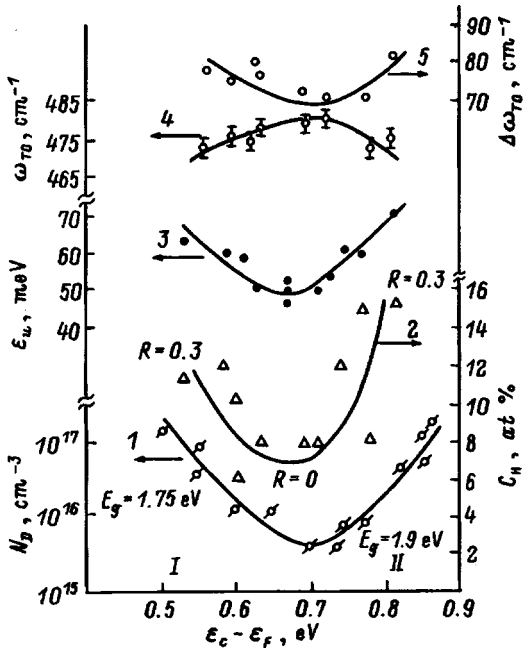

FIG. 5. Pre-light-soaking structural parameters of the films versus the Fermi level.[6] *1*—Defect density, *2*—bound hydrogen content, *3*—Urbach parameter, *4*—*TO*-phonon Raman frequency, *5*—width of *TO* peak. Data on the microstructural parameter R and the optical mobility gap E_g are also presented in the figure and regions I and II are shown (see Fig. 4).

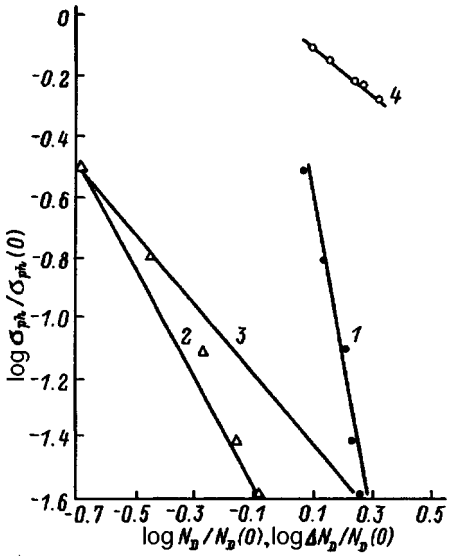

FIG. 6. Photoconductivity versus defect density during light soaking (film No. 3, see Figs. 1 and 3) ($\sigma(0)$ and $N_D(0)$—pre-light-soaking photoconductivity and defect density). Curve *1* was constructed as a function of $N_D/N_D(0)$, *2*—as a function of $\Delta N_D/N_D(0)$, *3*—as a function of D^0 defect density (see text for explanation). Curve 4 was constructed for film No. 4 (see Figs. 1 and 3) as a function of $N_D/N_D(0)$.

proached. In contrast, the photoconductivity in region II is determined by all defects (D^0 and D^+), whose density increases with distance from the point $\varepsilon_c-\varepsilon_F=0.70$ eV (Fig. 5).

Let us now return to the discussion of the results on light-induced kinetics of photoconductivity and re-examine the region I (Fig. 4). Since the light-induced defects are in the state D^0, even a small number of such defects strongly increases the effective electron trapping cross section. This is the reason why there is a large disparity between γ and β. In region II, as stated above, a large disparity between γ and β is not observed, since the formation of light-induced defects (D^0) cannot strongly alter the effective electron trapping cross section.

Thus, the data on the light-induced kinetics of $\sigma_{\rm ph}$ (Fig. 4) correspond to the data presented in Fig. 5, and they can be interpreted on the basis of the same ideas.

Next, the results obtained for region-I a-Si:H films were analyzed in order to determine the explicit form of the dependence of the photoconductivity on the defect density under light-soaking. In Fig. 6 (curve *1*) $\sigma_{\rm ph}/\sigma_{\rm ph}(0)$ is plotted as a function of $N_D/N_D(0)$ for one of the films. Before light-soaking it is characterized by the value $\varepsilon_c-\varepsilon_F=0.65$ eV and, according to Ref. 10, for it $N_D^0/N_D^-\simeq 0.1$. We see that $\sigma_{\rm ph}/\sigma_{\rm ph}(0)$ decreases rapidly with increasing $N_D/N_D(0)$: A power-law relation close to $\sigma_{\rm ph}\sim N_D^{-5}$ corresponds to the existing large disparity between β and γ (Figs. 2 and 4). Since $\sigma_{\rm ph}$ is determined not by all defects but only by those in the state D^0, one would expect an inverse proportionality between $\sigma_{\rm ph}/\sigma_{\rm ph}(0)$ and $\Delta N_D/N_D(0)$, where ΔN_D is the density of photoinduced defects, but this is not observed for region-I films. A relation close to $\sigma_{\rm ph}\sim(\Delta N_D)^{-2}$ (Fig. 6, curve *2*) is obtained for the films examined above.

However, the foregoing analysis of the results disregarded the light-induced shift of the Fermi level. According to the the data on σ_d for the film under study, after light soaking for 5 h ε_F shifts to the point corresponding to intrinsic a-Si:H, where all defects (presoaking and light-induced) are in the state D^0. Therefore, if at the initial stage of soaking, when $N_{D^0}/N_{D^-}\simeq 0.1$, the density of defects in the D^0 state can be assumed to equal ΔN_D, then at the end of soaking it equals N_D. Curve *3* in Fig. 6 was constructed on this basis. It indeed reflects, to a high degree of accuracy, the inverse proportionality between $\sigma_{\rm ph}$ and the density of defects in the state D^0.

Let us now consider the data obtained for intrinsic a-Si:H. Figure 6 shows $\log \sigma_{\rm ph}/\sigma_{\rm ph}(0)$ versus $\log N_D/N_D(0)$ for film *N4* (curve *4*). We see that $\sigma_{\rm ph}\sim N_D^{-1}$ (this corresponds to $\beta=\gamma$, Figs. 2 and 4), and since here $N_D=N_{D^0}$, we have $\sigma_{\rm ph}\sim N_{D^0}^{-1}$.

As shown above, a similar result is obtained for region-I films provided that the change in the ratio between N_{D^-} and N_{D^0} at the initial stage of light soaking and the shift of the Fermi energy into the point $\varepsilon_c-\varepsilon_F=0.70$ eV at the end of soaking are taken into account. It is obvious that this is not required for intrinsic a-Si:H. In the case of light-soaked region-II films the effect of D^0 defects on their photoconductivity cannot be determined, since the simultaneously existing D^+ defects are even more effective electron trapping centers.

4. CONCLUSIONS

Investigations of the light-induced kinetics of the photoconductivity ($\sigma_{\rm ph}\sim t^{-\gamma}$) and defect density ($N_D\sim t^{\beta}$) for nondoped a-Si:H films variations of the position of the Fermi level ($\varepsilon_c-\varepsilon_F=0.45-0.85$ eV) established that the

ratio of γ and β depends strongly on $\varepsilon_c-\varepsilon_F$. In region I, where $\varepsilon_c-\varepsilon_F=0.45-0.69$ eV, γ is much larger than β. Then, β decreases rapidly and in region II, for a large $\varepsilon_c-\varepsilon_F$, $\gamma\simeq\beta$. The characteristic features of the light-induced kinetics of $\sigma_{\rm ph}$ can be explained by the differences of the charge states of the defects, depending on the position of ε_F: predominantly D^- in region I, D^0 for the intrinsic material ($\varepsilon_c-\varepsilon_F=0.70$ eV), and predominantly D^+ in region II. As a result, in region I even a comparatively small light-induced increase in N_D results in a large increase in the effective electron trapping cross section, while for intrinsic a-Si:H and in region II this does not occur, since intrinsic a-Si:H and region-II films are distinguished by a higher stability of $\sigma_{\rm ph}$. It was also established that not only the presoaking charge state of defects but also the change in the charge state during soaking and as a result of Fermi level shifts, which occur so that the Fermi level ultimately is located at the point $\varepsilon_c-\varepsilon_F=0.70$ eV, influences the light-induced kinetics of the photoconductivity of a-Si:H. Taking this circumstance into account, it was shown that the photoconductivity and density of defects during soaking are related as $\sigma_{\rm ph}\sim N_{D^0}^{-1}$, which is obtained automatically for intrinsic a-Si:H, since for it $\gamma=\beta$ and all defects (presoaking and induced) are in the state D^0.

In summary, the interpretation of the data on the light-induced kinetics of the photoconductivity of a-Si:H, which were obtained by us, does not require making any assumptions about light-induced structural changes that affect $\sigma_{\rm ph}$ other than an increase in the density of defects. However, the changes occurring in the kinetics of $\sigma_{\rm ph}$ as a function of the position of the Fermi level are due to the above-listed structure features of the films prior to light-soaking, which also depend on $\varepsilon_c-\varepsilon_F$: The different charge states of defects are interrelated with the characteristic structural features of a-Si:H films.

This work was supported by INTAS Grant No. 931916.

[1] P. Tzanetakis, N. Kopidakis, M. Androulidaki, C. Kalpouzos, P. Stradins, and H. Fritzsche, MRS Symp. Proc. **377**, 245 (1995).
[2] C. M. Fortmann, R. M. Dawson, H. Y. Liu, C. R. Wronski, J. Appl. Phys. **76**, 768 (1994).
[3] H. M. Branz and P. A. Fedders, MRS. Symp. Proc. **338**, 129 (1994).
[4] F. Irrera, J. Appl. Phys. **75**, 1396 (1994).
[5] D. Caputo, G. de Cesare, F. Irrera, F. Palma, M. C. Rossi, G. Conte, G. Nobile, and G. Fameli, J. Non-Cryst. Solids **170**, 278 (1994).
[6] O. A. Golikova and V. Kh. Kudoyarova, Fiz. Tekh. Poluprovodn. **29**, 1128 (1995) [Semiconductors **29**, 584 (1995)].
[7] O. A. Golikova, Fiz. Tekh. Poluprovodn. **25**, 1517 (1991) [Sov. Phys. Semicond. **25**, 915 (1991)].
[8] E. Sauvain, P. Pippoz, A. Shan, and J. Hubin, J. Appl. Phys. **75**, 1772 (1994).
[9] P. Morin, C. Godet, B. Equer, and P. Roca i Cabarrocas, in *Proceedings of the 12th European Photovoltaic Solar Energy Conference*, Amsterdam, April 1994, p. 687.
[10] M. Sturzmann and W. B. Jackson, Solid State Commun. **62**, 153 (1987).

Translated by M. E. Alferieff

Effect of ion irradiation of amorphous-silicon films on their crystallization

N. V. Bakhtina, A. I. Mashin, A. P. Pavlov, and E. A. Pitirimova

N. I. Lobachevskiĭ Nizhegorod State University, 603600 Nizhniĭ Novgorod, Russia
(Submitted April 3, 1996; accepted for publication October 2, 1997)
Fiz. Tekh. Poluprovodn. **32**, 349–352 (March 1998)

The change in the structure of amorphous Si films implanted with inert-gas ions and chemically active impurity was investigated by transmission electron microscopy and electron diffraction methods. It was shown that as a result of radiation-induced formation of thermally stable vacancy complexes, Si films irradiated with Ar^+ and P^+ ions with doses above 7×10^{15} cm^{-2} do not crystallize up to temperature 680 °C. It was established that crystallization of Si films after implantation of lower doses of P^+ ions accelerates the growth of grains in the films as a compared with the unirradiated films. A model of the mechanism by which the ion irradiation influences the crystallization of Si films is discussed. [S1063-7826(98)01203-4]

1. INTRODUCTION

Polycrystalline Si is a promising material for modern microelectronics. It is used for gates in MOS transitors, decouplers for interconnections, resistors, and so on. One of the most important parameters of polycrystalline Si is its fine structure. To obtain polycrystalline-Si films with satisfactory performance characteristics the grain size must be no less than 20–30 nm. To achieve such characteristics in modern technology it is necessary to employ temperatures exceeding 800 °C, which has a deleterious effect on other structures in the electronic devices fabricated.

The objective of the present work is to investigate the effect of ion irradiation of amorphous Si films on their crystallization and to determine the physical processes and mechanisms of the effect of ion implantation on heat treatment.

2. EXPERIMENTAL PROCEDURE

The initial films were obtained by molecular-beam deposition of Si from a sublimating source on a silicon substrate coated with a thin ($\sim$0.1 μm) layer of SiO_2. Films of the order of 100 nm thick were used. The substrate temperature in the process of formation of the layers did not exceed 200 °C. The residual-gas pressure in the growth chamber was equal to $(1.6-2.5)\times10^{-4}$ Pa. The Si films obtained were irradiated with 40-keVP and Ar ions with doses in the range $10^{15}-10^{16}$ cm^{-2}. Ion implantation was performed in an ILU-3 accelerator with a room-temperature target. Post-implantation annealing was conducted in a 10^{-4} Pa vacuum at temperatures of 680 and 800 °C. The annealing times were equal to 60 min at $T=680$ °C and 30 and 60 min at $T=800$ °C.

Films for electron-diffraction and transmission electron microscopy investigations were separated from the substrates by etching off the intermediate SiO_2 layer. The atomic-distribution function was reconstructed from the electron-scattering data by the Fourier analysis method.[1–3] It should be noted that most electron-diffraction investigations of the structure of amorphous substances are performed taking into account the intensity up to values of the parameter $s=4\pi(\sin\alpha)/\lambda<8$ Å^{-1}, where α is the diffraction angle and λ is the electron wavelength. The radial distribution is calculated by integrating up to the most diverse values of the upper limit and corrections for the effect of the cutoff, which investigators always encounter, are disregarded. A consequence of the experimental cutoff of the intensity curve is, as pointed out in Ref. 4, that the coordination number is overestimated (in some cases by up to 18%). In Ref. 4 a correction factor, which we employed for determining the coordination number, is introduced in this connection.

We employed the methods proposed in Refs. 5 and 6 to obtain information about the value of the dihedral angle θ, characterizing the rotation of the silicon tetrahedra relative to one another, and about the structure of the third coordination sphere.

The investigations of polycrystalline Si were performed on an ÉM-200 electron microscope with an accelerating voltage of 150 kV. Grain size was measured with a spectrum projector, giving a twentyfold magnification, and histograms of the grain-size distribution in polycrystalline-Si film were constructed from these data.

3. EXPERIMENTAL RESULTS AND DISCUSSION

The initial amorphous-Si films were irradiated with Ar and P ions with doses $D=10^{15}$, 3×10^{15}, 5×10^{15}, 7×10^{15}, and 10^{16} ions/cm^2. The films retained their amorphous structure after irradiation. Post-implantation annealing at $T=680$ °C for 60 min led to crystallization of the films irradiated with the three lowest doses from the chosen range (irrespective of the type of ion). In this case, sharp rings characteristic of a polycrystalline structure are observed in the electron diffraction patterns. Complete crystallization did not occur in films irradiated with the two higher doses from the chosen range (irrespective of the type of ion). Separation of the second and third diffraction rings was not observed in the electron diffraction patterns, and the first ring was found to be diffuse, suggesting that the structure of these films remained amorphous. To explain this fact, which we attribute to the influence not only of irradiation but also the

TABLE I. Short-range order parameters of initial and irradiated amorphous-Si films.

Irradiation with ions	D, cm^{-2}	ρ_0, Å^{-3}	n_1	r_1, Å	n_2	r_2, Å	φ_b, °	$\Delta\varphi_b$, °	$\overline{\theta}$, °
Nonirradiated Si	0	0.045	3.95	2.35	12.00	4.04	119	36	15
Ar^+	1×10^{15}	-	-	-	-	-	-	-	-
Ar^+	3×10^{15}	-	-	-	-	-	-	-	-
Ar^+	5×10^{15}	0.045	3.94	2.35	12.04	3.89	112	33	14
Ar^+	7×10^{15}	0.043	3.93	2.35	12.00	4.00	116	34	16
Ar^+	1×10^{16}	0.043	3.92	2.35	11.85	4.03	117	34	31
P^+	1×10^{15}	-	-	-	-	-	-	-	-
P^+	3×10^{15}	0.043	3.93	2.35	12.02	4.06	119	36	33
P^+	5×10^{15}	0.042	3.63	2.35	12.10	4.00	116	34	37
P^+	7×10^{15}	0.041	3.92	2.35	12.03	4.16	122	31	36
P^+	1×10^{16}	0.039	3.76	2.35	11.93	4.15	121	30	36

parameters of the annealing process, structural investigations of the films were performed after irradiation and after annealing.

The radii (r_1 and r_2) of the first and second coordination spheres, the first and second coordination numbers (n_1 and n_2), the angle φ_b between the bonds, and the dihedral angle θ were determined from the radial distribution curves (the results are presented in Table I). The data obtained again confirm that short-range order, characteristic of crystal Si, remains in a-Si. Structural disorder is manifested as a small deviation of n_1 from the value 4, which is characteristic of crystalline Si and as a deviation of the average angle $\overline{\theta}$ between the bonds from the ideal tetrahedral angle 109°28′. The decrease in the coordination number can be explained by the presence in a-Si of dangling bond (or vacancy) type defects. Thus, some atoms will have not 4 but 3 nearest neighbors. But the relative fraction of such atoms is very small, so that the resulting coordination number will be slightly less than 4. The value of the dihedral angle $\theta=15°$ for the initial a-Si indicates that an obstructing configuration of tetrahedra, which is characteristic of an amorphous structure consisting of five-unit rings,[7,8] predominates in this material. An estimate of the variance in the values of the valence angles gives $\Delta\varphi_b=36°$. This value is greater than the value for a-Si obtained by high-frequency ion-plasma deposition in Ref. 6, where $\Delta\varphi_b=22°$. This indicates that the structural disordering is greater in our initial films.

The choice of Ar^+ and P^+ impurities for deeper study of the structural rearrangements arising in amorphous Si with ion implantation was not made randomly. Phosphorus actively incorporates itself into the Si lattice. Having approximately the same covalent radius as Si, it does not generate high local stresses. Argon, however, because of its inertness, does not form any bonds with Si and does not affect the length of the Si–Si bond.

Ion implantation in a film introduces radiation-induced defects (vacancies and vacancy complexes). Since the bond length in a continuous network remains virtually unchanged, the appearance of such defects can be interpreted as a decrease in the average atomic density. In addition, the higher the ion (Ar^+ or P^+) irradiation dose, the more defects are produced and the lower the density of the film is (as one can see from Table I). In this connection, the average number of nearest neighbors becomes even smaller than in the initial a-Si film; the second coordination numbers also decrease with increasing dose.

Moreover, as a result of irradiating the films, the dihedral angle increases with dose. This attests to an increase in the number of star-shaped configurations of tetrahedra.[6] For $\theta=31°$ or 36° (which is characteristic of films irradiated with a high dose of Ar and P, respectively) the relative fraction of star-shaped configurations becomes equal to that of blocking configurations. However, θ increases with dose differently for films irradiated with different ions. Because of its chemical activity and capability to incorporate itself in the lattice, phosphorus promotes rotation of the tetrahedra. This shows up even at low doses, when the tetrahedra are found to be rotated relative to one another by an angle of the order of 33°; i.e. the number of star-shaped configurations characteristic of the crystal increases. This is manifested as an increase in grain size during the subsequent annealing (see below). Because of its inertness, argon retards the restructuring process, and rotation of the tetrahedra occurs gradually with increasing irradiation dose.

When amorphous films are annealed, they should crystallize and polycrystalline grains should form. Annealing at $T=680$ °C for 60 min is found to be sufficient to produce a crystal structure of the initial films with an average grain size

TABLE II. Structural parameters of Si films after irradiation and annealing at $T=680$ °C for 60 min.

Irradiation with ions	D, cm^{-2}	Film structure	Grain size d, Å	
			variance	average
Nonirradiated Si	0	Polycrystalline	240–280	260
Ar^+	1×10^{15}	Polycrystalline	120–160	140
Ar^+	3×10^{15}	Polycrystalline	200–240	220
Ar^+	5×10^{15}	Polycrystalline	200–280	240
Ar^+	7×10^{15}	Amorphous	-	-
Ar^+	1×10^{16}	Amorphous	-	-
P^+	1×10^{15}	Polycrystalline	160–280	220
P^+	3×10^{15}	Polycrystalline	200–280	260
P^+	5×10^{15}	Polycrystalline	300–440	360
P^+	7×10^{15}	Amorphous	-	-
P^+	1×10^{16}	Amorphous	-	-

TABLE III. Short-range order parameters of Si after irradiation with Ar and P ions and annealing at $T=680$ °C for 60 min.

Irradiation with ions	D, cm^{-2}	ρ_0, Å^{-3}	n_1	r_1, Å	n_2	r_2, Å	φ_b, °	$\Delta\varphi_b$, °	$\overline{\theta}$, °
Ar^+	7×10^{15}	0.045	3.99	2.35	12.09	3.94	113	33	33
Ar^+	1×10^{16}	0.046	3.98	2.35	12.08	3.93	114	35	31
P^+	7×10^{15}	0.043	4.06	2.35	11.98	4.11	113	28	38
P^+	1×10^{16}	0.044	4.062	2.35	12.08	3.97	116	35	31

of the order of 260 Å. However, it should be noted that a large variance is observed in the grain-size distribution.

The situation is more complicated in the case of irradiated Si. In the case where samples irradiated with the three lowest doses (irrespective of the type of ion) are annealed, a crystalline structure, whose parameters are given in Table II, is formed and the average grain size is observed to increase with dose. The effect of P is manifested in the fact that the average grain size in films irradiated with P ions is larger than in the initial films. The effect of P first appears at the irradiation stage, when P is capable of increasing the number of star-shaped configurations of tetrahedra and therefore making the structure approach a crystal structure. This fact plus the additional thermally stimulated formation of Si–P bonds in the process of crystallization probably have the effect that the average grain size in the irradiated films is larger than in the nonirradiated films. On the other hand, by virtue of its inertness, argon retards the crystallization process. For this reason, here the grain size is on the average smaller than in the nonirradiated annealed samples (see Table II). These data correlate well with the changes in the dihedral angle. In Ref. 9 it is noted that for polycrystalline Si films the perfection of the crystals and the grain size increase as the deposition temperature increases from 800 to 1100 °C. In the present work we achieve the same effect by using only low-temperature processes, which is very important for the technology of fabrication of integrated circuits.

The defect density increases with irradiation dose.[10] During heat treatment some defects are annealed and some participate in the formation of more intricate complexes[11] that slow down the reconstruction of the crystal lattice. Since the defect-formation power of Ar is approximately the same as that of P,[12,13] the situations in films irradiated with Ar and P are similar. We assume that in our case a complex defect is a pentavacancy, whose annealing temperature is $\geqslant 750$ °C.[14] The results of structural investigations of these films are presented in Table III. Since annealing decreases the defect density, the density of these films is higher than that immediately after irradiation (see Table I). This shows up in the coordination number—it also increases. The valence angle decreases and becomes closer to the ideal tetrahedral angle. All these factors attest to onset of rearrangement of the structure from amorphous to crystalline.

To check our assumption that a defect such as a pentavacancy interferes with the annealing of samples irradiated with high doses, annealing was performed at a temperature higher than the annealing temperature of the pentavacancy, i.e., at $T>750$ °C. Treatment of the samples at $T=800$ °C for 30 and 60 min results in complete crystallization of the films irradiated with all doses from the chosen range. It should be noted that doubling the annealing time ($T=800$ °C) approximately doubles the average grain size (Table IV), and the average grain size after irradiation and annealing is larger than in the nonirradiated annealed films. In addition, it should be noted that annealing at $T=800$ °C for 30 min leads to the formation of a structure with approximately the same average grain size as that obtained with annealing for 60 min at $T=680$ °C. Therefore, to obtain a polycrystalline-Si structure with prescribed parameters there is no need to increase the temperature, it is sufficient to increase the annealing time at lower temperatures.

TABLE IV. Structural parameters of Si films after irradiation and annealing at $T=800$ °C.

Irradiation with ions	D, cm^{-2}	Annealing time t, min	Grain size d, Å	
			variance	average
Irradiated Si	0	30	180–240	210
P^+	1×10^{15}	30	180–240	220
P^+	3×10^{15}	30	200–240	229
P^+	5×10^{15}	30	200–260	240
P^+	7×10^{15}	30	200–280	240
P^+	1×10^{16}	30	200–320	256
Nonirradiated Si	0	60	380–460	420
P^+	1×10^{15}	60	360–480	420
P^+	3×10^{15}	60	300–480	437
P^+	5×10^{15}	60	360–560	466
P^+	7×10^{15}	60	360–600	500
P^+	1×10^{16}	60	360–720	569

4. CONCLUSIONS

1. It has been established that irradiation with P^+ ions with dose less than 7×10^{15} cm^{-2} followed by annealing of amorphous Si films increases the average grain size as compared with annealed nonirradiated samples. This is caused by the chemical activity of P, which promotes an increase in the dihedral angles.

2. Irradiation with Ar^+ and P^+ ions with doses 7×10^{15}–10^{16} cm^{-2} has the effect that, as a result of radiation-induced formation of thermally stable vacancy complexes, Si films do not crystallize with an annealing temperature $T=680$ °C.

[1] L. I. Tatarinova, *Electron Diffraction Analysis of Amorphous Materials* [in Russian], Nauka, Moscow, 1972.
[2] B. K. Vaĭnshteĭn, Kristallografiya **2**, 29 (1957).
[3] A. F. Skryshevskiĭ, *Structural Analysis of Liquids and Amorphous Bodies:*

Textbook of Physical Professions [in Russian], Vyssh. Shkola, Moscow, 1980.
[4] Ya. I. Statsiv, Author's Abstract of Doctoral Dissertation, L'vov (1985).
[5] N. F. Mott and E. A. Davis, *Electronic Processes in Non-Crystalline Materials*, Clarendon Press, Oxford, 1971 [Russian translation, Mir, Moscow, 1974].
[6] V. N. Gordeev, A. I. Popov, and V. A. Filikov, Neorg. Mater. **16**, 1733 (1980).
[7] R. Grigorovici and R. Manaila, Thin Solid Films **1**, 343 (1967).
[8] M. V. Coleman and D. J. D. Thomas, Phys. Status Solidi **25**, 241 (1968).
[9] E. I. Sokolov, E. P. Prikhod'ko, S. P. Pavlov, and I. V. Korobov, Élektron. Tekhn. Materialy, No. 1, 2412 (1977).
[10] N. N. Gerasimenko, A. V. Dvurechenskiĭ, and G. P. Levedev, Fiz. Tekh. Poluprovodn. **7**, 2297 (1973) [Sov. Phys. Semicond. **7**, 1530 (1973)].
[11] N. N. Gerasimenko, V. B. Glazman, and A. V. Dvurechenskiĭ, Fiz. Tekh. Poluprovodn. **9**, 1734 (1975) [Sov. Phys. Semicond. **9**, 1139 (1975)].
[12] *Tables of the Spatial Distribution Parameters of Ion-Implanted Impurities* [in Russian], Belorussian State University Press, Minsk, 1980.
[13] D. I. Mirkin, *Handbook of X-Ray Crystallographic Analysis of Polycrystals* [in Russian], Fizmatgiz, Moscow, 1961.
[14] *Point Defects in Solids: Collection of Works* [Russian translation], Mir, Moscow, 1979.

Translated by M. E. Alferieff

Photosensitivity of porous silicon–layered III–VI semiconductors heterostructures

A. A. Lebedev and Yu. V. Rud'

A. F. Ioffe Physicotechnical Institute, Russian Academy of Sciences, 194120 St. Petersburg, Russia

V. Yu. Rud'

St. Petersburg State Technical University, 195251 St. Petersburg, Russia
(Submitted June 6, 1997; accepted for publication June 10, 1997)
Fiz. Tekh. Poluprovodn. **32**, 353–355 (March 1998)

Rectifying heterojunctions with photosensitivity 1–5 V/W at $T=300$ K were obtained by forming optical contacts between free porous silicon and layered InSe and GaSe semiconductors. A wide-band photovoltaic effect was obtained when these heterostructures were illuminated on the free porous silicon plate side. The long-wavelength photosensitivity edge of these devices is determined by direct transitions in InSe or GaSe, respectively. It is concluded that heterojunctions based on free porous silicon plates can be used as wide-band phototransducers.
 [S1063-7826(98)02603-9]

The discovery of efficient visible-range radiative recombination at first in silicon and then in binary diamond-like semiconductors after anodic etching is unquestionably of interest for studying the potential applications of such materials in optoelectronics.[1–3] To this end, the possibilities of producing and the properties of different types of energy barriers on porous silicon and other substances are under study. In the present paper we report the results of an investigation of the photosensitivity of heterojunctions (HJs), obtained by the method of putting plates of free porous silicon (FPS) into optical contact with plates of direct-gap compounds InSe and GaSe with a band gap at 300 K of 1.23 and 2.0 eV, respectively.[4]

InSe and GaSe single crystals were grown by directed crystallization of nearly stoichiometric melts. The electrically homogeneous crystals were of n-type with free electron density $\approx 10^{14}-10^{16}$ cm^{-3} at 300 K. To produce HJs, thin (40–80 μm) plane-parallel wafers with average dimensions of 4×4 mm^2 and high-quality (0001) planes were pricked from the ingots. The high quality of the (0001) faces is due to the strong anisotropy of the interatomic forces in III–VI semiconductors.[4]

Free porous silicon films 40–100 μm thick were used as the second component of the HJs. The free films were obtained by anodic etching of the initial p-Si wafers with (111) orientation.[5] The optical quality of the surface of the FPS wafers, which is formed by etching on the single-crystal silicon side and remains after separation from the substrate, was found to be approximately the same as that of III–VI wafers. The exterior surface of the FPS wafers was appreciably worse in most cases.

The heterojunctions were obtained by uniform mechanical clamping of FPS wafers and III–VI crystals together in a special holder. Contacts with each component of the HJ were soldered using pure indium. The structures obtained in this manner had diode current-voltage characteristics with a rectification coefficient of the order 5–10 at $\simeq 10$ V. The forward direction in both types of structures was obtained with a negative polarity of the external voltage on the III–VI crystals. A photo-emf with the III–VI crystals being charged negatively relative to the FPS appears when the HJ is illuminated. The photosensitivity was higher in the case of FPS side illumination and reached $\simeq 1-5$ V/W. The sign of the photo-emf did not depend on the photon energy and the location of the light probe on the surface of the HJ. In Ref. 6 it was shown that the InSe–InSe and GaSe–GaSe structures obtained by putting these crystals into optical contact have linear current-voltage characteristics, i.e. rectifying barriers do not form on the InSe and GaSe surfaces. It can be concluded from these facts that the photovoltaic effect is due to the separation of nonequilibrium pairs by the active region forming in the HJ between the FPS and III–VI surfaces.

The quantum efficiency η was measured on the linear section of the curve of the photo-emf versus the intensity of the light incident on the sample and was normalized to the incident photons. The η spectra for several samples are displayed in Figs. 1 and 2. In the case of InSe/FPS HJs the long-wavelength photosensitivity edge is characterized by an exponential photon energy dependence and it possesses at $\hbar\omega=1.23$ eV a sharp step or inflection in the spectral dependences of η for different HJs (Fig. 1). The position of the long-wavelength edge of η on the energy axis makes it possible to attribute this edge to the onset of interband transitions in InSe. In the experiments, contacts of different FPS wafers were used (Fig. 1, curves *1* and *2*) or the same FPS wafer was put into contact with the same InSe surface but using different surfaces (Fig. 1, curves *2* and *3*). The slope of the exponential edge of η varies from 11.5 to 38 eV^{-1}, which could be due to variations in the quality of the contact boundary. On the whole, in contrast to the current-voltage characteristics, the photo-emf spectra of these HJs were reproducible when one FPS wafer was replaced by another or when the different FPS–InSe contact surfaces were used (Fig. 1).

The main feature of the spectra of η in these structures is that the photoresponse increases in the experimental range of $\hbar\omega$ right up to 3.5 eV. The step near $\hbar\omega\simeq 1.6$ eV corresponds to the spectral position of the wide band of stationary photoluminescence of FPS, while the increase in photoresponse for $\hbar\omega>2$ eV falls in the range of the ''fast'' component of photoluminescence of porous silicon.[7] Therefore, there are grounds for assuming that the photosensitivity of

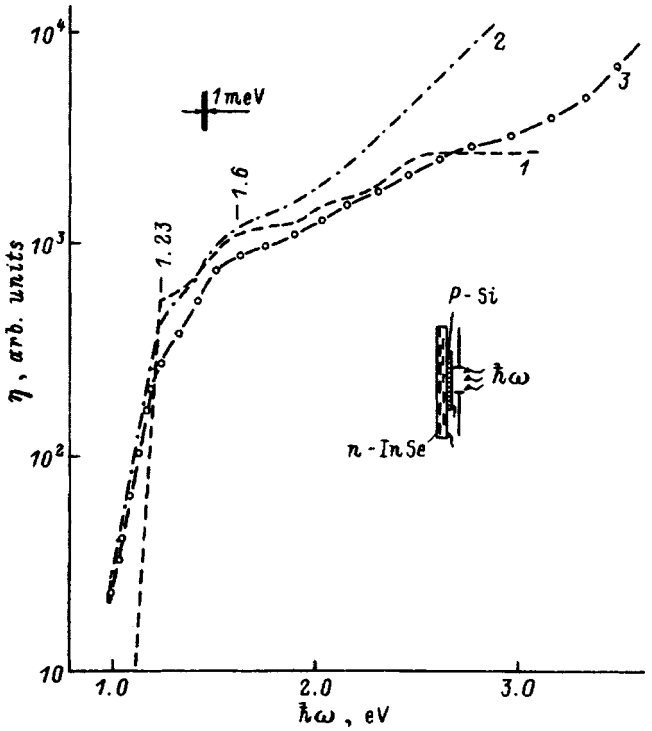

FIG. 1. Spectral dependences of the relative photoconversion quantum efficiency η for InSe/FPS heterojunctions at $T=300$ K. Inset: Construction of the HJ and its illumination scheme. FPS–InSe contact surface: *1, 2*—plane on the substrate side, *3*—plane on the etchant side. Wafer thicknesses, μm: *1* — 40, *2, 3* — 80, InSe — 80.

these HJs and the photoluminescence of FPS are due to the same optical transitions in FPS.

A HJ of a different form was obtained by putting the same FPS wafers in contact with *n*-GaSe wafers. The spectral curves of η for these junctions are similar to the preceding curves (Fig. 2), but the exponential long-wavelength edge of $\eta(\hbar\omega)$ is shifted in the short-wavelength direction in accordance with the increase in E_G. Its slope in such HJs is usually of the order of 35–40 eV^{-1} and is determined by direct interband transitions in GaSe. As the photon energy increases above the band gap of GaSe, the photosensitivity either increases (Fig. 2, curve *1*) or remains virtually unchanged in the region $\hbar\omega \simeq 2-2.6$ eV and a short-wavelength dropoff is observed only for $\hbar\omega \gtrsim 2.6$ eV. Figure 2 shows the typical spectra $\eta(\hbar\omega)$ for two HJs differing only by the FPS wafers used for contact, which were obtained in different processes, and ''set'' with the same side, which was turned toward the silicon substrate during the preparation of the FPS, on the same face of *n*-GaSe. Since no differences were observed in the spectra $\eta(\hbar\omega)$ for the same FPS wafers in contact with *n*-GaSe, there are grounds for assuming that the dropoff of η for $\hbar\omega > 2.6$ eV (Fig. 2, curve *2*) is due to the appearance of interface recombination of nonequilibrium carriers when the FPS is joined with GaSe. The fact that in the second type of HJ (Fig. 2, curve *1*) for $\hbar\omega > 2.6$ eV we no longer observe the short-wavelength growth of η (Fig. 1) appearing for InSe/FPS structures is likewise consistent with the conjecture made above that an increase in recombination occurs at the interface when InSe replaced by GaSe.

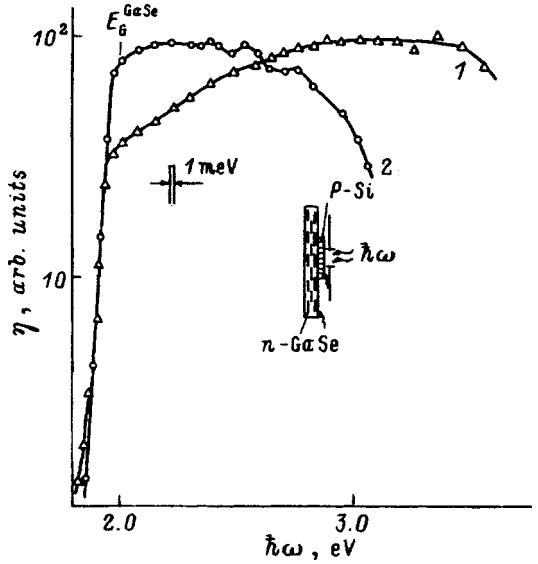

FIG. 2. Spectral dependences of η for GaSe/FPS heterojunctions at $T=300$ K. Inset: Construction of the HJ and its illumination scheme. Number of HJs: *1*—25–11, *2*—27–5. FPS–GaSe contact occurs along the plane on the substrate side. Wafer thicknesses, μm: *1*—80, *2*—40, GaSe—25.

The photosensitivity of the obtained HJs under illumination with linearly polarized radiation in a direction normal to the plane of the FPS does not show any dependence on the position of the polarization plane in the entire region of photosensitivity. This is due to the fact that the light enters the active region of the HJ along the isotropic direction of the III–VI crystals and therefore there is no natural photopleochroism.

In summary, a wide-band photovoltaic effect is observed in III–VI/FPS heterojunctions obtained by the optical-contact method. This indicates that an effective energy barrier forms at the boundary of the two semiconductors. Such structures can be used to produce wide-band phototransducers, whose long-wavelength sensitivity edge can be regulated between certain limits by varying the composition of the solid solutions InSe–GaSe.[4]

We thank E. V. Astrov for providing the FPS samples and for a discussion of the results of the investigations.

This work was supported in part by the program ''Physics of solid-state nanostructures'' (Project No. 1-079/4).

[1] L. T. Canham, Appl. Phys. Lett. **57**, 1046 (1990).
[2] A. A. Lebedev and Yu. V. Rud', Pis'ma Zh. Tekh. Fiz. **21**, 80 (1995) [Tech. Phys. Lett. **21**, 79 (1995)].
[3] A. A. Lebedev and Yu. V. Rud', Pis'ma Zh. Tekh. Fiz. **22**, 12 (1995) [Tech. Phys. Lett. **22**, 483 (1995)].
[4] *Reference Data on the Physical and Chemical Properties of Semiconductor Materials* [in Russian], Nauka, Moscow, 1978.
[5] E. V. Astrova, A. A. Lebedev, A. D. Remenyuk, and Yu. V. Rud', Fiz. Tekh. Poluprovodn. **29**, 1649 (1995) [Semiconductors **29**, 858 (1995)].
[6] V. L. Bakumenko, Z. D. Kovalyuk, L. N. Kurbatov, V. G. Tagaev, and V. F. Chishko, Fiz. Tekh. Poluprovodn. **12**, 374 (1978) [Sov. Phys. Semicond. **12**, 216 (1978)].
[7] V. F. Agekyan, Yu. V. Rud', Yu. A. Stepanov, and A. A. Lebedev, Fiz. Tverd. Tela (St. Petersburg) **38**, 2994 (1996) [Phys. Solid State **38**, 1637 (1996)].

Translated by M. E. Alferieff

Magnetic-resonance spectroscopy of porous quantum-size structures

A. I. Mamykin, V. A. Moshnikov, and A. Yu. Il'in

St. Petersburg State Electrical Engineering University, 197378 St. Petersburg, Russia
(Submitted September 9, 1997; accepted for publication October 2, 1997)
Fiz. Tekh. Poluprovodn. **32**, 356–358 (March 1998)

The results of investigations of nuclear magnetic resonance of water protons in porous silicon are reported. It is shown that magnetic-resonance spectroscopy with a ''flexible probe'' consisting of water molecules is an effective method for analyzing porous quantum-size structures with a complicated spatial configuration of the pores. The ''NMR isotherms'' of hydrated layers of porous silicon obtained in different technological regimes are presented and discussed. Sorption processes are studied and a model is proposed for forming water monolayers on a porous surface. It is established that a por fine structure with an average diameter of 1.4 nm is present in the layers. © *1998 American Institute of Physics.* [S1063-7826(98)02703-3]

The interest shown in quantum-size structures in recent years, specifically, porous layers formed in crystalline silicon, has stimulated an intense search for methods of investigating such objects. The method of nuclear magnetic resonance (NMR), used for detecting water molecules sorbed in a porous layer of silicon,[1] makes it possible to develop a unique ''flexible probe'' that can penetrate into atomic-size pores with configurations of unlimited complexity. The characteristic features and the character of the experimental NMR spectra of hydrated layers of porous silicon, employed for moisture sensors, have been discussed in Ref. 2.

This paper reports the results of magnetic-resonance spectroscopy of porous silicon layers in connection with the technological conditions of production of the silicon and proposes a model for the formation of water monolayers sorbed by the porous surface. Predehydrated samples (heating for 3 h at 600 K) were saturated in a moist medium with a relative humidity of 14–98% at 300 K. The NMR spectra of the moisture-saturated samples were obtained on a wide line spectrometer with a working frequency of 37 MHh. The spectra had the form of single narrow lines (about 0.02 mT wide) with a signal/noise ratio exceeding 70. The experimental data are presented in the form of isothermal curves of the intensity of the water-proton line in the NMR spectra versus the partial water vapor pressure for sorption and desorption processes.

The experimental ''NMR isotherms'' for porous silicon samples produced by anodization with different current densities are shown in Fig. 1. The figure also shows an isotherm for a single-crystal silicon sample subjected to electropolishing. In the latter case the intensity of the NMR line remains practically unchanged in a wide pressure range. The isotherms of porous silicon demonstrate a number of features, including pronounced hysteresis, indicating capillary condensation. This attests to the fact that besides the nanopores with an average diameter of 10–30 nm well-known from electron-microscopic measurements porous silicon contains much smaller pores (subnanopores).[3]

Taking account of the existence of subnanopores in porous silicon, we shall examine a porous model of the process leading to the establishment of dynamic equilibrium between the gas phase and the sample as well as the characteristic features of the formation of layers of sorbed water. In the presence of surface adsorption, the total surface area S_t of the sample consists of the active surface area S_a, including the surface area of the nanopores and the external nonporous surface area (it is in constant equilibrium with the gas phase because of rapid particle exchange) as well as the surface area of subnanopores S_s (it is filled much more slowly in the process of self-diffusion of sorbed molecules, which behave as a classical two-dimensional Langmuir gas).

The kinetics of the population density on the active surface is described by the equation

$$\frac{dN_a}{dt}=\frac{1}{6}\alpha\frac{p}{kT}\langle v\rangle S_a(N_{a0}-N_a)-\frac{N_a}{\tau}, \tag{1}$$

where α is the probability that a molecule is trapped by an adsorption center, p is the partial pressure of the water vapor, $\langle v\rangle$ is the average thermal velocity of molecules in the gas phase, N_{a0} is the number of adsorption centers on the active surface, τ is the residence time of a molecule on the surface, k is Boltzmann's constant, and T is the absolute temperature.

The rate of change of the number of particles on the surfaces of the subnanopores is expressed by the equation

$$\frac{dN_s}{dt}=\beta N_a\left(1-\frac{N_s}{N_{se}}\right), \tag{2}$$

where the coefficient β takes account of the probability for molecules to escape into nanopores and N_{se} is the equilibrium number of molecules in subnanopores.

Since the sorption mechanisms on an active surface and on the surface of the subnanopores are different and

$$\frac{dN_s}{dt}\ll\frac{dN_a}{dt},$$

the total number of molecules sorbed on the surface equals

$$N_{ae}+N_{se}=N_{a0}\left(1+\frac{S_s}{S_a}\right)\frac{p/p_s}{p/p_s+A/\tau p_s}, \tag{3}$$

where p_s is the partial pressure of saturated vapor above the flat surface at 300 K and A is Avogadro's number. The expression obtained corresponds to a Langmuir isotherm.

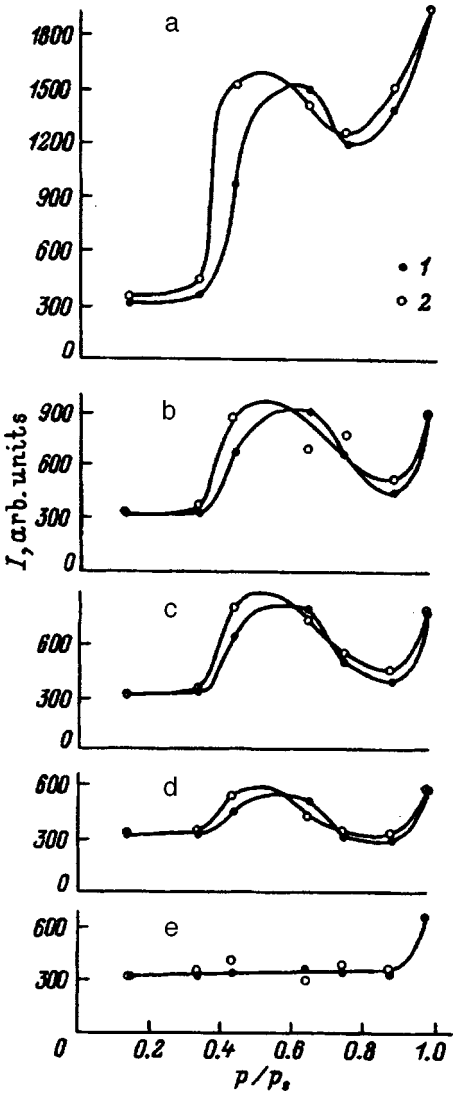

FIG. 1. NMR isotherms of sorbed water in porous silicon. The isotherms were obtained with different current densities j_a (a–d) and in single crystal silicon (e). j_a, mA/cm^2: a — 20, b — 15, c — 10, d — 5. *1*—sorption, *2* —desorption.

As follows from the expression (3), in the case of surface adsorption the sorption capacity of the sample is saturated even at low pressures (less than 1% relative humidity). In the process a monolayer of mobile molecules, which virtually do not interact with one another, is formed. The properties of this monolayer do not change with pressure. The intensity of the NMR absorption line also does not change. The horizontal section (or the section close to it) observed for all experimental samples determines the surface-adsorption isotherms. In the case of single-crystal silicon the horizontal section is a larger fraction of the curve — over virtually its entire extent the isotherm is described by the Langmuir law, while the monolayer exists in a wide pressure range. The situation is different for porous silicon — the Langmuir isotherm corresponds only to the initial part of the curve, while the monolayer remains only up to pressures less than $0.35p_s$. Above this value a jump occurs in the intensity of the NMR line, attesting to the onset of capillary condensation.

In the presence of capillary condensation aggregation of water molecules can start both at the bottom and at the walls of the pores, depending on the cross-sectional sizes of the pores.[4] It can be shown that for subnanopores the second mechanism, which is accompanied by the formation of a cylindrical meniscus in the case of adsorption or a hemispherical meniscus in the case of desorption, is more likely. The saturated-vapor pressure above the cylindrical and hemispherical menisci is determined by Kelvin's formulas, respectively, as

$$\frac{p}{p_s}=\exp\left\{-\frac{\sigma\nu_m}{rRT}\right\} \quad \text{and} \quad \frac{p}{p_s}=\exp\left\{-\frac{2\sigma\nu_m}{rRT}\right\}, \tag{4}$$

where σ is the surface tension of water, ν_m is the molar volume of the water, r is the pore radius, and R is the universal gas constant.

Filling of the subnanopores corresponds to a sharp inflection of the isotherm, whose slope is determined by the pore-size distribution. The difference in the shape of the meniscus in the case of adsorption and desorption results in the appearance of a hysteresis loop appears in the isotherm. As one can see, a hysteresis loop is characteristic for all experimental samples of porous silicon and increases with increasing density of the anodic current, while the region of capillary condensation remains the same in all cases. A quantitative estimate of the sizes of subnanopores can be obtained by a simple calculation using Eqs. (4). Their average diameter determined in this manner equals 1.4 nm, which correlates with the description of the crystal matrix of porous silicon as a system of quantum wires with average diameter ranging from 1.4 to 8 nm.[5,6]

At moderate pressures the NMR line intensity decreases with increasing relative humidity. The dropoff of the isotherm on this section can be explained keeping in mind the fact that only the narrow NMR component, which is due to mobile water molecules, is recorded in the measurements. For this reason, the decrease in intensity attests to a decrease not of the total number of sorbed particles but rather only the number of mobile molecules. This leads to the following hypothetical picture of the formation of the adsorbed layer. The concave menisci formed as a result of condensation on the open ends of subnanopores play the role of adsorption centers, binding water molecules migrating along the surface by means of hydrogen bonds parallel to the surface. In this manner islands of molecules with limited mobility appear near the locations of emergence of subnanopores on the surface of porous silicon. This process leads to the formation of a coordination-saturated monomolecular layer with a corresponding increase in moisture content.

The NMR line intensity once again increases at high pressures. In our opinion this section of the isotherm corresponds to capillary condensation in nanopores. Since the nanopore sizes are much larger than the interproton distance in a water molecule, filling of nanopores (in contrast to subnanopores) starts from the bottom of the pore and proceeds with the formation of a hemispherical meniscus. At a vapor pressures close to saturation polymolecular condensation on the coordination-saturated monolayer is also possible.

Our results attest to the fact that magnetic-resonance spectroscopy is an effective method for investigating both the structure and surface properties of porous silicon and other similar quantum-size structures. It yields information about pore sizes and mechanisms of sorption processes and enables identifying water monolayers adsorbed by the surface.

[1] A. I. Mamykin, A. J. Iljin, V. A. Moshnikov, and A. I. Pershin, in *Abstracts of EENC-94*, Oulu, Finland, 1994, p. 93.

[2] A. I. Mamykin, A. Yu. Il'in, V. A. Moshnikov, A. A. Mamykin, and N. E. Mokrousov, Fiz. Tekh. Poluprovodn. **29**, 1874 (1995) [Semiconductors **29**, 979 (1995)].

[3] A. I. Mamykin, A. Yu. Il'in, A. I. Gorelik, and A. V. Moshnikov, in *Abstracts of Reports at the 1st All-Russia Conference ''Silicon-96,''* Moscow, 1996.

[4] S. J. Gregg and K. S. W. Sing, *Adsorption, Surface Area, and Porosity*, Academic Press, N. Y., 1967 [Russian translation, Mir, Moscow, 1970].

[5] I. I. Reshina and E. G. Guk, Fiz. Tekh. Poluprovodn. **27**, 728 (1993) [Semiconductors **27**, 475 (1993)].

[6] M. S. Bresler and I. N. Yassievich, Fiz. Tekh. Poluprovodn. **27**, 871 (1993) [Semiconductors **27**, 475 (1993)].

Translated by M. E. Alferieff

Properties of p^+-n structures with a buried layer of radiation-induced defects

A. M. Ivanov, N. B. Strokan, and V. B. Shuman

A. F. Ioffe Physicotechnical Institute, Russian Academy of Sciences, 194021 St. Petersburg, Russia
(Submitted April 18, 1997; accepted for publication May 21, 1997)
Fiz. Tekh. Poluprovodn. **32**, 359–365 (March 1998)

The p^+-n structures based on n-type Si with dopant density 1.7×10^{13}–1.2×10^{14} cm^{-3} were irradiated with ^{238}Pu α particles. A layer containing radiation-induced defects with a density of the order of 3×10^{13} cm^{-3} was produced at a depth of 20 μm. This defect density gave rise to intense draining of nonequilibrium carriers in the injection-extraction regime with stationary injection as well as with pulsed generation by single particles. This makes it possible to treat the damaged layer as a plane, introduced into the bulk, with an infinite surface recombination rate. The radiation-induced defects also participated in decreasing the conductivity. A characteristic space charge distribution and, correspondingly, a bias dependence of the capacitance are observed in the structure under reverse bias. Despite the presence of formally three charge regions, four sections appear on the capacitance curve. This latter effect is due to the ''additional'' charge step arising in the contact potential difference field and is characteristic of compensated deep levels in semiconductors. [S1063-7826(98)01303-9]

1. INTRODUCTION

The production of a prescribed profile of deep centers in Si is a complex technological problem. At the same time, in practice it is often necessary to introduce recombination centers (RCs) or to vary the conductivity of the material. In this connection, we note that there is great interest in so-called ''buried layers.''[1,2] The possibilities of the conventional diffusion method are found to be very limited here. For example, it is possible to obtain an U-shaped Au profile with short diffusion from an unbounded source.[3] However, it is impossible, in general, to produce a prescribed RC profile by the diffusion method. At present, a promising solution of this problem is to use radiation-induced defects (RDs), which can serve as RCs, and to influence the conductivity.

It is well known that radiation-induced defects form continuously along the track of an ion—their density increases toward the end of the track. It is obvious that the profile of RDs in Si subjected to irradiation will depend on the relative arrangement of the source and the sample. Such a profile was first investigated in Ref. 4, where a plate-shaped source of α particles (light ions) was used. The dimensions of the plate were much larger than those of the sample, which was placed directly on the source-plate. Thus, irradiation was performed by a noncollimated beam of α particles. This explains the RD profile, which resembles a Gaussian profile (the maximum RD density was located at the Si surface), observed in Ref. 4. A collimated beam can be obtained by placing the sample sufficiently far away from the source (in vacuum). In this case, a different RD profile is obtained—the profile possesses a maximum located in a plane parallel to the surface of the sample at a distance determined by the initial particle energy. In principle, any RD profile (square, triangular, and so on) can be obtained by varying the sample-source distance according to a definite program (as well as by using ions of different nature and energy). The problem is simplified by using ion accelerators, where the type and energy of the ions can be easily varied.

The presence of a DC profile in turn influences the characteristic features of carrier transport. For example, we observed an unconventional dependence of the charge carrier lifetime on the irradiation dose.[5] We used a diode structure to study the effect of a buried layer of RDs on the transport of nonequilibrium carriers, on the effective lifetime, and on the space charge distribution under a reverse bias.

In connection with this problem, we employed deep level transient spectroscopy (DLTS) and stationary capacitance methods. We analyzed the transport of holes in the base through the damaged layer under conditions of hole injection-extraction and also the transport of magnitude-calibrated charge, using a p^+-n diode as a detector of single α particles, were analyzed.

2. IRRADIATION OF THE SAMPLES AND CAPACITANCE MEASUREMENTS

Radiation-induced defects produced in Si by irradiation with α particles from a ^{238}Pu (5.5 MeV) source were used to produce nonuniformities of the electrical properties in the base of the p^+-n structure. For α particles with natural-decay energies, energy losses in Si characteristically occur in events of ionization of electronic shells in the process of stopping. The main interaction with the Si nuclei occurs at the end of the path, where the particle energy E is low. This is due to the fact that the differential cross section $d\sigma_{ns}$ for nuclear scattering with energy transfer T is inversely proportional to E and can be expressed as

$$d\sigma_{ns}\sim(dT/T^2)/E. \tag{1}$$

It follows from the relation (1) that small portions of energy T are most likely to be transferred to the Si atoms. Ulti-

 1063-7826/98/030325-07$15.00

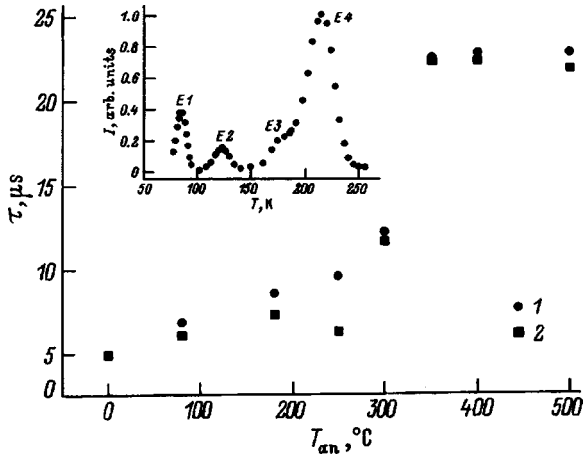

FIG. 1. Variation of the hole lifetime τ in a sample irradiated with α particle flux $\Phi = 1.4\times10^{9}$ cm^{-2} and subjected to isochronous annealing for 1 h. Injection-extraction measurements with forward current density j, A/cm^2: *1*—0.3, 2—0.4 and forward to reverse current ratio: *1*—3, *2*—2. Inset: DLTS spectrum of deep centers (1—signal intensity) lying in the top half of the band gap in Si: The sample was irradiated with α particle flux $\Phi = 2\times10^{9}$ cm^{-2}.

mately, Frenkel' pairs ⟨interstitial atom⟩-vacancy are concentrated in a narrow region at the end of the particle path. Increasing the dose to a certain level, where the tracks of separate particles overlap ($\Phi \geqslant 10^{9}$ cm^{-2}), produces a layer of width δ, which is saturated with structural defects. The components of Frenkel' pairs rapidly enter into physicochemical reactions leading to the formation of complexes with impurities P, O, and C, and they also form associations in the form of divacancies. The density of centers in the layer is estimated as $M = \beta\Phi/\delta$, where β is the number of Frenkel' pairs (per particle) participating in the formation of centers. This number is small in view of the substantial recombination of pairs along the track of an α particle,[6] it is $\beta = 2$ (Ref. 7).

Silicon diodes with a diffused p^+ layer with surface boron density 10^{20} cm^{-3} and a 350-μm-thick n-base with P density 1.2×10^{14} and 1.7×10^{13} cm^{-3} (for group I and II samples, respectively) were irradiated. The initial hole lifetime in the base of the diodes is $\tau_0 = 20$ μs. Irradiation was conducted in vacuum in a close to orthogonal geometry. The effect of low doses on the properties of the p^+-n structure was followed. The dose was monitored using the same p^+-n structure. Here the diode was used in the detector mode. We note that the particle energy released in the n-base was less than 5.5 MeV due to self-absorption in the source and in the p^+ layer of the diode. All experiments were conducted at room temperature.

Our first problem was to check the corresponding systems of radiation-induced defects, according to the picture which has emerged in the literature, and also to establish the density profile of electrically active centers in Si. Since these measurements are associated with the DLTS method, it was important to follow the effect of the appearance of a δ-layer in the p^+-n structure on the capacitance of the structure.

The DLTS spectrum for a group-II sample irradiated with α particle dose 2×10^{9} cm^{-2} is presented in the inset in Fig. 1. In sum, four levels are observed in the top half of the band gap. The first level is an $E1$ level (due to a A center) with energy $E_c - 0.18$ eV and electron trapping cross section $\sigma_n = 2\times10^{-14}$ cm^2. The next level is an $E2$ level ($E_c - 0.22$ eV, $\sigma_n = 2\times10^{-16}$ cm^{-2}), belonging to a doubly negatively charged state of a divacancy. This is followed by a peak corresponding to an $E3$ level ($E_c - 0.29$ eV, $\sigma_n = 2\times10^{-17}$ cm^{-2}), which is associated with a ⟨interstitial C⟩–P pair. At least two defects are responsible for the position of the $E4$ peak ($E_c - 0.4$ eV, $\sigma_n = 2\times10^{-16}$ cm^{-2}): an E center (vacancy—P) and a divacancy (singly negatively charged state). It follows from the figure that under the measurement conditions the highest density of deep centers corresponds to the $E4$ level. This should be manifested as a change in the recombination lifetime in Si and in a decrease of the conductivity as a result of compensation by deep centers.

In addition, the energy levels in the bottom half of the band gap were investigated in a hole-injection regime. Here only a C_i-O_i center was clearly manifested: ⟨interstitial carbon⟩–⟨interstitial oxygen⟩ with energy $E_v + 0.4$ eV and $\sigma_p = 3\times10^{-14}$ cm^{-2}. We note that in our case very few centers are due to single interstitial carbon ($E_v + 0.33$ eV, $\sigma_p = 9\times10^{-14}$ cm^2). This can be explained by the fact that the defects C_i and O_i are already bound in the irradiation cycle, which was performed at room temperature, where the migration of C_i centers is high. The second factor could be the high concentration of oxygen in the sample.

On the whole, the observed system of defect levels is characteristic of pure n-Si.[8,9] Their comparative recombination activity is manifested in the behavior of the lifetime τ of the minority charge carriers. Thus, for a sample irradiated with a flux 1.4×10^{9} cm^{-2} τ dropped to 5 μs. Isochronous annealing in air for 1 h restored τ up to 22.5 μs. The stage of the greatest increase occurs at the temperature $T_{an} = 350$ °C (see Fig. 1), which corresponds to the main annealing of centers such as divacancies and A centers.[8,10] This agrees with the existing belief that the recombination rate through the levels of a divacancy and a A center is high.[11] On the other hand, we did not observe, as was the case in Ref. 12, activity of the deepest RD—an E center. Annealing at $T_{an} = 200$ °C changed τ very little. This should be attributed to weak production of E centers in the damaged layer.

In connection with what we have said above, it can be assumed that under our conditions the main radiation-induced defect is a divacancy. Aside from the above-noted recombination activity, it should also be manifested (as a deep center) in the compensation of Si. Ultimately, the spatial distribution of the divacancies characterizes the geometry of the buried layer. We underscore that divacancies are formed directly in the particle track and are not associated with diffusion outside the track, i.e. broadening of the profile of the primary defects.

Figure 2 shows the density of defects forming the $E4$ peak versus the coordinate of the boundary of the space charge region (SCR) of the p^+-n junction. This boundary was determined from the values of the capacitance versus the reverse bias (see the inset in Fig. 2). As noted above, the divacancies were found to be concentrated in a very narrow region at the end of the particle path.

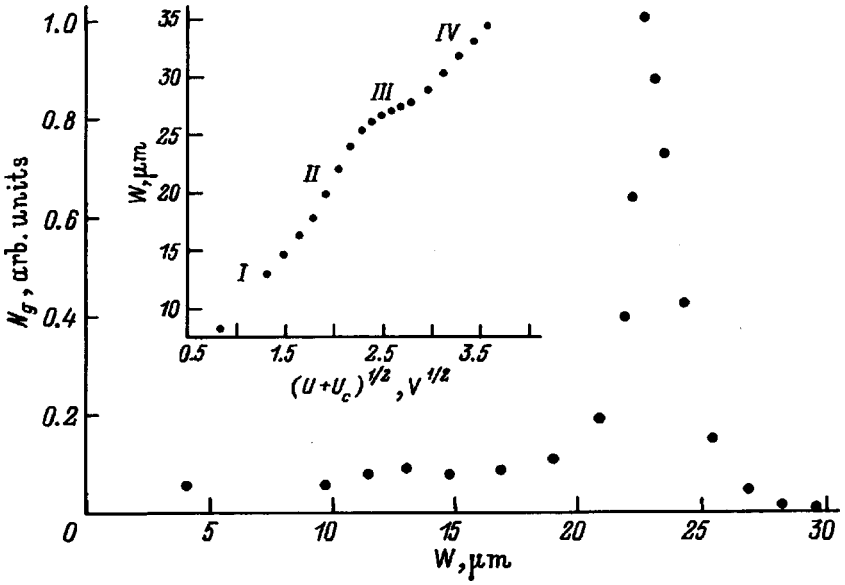

FIG. 2. Track depth distribution of the number of centers forming the peak $E4$ in a sample irradiated with α particle flux $\Phi=2\times10^9$ cm^{-2}. The measurements were performed by the DLTS method at $T\approx210$ K. Inset: Width W of the space charge region versus the applied voltage U; the I–IV mark different sections of the curve.

However, the data in Fig. 2 require a number of explanations, primarily with respect to the difference of the dependence of the SCR boundary on the applied voltage U in the coordinates $W=f(\sqrt{U+U_c})$, where U_c is the contact potential difference, from the conventional linear function. The observed dependence has four distinguishing sections. Initially, at low voltages, the p^+-n junction expands in the region where there is very little damage. Approximately at 20 μm W starts to grow rapidly with voltage. This is due to the compensation of shallow donors by deep acceptors. At 25 μm growth starts to slow down, and this is followed at $W>28$ μm by a section associated with expansion of the p^+-n junction into the region of undamaged Si.

To explain the behavior of $W(U)$, we examined the situation, which we expected, in which three regions with different values of the space charge ρ are present in the SCR of an asymmetric p^+-n structure (see inset A in Fig. 3). For simplicity, the charge distribution in each region was assumed to be uniform with a sharp transition to new values at the boundaries a, b, and W. In this model the initial value $\rho=\rho_3$ remains in the region (b,W) beyond the limits of the particle path $(b\geqslant R)$. The region (a,b) is the damaged layer, and in the zone $(0,a)$ very small number of radiation-induced defects can form and $\rho_1\neq\rho_3$. Correspondingly, it is assumed that $\rho_2<\rho_1<\rho_3$.

Solving the Poisson equation leads to an expression for the distribution of the applied potential difference U over the regions

$$U/U_0=1+[(b^2-a^2)\rho_2+(W^2-b^2)\rho_3]/a^2\rho_1. \qquad (2)$$

Here the voltage U_0 corresponds to depletion of the zone $(0, a)$ with space charge ρ_1. We obtain from Eq. (2) the normalized total length W/a of the SCR as

$$(W/a)^2=(\rho_1/\rho_3)(U/U_0-1)+(b/a)^2(1-\rho_2/\rho_3)+\rho_2/\rho_3. \qquad (3)$$

This function is plotted in the coordinates $W/a=f(\sqrt{U/U_0})$ in Fig. 3 for the case $b/a=1.5$ and $\rho_1:\rho_2:\rho_3=0.75:0.3:0.1$. Three sections can be discerned in the plot with increasing U: In the first section—the SCR spreads in the zone $(0,a)$—$W/a\sim\sqrt{U/U_0}$; this is obvious. As the SCR moves into the region (a,b), where $1\leqslant W/a\leqslant1.5$, the SCR grows with a larger slope $(\rho_2<\rho_1)$ but the function is now nonlinear:[1]

$$W/a=[1+\rho_1/\rho_2(U/U_0-1)]^{1/2}. \qquad (4)$$

Finally, after the damaged layer is depleted a third section is observed. Here W/a grows according to Eq. (3) and approaches $W\approx\sqrt{U/\rho_3}$ for $U/U_0\gg b/a$. It is easy to see that the dependences given by the expressions (2) and (3) above rectify in the coordinates $W^2=f(U/U_0)$.

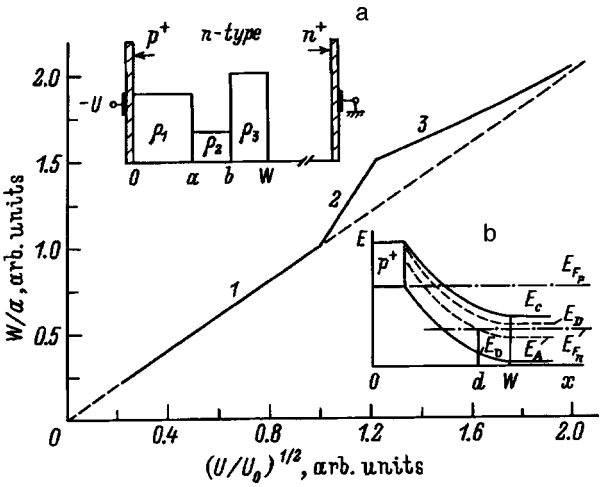

FIG. 3. Computed dependence of the width W of the space charge region versus the applied voltage U for the case where three regions with different space charges are present in the base of the diode. The numbers on the curves correspond to the relations $W=f(U)$ with different values of the parameters ρ_i: *1*—$W/a=(U/U_0)^{1/2}$ with $\rho_1=\rho_2=\rho_3$; *2*—(4) with $\rho_2=\rho_3$, $\rho_1/\rho_2=2.5$; *3*—(3) with $\rho_1/\rho_3=0.75$, $\rho_2/\rho_3=0.3$. The dashed straight line corresponds to $W=(U/\rho_3)^{1/2}$. Inset *A*: Diagram of the charge distribution; see text for explanation. Inset *B*: Arrangement of the energy bands and filling of the deep level in the p^+-n junction; E_{Fp}, E_{Fn}—Fermi quasi-levels.

The presence of the ''excess'' fourth section in the experimental curve $W(U)$ in Fig. 2 must be attributed, in our view, to a characteristic feature of the compensation of donors by deep acceptor levels. The region of the field of the p^+-n junction is where the level of a DC can cross the Fermi level. Then, for a stationary state the filling of the levels with electrons will look like that shown in inset *B* in Fig. 3 (see, for example, Ref. 13). The width of the zone $(0, d)$ (see inset) will be determined by the initial density of ionized shallow donors, and the filling of deep acceptors with electrons in the region (d,W) will be preserved. The voltage drop across it is small ($E_F-E_A\cong 0.1$ eV) and does not depend on the applied voltage.[14] However, its extent can be substantial when $N_D^+-N_A^-$ is small.[15]

In capacitance measurements there arise two opposite cases where the period of the probe signal is greater or less than the ejection time of electrons from the level E_A. In the first case the boundary d changes predominantly; in the second case the region $(0,W)$ reacts as a whole. Ultimately, depending on the frequency of the probe signal, the temperature, and the depth of the level, a value of the order of d or W can be obtained for SCR (the so-called low- and high-frequency capacitance; see Ref. 13 for a more detailed discussion). Under our conditions with $f=100$ kHz and $T\approx 200$ K there is too little time for electrons to be transferred from levels lying deeper than 0.25 eV ($\sigma=3\times 10^{-15}$ cm^2) into the c band. In other words, the capacitance measurements gave us the right-hand boundary of the SCR, i.e., the quantity W.

In application to the question of the production of a space charge in the δ layer, the situation with deep compensation, when the weak-field region

$$\Delta=\left[\frac{2\varepsilon(E_F-E_A)}{e^2(N_D^+-N_A^-)}\right]^{1/2}>\delta,$$

is simplest. Then the electric field extends immediately to the entire δ layer from the moment the SCR touches its left-hand boundary. Under these conditions the section II in Fig. 2 is represented by a vertical line. As U increases further, the field of the applied potential difference penetrates into the δ layer. In the process, the region Δ is displaced ouside the layer (where it cannot exist), and thereby decreases in absolute magnitude. This process of redistribution of the field in the δ layer under our measurement conditions does not influence the values of the capacitance and corresponds to $W=$ const, i.e., to the horizontal section III. Finally, when the field enters the undamaged Si, W grows, which is reflected as the appearance of section IV. In the case of shallower compensation with $\Delta<\delta$ the sections II and III will not form steps. The finite slope of section II reflects the above-indicated redistribution of the space charge in the layer δ, and the horizontal section should be shorter along the voltage axis.

The experimental data in Fig. 2 refer to a real situation in which the edges of the distribution of DCs are somewhat diffuse. For this reason, there is only a qualitative correspondence to the picture presented above, as is observed with respect to the number and character of the sections. It is also significant that the rates of growth of the function $W(U)$ are the same for the initial and final sections. This is additional evidence that there is very little damage in the volume of Si right up to the end of the particle path.

The considerations stated above were also taken into account in determining the coordinates of the maximum density of the center $E4$. The position of this center, calculated from the measured value of the capacitance, will lie deep in the base, since the DCs with coordinates $x<d$ will contribute to the DLTS signal (see the inset in Fig. 3). Deep centers in the section from d to W do not ionize when a reverse bias is applied and do not participate in the formation of the signal. The DLTS signal appears when the value of d coincides with the left-hand edge of the peak corresponding to the DC density, but the thickness of the p^+-n junction obtained from the capacitance measurements will be greater by the thickness of the region Δ. Estimation of this quantity, following Ref. 13, gives $\Delta\cong 4$ μm, which was used to correct the position of the maximum of the density N_g in Fig. 2.

On the whole, it can be concluded from the capacitance measurements that the profile of radiation-induced DCs (divacancies) along a particle track has the character of a rather sharp peak. The position of the top of the peak corresponds to the range R. When observing divacancies, the contour of the peak most accurately describes the distribution of primary defects (Frenkel' pairs) along the track.

3. HOLE TRANSPORT IN THE INJECTION-EXTRACTION REGIME

Let us now turn to the manifestation of induced centers in charge-carrier recombination processes. The values of τ presented in annealing experiments (see Fig. 1) were determined by the injection-extraction method. In addition, as customary in the literature, the quantity

$$1/\tau=1/\tau_0-1/\tau_{\text{fin}},$$

where τ_0 and τ_{fin} are the initial and measured values of the lifetime, was plotted. It was expected that $1/\tau$, which is proportional to the total density of induced recombination centers, will grow linearly with dose. However, substantial nonlinearity, which eventually reaches saturation, is observed (see Fig. 4). It was found that in the dose interval $\Phi=5\times 10^8-10^{10}$ cm^{-2} the quantity $1/\tau$ is close to a power-law function with exponent 1.7. To explain this behavior of $1/\tau=f(\Phi)$, it is necessary to consider the basic formula of the method (see, for example, the monograph Ref. 16):

$$\operatorname{erf}\sqrt{T/\tau}=I_f/(I_f+I_r), \tag{5}$$

where T is the duration of the shelf of the reverse phase and I_f and I_r are the currents of the forward and reverse phases (see the inset in Fig. 4). The expression (5) was obtained under the condition that the diode base is long compared with the diffusion length $L_D=(D\tau)^{1/2}$, where the hole diffusion coefficient in Si is $D=11.6$ cm/s. For initial values $\tau_0=20-30$ μs we have $L_D\leqslant 185$ μm and the conditions under which Eq. (5) is derived hold satisfactorily. As defects are introduced, a layer with a low value of τ is erected in the base at a depth equal to the particle range $R\cong 20$ μm. This violates the conditions of the initial model, since a drain for holes is produced at a distance $R\ll L_D$ near the p^+-n junc-

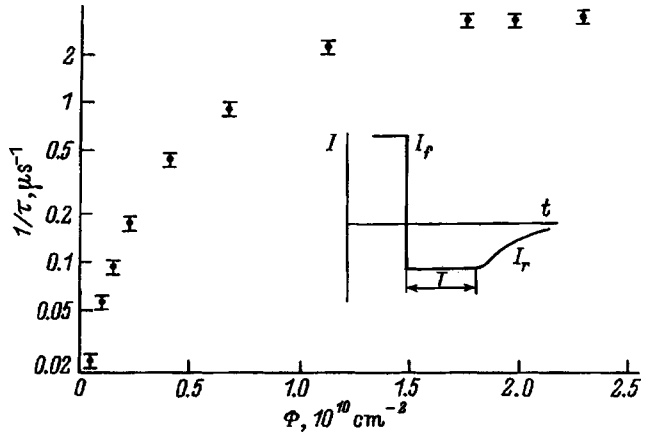

FIG. 4. Reciprocal $1/\tau$ of the hole lifetime in the diode base as a function of the α particle irradiation dose Φ. Measurements by the injection-extraction method; see Eq. (5). The forward current density equals 0.3 A/cm^2. Inset: Form of the current pulse I, elucidating the notation in Eq. (5).

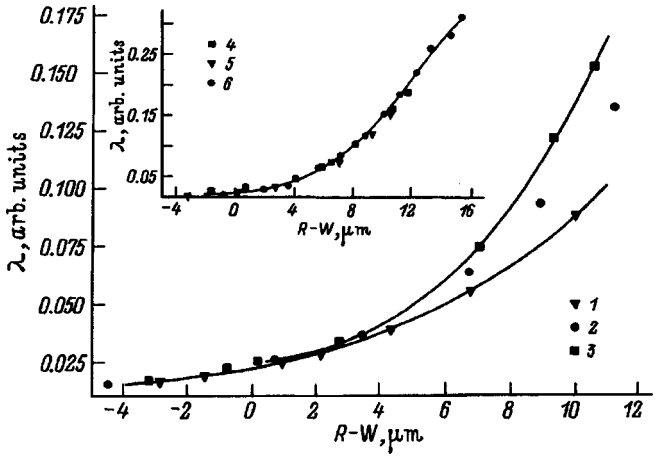

FIG. 5. Recombination charge losses λ as a function of the extent of the part of the track extending beyond the boundary of the region of the field $R-W$. The α-particle irradiation dose Φ, 10^9 cm^{-2}: *1*—0, *2*—1, *3*, *4*—3, *5*—6, *6*—10.

tion. In the limit the δ layer can be treated as a plane with surface recombination rate $S\to\infty$, which reduces the problem to the case of a ''thin'' diode with a recombination-type back contact. This problem is solved in Ref. 17.

The following approximate formula relating the duration of the shelf and the depth of the δ layer is presented in Ref. 16:

$$T=\ln[0.8(1+I_f/I_r)]R^2/2.5D. \tag{6}$$

For our measurements this signifies that the function $1/\tau(\Phi)$ should saturate. This corresponds to the moment at which $1/\tau$ in the δ layer decreases to a level formally described by the value $S\to\infty$. Saturation was clearly observed in the dose range $\Phi\cong 2\times10^{10}$ cm^{-2} (see Fig. 4). The value of τ in the layer can be estimated as $\tau=(V_{th}\sigma M)^{-1}$. Taking the thermal velocity $V_{th}=3\times10^7$ cm/s and trapping cross section $\sigma=3\times10^{-15}$ cm^2, we obtain $\tau=1.4\times10^{-7}$ s. The two orders of magnitude difference from the initial value (which remains in the main, undamaged part of the base) is sufficient for an intense hole drain in the damaged layer. A quantitative estimate also confirms this. Thus, substituting into the expression (6) the shelf duration $T=0.2$ μs, we obtain $R=22.3$ μm. This value is in good agreement with the value $R=23.2$ μm for group-I samples on which the measurements were performed.

4. TRANSPORT OF NONEQUILIBRIUM CHARGE DURING PULSED GENERATION

Another possibility of tracing the contribution of the damaged layer to the characteristic features of charge transport is to detect the signal from single α particles. Here the main mechanism of energy losses during stopping in a solid—ionization, which we mentioned earlier, is used. The structure of the p^+-n diode acts as a detector of separate particles, the SCR of the diode serving as the ''working zone.'' By varying the reverse bias it is possible to control the value of W and determine the desired conditions of transport. From the technical standpoint it is important that monoenergetic particles contribute a pulse of charge of electron-hole pairs that is calibrated in magnitude. This pulse is detected with apparatus that is conventionally used in nuclear spectrometry. The final characteristic of the structure as a detector is the shape of the spectrum of signal amplitudes.

4.1. Let us trace first the behavior of the average amplitude of the spectrum with increasing dose Φ in Fig. 5. Let the geometry of the experiment be such that the particle tracks emerge behind the defective layer (see the inset *a* in Fig. 6). We used ^{244}Cm α particles. Under the conditions of complete transport these α particles released in group-II structures 5.11-MeV particles ($R=24.6$ μm). Let W be less than the coordinate x_1. Then, the ionization produced by the particle spreads over three regions: in the SCR zone (W); in the undamaged zone (x_1-W); and, finally, directly in the δ layer and to the right of this layer in the region $R-x_2$.

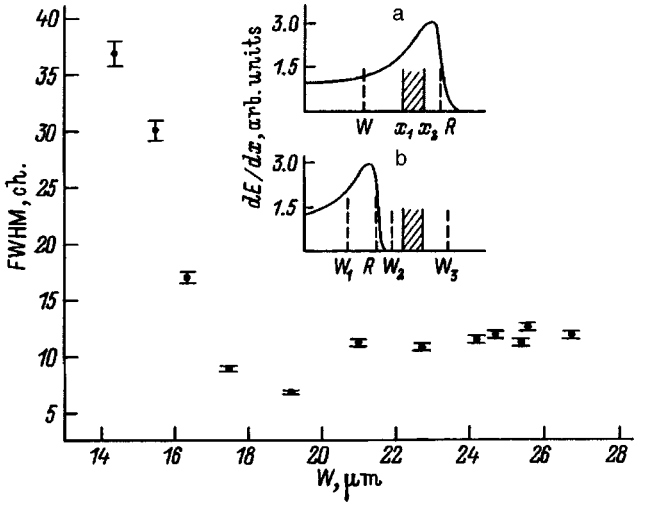

FIG. 6. FWHM of the spectral line of a p^+-n diode as a function of the width W of the region of the field. The diode was irradiated with α particle flux 1.7×10^{10} cm^{-2} and used as a detector of single 4.5-MeV α particles with range $R=21$ μm. Insets: Geometry of experiments. The α-particle track: a—Extends beyond the buried layer (see Fig. 5); b—lies in the region in front of the buried layer.

The signal amplitude is determined by the integrated charge flowing in an external circuit—as the resultant of fast drift transport of carriers in the electric field of the SCR and the slower diffusion transport in the zone $R-W$. The latter is associated with recombination losses, which is reflected in Fig. 5 (curve *1*). As recombination centers are introduced as a result of radiation-induced defects, the charge losses λ, naturally, grow (curves *2–6*). It is significant that λ saturates even at a flux $\Phi \geqslant 3\times 10^9$ cm^{-2} (see the inset in Fig. 5). Here, the value of λ corresponds to a transport pattern in which the charge introduced into the region $R-x_1$ is completely lost. At the same time, charge is completely transported into the zone $(0,W)$. Only half of the charge in the layer (x_1-W) flows onto the p^+-n junction. This picture is correct to a high degree of accuracy. Thus, a calculation based on a Bragg ionization distribution for $R-W=10$ μm gives losses $\lambda=0.12$ as compared to the experimental value $\lambda=0.145$. Thus, the damaged layer is manifested as an efficient drain for carriers even at fluxes $\Phi \geqslant 3\times 10^9$ cm^{-2}. We recall that in the injection-extraction method this state appeared at $\Phi \geqslant 2\times 10^{10}$ cm^{-2}.

The high sensitivity to DCs in the δ layer in the case of pulsed injection of charge by α particles should be attributed to the difference in the filling of the trapping centers. In the injection-extraction method filling occurs during the phase of a stationary forward hole current. In the phase of a reverse current through a layer with centers, which is already filled with holes, holes flow out of the region $L_D-\delta$. When charge is generated by α particles, the initial filling of the centers is determined by the equilibrium conditions. Centers below the Fermi level are filled with electrons and can effectively trap holes. The trapping is increased by a high injection level in a track, when the diffusion current densities in the δ layer equal tens of A/cm^2.

4.2. In the above discussion we traced the behavior of the average amplitude of a pulse. However, the amplitude spectrum also gives a second parameter—the line width. This quantity is determined as the product of the charge losses λ to hole trapping and the nonuniformity factor F of the losses.[18] In practice $F\cong 1$ and the smearing of the line is directly attributable to incomplete charge transport.

Let us now choose the α particle energy so that the range of the α particles falls in the region below the coordinate x_1 (see the inset in Fig. 6). Let us distinguish two cases according to the position of the region W of the field relative to the δ layer: In the first case W also does not reach x_1, i.e. R, $W_2<x_1$. In the second case, conversely, the damaged layer is captured by the region of the field and $W_3>x_2$. Under conditions $W_2<x_1$ the electrons flowing from the region of the field are the majority carriers in the base. For this reason, an equal number of electrons is removed into the n^+ contact over the Maxwellian relaxation time. Ultimately, the defects in the δ layer will have no effect on the signal. In the case $W_3>x_2$ the electrons must drift out of the track through the δ layer as a packet of nonequilibrium carriers. In the process, they will be subject to trapping, which should be manifested, first and foremost, in broadening of the spectral line.

Figure 6 illustrates the behavior of the FWHM of the line (expressed as the number of channels of the amplitude analyzer) as a function of the thickness of the region of the field for a group-I sample. For the α particles the tracks were 19-μm long, which was close to the range of the particles producing the damaged layer (23.2 μm). However, the characteristic behavior of the line width can be clearly followed. The line is wide until the track settles completely in the region of the field $(W_1<R)$. This is due to the contribution of the losses resulting from diffusion transport for the part of the track that penetrates into the base. As W increases, the line narrows sharply and the minimum values are observed for $W_2 \geqslant R$. When trapping centers in the δ layer are drawn into the working zone, the line width approximately doubles.

5. CONCLUSIONS

Irradiation with α particles with natural-decay energies makes it possible to obtain a ''buried layer'' of radiation-induced defects with a sharp profile. Deep centers are predominantly observed. They are manifested, first and foremost, in the recombination of nonequilibrium carriers but also in a decrease of the conductivity as a result of compensation of current carriers. Very moderate fluxes $\Phi=3\times 10^9-3\times 10^{10}$ cm^{-2} are sufficient for the buried layer to be treated as an internal boundary with an infinite surface recombination rate. The correctness of this assumption was checked for two typical variants of carrier transport: for initial filling of centers under stationary current conditions and for pulsed generation in a volume which was at equilibrium earlier.

The manifestation of deep centers in the decrease of the conductivity was also observed at low fluxes according to the characteristic features of the production of space charge in a reverse-biased p^+-n structure. It was shown that under conditions of incomplete depletion of the damaged layer the presence of space charge, arising in the field of the contact potential difference, in it must be taken into account.

The above-noted facts are also helpful in the procedural sense. It was shown how a layer of deep centers influences the results obtained by widely used methods, such as DLTS and injection-extraction of charge carriers.

[1)]The nonlinearity of the second section is hardly discernible in Fig. 3 because of the smallness of the values of $(U/U_0)^{1/2}$.

[1] S. M. Sze, *Physics of Semiconductor Devices*, Wiley, N. Y., 1969 [Russian translation, Mir, Moscow, 1984, Vol. 1].
[2] J. von Borany, B. Schmidt, and R. Grotzschel, Nucl. Instrum. Methods Phys. Res. A **377**, 514 (1996).
[3] J. Martin, E. Haas, and K. Raithel, Solid-State Electron. **9**, 83 (1966).
[4] L. S. Berman, A. D. Remenyuk, and V. B. Shuman, Fiz. Tekh. Poluprovodn. **15**, 1155 (1981) [Sov. Phys. Semicond. **15**, 665 (1981)].
[5] A. M. Ivanov, N. B. Strokan, and V. B. Shuman, Pis'ma Zh. Tekh. Fiz. **23**, 79 (1997) [Tech. Phys. Lett. **23**, 369 (1997)].
[6] A. M. Ivanov, I. N. Il'yashenko, N. B. Strokan, and B. Shmidt, Fiz. Tekh. Poluprovodn. **29**, 543 (1995) [Semiconductors **29**, 281 (1995)].
[7] V. V. Emtsev, T. B. Mashovets, and V. V. Mikhnovich, Fiz. Tekh. Poluprovodn. **26**, 20 (1992) [Sov. Phys. Semicond. **26**, 12 (1992)].
[8] E. M. Verbitskaya, V. K. Eremin, A. M. Ivanov, and N. B. Strokan, Fiz. Tekh. Poluprovodn. **27**, 205 (1993) [Semiconductors **27**, 115 (1993)].
[9] N. V. Kuznetsov, V. N. Filatov, and V. G. Vinogradova, Fiz. Tekh. Poluprovodn. **21**, 609 (1987) [Sov. Phys. Semicond. **21**, 374 (1987)].
[10] V. S. Vavilov, V. F. Kiselev, and B. N. Mukashev, *Defects in and on the Surface of Silicon* [in Russian], Nauka, Moscow, 1990.

[11] A. Hallen, N. Keskitalo, F. Masszi, and V. Nagl, J. Appl. Phys. **79**, 3906 (1996).
[12] P. V. Kuchinskii and V. M. Lomako, Solid-State Electron. **29**, 1041 (1986).
[13] L. S. Berman and A. A. Levedev, *Capacitance Deep Level Spectroscopy of Semiconductors* [in Russian], Nauka, Leningrad, 1981.
[14] S. M. Ryvkin, L. L. Makovskiĭ, N. B. Strokan, and A. Kh. Khusainov, Fiz. Tekh. Poluprovodn. **3**, 1434 (1969) [Sov. Phys. Semicond. **3**, 1205 (1969)].
[15] L. L. Makovskiĭ, S. M. Ryvkin, N. B. Strokan, V. P. Subasheva, and A. Kh. Khusainov, in *Physics of Electron-Hole Junctions and Semiconductor Devices* [in Russian], Nauka, Leningrad, 1969.
[16] Yu. N. Nosov, *Physical Principles of Pulsed Operation of Semiconductor Diodes* [in Russian], Nauka, Moscow, 1968.
[17] M. Byczkowski and J. R. Madigan, J. Appl. Phys. **28**, 878 (1957).
[18] L. L. Makovsky, N. B. Strokan, and N. I. Tisnek, IEEE Trans. Nucl., Ser. **15**, 304 (1968).

Translated by M. E. Alferieff

Lifetime of nonequilibrium carriers in semiconductors from the standpoint of a collective interaction in the process of radiative recombination

S. V. Zaĭtsev and A. M. Georgievskiĭ

A. F. Ioffe Physicotechnical Institute, Russian Academy of Sciences, 194021 St. Petersburg, Russia
(Submitted June 25, 1997; accepted for publication July 14, 1997)
Fiz. Tekh. Poluprovodn. **32**, 366–368 (March 1998)

InGaAsP/InP laser heterostructures in the continuous pumping regime were investigated by autocorrelation methods. It was shown that below and above the lasing threshold the laser radiation consists of ultrashort coherent pulses and the temporal coherence of these pulses was measured. The dependence of the pulse duration on the pump current was also investigated. The results obtained can be interpreted in terms of collective resonances in the process of radiative recombination. To explain the observed effects the carrier lifetime was treated as a combination of the accumulation time and the collective emission time. © *1998 American Institute of Physics.* [S1063-7826(98)01403-3]

1. INTRODUCTION

The conventional working electron-hole pair densities in semiconductor lasers are much higher than the radiating-dipole densities in gas and solid-state lasers. An estimate of the nonequilibrium charge-carrier density in the active layer shows that the distance between charge carriers is much smaller than the wavelength of the radiation emitted by them. Therefore, they should interact during the radiative recombination process, just as in the case of Dicke superradiance.[1,2] As Dicke showed for two-level systems, if the dipole density is high, resonance interaction of the dipoles occurs and short pulses of coherent radiation are formed. However, this theory cannot be applied to semiconductors because of the wide energy distribution of the carriers. Nonetheless, a similar pulse structure of the radiation from semiconductor lasers has been observed,[3] although the formalism of such an interaction of the carriers in a semiconductor has still not been developed.

To investigate this phenomenon experimentally the autocorrelation functions (ACFs) of continuously pumped lasers have been studied.[4] It was first shown in Ref. 4 that ultrashort radiation pulses appear below the lasing threshold. It has been proved recently that such pulses exist above threshold and two different regimes of evolution of such pulses in a laser cavity have been observed.[5]

Detailed investigations of the temporal coherence of the radiation were performed in order to estimate the duration of the observed pulses and to study the dependence of the pulse duration on the pump current.

2. RESULTS

The experimental InGaAsP/InP ($\lambda = 1.3\ \mu$m) separate-confinement injection laser was grown by liquid-phase epitaxy. The waveguide was 0.5 μm thick, and the total thickness of the active layer was equal to about 500 Å.[6] The sample consisted of a planar-geometry laser diode with a 365-μm-long cavity and a 20-μm-wide waveguide. The threshold current density J_{th} was equal to 2750 A/cm^2.

Measurements of the temporal structure of the radiation were performed above the lasing threshold with continuous pumping.[5] A high-sensitivity optical autocorrelator based on the two-photon absorption in AlGaAs waveguide was built for the experiment.[7] The methods used for numerical processing and analysis of the ACFs are described in Ref. 5. The temporal coherence was also investigated as a function of the length Δx of the delay line and was determined as the ratio

$$\frac{I_{\max} - I_{\min}}{I_{\max} + I_{\min}} = f(\Delta x),$$

where $I_{\max}$ and $I_{\min}$ are the intensities at the maxima and minima of the corresponding interference pattern. Figure 1 shows the ACF (solid line) and the temporal coherence (dashed line) as a function of the delay-line length for currents $1.5 \cdot I_{th}$ (a), $2 \cdot I_{th}$ (b), and $3 \cdot I_{th}$ (c), respectively. One division on the X axis corresponds to the roundtrip time through the laser cavity ($\tau = 8.8$ ps). Unfortunately, measurements of the ACF could not be performed below the lasing threshold because the signal-to-noise ratio was too low. On the basis of the contrast, the observed ACF can be interpreted as being due to the presence of individual pulses of coherent radiation. The corresponding dependences of the temporal coherence on the length of the delay line for currents $1.5 \cdot I_{th}$ and $2 \cdot I_{th}$ (Figs. 1a and 1b) show a temporal structure similar to that of the ACF. The period of the pulses equals the roundtrip time through the cavity, and this attests to the fact that at each moment in time only one pulse propagates in the cavity. The initial pulse must be engendered at the cavity mirror (otherwise, the period would have to be twice as short). In the case of a pump current of $3 \cdot I_{th}$ neither the ACF nor the curve of the temporal coherence contains maxima with the roundtrip period of the cavity.

Figure 2a shows the half-width of the main maximum of the temporal coherence versus the pump current. A similar dependence was measured for the laser described in Ref. 4: It is represented by the dashed line in the figure (Fig. 2b). The pulsed structure of the radiation for the sample was observed below threshold down to $0.8 \cdot I_{th}$. Below this current the ACF could not be measured because of the low signal-to-noise ratio.

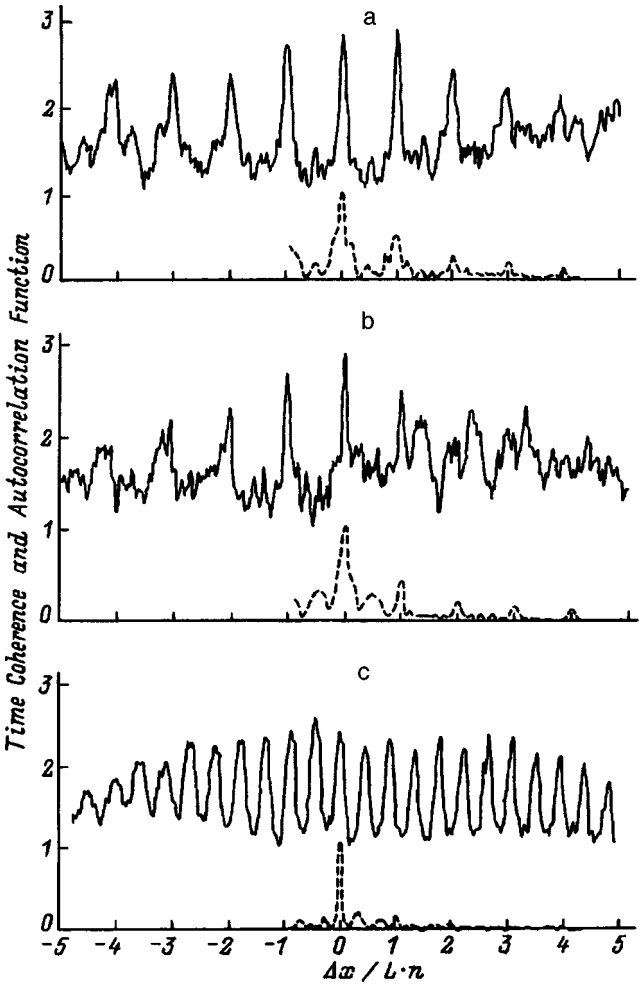

FIG. 1. Autocorrelation functions (solid line) and temporal coherence (dashed line) of radiation for pump currents I_{th} : a—1.5, b—2, c—3.

3. DISCUSSION

The results obtained are due to the fundamental properties of radiative recombination for the pump levels employed and the positive feedback at the resonance of the laser. As shown in Ref. 4, superluminescence in semiconductors should be in the form of short coherent pulses. However, the development and transformation of the pulses depend on the properties of the waveguide and the Fabry–Perot cavity.[8]

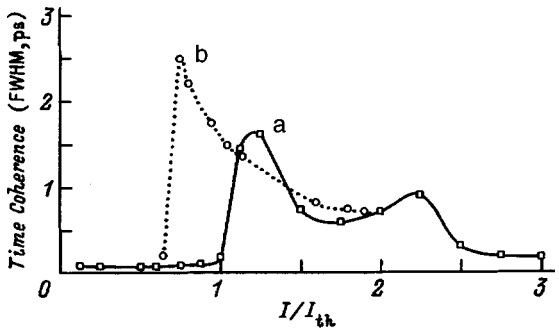

FIG. 2. Half-width of the central peak of the temporal coherence of the laser radiation versus the pump current.

We suggest the use of the collective-interaction model to explain the experimental results. The current dependence of the half-width of the central maximum of coherence and the ACF can then be regarded as being due to a change in the number of electron-hole pairs in the radiating aggregate. The number N of oscillators in the aggregate can be determined in terms of the modified lifetime of a radiating aggregate consisting of N pairs:[2] $\tau_N = \tau_1 / N$. Thus, in this scheme the spontaneous radiative lifetime is a function of N.

Below the lasing threshold the number of carriers in the aggregate (just as the local carrier density) gradually grows in time at a rate determined by the pump current density. At the moment of the collective resonant emission of an optical pulse the density in the corresponding spatial region and spectral interval will then drop rapidly. It will subsequently gradually build up as a result of the continuing pump current, thermal relaxation of the carriers and, possibly, spatial diffusion, and the process repeats. In this case the pulses cannot have a sharp period, although a characteristic carrier accumulation time should exist. The modulation of the carrier density should be strong in this case, while the peak density should be high. This can explain the short radiative lifetime of the aggregate as being due to the large value of N.

A substantially different situation is observed near the lasing threshold. After a round trip through the cavity the optical pulses return, having now a substantial amplitude, to their point of creation. This leads to induced emission and prevents further accumulation of carriers. It is natural to assume that at least in our case the characteristic carrier accumulation time below the lasing threshold is much longer than the roundtrip period of the cavity. Then, provided that the carrier accumulation rate changes very little, a decrease of the accumulation time signifies a substantial decrease of the peak carrier density in this region and energy interval. For this reason, the characteristic number N of carriers in the drops collectively, and the radiative lifetime of the group increases. Such changes are usually observed at the threshold, but they can also be observed below the threshold (Fig. 2b), if the amplitude of the returning pulses is sufficiently high to disrupt the carrier accumulation process.

As the pump current increases further, N likewise should increase and the radiative lifetime should gradually decrease. The existence of a second maximum apparently reflects the possibility that more than one such pulse appears during the round trip through the cavity.

Assuming that the temporal profile of the observed pulses is symmetric, we obtain a half-width of 0.4 ps for a current of $1.8 \cdot I_{th}$. The data obtained from the ACF and coherence measurements with equal currents in this interval are identical. The curve in Fig. 2a shows the presence of even shorter pulses at $I > 2.5\ I_{\text{th}}$, but the central peak corresponding to the ACF (Fig. 1c) is broadened. This could be due to the interaction of coexisting pulses in the laser cavity.

4. CONCLUSIONS

As shown in Refs. 4 and 5, superluminescence in semiconductors consists of ultrashort coherent pulses. Thus, the

results obtained pertain to the main properties of radiative recombination in semiconductors with typical levels of pumping.

In the present work it was demonstrated on the basis of an investigation of the ACF and the temporal coherence that optical pulses with a duration of 400 fs are formed with continuous pumping of an injection laser.

To explain the experimental results, a model of a collective interaction of carriers was proposed. The density of the variable number of oscillators in the radiating aggregate was introduced in order to interpret the pump-current dependence of the coherence (pulse duration). It was shown that the measured hyperfine pulsed structure of the laser radiation can be interpreted on the basis of a collective interaction under conditions of radiative recombination.

We thank N. A. Pikhtin and I. S. Tarasov for providing the experimental samples of injection lasers.

[1] R. H. Dicke, Phys. Rev. **93**, 99 (1054).
[2] L. Allen and J. H. Eberly, *Optical Resonance and Two-Level Atoms*, Wileym, N.Y., 1975.
[3] A. I. Gurevich, A. B. Grudinin, A. G. Deryagin, S. V. Zaĭtsev, V. I. Kuchinskiĭ, D. V. Kuksenkov, E. L. Portnoĭ, and I. Yu. Khrushchev, Pis'ma Zh. Tekh. Fiz. **18**, 38 (1992) [Sov. Tech. Phys. Lett. **18**, 74 (1992)].
[4] S. V. Zaitsev and A. M. Georgievski, in *Proceedings of the Int. Conf. SPIE on OPTDIM'95*, Kiev, 1995, Vol. **2648–50**, p. 319.
[5] S. V. Zaitsev and A. M. Georgievski, in *Proceedings of the International Conference QDS'96*, Sapporo, Japan, November 4–7, 1996, published in JJAP, part 1, **36**, 4209 (1997).
[6] I. S. Tarasov, L. S. Vavilova, N. I. Katsavets, A. V. Lyutetskiy, A. V. Murashova, N. A. Pikhtin, N. A. Bert, and Zh. I. Alferov, in *Proceedings of the International Conference on Nanostructures*, St. Petersburg, 1996, p. 351.
[7] A. M. Georgievskiĭ and S. V. Zaĭtsev, Prib. Tekh. Éksp. **1**, 132 (1996).
[8] O. Hess and T. Kugn, Phys. Rev. A **54**, 3360 (1996).

Translated by M. E. Alferieff

Current-voltage characteristics of GaN and AlGaN $p-i-n$ diodes

N. I. Kuznetsov

A. F. Ioffe Physicotechnical Institute, Russian Academy of Sciences, 194021 St. Petersburg, Russia

K. G. Irvine

Cree Research Inc. Durham, North Carolina 27713, USA
(Submitted July 1, 1997; accepted for publication July 14, 1997)
Fiz. Tekh. Poluprovodn. **32**, 369–372 (March 1998)

The current-voltage characteristics of GaN and $Al_{0.08}Ga_{0.92}N$ $p-i-n$ diodes were investigated. The experimental $p-i-n$ structures were grown by MOCVD on 6*H*-SiC with Si and Mg as dopants. The i region was formed by simultaneously doping with donor and acceptor impurities during growth. Analysis of the current-voltage characteristics showed that current flow in the $p-i-n$ diodes is due to either drift of thermally excited holes or electron-hole recombination in the i region via impurity centers—just as predicted by the Ashley–Milnes theory. These impurity centers are attributed to Mg acceptor levels. © *1998 American Institute of Physics.* [S1063-7826(98)01503-8]

1. INTRODUCTION

Group-III nitrides InN, GaN, and AlN and their solid solutions InGaN and AlGaN, which are wide-gap semiconductors with direct interband transitions, are now successfully used in optoelectronic devices emitting light in the short-wavelength region.[1–4] This progress was made possible by the use of Mg as an acceptor impurity to obtain p-type material.[5–7] The development of $p-n$ junctions based on GaN and AlGaN makes it possible to investigate their electrical and optical characteristics.[8–14]

Our objective in the present work is to investigate the current-voltage characteristics (IVCs) of GaN- and AlGaN-based $p-i-n$ diodes. The strong scientific interest shown in current flow in $p-i-n$ diodes is due to the fact that the observed complicated structure of the IVCs is determined by the electronic properties of the semiconductor material itself. Specifically, information about the ionization energies and carrier trapping cross sections of recombination centers can be extracted from the IVCs of $p-i-n$ diodes.

2. EXPERIMENTAL PROCEDURE

The GaN- and AlGaN-based $p-i-n$ structures were grown by gas-phase epitaxy using organometallic compounds (MOCVD) on silicon carbide substrates.[15] The $n-6H$-SiC wafers, produced commercially by Cree Research Inc. (USA), were used as substrates. The epitaxial layers were deposited on the (0001) face of a Si substrate; Mg and Si were used as acceptor and donor impurities, respectively. First, a n-GaN layer, doped with Si to density $N_d-N_a=2\times10^{18}$ cm^{-3}, were grown. This layer was 1.5 μm thick. A 0.5-μm-thick epitaxial layer of p^+-GaN, doped with Mg to density $N_a-N_d=10^{19}$ cm^{-3}, was grown last. The $p-i-n$ junctions based on GaN and AlGaN were formed between these epitaxial layers, and the i region was formed during epitaxial growth by simultaneously doping with donor and acceptor impurities. The AlN concentration in the AlGaN solid solution was equal to 8 mole %, as measured by Auger spectroscopy. Mesa structures 300 μm in diameter were etched by ion-plasma etching in order to measure the electrical characteristics of the $p-i-n$ junctions. To prevent the isotypic heterojunction GaN/SiC from influencing the experimental results, a planar geometry was used for the mesa structures. Pd and Al were deposited as ohmic contacts to p^+-GaN and n-GaN or n-AlGaN, respectively (see Fig. 1).

Measurements of the room-temperature capacitance–voltage characteristics (CVCs) at 1 MHz showed that the dependence of the barrier capacitance C of the mesa structures on the applied voltage V was linear in C^2-V coordinates. Here, the capacitance cutoff voltage equals 4–7 V. This value is much higher than the built-in potential for GaN and $Al_{0.08}Ga_{0.92}N$ $p-n$ junctions, whose p and n layers are doped with Mg and Si, respectively.[13,14] This indicates the presence of an i region between the p and n layers. Analysis of the CVCs showed the i region to be approximately 0.1 μm thick.

3. EXPERIMENTAL RESULTS AND DISCUSSION

Direct I-V characteristics of the $p-i-n$ diodes were investigated in the temperature range from 77 to 600 K. At room temperature the mesa structures possess the typical diode I-V characteristics. The cutoff voltage on the forward IVC varied from 4 to 7 V for different samples, in agreement with the data obtained from capacitance measurements.

The I-V characteristics measured at different temperatures are presented in Fig. 2 for GaN-based $p-i-n$ diodes and in Fig. 3 for AlGaN-based diodes. As one can see from the figures, the IVCs consist of several sections, which can be described by a power-law function $I\sim V^b$, where b ranges from 1 to 10. At temperatures below 100 K and when the applied forward bias exceeds 15 V, the experimental $p-i-n$ diodes switched rapidly into a state of higher conductivity, corresponding to the section of the IVC above the negative-resistance region (s-shaped IVC). Such a behavior of the forward current is characteristic of $p-i-n$ diodes and can be described by the Ashley–Milnes theory.[16] In this model, a

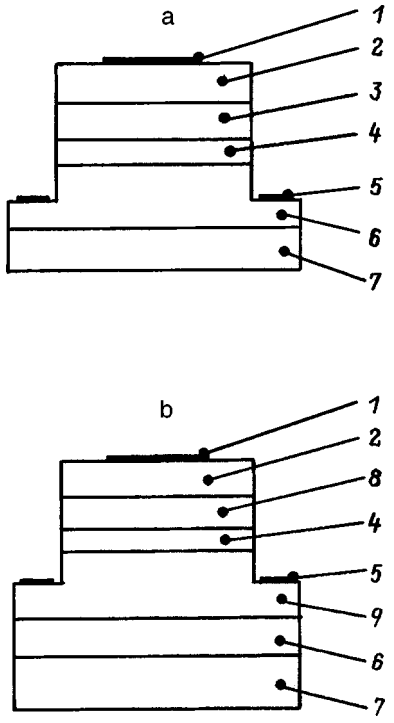

FIG. 1. Transverse section of mesa structures based on: a—GaN, b—AlGaN. Numbers on the figures: *1*—Pd contact, *2*—p^+-GaN, *3*—*p*-GaN, *4*—*i* region, *5*—Al contact, *6*—*n*-GaN layer, *7*—6*H*-SiC substrate, *8*—*p*-$Al_{0.08}Ga_{0.92}N$, *9*—*n*-$Al_{0.08}Ga_{0.92}N$.

high-resistance semiconductor, which exhibits impurity conductivity and possesses compensation centers partially filled by electrons, is studied. The position of the compensation level in the band gap can be arbitrary, but the level must be deep enough so that the density of thermally excited holes is much less than the density of the compensation centers themselves. It is assumed in the model that in the case of a forward current the compensation centers in the *i* region play the role of recombination centers for injected electrons and holes. In order for a negative-resistance section to be present

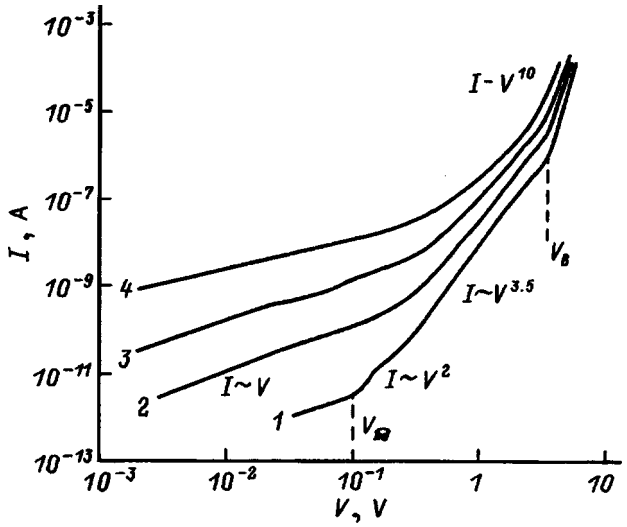

FIG. 2. Forward current-voltage characteristics of GaN-based *p*–*i*–*n* structures measured at temperatures *T*, K: *1*—300, *2*—400, *3*—500, *4*—600.

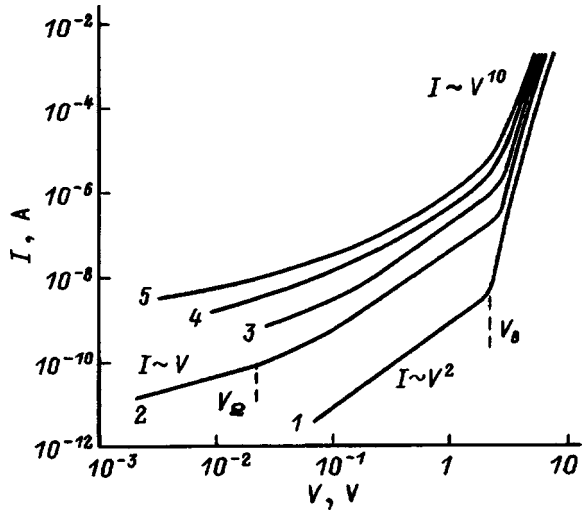

FIG. 3. Forward current-voltage characteristics measured on AlGaN-based *p*–*i*–*n* structure at temperatures *T*, K: *1*—200, *2*—300, *3*—400, *4*—500, *5*—600.

in the IVC, the hole trapping cross section σ_p must be much larger than the electron trapping cross section σ_n of recombination centers.

The IVCs of the experimental *p*–*i*–*n* diodes possess an ohmic current section ($b=1$), a quadratic current section ($b=2$) and a transitional current section ($b=10$), which at temperatures below 100 K passes into a current section with negative resistance. The recombination-limited current of injected electrons starts to dominate the thermally excited hole current on the section of the IVC where $I \sim V^2$. The transition of the ohmic section to the quadratic section occurs at a voltage V_Ω where the lifetime τ_n of the electrons becomes equal to the time it takes the electrons, $L^2/\mu_n V_\Omega$, to pass through the *i* region. The voltage V_Ω can be found from the expression[16]

$$V_\Omega \approx \frac{L^2}{\mu_n \tau_n} = \frac{L^2 \sigma_n v_n N_{te}}{\mu_n}, \tag{1}$$

where L is the length of the *i* region, μ_n is the electron mobility, ν_n is thermal velocity of the electrons, and N_{te} is the density of electronic traps.

The transitional section of the current on the IVC ($b=10$) is characterized by a substantial increase in the number of injected holes. For voltages above the breakdown voltage V_b the transit time of holes through the *i* region becomes equal to the hole lifetime τ_p. The value of V_b can be found from the expression[16]

$$V_b = L^2 \left(\frac{q \sigma_p v_p}{4 \pi \varepsilon \mu_p} \right)^{0.5} N_{th}, \tag{2}$$

where ν_p is the thermal velocity of the holes, ε is the dielectric constant, μ_p is the hole mobility, and N_{th} is the density of hole traps.

According to the Ashley–Milnes theory, the forward current at voltages less than V_b is directly proportional to the density of thermally excited holes. This feature can be used to determine the ionization energy of the recombination centers. We have therefore measured the temperature depen-

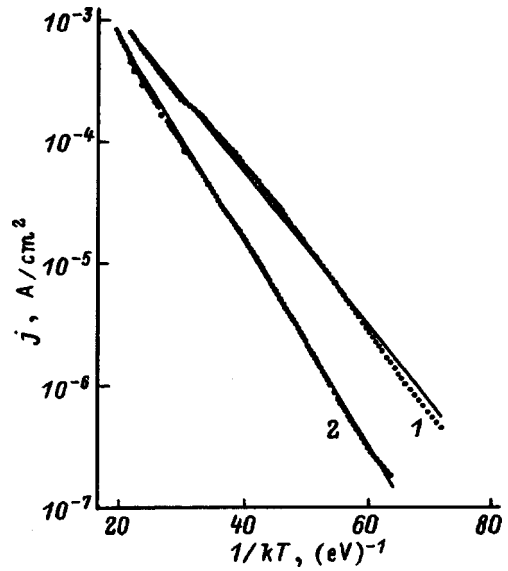

FIG. 4. Temperature dependences of the forward current with fixed voltage corresponding to the quadratic section of the IVC for diodes based on: *1*—GaN ($E_a=0.146$ eV), *2*—$Al_{0.08}Ga_{0.92}N$ ($E_a=0.191$ eV). Dots—experiment, the straight lines were drawn manually to determine the ionization energy.

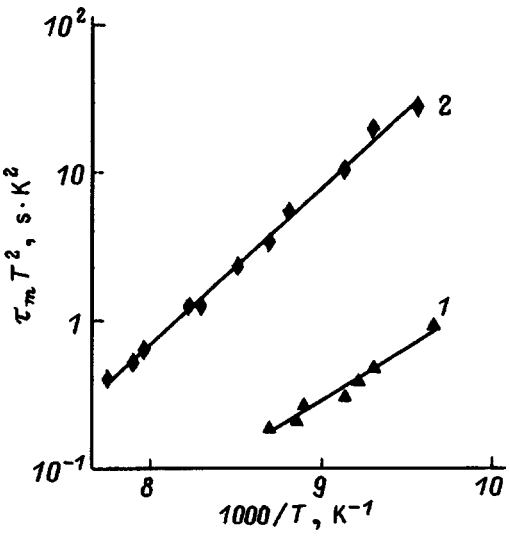

FIG. 5. Arrhenius plots, obtained from the families of *i*-DLTS spectra, for hole traps for the following layers: *1*—GaN ($E_a=1.141$ eV), *2*—$Al_{0.08}Ga_{0.92}N$ ($E_a=0.207$ eV).

dence of the current I with fixed voltage V (see Fig. 4). The slope of the straight lines drawn in Fig. 4 through the experimental points corresponds to the ionization energies of the recombination levels: *1*—0.146 eV and *2*—0.191 eV, which are attributed to acceptor levels of Mg in GaN and $Al_{0.08}Ga_{0.92}N$, respectively.

The expressions (1) and (2) can be used to calculate the electron and hole trapping cross sections of recombination centers. The hole mobilities for GaN and $Al_{0.08}Ga_{0.92}N$ $\mu_p=10$ cm^2/(V·s) were used to calculate the hole trapping cross section.[17] The following electron mobility in GaN was used to calculate the electron trapping cross section:[18] $\mu_p=200$ cm^2/(V·s). Since the electron mobility in $Al_{0.08}Ga_{0.92}N$ is unknown, we assumed that μ_n in $Al_{0.08}Ga_{0.92}N$ is close to the value of μ_n in GaN. The computational results are summarized in Table I.

Capacitance spectroscopy of deep levels—the *c*-DLTS method, proposed by Lang[19]—is widely used to investigate levels in the band gap of a semiconductor. However, capacitance methods are limited in investigations of levels in high-resistance semiconductor. For this reason, we employed current spectroscopy—the *i*-DLTS method—to investigate levels in the *i* region.[20] The *i*-DLTS measurements were performed in the temperature range from 77 to 300 K. A reverse bias of -5 V was applied to the mesa structure. To fill the traps with carriers the reverse bias was switched in a pulsed manner to a forward current of 10 mA. To determine the parameters of the levels a family of *i*-DLTS spectra with a constant ratio $t_2/t_1=2$ was recorded for different values of t_1, which was varied from 10 μs to 10 ms. Here t_1 and t_2 are the times at which the amplitude of the relaxation current is measured. The parameters of the observed levels were determined from an Arrhenius plot (Fig. 5), which was constructed from the family of *i*-DLTS spectra. The results of the calculations of the parameters of a Mg acceptor center on the basis of *i*-DLTS are summarized in Table I. The hole effective mass $m_h^*=0.8m_0$ was used to calculate the hole trapping cross section in GaN.[21] Since the hole effective mass in $Al_{0.08}Ga_{0.92}N$ is unknown, we assumed that m_h^* in it is close to m_h^* in GaN.

It should be noted that the ionization energies obtained for the Mg acceptor level in GaN and $Al_{0.08}Ga_{0.92}N$ from IVC and *i*-DLTS measurements are in good agreement with Hall effect measurements.[17]

4. CONCLUSIONS

The current-voltage characteristics of $p-i-n$ diodes fabricated on the basis of GaN and $Al_{0.08}Ga_{0.92}N$ layers grown by the MOCVD method on silicon carbide substrates were investigated. Analysis of the IVCs showed that current flow

TABLE I. Parameters of Mg acceptor center in GaN and $Al_{0.08}Ga_{0.92}N$.

	GaN		$Al_{0.08}Ga_{0.92}N$	
Parameter of acceptor center	$I-V$	*i*-DLTS	$I-V$	*i*-DLTS
E_a, eV	0.146	0.141	0.191	0.207
σ_p, cm^2	8×10^{-13}	4×10^{-15}	8×10^{-14}	2×10^{-13}
σ_n, cm^2	3×10^{-14}		3×10^{-15}	

The parameters were calculated according to the data: $I-V$—current-voltage characteristics, *i*-DLTS—current deep-level spectroscopy.

in the $p-i-n$ diodes is due either to drift of thermally excited holes or electron-hole recombination in the i region via impurity centers—just as the Ashley–Milnes theory predicts. These impurity centers are attributed to Mg acceptor levels. The ionization energies determined for the Mg acceptor level in GaN and $Al_{0.08}Ga_{0.92}N$ from IVC and i-DLTS measurements are in good agreement with Hall effect measurements.

We thank V. E. Sizov for etching the mesa structures, E. V. Kalinin for depositing the ohmic contacts, and V. A. Dmitriev for helpful discussions of the measurements.

This work was supported in part by the Arizona State University (USA).

[1] S. Nakamura, T. Mukai, and M. Senoh, Appl. Phys. Lett. **64**, 1687 (1994).
[2] S. Nakamura, M. Senoh, N. Iwasa, and S. Nagahama, Jpn. J. Appl. Phys. **34**, L797 (1995).
[3] S. Nakamura, M. Senoh, N. Iwasa, S. Nagahama, T. Yamada, and T. Mukai, Jpn. J. Appl. Phys. **34**, L1332 (1995).
[4] S. Nakamura, M. Senoh, N. Iwasa, S. Nagahama, T. Yamada, T. Matsushita, H. Kiyoku, and Y. Sugimoto, Jpn. J. Appl. Phys. **35**, L74 (1996).
[5] H. Amano, M. Kito, K. Hiramatsu, and I. Akasaki, Jpn. J. Appl. Phys. **28**, L2112 (1989).
[6] S. Nakamura, T. Mukai, M. Senoh, and N. Iwasa, Jpn. J. Appl. Phys. **31**, L139 (1992).
[7] H. Morkoc, S. Strite, G. B. Gao, M. E. Lin, B. Sverdlov, and M. Burns, J. Appl. Phys. **76**, 1363 (1994).
[8] I. Akasaki and H. Amano, J. Electrochem. Soc. **141**, 2266 (1994).
[9] S. Nakamura, T. Mukai, and M. Senoh, Jpn. J. Appl. Phys. **30**, L1998 (1991).
[10] B. Goldenberg, J. D. Zook, and R. J. Ulmer, Appl. Phys. Lett. **62**, 381 (1993).
[11] M. A. Khan, Q. Chen, R. A. Skoqman, and J. N. Kupnia, Appl. Phys. Lett. **66**, 2047 (1995).
[12] V. A. Dmitriev, K. G. Irvine, C. H. Carter Jr., A. S. Zubrilov, and D. V. Tsvetkov, Appl. Phys. Lett. **67**, 115 (1995).
[13] V. A. Dmitriev, K. G. Irvine, C. H. Carter Jr., N. I. Kuznetsov, and E. V. Kalinina, Appl. Phys. Lett. **68**, 229 (1996).
[14] V. A. Dmitriev, K. G. Irvine, J. A. Edmond, C. H. Carter Jr., N. I. Kuznetsov, A. S. Zubrilov, E. V. Kalinina, and D. V. Tsvetkov, in *Proceedings of the 6th International Conference*, Kyoto, Japan, 1995 [Inst. Phys. Conf. Ser. **142**, 1019 (1995)].
[15] V. A. Dmitriev, K. G. Irvine, J. A. Edmond, C. H. Carter Jr., A. S. Zubrilov, I. P. Nikitina, V. I. Nikolaev, A. I. Babanin, Yu. V. Melnik, E. V. Kalinina, and V. E. Sizov, in *Proceedings of the 21st Intern. Symp. on Compound Semicond.*, San Diego, CA, USA, 1994 [Inst. Phys. Conf. Ser. **141**, 497 (1995)].
[16] K. L. Ashley and A. G. Milnes, J. Appl. Phys. **35**, 369 (1964).
[17] T. Tanaka, A. Watanabe, H. Amano, Y. Kobayashi, I. Akasaki, S. Yamazaki, and M. Koike, Appl. Phys. Lett. **65**, 593 (1994).
[18] D. L. Rode and D. K. Gaskill, Appl. Phys. Lett. **66**, 1972 (1995).
[19] D. V. Lang, J. Appl. Phys. **45**, 3023 (1974).
[20] N. I. Kuznetsov, Fiz. Tekh. Poluprovodn. **27**, 1674 (1993) [Sov. Phys. Semicond. **27**, 925 (1993)].
[21] J. I. Pankove, S. Bloom, and G. Harbeke, RCA Rev. **36**, 163 (1975).

Translated by M. E. Alferieff

Spatial distribution of the radiation in the far zone of InAsSb/InAsSbP mesastrip lasers as a function of current

T. N. Danilova, A. P. Danilova, O. G. Ershov, A. N. Imenkov, V. V. Sherstnev, and Yu. P. Yakovlev[a)]

A. F. Ioffe Physicotechnical Institute, Russian Academy of Sciences, 194021 St. Petersburg, Russia
(Submitted August 4, 1997; accepted for publication September 15, 1997)
Fiz. Tekh. Poluprovodn. **32**, 373–376 (March 1998)

The far-zone directional pattern of diode mesastrip lasers with a 10 μm wide strip has been investigated as a function of the current. The directional pattern in the plane of the $p-n$ junction contains one longitudinal mode, whose width depends on the current. It is shown by comparing the theoretically computed and experimentally measured spatial modes that this dependence is determined by the variation of the light flux intensity and the free-carrier density distributions over the strip width as a function of the current. In the case when the distributions are close to uniform the maximum narrow spatial longitudinal mode and a unimodal radiation spectrum are observed. © *1998 American Institute of Physics.*
[S1063-7826(98)02803-8]

1. A great deal of attention is now being devoted to the investigation of current-tunable lasers, since such lasers are the key components of diode-laser spectroscopy. When current is used to tune the wavelength of the radiation, the spatial distribution of the radiation changes with the current. It is important to investigate the current dependence of the spatial distribution of the radiation both in order to understand the physics of laser tuning processes and for applications of lasers in diode spectroscopy.

The present paper is a continuation of our investigations of tuning by means of current[1,2] and of the spatial distribution[3] of the radiation of InAsSb/InAsSbP lasers operating in the spectral range 3.0–3.9 μm. In Ref. 3 the spatial modes of these lasers were investigated as a function of the geometric dimensions of the lasers. Our objective in the present work is to investigate the variation of the spatial distribution of the radiation of frequency-tunable diode lasers as a function of the current strength.

2. Lasers based on the heterostructures N-$InAs_{0.52}Sb_{0.18}P_{0.30}$/$n$-$InAs_{0.95}Sb_{0.05}$/$P$-$InAs_{0.52}Sb_{0.18}P_{0.30}$ were prepared by the method of liquid-phase epitaxy. The active region was ~ 1 μm thick and the wide-gap emitters were ~ 3 μm thick. The active region was specially not doped, and the electron density there was equal to $\sim 10^{16}$ cm^{-3}. The N-InAsSbP layer was doped with Sn up to electron density $(2-5)\times 10^{18}$ cm^{-3}, and P-InAsSbP was doped with Zn up to hole density $\sim 1\times 10^{18}$ cm^{-3}.

Mesostrips with a width of ~ 10 μm were formed on the grown structures using standard photolithography, since only one longitudinal spatial mode has been observed in such lasers with 13–14 μm wide strips.[3] Cavities with a length of 225–300 μm were obtained by cleaving.

The radiation of the lasers was investigated in a quasicontinuous mode with the lasers powered by square current pulses of alternating polarity with a repetition frequency of 80 Hz at liquid-nitrogen temperature.

3. The directional pattern, the intensity of the total radiation, and the radiation spectra of the lasers were measured in the current range from the threshold level I_{th} up to $I \simeq 5I_{th}$. The threshold current in the best lasers was equal to ~ 12 mA, and the threshold current density $I_{th} \simeq 530$ A/cm^2 at 77 K.

The half-width $\Delta\theta$ of the directional pattern (the width of the directional pattern at half-height of the maximum total intensity) was measured as a function of current (Fig. 1a). The measurements were performed in the plane of the $p-n$ junction (curve *1*) and in a plane perpendicular to the $p-n$ junction (curve *2*). In the plane of the $p-n$ junction $\Delta\theta$ decreases rapidly from 50 to 20° when $I<I_{th}$. At currents above threshold $\Delta\theta$ continues to decrease and reaches its minimum value of $\sim 17°$ in the current range $(2.0–2.5)I_{th}$. As current increases further, $\Delta\theta$ in the plane of the $p-n$ junction increases and once again reaches 20° for $I/I_{th} \simeq 4$, after which it increases strongly up to 40° at $I/I_{th} \simeq 5$. In a plane perpendicular to the $p-n$ junction, for currents $I<I_{th}$ $\Delta\theta$ increases with current from 40 to 46°. In the current interval from I_{th} up to 3.4 I_{th} $\Delta\theta$ remains unchanged and approximately equals 45°, and as current increases further, $\Delta\theta$ decreases to $\sim 36°$.

The current dependence of the total intensity F_Σ (Fig. 1b) up to currents less than $I=2.5I_{th}$ has a form characteristic for semiconductor diode lasers, but for higher currents this dependence changes from linear to sublinear. For currents $(3.5-4.5)I_{th}$ a shelf is observed in the curve. As current increases further, the total intensity once again starts to increase with current.

The laser investigated emits at the wavelength ~ 3.3 μm. In the current range from $1.25I_{th}$ up to $3.8I_{th}$ the same mode predominates in the radiation spectrum. However, its intensity F_{max} as a fraction of the sum of the intensities of all modes ΣF_i increases from 0.5 to 0.98 as current increases from $1.25I_{th}$ up to $2I_{th}$, and then decreases to 0.45 as current increases up to $3.8I_{th}$.

4. We shall now discuss the results obtained.

For currents $I<I_{th}$ the narrowing of the directional pattern is determined by the increase with current of the relative fraction of the stimulated radiation. To analyze the experimentally obtained directional patterns in the plane of the

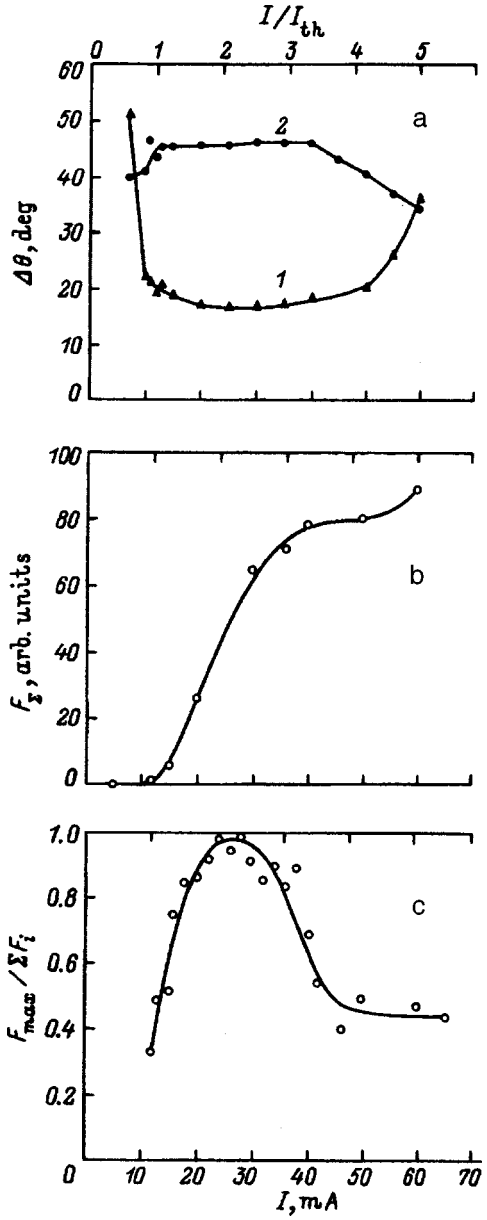

FIG. 1. The current dependence of the width $\Delta\theta$ (a) of the directional pattern at half-height of the maximum intensity in the plane of the $p-n$ junction (*1*) and in a plane perpendicular to the plane of the $p-n$ junction (*2*), the intensity of the total radiation F_Σ (b), and the curve of the ratio $F_{\max}/\Sigma F_i$ (c) of the intensity of the maximum mode in the spectrum to the sum of the intensities of all modes for a V12192-1 laser.

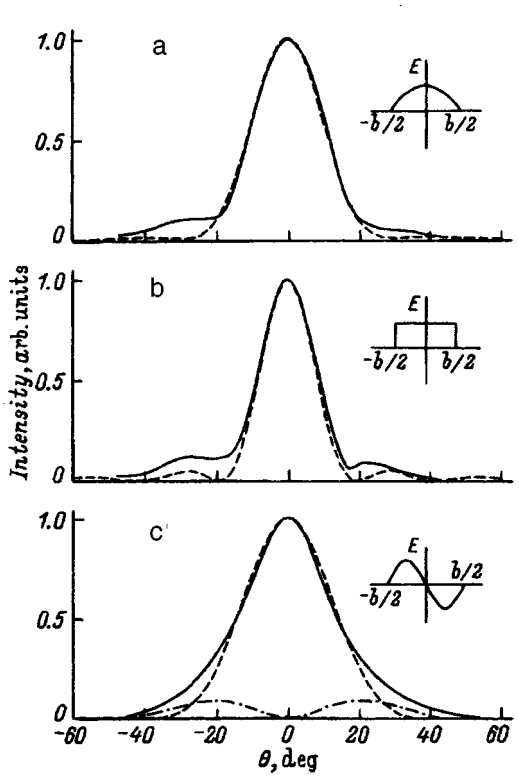

FIG. 2. Total radiation intensity versus the angle θ between the direction of detection and the normal to the cavity plane. The dashed and dot-dashed lines show the theoretical curves, the solid lines are the measured directional patterns for a V12192-1 laser. Insets: Distribution over the strip width b of the amplitude of the vector **E** of the electromagnetic wave at the exit mirror of the cavity. The theoretical curves of the longitudinal mode (dashed line) were calculated for strip widths (μm): a — 10, b — 10, c — 7.9. The experimental curves (solid lines) were measured at the currents: a —$1.1I_{\text{th}}$, b —$2.5I_{\text{th}}$, c —$4.6I_{\text{th}}$. c: The dot-dashed line represents the theoretical curve of the intensity of the transverse mode with $b=7.9$ μm.

$p-n$ junction for $I>I_{\text{th}}$ we compared these patterns with the theoretically computed patterns as done in Ref. 3. Figures 2a, 2b, and 2c show the theoretical curves (dashed and dot-dashed lines) of the total intensity distribution F_Σ of the radiation as a function of the angle θ between the direction of detection and the normal to the cacity plane, while the solid lines show the measured directional patterns.

The theoretical curve (dashed curve in Fig. 2a) corresponds to a calculation with a cosine distribution of the amplitude of the vector **E** of the electromagnetic wave at the output mirror of the cavity (see inset in Fig. 2a). The calculation was performed according to the simplified formula

$$F(\theta)\sim\left[\frac{\cos\alpha}{1-(2\alpha/\pi)^2}\right]^2;\quad \alpha=\frac{\pi b}{\lambda}\sin\theta, \tag{1}$$

where λ is the wavelength of the radiation and b is the width of the cavity. The curve is calculated for $b=10$ μm, which corresponds to the width of a mesostrip. As one can see, the measured directional pattern, obtained with the current of $1.1I_{\text{th}}$, agrees well with this theoretical curve. Therefore the directional pattern with a current of $1.1I_{\text{th}}$ corresponds to one longitudinal mode with a cosine distribution of the amplitude of the vector **E** of the electromagnetic wave over the width of the strip; this is due to the fact that for currents only slightly above the threshold current the refractive index is constant over the width of the strip.

Since the maximum narrowing of the directional pattern occurs for currents $(2.0–2.5)I_{\text{th}}$ (Fig. 1, curve *1*), the broadening of the light flux is maximum. In this case the distribution of the amplitude of the vector **E** of the electromagnetic wave over the width of a strip is not cosinusoidal. The distribution can be close to uniform because the role of surface recombination at the edge of the strip decreases with increasing current, while the injection density increases more strongly at the edges than at the center of a strip.

The theoretical curve (dashed line in Fig. 2b) for a uniform distribution of the amplitude of the vector **E** (see inset in Fig. 2b) was calculated according to the formula

$$I(\theta) \simeq \left[\frac{\sin\ \alpha}{\alpha}\right]^2, \tag{2}$$

with a strip width $b = 10\ \mu$m.

The experimental directional pattern measured with current $I = 2.5 I_{\text{th}}$ agrees well with this theoretical curve. This probably confirms the fact that the light flux is close to uniform for currents such that the narrowing of the directional pattern is maximum.

The width of the directional pattern increases as the current increases further (Fig. 1, curve *1*). This can happen as a result of the narrowing of the light flux because of the appearance of lateral optical confinement caused by an increase in the nonequilibrium carrier density at the strip edges and decrease of the nonequilibrium current density at the center of the strip. For currents exceeding $2.5 I_{\text{th}}$ the losses to surface recombination become very small compared with the current strength and can be neglected. On the other hand, as the current increases, the carrier density can increase at the edges and decrease at the center of the strip, since the rate of stimulated recombination is higher at the center an lower at the edges, where $\mathbf{E} \rightarrow 0$. As the carrier density increases, the refractive index decreases.[4,5] If the refractive index at the strip edges decreases by more than $(\lambda/2b)^2$, then lateral optical confinement forms within the strip, narrowing the light flux in the plane of the $p-n$ junction. The decrease in refractive index for high currents is also confirmed by the current dependence of the directional pattern in a plane perpendicular to the plane of the $p-n$ junction. In this region the width of the directional pattern is determined by losses to diffraction by the slit, since the width of the light flux is the same as the thickness of the active region, i.e. it is of the order of 1 μm. In this region the directional pattern becomes narrower as the light flux expands, which is observed for high currents$I > 3.5 I_{\text{th}}$ (Fig. 1, curve *2*). In a plane perpendicular to the plane of the $p-n$ junction, the decrease in the refractive index with increasing current degrades optical confinement, and the light flux penetrates into the wide-gap regions, increasing losses due to absorption by free carriers in these regions. This weakens the current dependence of the total intensity for $I > 3.5 I_{\text{th}}$ (Fig. 1b).

We endeavored to determine the narrowing of the light flux in the plane of the $p-n$ junction with high currents as a result of the appearance of lateral optical confinement. It was found that at current $I = 4.6 I_{\text{th}}$ the experimental points fall on the theoretical curve calculated from Eq. (1) with $b = 7.9\ \mu$m. This means that for $I = 4.6 I_{\text{th}}$ the width of the light flux in the plane of the $p-n$ junction decreases by approximately 2 μm. In addition, at this current the directional pattern at the base is somewhat wider than that corresponding to a cosine distribution. This is probably due to the appearance of a weak transverse mode of the first harmonic, associated with an antisymmetric distribution of the light flux, shown in the inset in Fig. 2c, over the width of the strip. The theoretical curve for this mode (dot-dashed curve in Fig. 2c) was calculated for the width of the light flux $b = 7.9\ \mu$m according to the formula

$$F(\theta) \sim \left[\frac{\sin\ \alpha}{1-(\alpha/\pi)^2}\right]^2. \tag{3}$$

The relative fraction ofthis radiation does not exceed 6%.

Let us consider the variation of the mode composition of the radiation as a function of the current (Fig. 1c). The interesting feature of this dependence is that in the current interval $I = (2.0-2.5) I_{\text{th}}$, where maximum narrowing of the longitudinal mode in the plane of the $p-n$ junction occurs (Fig. 1a, curve *1*) and, as shown by comparing with the theoretically computed mode, the distribution of the amplitude of the vector **E** over the width of the strip is uniform, the maximum unimodal regime is observed in the spectrum of the radiation (Fig. 1c). This could be due to the fact that in the case of a uniform distribution of the amplitude of the vector **E** the intensification is also distributed uniformly, and generation conditions are produced only for one spectral mode, located at the maximum of the gain spectrum. The regime is found to be unimodal.

For higher and lower currents, the carrier density is depressed at the center of the strip, because the vector **E** has a maximum here, and it is insufficient for radiation generation and adequate only for stimulation. In the stimulation regime many spectral modes arise and are intensified near the top of the gain spectrum. On account of diffraction divergence, the flux of this radiation propagates over the entire width of the strip, it is intensified at locations with high charge-carrier density, and its power is comparable to that of the radiation in the fundamental mode. The regime becomes multimodal.

In summary, the investigations of the current dependence of the directional pattern of the radiation of diode mesastrip lasers with a small strip width (10 μm) have shown that the spatial distribution of the laser radiation in the plane of the $p-n$ junction consists of a single longitudinal mode whose half-width varies with increasing current. Initially, for currents near threshold, the width of the pattern decreases, reaching its lowest value for $I = (2.0-2.5) I_{\text{th}}$, after which it starts to increase. This current dependence of the half-width of the directional pattern is due to the current dependence of the current-carrier and light flux distributions over the width of the strip. For currents near threshold the light flux distribution is cosinusoidal, in the current interval $(2.0–2.5) I_{\text{th}}$ the distribution becomes almost uniform, and for high currents, as a result of the fact that the carrier density at the strip edges is higher than at the center of the strip, lateral optical confinement appears, resulting in narrowing of the light flux, and the light flux distribution over the width of the strip once again becomes cosinusoidal. For currents for which the directionality of the radiation is maximum, the radiation spectrum has a maximum unimodal character, which is explained by the nearly uniform distribution of the gain over the strip width.

This work was supported in part by a grant from the Ministry of Science of the Russian Federation as part of the program ''Optics and laser physics'' and in part by a contract with INCO-Copernicus No. PL965093.

[a)]e-mail: yak@ioptl.ioffe.rssi.ru

[1]T. N. Danilova, O. I. Evseenko, A. N. Imenkov, N. M. Kolchanova, M. V. Stepanova, V. V. Sherstnev, and Yu. P. Yakovlev, Pis'ma Zh. Tekh. Fiz. **22**, 7 (1996) [Tech. Phys. Lett. **22**, 645 (1996)].
[2]T. N. Danilova, A. P. Danilova, O. G. Ershov, A. N. Imenkov, M. V. Stepanov, V. V. Sherstnev, and Yu. P. Yakovlev, Fiz. Tekh. Poluprovodn. **32**, 241 (1998) [Semiconductors **32**, 218 (1998)].
[3]A. N. Baranov, T. N. Danilova, O. G. Ershov, A. N. Imenkov, V. V. Sherstnev, and Yu. P. Yakovlev, Pis'ma Zh. Tekh. Fiz. **19**, 30 (1993) [Tech. Phys. Lett. **19**, 543 (1993)].
[4]P. G. Eliseev and A. P. Bogatov, Trudy Fiz. Instit. Akad. Nauk **166**, 15 (1986).
[5]P. P. Saskov, Solid State Commun. **82**, 739 (1992).

Translated by M. E. Alferieff